

Compaction behaviour of (Mn,Zn)-ferrite granulate

Citation for published version (APA):

Glass, H. J. (1994). *Compaction behaviour of (Mn,Zn)-ferrite granulate*. [Phd Thesis 1 (Research TU/e / Graduation TU/e), Chemical Engineering and Chemistry]. Technische Universiteit Eindhoven.
<https://doi.org/10.6100/IR415055>

DOI:

[10.6100/IR415055](https://doi.org/10.6100/IR415055)

Document status and date:

Published: 01/01/1994

Document Version:

Publisher's PDF, also known as Version of Record (includes final page, issue and volume numbers)

Please check the document version of this publication:

- A submitted manuscript is the version of the article upon submission and before peer-review. There can be important differences between the submitted version and the official published version of record. People interested in the research are advised to contact the author for the final version of the publication, or visit the DOI to the publisher's website.
- The final author version and the galley proof are versions of the publication after peer review.
- The final published version features the final layout of the paper including the volume, issue and page numbers.

[Link to publication](#)

General rights

Copyright and moral rights for the publications made accessible in the public portal are retained by the authors and/or other copyright owners and it is a condition of accessing publications that users recognise and abide by the legal requirements associated with these rights.

- Users may download and print one copy of any publication from the public portal for the purpose of private study or research.
- You may not further distribute the material or use it for any profit-making activity or commercial gain
- You may freely distribute the URL identifying the publication in the public portal.

If the publication is distributed under the terms of Article 25fa of the Dutch Copyright Act, indicated by the "Taverne" license above, please follow below link for the End User Agreement:

www.tue.nl/taverne

Take down policy

If you believe that this document breaches copyright please contact us at:

openaccess@tue.nl

providing details and we will investigate your claim.

**COMPACTION BEHAVIOUR OF
(Mn,Zn)-FERRITE GRANULATE**

H.J. Glass

Compaction behaviour of (Mn,Zn)-ferrite granulate

PROEFSCHRIFT

ter verkrijging van de graad van doctor aan de
Technische Universiteit Eindhoven,
op gezag van de Rector Magnificus, prof.dr. J.H. van Lint,
voor een commissie aangewezen door het College van
Dekanen in het openbaar te verdedigen op
donderdag 14 april 1994 om 16.00 uur

door

Hylke Jan Glass

geboren te Delft

Dit proefschrift is goedgekeurd door de promotoren

prof.dr. G. de With

prof.dr. R. Metselaar

CIP-DATA KONINKLIJKE BIBLIOTHEEK, DEN HAAG

Glass, Hylke Jan

Compaction behaviour of (Mn,Zn)-ferrite
granulate / Hylke Jan Glass. - Eindhoven :
Eindhoven University of Technology
Thesis Eindhoven, - With refs. - With
summary in Dutch.

ISBN 90-3860-313-4

Subject headings: compaction / ceramics / porosimetry / modelling

Copyright © 1994 by H.J. Glass, Eindhoven, The Netherlands.
Printed by Letru Press, Helmond (04920-37797), The Netherlands.

aan mijn ouders
aan mijn grootmoeders

Contents

Chapter 1

Introduction	1
1.1. Classification of materials research	2
1.2. Introduction to ferrites	4
1.3. Magnetism of (Mn,Zn)-ferrite	6
1.4. Processing of (Mn,Zn)-ferrite	7
1.4.1. Homogeneity	7
1.4.2. Mechanical properties	8
1.4.3. Electromagnetic properties	9
1.4.4. Dimensional properties	9
1.5. Optimization of the compaction of granulate	10
References	11

Chapter 2

Physical homogeneity: the use of porosimetry	12
2.1. Significance of the physical homogeneity	12
2.2. Analysis of the MIP technique	13
2.2.1. Introduction	13
2.2.2. Derivation and application of the intrusion equation	13
2.2.3. Alternative pore shapes	15
2.2.4. Pore size distribution	17
2.2.5. Accuracy of MIP	18
2.2.6. Reproducibility of MIP	21
2.3. Nitrogen adsorption technique	22
2.3.1. Introduction	22
2.3.2. Pore size distribution	24
2.4. Statistical analysis	26
2.5. Characterization of (Mn,Zn)-ferrite products	27
2.5.1. Introduction	27
2.5.2. BET technique	28
2.5.3. MIP technique	28
2.5.4. Software	29
References	29

Chapter 3

Analysis of the compaction of (Mn,Zn)-ferrite	31
3.1. Introduction	31
3.2. Material, pressing equipment and analysis techniques	33
3.3. Influence of internal friction	34
3.4. Influence of external friction	37
3.5. Compaction model	38
3.6. Analysis of potcores	40
3.7. On the homogeneity of compacts	45
3.8. Discussion and conclusion	47
References	48

Chapter 4

Modelling compaction with representative cells	49
4.1. Introduction	49
4.2. Experimental data and compaction model	49
4.2.1. Definition of porosity	49
4.2.2. Subdivision of porosity	51
4.3. Construction of representative cells	56
4.3.1. Analysis of the compaction process	56
4.3.2. Classification of cells	59
4.3.3. Basic relations for N , N_c and L/r_p	60
4.3.4. Basic relations for Ψ	65
4.3.5. Basic relations for λ	66
4.3.6. Relation between two- and three-dimensional modelling	67
4.4. Characterization of the compaction process	68
4.4.1. Introduction	68

4.4.2.	Existence of agglomerates	68
4.4.3.	Compaction of granules	70
4.4.4.	Compaction of agglomerates	70
4.4.5.	Compaction of particles	71
4.5.	Verification of the model	72
4.5.1.	Introduction	72
4.5.2.	Initial shape of the granules and particles	73
4.5.3.	On particle deformation during compaction	76
4.5.4.	Significance of the transition densities	77
4.6.	Discussion and conclusion	82
	References	83

Chapter 5

	Modelling compaction with the concept of fractal scaling	85
5.1.	Introduction	85
5.2.	Fractal characterization of the granulate	87
5.2.1.	Introduction	87
5.2.2.	Single particle	87
5.2.3.	Ordered particle packings	91
5.2.4.	Packing of granules	93
5.3.	Fractal characterization of compaction	96
5.3.1.	Introduction	96
5.3.2.	MIP data	96
5.3.3.	Sedimentation data	98
5.3.4.	Averaged data	99
5.3.5.	Compaction process data	100
5.4.	Fractal characterization of compaction	102
5.4.1.	MIP analysis	102
5.4.2.	Sedimentation analysis	103
5.4.3.	Averaged data	104
5.4.4.	Process data	105
5.4.	Discussion and conclusion	106
	References	107

Chapter 6

	Analysis of compaction curves	108
6.1.	Introduction	108
6.2.	Measurement of compaction curves	109
6.3.	Characterization of compaction curves	110
6.3.1.	Introduction	110
6.3.2.	Influence of the granulate	111
6.3.3.	Influence of the die characteristics	114
6.4.	Interpretation of compaction curves	115
6.4.1.	Description of the model	115
6.4.2.	Mathematical formulation	119
6.4.3.	Verification of the model	124
6.5.	Discussion and conclusion	126
	References	127

Chapter 7

	Modelling compaction using mechanical tests	128
7.1.	Introduction	128
7.2.	Review of mechanical tests	128
7.3.	Densification and deformation	132
7.4.	Modelling mechanical tests	133
7.4.1.	Characterization of deformation	133
7.4.2.	Characterization of densification	135
7.4.3.	Characterization of strength	139
7.5.	Experimental	141
7.5.1.	Three-point bend test	141
7.5.2.	Diametral compression test	142
7.5.3.	Free compression test	142
7.5.4.	Isotropic and die compaction tests	143

7.5.5.	Recovery of elastic strain	144
7.6.	Analysis of the three-point bend test	147
7.6.1.	Interpretation of the measured data	147
7.6.2.	Mechanical model	151
7.6.3.	Determination of model parameters	155
7.7.	Modelling compaction behaviour	157
7.7.1.	Introduction	157
7.7.2.	Two- and three-dimensional interpretation	159
7.7.3.	Correlations for compaction parameters	162
7.8.	Strength of compacts	164
7.9.	Discussion and conclusion	165
	References	166

Chapter 8

	Simulation of die compaction	168
8.1.	Introduction	168
8.2.	Die wall friction	171
8.3.	Differential method	172
8.3.1.	Axial stress model	172
8.3.2.	Gradient model	174
8.3.	Finite element method	177
8.3.1.	Introduction	177
8.3.2.	Truss model	179
8.3.3.	Element model	180
8.3.4.	Solution of equations	184
8.4.	Simulation results	187
8.4.1.	Introduction	187
8.4.1.	Cylinders and tablets	188
8.4.2.	Potcores	189
8.5.	Discussion and conclusion	191
	References	191

Chapter 9

	Discussion and final remarks	193
9.1	Framework of thesis	193
9.2.	Results	194
9.3.	Discussion and final remarks	197

List of symbols	200
Summary	201
Samenvatting (in Dutch)	202
Acknowledgements	203
Curriculum vitae	203

Chapter 1

Introduction

This thesis deals with the processing of a magnetic ceramic material known as (Mn,Zn)-ferrite. Its excellent electromagnetic properties have led to numerous commercial applications. In this thesis, attention is given to the conventional production route of this material, with emphasis on the relevant properties. In this introductory section, the position of (Mn,Zn)-ferrite in the broad spectrum of materials is indicated.

Scope of this thesis

Optimum product properties are obtained when the material is homogeneous. The homogeneity of the product is influenced by all stages of the processing. Three stages can be distinguished: preparation of the powder, compaction of the powder into the product shape and bonding the powder at elevated temperatures (sintering). During the preparation of the powder, agglomerates are formed. Agglomerates are groups of loosely-bonded particles, which lead to inhomogeneity after sintering. Therefore, it is essential to reduce the number of agglomerates before sintering. This is achieved by pressing the powder into a homogeneous compact. The compaction process is therefore analysed in detail.

During compaction, the density increases through reduction of the porosity. Significant is the development of the pore size distribution (PSD). In section 2, the use of techniques capable of measuring the PSD is analysed. In subsequent sections, approaches to model the powder pressing process are developed. In section 3, an empirical approach, which relates the overall density to the applied pressure, is presented. This approach indicates the relative significance of compaction parameters. On a smaller scale, an approach using representative cells is developed to model the processes underlying compaction (section 4). Combining this model and the evolution of the PSD allows identification of agglomerates. Because data on the initial stage of compaction is limited, the filling of the die is investigated using a three-dimensional representation (section 5). An alternative interpretation of the evolution of the PSD using the concept of fractal scaling is developed in section 6. This approach is also useful for identifying agglomerates.

The applied pressure varies with the position in the die on account of friction with the confining surfaces. Quantification of this effect is important when pressing powder into complicated product shapes. Therefore, an approach based on data obtained from compaction and strength tests is developed in section 7. Incorporating this model in a finite element scheme and simulating density distributions is presented in section 8. Finally, in chapter 9, an overview of the results is presented.

1.1. Classification of materials research

Materials research deals with the preparation and properties of existing and new materials. A distinction is usually made between metals, organic and inorganic materials. An important subclass of inorganic materials is formed by ceramics. These are materials containing compounds of metals with oxygen, nitrogen and/or carbon. On the basis of the atomic structure, three main categories of ceramics can be distinguished:

- crystalline ceramics, whose atomic structure may be represented by a three-dimensional lattice filled with spheres. When the material contains more than one type of metal, the atomic arrangement often corresponds to a basic structure named after the first material found to have the structure. Many ferrites belong to this group.
- non-crystalline ceramics, such as glass, where the arrangement of atoms is practically random.
- glass-ceramics, where crystalline and glassy regions are present. Old-fashioned materials like bricks as well as modern materials like 'Macor' belong to this category.

An alternative classification distinguishes ceramics which have been used for centuries and those which have emerged more recently. The latter category is subdivided according to functionality. Using current terminology:

- traditional ceramics, such as pottery, glass, etc.
- technical ceramics:
 - functional ceramics, which are primarily selected for their magnetic, electric, optical or chemical properties.
 - structural ceramics, which are chosen on account of their strength.

In table 1.1, a number of applications of technical ceramics are given together with the chemical constituents.

Table 1.1: Overview of applications of technical ceramics

Function	Application	Composition
Magnetic	Inducible magnets	$(\text{Mn,Zn})\text{Fe}_2\text{O}_4$
	Permanent magnets	$\text{BaFe}_{12}\text{O}_{19}$
Electric	Capacitors	BaTiO_3 , SrTiO_3
	Semiconductors for use in temperature sensors (NTC, PTC thermistors)	$\text{Mg}(\text{Al,Cr,Fe})_2\text{O}_4$, $\text{Co}_2\text{Al}_2\text{O}_4$, BaTiO_3 , SiC , VO_2
	Insulation material for use in IC's	Al_2O_3 , BeO , MgO , AlN
	Transducers, oscillators	$\text{Pb}(\text{Zr,Ti})\text{O}_3$
	Superconductors	$\text{Bi}_2\text{Sr}_2\text{CaCu}_2\text{O}_{8+\delta}$ $\text{YBa}_2\text{Cu}_3\text{O}_{7.6}$
	Solar battery cells	$\text{CdS-Cu}_2\text{S}$
	Oxygen sensors	ZrO_2
Optical	High pressure Na vapour lamp tubes	Al_2O_3
	Laser material	$\text{Y}_2\text{O}_3\text{-ThO}_2$
	Infrared detectors	PbTiO_3
	Data storage material	$(\text{Pb,Lu})(\text{Zr,Ti})\text{O}_3$
Chemical	Gas sensors	ZnO , SnO_2 , Fe_2O_3
	Humidity sensors	$\text{MgCr}_2\text{O}_4\text{-TiO}_2$, $\text{ZnCr}_2\text{O}_4\text{-LiZnVO}_4$
	Catalyst carrier, zeolite	SiO_2
Thermal	Infrared radiators	ZrO_2 , TiO_2
Mechanical	Cutting tools	Al_2O_3 , TiC , TiN
	Wear resistant materials	Al_2O_3 , ZrO_2
	Heat resistant materials	SiC , Al_2O_3 , Si_3N_4
Biological	Artificial bones, joints, teeth	$\text{Ca}(\text{OH})\text{PO}_4$, Al_2O_3

1.2. Introduction to ferrites

Ferrites is a collective denominator for compounds based on Fe and O which possess excellent electromagnetic properties. Two main types can be distinguished:

- spinel ferrites, with the general formula MeFe_2O_4 , where Me stands for a divalent metal (e.g. Fe^{2+} , Mn^{2+} , Zn^{2+} , Co^{2+} , Ni^{2+} , Mg^{2+}).
- hexagonal ferrites, with the general formula $\text{MeFe}_{12}\text{O}_{19}$, where Me represents an alkaline earth (e.g. Ba^{2+} , Sr^{2+}).

The atomic unit cell of spinel ferrites is cubic and has three directions of easy magnetization. In the absence of electric current or magnetic fields, the orientation of the magnetic moments is random, so that spinel ferrites are non-magnetic. In hexagonal ferrites, the magnetic moment is always oriented parallel to the c-axis. The term hexagonal refers to the structure of the unit cell. By aligning the magnetic moments during processing, a permanent magnet can be created. On account of this difference in magnetic properties, spinel and hexagonal ferrites are termed soft and hard magnetic materials respectively.

Table 1.2: Applications of some important ferrites

Structure	Elements	Applications
Spinel	(Mn,Zn)-ferrite	transformer cores inductor cores yoke rings recording heads
	(Ni,Zn)-ferrite	(same as (Mn,Zn) variety)
	(Mg,Mn)-ferrite	microwave elements
	(Li,Zn)-ferrite	antenna rods
Hexagonal	Ba-hexaferrite	segments for DC motors loudspeakers
	Sr-hexaferrite	(same as Ba variety)

In this thesis, polycrystalline spinel ferrite with composition $\text{Mn}_{0.66}\text{Zn}_{0.25}\text{Fe}_{2.09}\text{O}_4$ has been investigated. The material contains three types of spinel ferrites (MnFe_2O_4 , ZnFe_2O_4 and FeFe_2O_4). Variations in the ionic radii of Fe^{2+} , Mn^{2+} and Zn^{2+} are "absorbed" by the spinel structure so that the material is single phase. Given a suitable microstructure, ferrites with this

composition can have the following electromagnetic properties:

- high initial permeability μ_i
- low coercivity H_c
- high saturation magnetisation B_s
- low remanence B_r
- low power loss P_L

These properties are a function of the frequency and the temperature. The temperature where the magnetisation becomes zero is known as the Curie temperature T_C . The main magnetic properties are illustrated in fig.1.1.

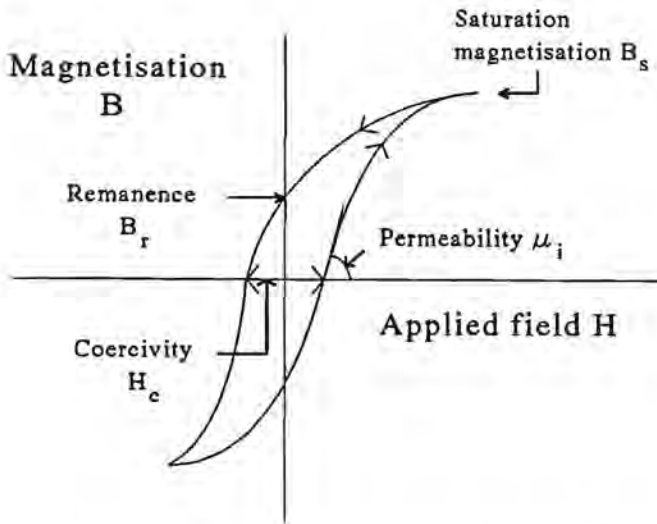


Fig.1.1: Typical B-H loop for a Fe-excess (Mn,Zn)-ferrite. Note that the area enclosed by the loop reflects the contribution of hysteresis to the power loss P_L of the material during use.

The power loss P_L is attributed to the effect of hysteresis and eddy currents. Eddy current losses may be reduced by increasing the resistivity of the material. In practice, this is achieved by adding small amounts of CaO and SiO₂. Previous studies [1] have revealed that an optimum addition of either oxide exists. Because the solubility of these oxides in the spinel lattice is low, they migrate to the grain boundary during sintering. At the grain boundary, they form a second-phase, which increases the mobility of the grain boundaries. SiO₂ may induce exaggerated grain growth if it is unevenly distributed, but no effect is observed below a critical content [2].

1.3. Magnetism of (Mn,Zn)-ferrite

The excellent electromagnetic properties of (Mn,Zn)-ferrite are determined by the chemical composition and the homogeneity of the material. Although this study is focussed on the relation between the homogeneity and the processing, it is useful to briefly review the relation between the electromagnetic properties and the chemical composition.

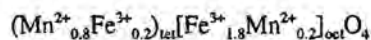
Magnetism originates from the spin of unpaired electrons. Alignment of the spins occurs when an atom has more than one singly-occupied orbital. Consequently, the largest magnetic moment is theoretically possible in elements with a partially filled f-subshell (7 orbitals) such as the lanthanides (e.g. europium, dysprosium and gadolinium). Although permanent magnetism is observed in these materials, it is weak on account of complex interactions between the electrons and the relatively large size of the atoms. These factors cause elements of the first series of the transition metals (iron, cobalt, nickel) with partially filled 3d-subshell to form stronger magnets.

In ionized form, divalent manganese (Mn^{2+}) and trivalent iron (Fe^{3+}), with half-filled 3d-subshells, have potentially the largest magnetic moment. The magnetic properties, however, also depend on the interaction with the anion. For example, a simple oxide such as MnO is diamagnetic because the bonding of Mn^{2+} with the anion, oxygen (O^{2-}), neutralizes the unpaired spins.

Ferrimagnetism occurs when the magnetic moments of the metal ions is opposite but unequal in size, so that a net magnetic moment is observed. More complex oxides, like all spinel ferrites, belong to this category. Relevant in this respect is the distinction between normal and inverse spinel structures. In the case of normal spinels, the trivalent ions are located in the octahedral interstices with the divalent ion occupying the tetrahedral interstice. With inverse spinels, the divalent ion has changed places with a trivalent ion.

In a normal spinel, the magnetic moments of the two Fe^{3+} ions are opposite on account of the interaction between the octahedral interstices and therefore cancel out. Any magnetism then results from the divalent metal ion. This explains the relatively high (saturation) magnetization of manganese ferrite. Zinc ferrite, by contrast, is diamagnetic because the outer subshell of Zn^{2+} is completely filled.

A combination of manganese and zinc ferrite is found to have a higher saturation magnetization B_s than manganese ferrite. A qualitative explanation is based on the inequality of tetrahedral ($]_{tet}$) and octahedral ($]_{oct}$) interstices. Assuming that manganese is divalent only, it is found that about 20% of the Mn^{2+} is located in the octahedral interstices. In formula:



Divalent zinc ions, always found in tetrahedral interstices, are able to reduce the amount of Mn^{2+} in the octahedral interstices, which improves the saturation magnetization B_s . Zinc ions

are also thought to prevent oxidation of divalent manganese to Mn^{3+} [2].

In this (Mn,Zn)-ferrite, the excess iron remains divalent. The amount of excess iron corresponds to the amount of Fe^{2+} required for (magnetic) anisotropy compensation at the operating temperature of (Mn,Zn)-ferrite products [3]. A secondary maximum in the permeability is observed when the magnetic anisotropy is zero. A reduced partial oxygen pressure during the final processing stage (sintering) is required to prevent oxidation of the Fe^{2+} to Fe^{3+} , which shifts the secondary maximum to higher temperatures. The opposite is observed if the partial oxygen pressure is too low.

These considerations make (Mn,Zn)-ferrite particularly suitable as a soft magnetic material, although careful processing is required.

1.4. Processing of (Mn,Zn)-ferrite

The manufacture of (Mn,Zn)-ferrite products by a conventional ceramic process consists of the following stages:

- weighing and mixing of the raw materials (Fe_2O_3 , $MnCO_3$ and ZnO).
- pre-sintering to obtain chemical homogeneity.
- milling to yield particles of smaller than 1 μm .
- addition of water and (organic) binder to form a slurry.
- spray-drying the slurry to produce granulate.
- forming the granulate into a product by die compaction.
- sintering of the compact.

Optimization and attuning of each stage is required to yield products with the desired properties. Besides mechanical and electromagnetic properties, dimensional properties are relevant. The importance of each property will be briefly discussed in sections 1.4.2 to 1.4.4. All three types of product properties are strongly influenced by the physical and chemical homogeneity, which is discussed in section 1.4.1.

1.4.1. Homogeneity

Homogeneity is defined at four levels that differ in nature and scale:

- macroscopic (> 1 mm):
 - large-scale phase- and/or structural inhomogeneity (e.g. cracks)
- mesoscopic (10 - 100 μm):
 - phase- and/or crystallite structure inhomogeneity within distinct regions
- microscopic (0.01 - 10 μm):
 - crystallite-pore inhomogeneities:

- pores of varying size
- extended defects such as:
 - line defects (e.g. dislocations)
 - plane defects (e.g. errors in the superposition of layers)
 - volume defects (e.g. clusters of particles)
- atomic (< 1 nm):
 - point defects such as vacancies and substituted ions.

The physical structure of a material is measurable down to a microscopic level, where it is called the microstructure. The microstructure refers to the pore and grain size distributions as well as the connectivity of the pores, pore and grain boundary surface areas, etc. An indication for the physical homogeneity is given by the breadth of the size distributions. The chemical structure is observed down to the atomic level, making chemical homogeneity relevant on all scales.

1.4.2. Mechanical properties

The main mechanical property of interest is strength. Ferrite products are brittle and therefore susceptible to damage during use. When the local stress intensity exceeds a critical value upon contact with another material, cracks are formed. These grow in the lateral and transversal directions. Lateral cracks may cause the product to break (fracture), while transversal cracks near the surface are responsible for loss of material during machining and chipping when in use. In general, maximum resistance to crack propagation is achieved when:

- pores are small and the pore size distribution is narrow.
- grains are uniform in size.
- intercrystalline bonding is strong and unaffected by the presence of second-phases on the grain boundaries.
- residual stresses are compressive.

These characteristics have bearing on the microstructure of the product and the chemical composition. When manufacturing (Mn,Zn)-ferrite products, the chemical composition is selected in consideration of the desired electromagnetic properties. Therefore, the maximum attainable resistance to fracture is obtained by optimizing the microstructure. In general, a uniform microstructure is considered advantageous. Control of the microstructure requires that both the physical and chemical homogeneity are optimized during processing. This is achieved by the following measures:

- using raw materials with high chemical purity.

- adding specific dopes which promote the sinter rate and lead to uniform grain growth.
- multi-stage or prolonged presintering.
- milling the calcined material to particles of an optimum size with a narrow particle size distribution.
- producing granulate with uniformly stacked particles.
- removing all intergranular porosity during compaction.
- adapting the sintering curve (temperature and oxygen content in the atmosphere as a function of time) to yield high-density products with the correct grain size.

1.4.3. Electromagnetic properties

The electromagnetic properties are determined by the chemical composition, the chemical homogeneity and the microstructure of the product.

Obtaining a material with the desired composition is complicated by an increase in the Fe-content resulting from attrition of the iron milling balls and evaporation of Zn during sintering [4]. The former may be corrected for by adjusting the initial composition. Restricting the evaporation of Zn requires adaptation of the sintering process. An option is to increase the partial pressures of oxygen or zinc in the sinter oven.

The maximum size of single-domain grains is roughly 3 μm [5]. In products with larger grains, the grain size distribution is not critical. Residual porosity should be minimized because pore space reduces the saturation magnetization. Furthermore, pores should be evenly distributed, which requires a high physical homogeneity.

1.4.4. Dimensional properties

Dimensional properties concerns the shape and size of the product. If prescribed tolerances are exceeded, post-processing is required. Therefore, control of product dimensions is important. This is achieved by optimization of the parameters of the pressing and sintering stages, where the product is formed and densified. With the specified product size, dies are designed on the basis of the (optimum) compact density and shrinkage during sintering. Compaction parameters should be optimized to produce a physically homogeneous compact, while sinter parameters should be selected to yield the specified shrinkage without affecting product shape or the desired microstructure. These conditions generally make use of specialized equipment necessary.

If variation of compaction and sinter parameters alone is not sufficient, granulate properties have to be modified. Characteristics of the granulate, determined by the process stages prior to compaction, are:

- the binder. Significant is the type and content as well as the distribution within the granules.

- the size distribution of the granules.
- the particles. Relevant are physical aspects, such as the size distribution and stacking within the granules, as well as chemical aspects, such as the degree of conversion to spinel ferrite and the distribution of various oxides.

Suitable granulate should have excellent flowability and readily deform under pressure. Furthermore, compacts or deformed granulate should possess sufficient strength to be handled. Finally, stacking of the particles affects the sinter behaviour. As a rule, spherical particles with high chemical homogeneity yield optimum sinter behaviour.

In conclusion, both types of homogeneity are important for optimum properties. However, a rough subclassification is possible: physical homogeneity has the largest effect on the mechanical and dimensional properties, while chemical homogeneity is more important for the electromagnetic properties.

1.5. Optimization of the compaction of granulate

Optimization of the compaction process requires attuning of the process parameters of all the processing stages. For the compaction of (Mn,Zn)-ferrite granulate, the following sequence is suggested:

- 1) establish the dimensions of the final product. Relevant aspects include:
 - electromagnetic properties. Note that the permeability and the power loss vary with the composition and microstructural parameters such as the grain size and the density.
 - spatial constraints, imposed by ongoing trend towards miniaturization.
- 2) select a suitable granulate. Issues include the sprayability of the slurry used to produce the granulate, the type and content of the binder used and the bulk density of the granulate.
- 3) establish the optimum pressed density. This is a trade-off between the homogeneity of the compact and die wear.
- 4) design a compaction process which produces compacts with the optimum density. With complex-shaped products, compaction from two sides in several stages may be required.
- 5) sinter the compacts and determine whether the differences in the local shrinkage are within the set limits.

In the following chapters, techniques are developed which facilitate or accelerate the

optimization of the compaction process. These have bearing on the characterization of granulate properties, the determination of the optimum density and prediction of the density distribution within the compact.

References

1. T. Akashi, 'Precipitation in Grain Boundaries of Ferrites and Their Electrical Resistivities-Part I', NEC Research & Development, no. 8, 1966, 89-106.
2. A.A. Shernyakov et al., 'NMR study of the distribution of manganese and iron ions of different valence in manganese-zinc ferrites', Inorganic Chemistry, 1990, 1305-1320.
3. G.H. Jonker, A.L. Stuijts, 'Controlling the properties of electroceramic materials through their microstructure', Philips technical Review, vol. 32, no. 3/4, 1971, 79-95.
4. C.R. Hendricks, V.W. Amarakoon, D. Sullivan, 'Processing of Manganese Zinc Ferrites for High-Frequency Switch-Mode Power Supplies', Ceramic Bulletin, vol. 70, no. 5, 1991, 817-823.
5. P. van der Zaag et al., 'The initial permeability of polycrystalline MnZn ferrites: The influence of domain and microstructure', vol. 74, no. 6 (1993), 4085-4095.

Chapter 2

Physical homogeneity: the use of porosimetry

2.1. Significance of the physical homogeneity

In view of the influence of physical homogeneity on the properties of (Mn,Zn)-ferrite products, it is necessary to characterize the physical homogeneity experimentally. Various types of physical homogeneity can be distinguished. On a macroscopic level, high homogeneity implies that there are no visible cracks. Cracks may be formed during sintering if local variations in the microscopic homogeneity of the compact are large. The latter also produces shape irregularities, which affects the dimensional properties.

Given the importance of homogeneity, it is necessary to characterize of the microstructure of the 'green' and final product. An ideal microstructure is represented by equisized grains with residual porosity evenly distributed throughout. In other words, high physical homogeneity is reflected by narrow size distributions.

Control of the final microstructure requires knowledge of consolidation behaviour of the 'green' product. This is determined by the parameters of the compaction and sintering processes and the granulate properties. During each process stage, densification occurs through reduction of porosity. However, during sintering, grain growth impedes the rate of densification.

Measuring pore size distributions during processing provides insight into the evolution of the physical homogeneity. Because pore size distributions cannot be determined in situ, two types of samples are collected: compacts pressed to various densities and partially sintered products which are quenched in air. The pore size distributions are measured with:

- mercury intrusion porosimetry (MIP).
- nitrogen adsorption porosimetry, referred to as the BET technique, after Brunauer, Emmett and Teller.

The objective of this section is to analyze the interpretation of raw data obtained with these techniques. Important aspects are the accuracy and the reproducibility in general and when applied to (Mn,Zn)-ferrite compacts or products.

2.2. Analysis of the MIP technique

2.2.1. Introduction

Mercury intrusion porosimetry (MIP) makes use of the non-wetting property and high surface tension of liquid mercury. Mercury will not flow into (small) cavities, pores or cracks spontaneously unless pressure is applied (fig. 2.1). The intruded volume of mercury as a function of the applied pressure constitutes the raw data of this technique. In the sections 2.2.2 and 2.2.3, interpretation of the pressure in terms of a pore size and shape has been evaluated by developing a new set of equations. Once the relation between pore volume and pore size is established, the pore size distribution can be obtained. Furthermore, detailed attention is given to the accuracy and reproducibility of the pore size distribution.

All measurements were performed with the Micromeritics 9310 PoreSizer apparatus. The resolution of the AD convertor was such that the smallest measuring interval is about 0.15 % of the total measuring range of 200 MPa. This restricts the number of data points to 670, which limits the accuracy of the experimental pore size distribution.



Fig. 2.1: Non-wetting property of mercury. With mercury, the contact angle θ is larger than 90° (left), whereas, with most liquids, θ is smaller than 90° (right).

2.2.2. Derivation and application of the intrusion equation

Pores are modelled as simple non-connected channels. The condition of equilibrium states that the mechanical work, dW , should balance the change in surface energy, dG . If the pressure is raised slowly, equilibrium is maintained continuously. The mechanical work is given by:

$$dW = PdV \quad (2-1)$$

where P is the pressure and dV the volume change. The surface energy is somewhat more complicated. Consider a three-phase system solid(s)/vapour(v)/liquid(l). The change in free energy, at constant P and T , is given by:

$$dG = \gamma_{sl}dA_{sl} + \gamma_{sv}dA_{sv} + \gamma_{lv}dA_{lv} \quad (2-2)$$

where γ is the surface energy at the various interfaces and dA the change in interfacial area.

In the following, the surface energy is assumed to be equal to the surface tension. During intrusion, the area of the solid covered with mercury is equal to the area originally covered with gas so that $A_s = A_{sv} = A$. This simplifies eq. (2-2):

$$dG = (\gamma_{st} - \gamma_{sv})dA + \gamma_{lv}dA_{lv} \quad (2-3)$$

All three surface tensions are present along the boundary where mercury, solid and vapour meet. They are related by the Young-Dupré equation:

$$\gamma_{sv} - \gamma_{st} = \gamma_{lv}\cos(\theta) \quad (2-4)$$

This yields:

$$dG = \gamma_{lv}(-\cos(\theta)dA + dA_{lv}) \quad (2-5)$$

At equilibrium, eqs.(2-1) and (2-5) are equal:

$$PdV = \gamma_{lv}(-\cos(\theta)dA + dA_{lv}) \quad (2-6)$$

The quantity dA_{lv} is usually assumed to be zero, i.e. the area and shape of the cross-section is constant, since inadequate information on the change of cross-sectional area is available. Accordingly, with $\gamma' = \gamma_{lv} \cos(\theta)$:

$$P = -\gamma' dA/dV \quad (2-7)$$

For pores with regular geometry, it is possible to derive general expressions for the area A and volume V :

$$\begin{aligned} A &= \int (\alpha_s r l(r)) dr \\ V &= \int (\alpha_v r^2 l(r)) dr \end{aligned} \quad (2-8)$$

where α_s and α_v are shape-dependent constants and $l(r)$ the length of pores with size r . For an infinitesimal change in the area covered and the volume intruded:

$$\begin{aligned} dA &= \alpha_s r l(r) dr = B l(r) dr \\ dV &= \alpha_v r^2 l(r) dr = A l(r) dr \end{aligned}$$

or

$$dA/dV = \alpha_s / (\alpha_v r) = B/A \quad (2-9)$$

where B and A denote the boundary and area of the channel cross-section respectively. The ratio α_A/α_V effectively represents a shape factor characterizing the geometry of the pore. Combining eq. (2-7) and (2-9) produces the relation between the pressure P and the pore 'size' r :

$$P = -\gamma' \alpha_A / (\alpha_V r) = -\gamma' B/A \quad (2-10)$$

In general, the pores are assumed to be cylindrical. If we associate r with the radius, the shape factor α_A/α_V equals 2. Consequently, eq. (2-10) becomes:

$$\begin{aligned} P &= -2\gamma'/r \\ &= -2\gamma_{lv} \cos(\theta)/r \end{aligned} \quad (2-11)$$

This corresponds to the equation originally proposed by Washburn [1], which is the most widely applied intrusion equation.

The surface tension γ and contact angle θ vary according to the chemical nature of the sample and its structure. Though no consensus exists in the literature, the following general values have been adopted:

$$\gamma = 48.5 \cdot 10^{-2} \text{ N/m}$$

$$\theta = 130^\circ$$

The use of these values yields good correspondence when comparing the average pore size determined with MIP and SEM [2,3].

Mercury will not fill a distribution of pore sizes at one pressure. Mercury will only penetrate into the smaller cavities when the pressure is further increased. Therefore the volume of intruded mercury at one pressure is a result of penetration into all pores larger than a particular size. The cumulative pore volume measured in this way as a function of pressure serves as a starting point for further interpretation.

2.2.3. Alternative pore shapes

The application of mercury intrusion porosimetry (MIP) is extended if it is possible to derive an indication of the shape of the pores or if a shape other than the cylindrical shape can be used for the interpretation. In order to incorporate the shape factor α_A/α_V , introduced in the previous subsection, an alternative derivation is considered.

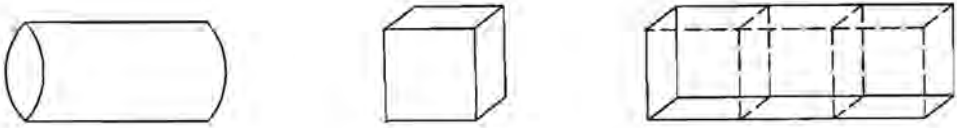


Fig. 2.2: Representation of elementary pore shapes used to interpret MIP data.

Table 2.1 lists α_A/α_V for the geometries shown in fig. 2.2 as well as the physical interpretation of the 'size' r in eq. (2-9).

Table 2.1: Shape factors and interpretation for various model pore geometries

Shape	α_A/α_V	r
cylinder with radius r	$2\pi/\pi = 2$	$2\pi r^2/(2\pi r) = r$
cube with edge L	$4/1 = 4$	$4L^2/(4L) = L$
block with n cubes	$(2n+2)/n \rightarrow 2$	$2nL^2/(L(2n+2)) \rightarrow L$

Given that the cross-section of a pore has a constant and known shape, the use of the shape factors in table 2.1 is not restricted by the assumptions underlying the derivation of the intrusion equation based on work equilibrium (section 2.2.2). In order to verify the validity of this statement, a mechanical derivation is considered. Applying the Young-Laplace equation for pressure differences over any curved surface to an infinitesimally small area:

$$\Delta(P_v - P_{Hg}) = \gamma(1/r_1' + 1/r_2') \quad (2-12)$$

where r_1', r_2' are the principal radii of curvature of the mercury-vapour interface. Subscripts v and Hg represent vapour and mercury respectively. The total pressure difference over the meniscus is given normalized integration of the radii over S :

$$P_v - P_{Hg} = \gamma \int (1/r_1' + 1/r_2') dS / \int dS \quad (2-13)$$

Solution of the integral in eq. (2-13) requires information on the shape of the boundary of the

(pore) cross-section, which is usually not available. In the case of a circular cross-section, the principal radii are given by:

$$r_1' = r_2' = r/\cos(\theta) \quad (2-14)$$

where r denotes the principal radius of curvature of the pore.

In the absence of information on the shape, one has to assume a shape and verify the validity for a certain material from experimentally obtained data. The most simple, open-ended three-dimensional shape is that of a cylinder. With the circular cross-section extending into the plane, the principle radii at the boundary of a cylinder at any depth are similar to those of a two-dimensional circle. Substituting r_1 and r_2 in eq. (2-13) with eq. (2-14) and recognizing that $P_{Hg} \gg P_v$:

$$P_{Hg} = -\gamma \int (2\cos(\theta)/r) dS \quad (2-15)$$

Since r is a constant, eq. (2-15) is integrated with respect to S :

$$P_{Hg} = -2\gamma\cos(\theta)/r \quad (2-16)$$

The derivation shows that, for pore shapes other than the cylinder, a spatial description of the mercury meniscus is required in order to solve eq. (2-13). Because such descriptions are highly complicated, this affects the entire form of eq. (2-16), so that merely adapting the shape factor F is not sufficient. Furthermore, the pore size distribution is only fully determined for cylindrically shaped pores. In all other cases, a smearing of the pore size distribution occurs. Finally, in practical situations, the shape of the meniscus is expected to deviate in a random manner, which makes the use of more complicated pore shapes than the cylinder suspect.

2.2.4. Pore size distribution

A pore size distribution (PSD) indicates the volume of pores of a particular size present. Using MIP data, the PSD is defined as the differential volume of pores V as a function of the pressure P :

$$PSD = dV/dP \quad (2-17)$$

Recognizing that $P=C/r$, where C is a constant and r the pore radius:

$$dP = Cd(1/r) = -C/r^2 dr \quad (2-18)$$

Substituting dP in eq. (2-17):

$$\text{PSD} = (-r^2/C) dV/dr \quad (2-19)$$

Note that physical significance of the dimension of the PSD, $[m^5/N]$, is unit volume per unit pressure.

2.2.5. Accuracy of MIP

The accuracy of MIP is determined by the measurement technique and the interpretation of the raw data. the compressibility of the components within the apparatus. Relevant is expansion of the glass burette and compression of the mercury and the sample. By measuring the intrusion without a sample, the net effect of the glass expansion and mercury compression is found as a function of pressure. Sample compression is only measurable if the sample is non-porous.

The effect of compressibility can be corrected by calculating the coefficients of compressibility. Under isothermal conditions, the compressibility coefficient β is defined as follows:

$$\beta = - 1/V(dV/dP)_T \quad (2-20)$$

Throughout the pressure range of interest (1-2000 bar), β varies linearly with the pressure P [4]:

$$\beta = \beta_0 + \beta_1 P \quad (2-21)$$

Combining eqs.(2-20) and (2-21), followed by integration with respect to pressure, yields:

$$\ln(V/V_0) = \beta_0 P + \beta_1 P^2/2 \quad (2-22)$$

Expansion of $\ln(V/V_0)$ in a Taylor series yields:

$$\ln(V/V_0) = \Delta V/V_0 - (\Delta V/V_0)^2/2 + \dots \quad (2-23)$$

where $\Delta V=(V-V_0)/V_0$. As the ratio $\Delta V/V_0$ is small, higher order terms can be neglected. Eq. (2-23) becomes:

$$\Delta V = (\beta_0 P + \beta_1 P^2/2)V_0 \quad (2-24)$$

The volume change due to compressibility is due to both mercury and glass:

$$\Delta V(\text{overall}) = \Delta V(\text{mercury}) - \Delta V(\text{glass}) \quad (2-25)$$

The individual contributions are represented by eq. (2-24), so that eq. (2-25) contains four parameters.

The measured intrusion during a measurement without sample increases non-linearly with pressure. Because the curve has no extremes within the pressure range under consideration, numerical determination of at most two parameters is justified. Therefore, the coefficients for mercury, being relatively invariant, are taken from literature [5]:

$$\begin{aligned} \beta_0(\text{mercury}) &= (4.02 \pm 0.02)10^{-11} \text{ Pa}^{-1} \\ \beta_1(\text{mercury}) &= (1.3 \pm 0.2)10^{-20} \text{ Pa}^{-2} \end{aligned}$$

The volume of mercury intruded as a result of compression was fitted to eq. (2-25) using the least-squares criterium. The following compressibility coefficients β for the glass of the burette were determined:

$$\begin{aligned} \beta_0(\text{glass}) &= (2.85 \pm 0.11)10^{-11} \text{ Pa}^{-1} \\ \beta_1(\text{glass}) &= (0.0 \pm 0.6)10^{-20} \text{ Pa}^{-2} \end{aligned}$$

The validity of this approach can be verified by determining the compressibility of the glass with the pulse-echo technique. For this purpose, a sample of burette glass is prepared with two plan parallel faces. The longitudinal and transverse wave velocities, which were measured at 10 and 5 MHz respectively, were found to be:

$$\begin{aligned} v_l &= 5.542 \text{ km/s} \\ v_s &= 3.466 \text{ km/s} \end{aligned}$$

where v_l is the longitudinal and v_s the transverse wave velocity. The compressibility β was calculated from these values together with the density of the glass (2.22 g/cm^3). Using the formula for isotropic materials, the loss tangent was found to be smaller than 0.15, so no correction for damping is required. The resulting value for β_0 , $3.09 \cdot 10^{-11} \text{ Pa}^{-1}$, compares favourably with the value determined from MIP.

The accuracy of the pulse echo technique was verified by measuring the compressibility of borosilicate (type 142) glass. The value of β_0 was found to be $3.16 \cdot 10^{-11} \text{ Pa}^{-1}$, which compares well with the values in the literature [5]. This confirms that the correction of MIP data is performed with reliable data.

The compressibility β of non-porous solids may be determined by extending eq. (2.27):

$$\Delta V = \Delta V(\text{Hg}) - \Delta V(\text{glass}) + \Delta V(\text{sample}) \quad (2-26)$$

When the β 's of glass and mercury are known, the remaining volume change can be attributed to compression of the sample. The compressibility of the sample is also characterized with β_0 and β_1 . Using two fully-dense synthetic materials, polyethylene (PE) and rubber, the accuracy of this technique is investigated. The following coefficients have been determined with MIP:

$$\begin{aligned} \beta_0(\text{PE}) &= (4.43 \pm 0.32)10^{-10} \text{ Pa}^{-1} \\ \beta_1(\text{PE}) &= (-1.5 \pm 0.1) 10^{-16} \text{ Pa}^{-2} \\ \beta_0(\text{Rubber}) &= (2.06 \pm 0.26)10^{-8} \text{ Pa}^{-1} \\ \beta_1(\text{Rubber}) &= (-4.5 \pm 0.7) 10^{-17} \text{ Pa}^{-2} \end{aligned}$$

Comparison with literature values shows good correspondence when considering the large range of chemical compositions of PE and rubber [4,5]:

$$\begin{aligned} \beta_0(\text{PE}) &= 3.2 \cdot 10^{-10} \text{ Pa}^{-1} \\ \beta_1(\text{PE}) &= -2.5 \cdot 10^{-18} \text{ Pa}^{-1} \\ \beta_0(\text{Rubber}) &= 2.0 \cdot 10^{-8} \text{ Pa}^{-2} \\ \beta_1(\text{Rubber}) &= -5.0 \cdot 10^{-17} \text{ Pa}^{-2} \end{aligned}$$

After correcting for the compressibility of mercury and glass, the accuracy of MIP is obtained by analysing a filter membrane produced by ANOTEC Separations. SEM photos taken perpendicular to the surface indicate that these membranes have a regular pore structure with a narrow pore size distribution. The median pore size of three types of membranes (specified average pore size: 0.02, 0.1 and 0.2 μm) was determined with MIP and image analysis of SEM photos. With the latter, the pore size was determined by averaging the size of 100 randomly-intersected pores. Results are given in table 2.2.

Table 2.2 shows that the difference between the direct (image analysis) and indirect determination (MIP) of the mean pore size is small. Therefore, the MIP technique gives an accurate impression of the pore size (distribution). Furthermore, the limited influence of the compressibility correction is clearly demonstrated.

Table 2.2: Determination of accuracy of MIP

Specified size (μm)	Measured pore size		Δ (%)	MIP (uncorrected) (μm)
	MIP (corrected) (μm)	Image analysis (μm)		
0.02	0.0738	0.0743	0.67	0.0730
0.1	0.1020	0.1032	1.16	0.1015
0.2	0.1139	0.1160	1.81	0.1137

2.2.6. Reproducibility of MIP

The reproducibility of MIP is determined by measuring the pore size distribution of a series of 9 (Mn,Zn)-ferrite compacts with similar densities. The density of the compact can be found from mass m and sample volume V or from the theoretical density ρ_{th} combined with the total sample and pore volume. In equations:

$$\rho = m/V \quad (2-27a)$$

or

$$\rho = \rho_{th} (V - V_p)/V \quad (2-27b)$$

where V_p is the total pore volume of the sample. Comparison of the densities indicates whether all pores are intruded during a MIP measurement.

Table 2.3: Reproducibility of compaction and MIP

Binder: acrylic II, die diameter: 14.09 mm, compaction pressure: 125.0 MPa

	Mean	Standard deviation	Variation (%)
Pore size	0.1282 μm	0.0030 μm	2.34
Density	2.649 g/cm^3	0.038 g/cm^3	1.44

Table 2.3 shows that the reproducibility of MIP measurements is good.

Summarizing, we conclude that, although the precise interpretation of the MIP data is difficult, the method yields reproducible results, which correspond well with results from independently determined data.

2.3. Nitrogen adsorption technique

2.3.1. Introduction

Measurable quantities of nitrogen are absorbed on solid surfaces at temperatures close to the temperature at which liquefaction of nitrogen occurs (77.2 K). When nitrogen is passed into a previously evacuated chamber, the pressure in the chamber is determined by the volume of nitrogen admitted and the volume adsorbed on the surface. Two types of adsorption can be distinguished: physical adsorption, where the molecules are bonded to the surface by van der Waals interaction, and chemisorption, where molecules are bonded to the surface chemically. The difference between these types of adsorption is shown in fig. 2.3.

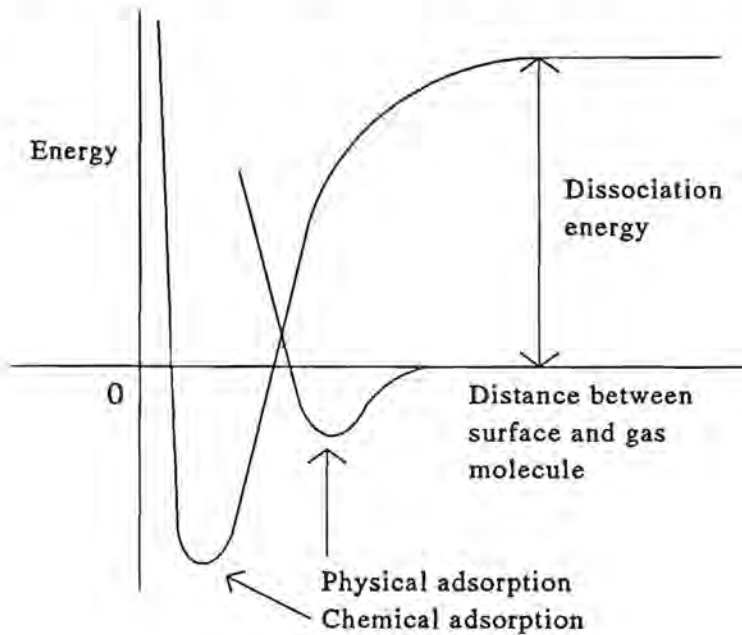


Fig. 2.3: Schematic representation of adsorption. On account of the smaller bonding energy, physical adsorption is a faster and reversible process than chemisorption. Often physical adsorption precedes chemisorption, lowering the activation energy required to dissociate the diatomic gas molecules.

The surface area is proportional to the volume of nitrogen required to form a monolayer. In practice, two extremes are distinguished: the surface is covered by a monolayer only or by an infinite number of layers. In both cases, the layers are only complete when the pressure

in the chamber approaches the saturation pressure of nitrogen. When a chemical reaction occurs between the nitrogen and the surface, it is realistic to assume that the coverage consists of a monolayer only. Without this interaction, formation of multilayers occurs. This difference is reflected by the relation between the pressure and the adsorbed volume of nitrogen V_{ads} , which is known as the adsorption isotherm (fig. 2.4). Note that the pressure is normalized with P_o , which is defined as the saturated equilibrium (vapor) pressure of nitrogen at 77.2 K.

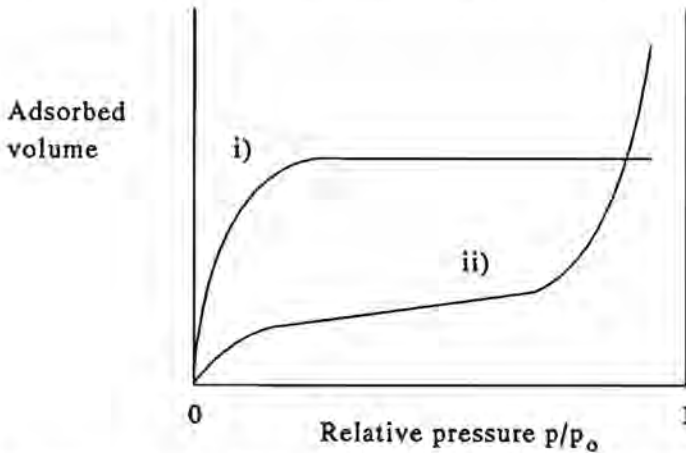


Fig. 2.4: Adsorption isotherm when i) chemisorption and ii) physical adsorption occurs.

The surface area can be represented by a finite number of adsorption sites when the cross-sectional area of nitrogen is known. By assuming that all sites are equivalent, the relation between the adsorbed volume of nitrogen, the volume required for monolayer coverage and the pressure in the chamber can be modelled. Two prominent models will be briefly discussed. Both models require that equilibrium exists in the chamber, i.e. the rate of adsorption equals the rate of desorption. For monolayer coverage, an equation known as the Langmuir isotherm is obtained:

$$V_{ads}/V_{mono} = KP/(1 + KP) \quad (2-28)$$

where V_{ads} = adsorbed volume of nitrogen
 V_{mono} = volume of nitrogen in a monolayer
 K = adsorption parameter
 P = pressure

For multilayer coverage, an isotherm due to Brunauer, Emmett and Teller (BET) is derived:

$$V_{\text{ads}}/V_{\text{mono}} = CP/((P_0 - P)(1 - (1 - C)(P/P_0))) \quad (2-29)$$

where C is an interaction parameter and P_0 the saturation pressure of nitrogen. Because either equation contains an additional parameter (K respectively C), more than one point (V_{ads}, P) is required to determine V_{mono} . Through rearrangement, linear expressions are obtained. For the Langmuir isotherm:

$$1/V_{\text{ads}} = 1/V_{\text{mono}} + 1/(V_{\text{mono}}KP) \quad (2-30)$$

A plot of $1/V_{\text{ads}}$ versus $1/P$ allows determination of V_{mono} from the intercept and K from the slope. For the BET isotherm:

$$P/(V_{\text{ads}}(P_0 - P)) = 1/(V_{\text{mono}}C) + P(C - 1)/(V_{\text{mono}}CP_0) \quad (2-31)$$

Plotting $P/(V_{\text{ads}}(P_0 - P))$ versus P/P_0 yields C and V_{mono} . The latter can be converted to the surface area A given the density of liquid nitrogen and the cross-sectional area of molecule of nitrogen. The suitability of either model is determined by the goodness-of-fit. In general, the BET isotherm applies because nitrogen is relatively inert.

The shape of pores in a sample can be determined if reference measurements are available. Reference measurements should reflect the thickness of the adsorbed layer on a *flat* surface as a function of the pressure. If a graph of the adsorbed volume V_{ads} versus the thickness of the reference layer for similar pressures is linear, the sample contains no pores. An increase of the slope of the graph indicates the presence of cylindrical pores, where condensation occurs on account of the curved surfaces. On the other hand, a decrease of the slope at higher thicknesses indicates that the pores are slit-shaped. This shape limits the thickness of the layer whilst reducing the surface area where nitrogen can be adsorbed.

All measurements were performed with a Omicron Omnisorp 100. In this apparatus, a continuous flow of nitrogen is administered into the sample burette. The corresponding ambient pressure is also measured continuously. This principle achieves a higher resolution when compared to periodic introduction of fixed volumes into the sample burette. However, a disadvantage of the continuous introduction is higher sensitivity to external disturbances.

2.3.2. Pore size distribution

The pore size distribution obtained from BET measurements is based on processing of the desorption isotherm rather than the adsorption isotherm. This is a result of the improved stability of adsorbed molecules when compared to adsorbing molecules [6]. Quantitative interpretation makes use of the Kelvin equation, which can be derived on thermodynamic grounds [7]. This equation relates the relative pressure P/P_n at which adsorbed gas will

spontaneously evaporate to the principal radii of curvature of the pore:

$$RT \ln(P_0/P) = \gamma_{lv} \cos(\theta) V_m (1/r_1 + 1/r_2) \quad (2-32)$$

where R = gas constant = 8.3144 J/mol/K

T = temperature = 77.2 K

P_0 = saturation pressure of nitrogen at 77.2 K

P = ambient pressure

γ_{lv} = surface tension of liquid nitrogen = 8.85 10^3 N/m

θ = the contact angle in the pore = 0°

V_m = molar volume of nitrogen = 3.469 10^5 m³/mol

r_1, r_2 = principal radii of curvature

For cylindrical pores, r_1 and r_2 both equal the pore radius r . Because only the relative pressure P_0/P and the pore size r will vary strongly, eq. (2-32) can be reduced to:

$$r = 9.55 / \ln(P_0/P) \text{ [nm]} \quad (2-33)$$

The adsorbed volume of nitrogen V_{ads} is known as a function of the relative pressure. However, V_{ads} refers to the volume of gas adsorbed. In order to relate to the actual pore space, V_{ads} is converted to the liquid volume V_l . At 77.2 K, the ratio of the gas and liquid density is 1.54 10^{-3} . In equation:

$$V_l = 1.54 \cdot 10^{-3} V_{ads} \text{ [cm}^3\text{]} \quad (2-34)$$

Plotting V_l versus r as a function of the relative pressures yields the pore size distribution.

This framework has been refined by developing increasingly sophisticated theories. These are based on the experimentally-supported assumption that nitrogen will remain adsorbed on the pore wall after the centre of the pore has emptied [8,9,10,11,12,13]. The thickness of the layer has been determined in model systems and has led to various correlations and tables. The best known semi-empirical equation is due to Halsey [10], who correlated the thickness t directly to the relative pressure:

$$t = a / (5 / \ln(P_0/P)) \quad (2-35)$$

where a is the thickness of a monolayer of nitrogen. Usually, the value of a is taken to be 0.354 nm, which is less than expected on the basis of the cross-sectional area of a nitrogen molecule (= 0.162 nm²). In a liquid state, however, this is considered acceptable. The

effective pore radius is then given by summation of the Kelvin pore radius derived from eq. (2-31) and the thickness which remains after desorption:

$$r = r_k + t \quad (2-36)$$

where r_k is the pore radius found from eq. (2-33). Because both r_k and t vary with the relative pressure only, a pore size distribution is found.

A further refinement assumes that the thickness of the layer that remains adsorbed will gradually decrease with decreasing pressure. It has been experimentally found that, for every relative pressure, the thickness of the layer has an equilibrium value. This value is further determined by the pore radius. The volume desorbed due to decrease in the thickness of layers in partially emptied pores is then subtracted from the volume attributed to pores of a size given by eq. (2-34). With this approach, due to Broekhoff and de Boer [11,12], the pore volume corresponding to the largest pores is calculated first. Then the pore volumes corresponding to (increasingly) smaller pores are found after correcting for the desorption due to thinning of the layers in all larger pores. The equilibrium values of the thickness are tabulated and require interpolation at the required relative pressure.

The most advanced refinement is due to Le Cloux [13], who found that the interaction of nitrogen with the pore wall affects the equilibrium thicknesses defined by Broekhoff and de Boer. The interaction is of a chemical nature, and can be expressed in the BET parameter C (see previous section) obtained from the BET-plot. Essentially, Le Cloux extends the Broekhoff-de Boer approach by using five tables, which contain equilibrium thicknesses valid for a certain range of C .

2.4. Statistical analysis

A single-peaked pore size distribution can be characterized in terms of position, breadth (at some height) and shape. When the distribution is discretized, the data can be processed to yield characteristic parameters. A consistent technique to derive these parameters is to calculate the moments m_i of the distribution. Moments are defined about an arbitrary r_0 :

$$m_i = \sum(r_j - r_0)^i / N \quad (2-37)$$

The first moment ($i=1$) with respect to the origin ($r_0=0$) is the average or mean pore size r_m . This quantity indicates the position of the distribution. In order to characterize the distribution, all other moments are defined about the mean pore size so that $r_0=r_m$. For $i>1$:

$$m_i = \sum(r_j - r_m)^i / N \quad (2-38)$$

The second moment ($i=2$) represents the variance σ^2 . The standard deviation σ is a measure for the width of the distribution. The standard deviation relative to the mean yields a dimensionless quantity known as the coefficient of variation v :

$$v = \sigma/r_m \quad (2-39)$$

Higher moments describe the shape of the distribution. These are generally normalized by dividing with the standard deviation σ to the power i . For $i>2$:

$$m_i' = m_i/\sigma^i \quad (2-49)$$

The third moment (m_3') is the skewness and represents the degree of asymmetry of the distribution. The parameter m_3' has a positive value if the tail to the right of the peak is longer than the tail to the left. The skewness of perfectly symmetric peaks is necessarily zero.

Finally, the kurtosis (m_4') indicates the degree of peakedness of the distribution. It is usually interpreted relative to the so-called normal distribution. The kurtosis of a normal distribution is 3. Distributions having relatively higher peaks have higher values for the kurtosis, whereas relatively flat-topped distributions have lower values.

Besides the parameters obtained from moments, other convenient measures are possible. For example, the position of the distribution may also be characterized by the mode, which is the pore size at which the peak has the maximum value. Another useful measure is the median which corresponds to the pore size at which half the pore volume is intruded.

Pore size distributions may consist of more than one distinct peak. Because simultaneous characterization is subject to arbitrary conditions, these peaks should be analysed separately using moments.

2.5. Characterization of (Mn,Zn)-ferrite products

2.5.1. Introduction

Because the MIP and BET techniques span complementary pore size ranges, they are theoretically an excellent combination for characterization of the complete pore size distribution. Unfortunately, there are some restrictions. The main restriction is that both techniques require open porosity because closed porosity is not measurable. During compaction and sintering, where the total pore volume is continuously decreased, the fraction of closed porosity increases. In the following subsections, aspects relevant to the application of either technique are presented.

2.5.2. BET technique

Pore size distributions measured with BET essentially reflect the irregularity of the particle surface because the interparticle pores are too large to be measured. Even though the pores decrease in size with the density, the interparticle pore size is still $0.08 \mu\text{m}$ at a density of 3.2 g/cm^3 , which is a relatively high compact density (see section 3.4). A measurement using ferrite particles has been performed in order to measure the volume of surface pores, cavities and cracks. By evacuating the granulate for 16 hours at $250 \text{ }^\circ\text{C}$ prior to the measurement, the binder bonding the particles is removed. The measured volume of pores is found to be negligible. This indicates that the ferrite particles have relatively smooth surfaces. Consequently, the BET technique is less suitable for pore size analysis of particles and compacts than might be expected beforehand.

2.5.3. MIP technique

An accurate measurement with the MIP technique requires that pores have a specific, constant size. The presence of necks can lead to overestimation of the volume fraction of small pores. However, because necks are likely to yield at lower pressures than required to force mercury through through them, rapid filling can occur at lower pressures. This would lead to overestimation of the volume of larger pores. These contradictory mechanisms obscure the significance of the pore size distribution measured with MIP.

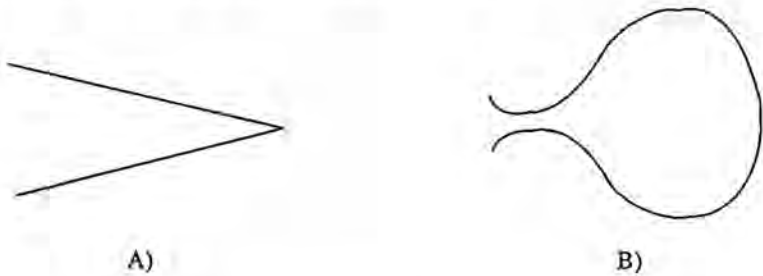


Fig.2.5: Pore structure which is A) ideally suited for MIP measurement and B) corresponding to the real structure.

In accordance with the above, one or at most two distinct peaks are observed in practice. Measurement of the extrusion curve shows that hysteresis occurs but the reproducibility is poor. This can be attributed to the physical change in the structure during intrusion [14].

Interpretation of the measured curve in terms of pore size is not unambiguous either: pores are assumed to be cylindrical. This is expressed in the shape factor α_A/α_V of the pore, which is the ratio of the perimeter and cross-sectional area. For cylinders, α_A/α_V has a value of 2 (see section 2.2.2). Other pore shapes lead to complications in the derivation: the shape

of the meniscus of the intruding mercury in non-circular cross-sections can, in theory, be predicted for ideal cases only.

Despite the many assumptions, results of MIP compare favourably with data from other measurements. They also make the search for improvements of the accuracy, through variation of γ and θ with pressure and correction for the compressibility, questionable.

Compared with the BET technique, however, the MIP technique finds more application in view of the large fraction of porosity which is intruded during a measurement. The pore volume is attributed to pores ranging in size from 0.01 to 2 μm . With the unit cell approach introduced in section 2.3, further interpretation of MIP data is sought.

2.5.4. Software

Computer programs have been written in Turbo Pascal 5.0 for the MIP and BET techniques. Each program consists of two parts: i) a program for data acquisition and ii) a program for data processing. Routines for input from or output to the disk drive, plotter, printer, keyboard or console are used by all the programs. The user interface consists of a series of menus, which, for both cases, contains options not present in the software supplied by the manufacturer of the apparatus. For the acquisition of data, the programs offer greater flexibility through an increase of the number of data points and the measurement options. For the processing of data, additional features such as the compressibility correction (MIP) and the choice of various theories (BET) is included. These programs have been used to perform all porosimetry measurements during this study.

References

1. E. Washburn, 'Note on a Method of Determining the Distribution of Pore Sizes in a Porous Material', *Proceedings of the National Academy of Sciences of the United States of America*, vol. 7, 1921, 115-116.
2. J. van Brakel, 'Mercury Porosimetry: State of the Art', *Powder Technology*, vol. 29, 1981, 1-12.
3. A. Liabastre, C. Orr, 'An Evaluation of Pore Structure by Mercury Penetration', *Journal of Colloid and Interface Science*, vol. 64, no. 1 (1978), 1-18.
4. H. Huisman, C. Rasenberg, J. van Winsum, 'An Improved Mercury Porosimetry Apparatus-Some Magnetic Tape Applications', *Powder Technology*, vol. 36, 1983, 203-213.
5. *Handbook of Chemistry and Physics*, 55th edition, edited by R. Weast, CRC Press.
6. S. Brunauer, P. Emmett, E. Teller, 'Adsorption of Gases in Multimolecular Layers', *Journal of the American Chemical Society*, vol. 60, 1938, 309-319.
7. S. Lowell, 'Introduction to Powder Surface Area', Wiley-Interscience Publication, 57-79.

-
8. C. Shull, 'The Determination of the Pore Size Distribution from Gas Adsorption Data', *Journal of the American Chemical Society*, vol. 70, 1948, 1405-1410.
 9. E. Barrett, L. Joyner, P. Halenda, 'The Determination of Pore Volume and Area Distributions in Porous Substances', *Journal of the American Chemical Society*, vol. 73, 1951, 373-380.
 10. G. Halsey, 'Physical Adsorption on Non-Uniform Surfaces', *Journal of Chemical Physics*, vol. 16, no. 10, 1948, 931-937.
 11. J. Broekhoff, B. Linssen, 'Studies on Pore Systems in Adsorbents and Catalysts', *Physical and Chemical Aspects of Adsorbents and Catalysts*, ed. B.G. Linssen, 1-62.
 12. J. de Boer et. al., 'The t-Curve of Multimolecular N₂ Adsorption', *Journal of Colloid and Interface Science*, vol. 21, 1966, 405-414.
 13. A. Lecloux, J. Bronckart, F. Noville, J.-P. Pirard, 'The generalized Broekhoff-de Boer method', *Characterization of Porous Solids*, ed. K.K. Unger et. al., 1988.
 14. M. Ciftcioglu, D. Smith, S. Ross, 'Mercury Porosimetry of Ordered Sphere Compacts: Investigation of Intrusion and Extrusion Pore Size Distributions', *Powder Technology*, 55 (1988), 193-205.

Chapter 3

Analysis of the compaction of (Mn,Zn)-ferrite granulate

3.1. Introduction

Compaction serves to mold powder into the product shape whilst reducing the pore space between the powder particles. The latter is accompanied by an increase in the number of contacts between the particles, which enhances the cohesive strength of the powder. When the powder has sufficient strength to be handled, it is called a compact. However, with (Mn,Zn)-ferrite powder, addition of an organic binder is required to improve the strength. Because the binder has to be removed during the subsequent sintering process, a minimum of binder is used. In order to distribute the binder uniformly over the powder surface, the binder is dissolved in water before being mixed with the powder. The resulting slurry is spray-dried to yield granulate, which consists of agglomerated particles. Because the agglomerates, known as granules, represent preconsolidated units, the stress gradients which occur during compaction are initially reduced. This contributes to reduction of the local differences in the density. Consequently, the use of granulate is advantageous both in terms of compact strength and compaction behaviour.

When pressing (Mn,Zn)-ferrite granulate, two types of friction are distinguished:

- internal friction, which relates to friction between the ferrite particles and between the granules.
- external friction, which refers to friction between the granulate and the containing surfaces (die wall and punch).

The magnitude and variation of the frictional forces is determined by the compaction parameters. Three groups of parameters are distinguished:

- granulate : binder type and content, granule and ferrite particle size, hardness.
- process : pressure, pressing velocity, pressing mode, die wall roughness and hardness, mode of filling.
- product : density, shape and size.

The effects of internal and external friction are investigated separately by varying the compact shape and size. In tablet-shaped compacts, the compact properties are determined mainly by the effect of internal friction (section 3.3). Alternatively, in compacts with a large length-to-diameter (L/D) ratio and/or small dimensions, the effect of external friction is more pronounced (section 3.4).

The compact properties of interest are the density and the homogeneity. The density is

related to the porosity through the theoretical density (i.e. the zero-porosity density). Using mercury intrusion porosimetry (MIP), the porosity and corresponding pore size distribution are experimentally determined. Analysis of the complete compact produces averaged (position-independent) data. Because of the effect of external friction, the microstructure varies with the position in the compact. Therefore, sections of compacts have been analysed.

Given insight into the effects of internal and external friction, a compaction model is established (section 3.5). This model is then used to analyse the density distribution in a cup-shaped compact ('potcore') as a function of the compaction parameters (section 3.6).

Compaction technology

Compaction of granulate occurs when force is applied in one or more directions. The following pressing modes are distinguished:

- in one direction: this process is known as uniaxial compaction, because granulate is compressed by punch displacement parallel to the axis of the die. When both the lower and upper punch are movable, the granulate can be compacted from two sides. This is either performed simultaneously or sequentially. The latter is referred to as phased compaction.
- in two directions: this process, called cylindrical compaction, consists of two compaction steps. Granulate is prepressed uniaxially and placed in a rubber bag. The rubber bag is attached to a punch which is positioned in a pressure chamber filled with fluid. The granulate is compressed by 1) punch displacement in the axial direction and 2) fluid pressure in the radial and circumferential directions.
- in three directions: simultaneous compaction in three principal directions requires that the granulate, packed in a rubber bag, is submerged in a fluid. When the fluid pressure is raised, the granulate is compacted isotropically. Before placing the granulate into a rubber bag, it is pressed into the required shape. Contrary to cylindrical compaction, the rubber bag and compact are evacuated prior to the isotropic compaction.

During this study, the following pressing modes were used:

- uniaxial compaction:
 - single-sided
 - double-sided
 - simultaneous ("synchronous") pressing
 - sequential ("phased") pressing
- isotropic compaction.

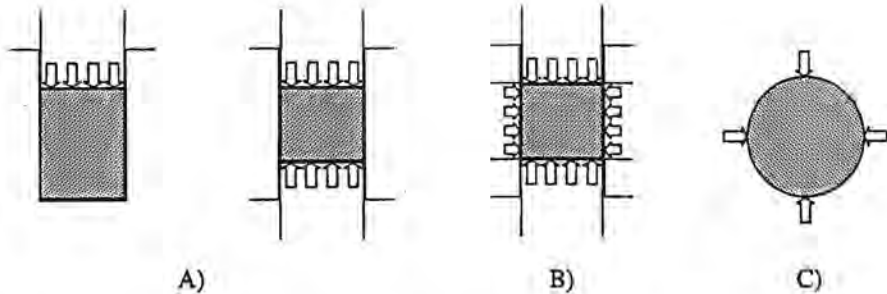


Fig.3.1: Schematic representation of the various pressing modes. Options: A) in one direction, either single or double-sided, B) in two directions and C) in three directions.

In general, the density of the compact can be correlated to the maximum applied pressure. In order to obtain a constant density throughout the compact, a suitable mode of pressing is selected. Single-sided pressing to a high pressure is sufficient when producing cylindrical compacts with a small length-to-diameter (L/D). However, when pressing cylindrical compacts with large L/D ratio's or complex shapes, double-sided pressing is required. In this case, the punch displacement from *either* side has to be specified.

Specification of the punch displacement instead of the maximum pressure requires sophisticated pressing equipment. Control of the punch displacement is influenced by the pressing velocity and knowledge of the compliance of the apparatus. This is especially significant when pressing small compacts.

3.2. Material, pressing equipment and analysis techniques

The (Mn,Zn)-ferrite used has the following composition: $Mn_{0.66}Zn_{0.25}Fe_{2.09}O_4$. Quantities of raw materials corresponding to this composition are mixed, prefired and milled to produce particles with an average size of 2 μm . Slurries are prepared by mixing the particles with water and one of the following binders:

- acrylic supplied by Rohm and Haas (denoted as acrylic I).
- acrylic supplied by Roehm (denoted as acrylic II).
- polyvinylalcohol (PVA) supplied by Hoechst.
- mixture of PVA and acrylic II.

The content of the binders varies slightly:

- acrylic I : 1.25 mass %
- acrylic II : 0.86 and 1.70 mass %.

- PVA : 1.0 mass %
- mixture : 0.72 mass %

The solids content of each slurry is maintained at 70 %. Spray-drying yields granulate with individual granules varying in size from 60 to 500 μm .

Compacts are pressed in dies made from hardened steel of the type N1019 (composition 1.65C-12Cr-W-Mo-V). Die diameters range from 14.0 to 28.12 mm. The wall roughness of all dies is less than 0.09 μm (R/ISO/0.8mm normal procedure). Both manual and automatic pressing equipment constructed by Fontijne, National Forge, Müller and Federhoff is used for compaction of tablets and cylindrical products. Potcores are pressed with equipment at TNO-Apeldoorn.

Pore size distributions are measured with a Micromeritics PoreSizer (type 9310). Densities are found by measuring the mass with a Sartorius balance (type MP-2002, accuracy 0.1 mg) and the dimensions with a Heidenhahn extensometer (type MT-30, accuracy 1 μm).

3.3. Influence of internal friction

The effect of internal friction is investigated through analysis of samples obtained from the cores of tablet-shaped compacts (thickness 4 mm, diameter 44 mm). The combination of the small L/D ratio and the sample location minimizes the influence of friction with the die wall. The following compaction parameters are expected to strongly influence the pore size distribution of the sample:

- granulate parameter : type of binder
- process parameters : pressure, pressing velocity and pressing mode.
- product parameter : density

Of these parameters, the density and the pressure are directly related. The nature of this relation is examined separately in chapters 6, 7 and 8. Because application of pressure produces both normal and shear stresses during compaction of granulate in a die, only variation of the *overall* density is considered. Two extremes of each parameter were selected:

- binder type (*) : acrylic II - mixture
- density (**) : 2.6 - 3.2 g/cm^3
- pressing velocity : 0.35 - 7.00 cm/s
- pressing mode (***) : three-phased - synchronous

(*) In this study, binders are distinguished by the strength of compacts produced with them. Compacts which contain acrylic II are typically much stronger than compacts

of the same density containing a mixture of acrylic and PVA.

- (**) The density of 2.6 g/cm^3 is the minimum density at which compacts with both types of binder have sufficient strength. Increasing the density requires an exponential increase of the pressure. Therefore, a density of 3.2 g/cm^3 , which equals 62.6 % of the zero-porosity density, is high for all practical purposes.
- (***) Three-phased pressing is performed as follows: first only the upper punch moves, then joined by the die wall and finally only the upper punch again. During the middle phase, the die wall is moved faster in order to simulate movement of the lower punch. Synchronous pressing is simulated by moving both punch and die wall move in the same direction at the same velocity.

Tablets were pressed for all combinations of these parameters although it was not possible to press tablets to 3.2 g/cm^3 synchronously. The cubes were cut from the centre of each tablet with a diamond saw after securing the tablets with double-sided tape. An indication of the physical homogeneity was obtained by measuring the pore size distribution with MIP. Characterization of the pore size distribution with the mean pore size is given in table 3.1.

Table 3.1: Mean pore size (in μm) of compacts pressed with selected parameters

	Pressing mode	Three-phased		Synchronous	
	Velocity (cm/s)	0.35	7.00	0.35	7.00
Binder type	Density (g/cm^3)				
Acrylic II	2.6	0.15	0.15	0.15	0.15
	3.2	0.08	0.08	-	-
Mixture	2.6	0.16	0.15	0.15	0.15
	3.2	0.08	0.09	-	-

Table 3.1 indicates that the mean pore size is mainly influenced by the compact density, while the effects of binder, pressing mode and velocity are negligible. The insensitivity to the binder type suggests that the pore size is determined by the size of the ferrite particles. This is understandable when considering that the binder only constitutes 5 volume-% of the solid material. Variations in the arrangement of the particles, and therefore the pore size, are not observed for variations of the pressing mode and velocity. It is possible that the variations are

not large enough to observe an effect on the pore size.

Table 3.1 shows that the mean pore size decreases with the density. A quantitative relation is obtained from analysis of a series of 8 tablet-shaped compacts. The mean pore size for each compact is given in table 3.2.

Table 3.2: Mean pore size as function of the density of the compact.

Binder type: acrylic II, die diameter: 14.1 mm, compact mass: 2.0 g

Pressure (MPa)	Density (g/cm ³)	Mean pore size (μm)	Pressure (MPa)	Density (g/cm ³)	Mean pore size (μm)
68.1	2.64	0.16	168.9	2.89	0.13
93.3	2.78	0.15	194.1	2.93	0.12
118.5	2.83	0.14	219.3	2.96	0.12
143.7	2.89	0.13	244.5	2.98	0.11

It follows from table 3.2 that the mean pore size is linearly related to the density. Using linear regression, the following relation is obtained:

$$r = -0.134\rho + 0.513 \quad (3-1)$$

This relation is valid for unimodal pore size distributions, i.e. consisting of a single peak. Below a density of 2.8 g/cm³, however, a second peak is observed to the right of the main peak. Although this peak becomes larger as the density decreases, it is still relatively small at the lowest density in table 3.2. Therefore, the use of all the points in table 3.2 for the determination of the parameters in eq. (3-1) is justified.

The emergence of a second peak indicates the presence of another type of pores. This is understandable in view of the structure of granulate: pores between the granules are significantly larger than pores between the particles inside the granules. Alternatively, the second peak could reflect the presence of relatively large pores inside the granules. Such pores are observed when the granules contain distinct clusters or agglomerates of particles which are formed during the granulation process.

When more than one peak is observed, these should be characterized separately. A suitable measure is then the modal pore size, which corresponds to the size where a peak reaches its maximum value.

3.4. Influence of external friction

The effect of friction between the granules and the containing surfaces is investigated by analyzing axisymmetric compacts with large length-to-diameter (L/D) ratio's. A suitable shape is the (massive) cylinder. Because external friction introduces density gradients, the pore size distribution of the whole compact reflects the sum of the local pore size distributions. In order to identify the local variations, cylindrical compacts with respectively a low (2.46 g/cm^3) and a high (2.96 g/cm^3) density have been sectioned and analysed with MIP. The density distributions derived from MIP measurements are given in figs. 3.2 and 3.3.

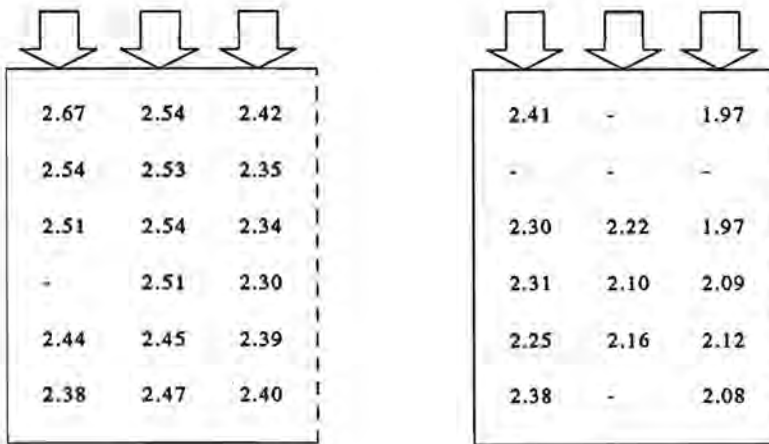


Fig. 3.2: Density distribution in a cylindrical compacts as measured with MIP. The dashed line coincides with the centre of the compact. Compact characteristics: binder acrylic I, density 2.46 g/cm^3 (left) and 2.25 g/cm^3 (right), diameter 28.1 mm and height 32.4 mm . Compaction mode: single-sided uniaxial pressing. Note that variations in the density are relatively larger in the low-density compact.

Fig. 3.2 shows that the highest density is found in the corner directly below the punch. This indicates that friction between the wall and the particles retards the flow of particles. Near the wall, this leads to a relatively high density at the top and a low density at the bottom of the compact. Towards the centre of the compact, the density always decreases. The effect of external friction on this trend appears to be limited.

In fig. 3.3, the density distribution in high-density compacts is shown. Note that the trends are similar but less obvious to those in fig. 3.2. This leads to the important observation

that the density profiles are *independent* of the overall density.

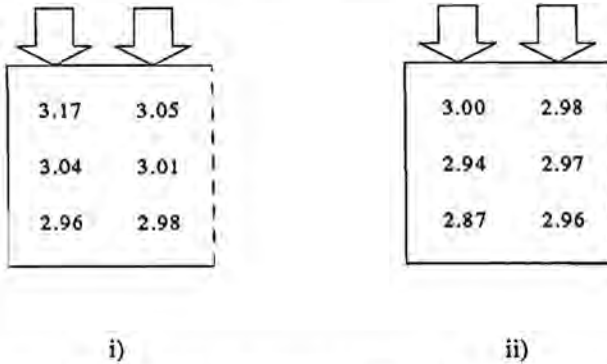


Fig. 3.3: Density distribution in cylindrical compacts as measured with MIP. Compact i) contains acrylic II binder (density 3.01 g/cm^3) while compact ii) contains a mixture of PVA and acrylic II binder (density 2.97 g/cm^3). Both compacts have a diameter of 18.1 mm and a height of 18.4 mm. Compaction mode: single-sided uniaxial pressing.

3.5. Compaction model

The density distributions given in section 3.3 are used to establish a qualitative model for uniaxial die compaction. A model can be based on a *dynamic* representation of the flow of granules, agglomerates and particles. Alternatively, a *static* representation can be used which is based on the equilibrium of the forces. Because both approaches produce the same result, a model based on both representations is developed.

When the punch is moved into a die filled with granules, the granulate resists movement of the punch. However, upon application of force, the granules are deformed. This process increases the number of mutual contacts, which increases the resistance to compaction. It is assumed that the imposed force is balanced by friction between the ferrite particles rather than friction between the granules (internal friction). Deformation of the granules produces radial forces which are ultimately balanced by the die wall. These radial forces generate friction between the die wall and the granulate (external friction), which opposes axial displacement. Therefore, the gradient in the axial compaction force is enhanced near the die wall. Consequently, the largest axial compaction force is expected near the die wall directly below the punch. Considering that the local density is proportional to the locally applied force, it follows that the density near the die wall decreases with increasing distance to the punch. Note the radial force exerted on the die wall is reduced by friction between the granulate and the punch. The bottom of the die produces a similar effect. The model is represented in fig. 3.4.

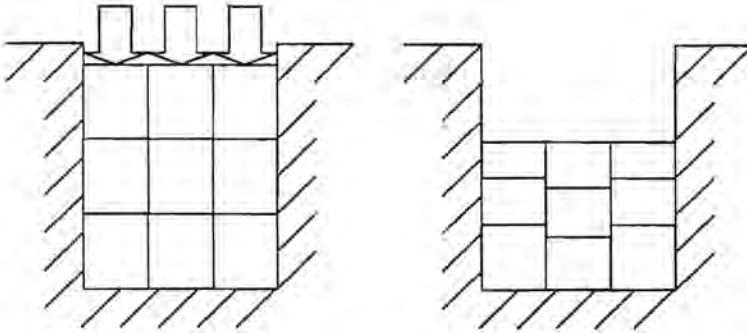


Fig. 3.4: Compaction of granules in an axisymmetric die. The granules are represented by blocks. Friction between granules and the wall has a local effect only although it is larger than friction between the granules themselves. This implies that the axial density gradient is larger near the die wall than in the centre of the compact. Note that the radial granule displacement is zero.

Note that the granules in fig. 3.4 are large compared to the die dimensions and deform as a whole without displacing radially. In practice, the applied force is mainly balanced by internal friction of the particles within the granules. This implies that the density fluctuates with the size of the particles. When considering the density on the scale of a number of granules, the compact can be regarded as a continuum. This representation is advantageous when modelling and simulating the density distribution in compacts without considering the individual particles and granules: only significant trends in the density have to be traced.

The effect of the punch and the die bottom on the density distribution in the compact is different. When the punch moves downwards into a die, granulate is forced to move in the same direction. However, the granules also tend to move outwards in order to relieve the applied force. Near the die wall, this radial movement produces an increase in the local density. On the other hand, near the bottom of the die, the downward movement of the granules is restricted, which also increases the local density. Because friction with the die wall has reduced the axial compaction force along the die perimeter, the radial density at the bottom of the die is the highest in the centre of the die.

The effect of both mechanisms is determined by the ratio of the particle size and die diameter and the length-to-diameter (L/D) ratio of the compact. Other compaction parameters are considered less significant. For example, the die wall roughness, expressing the irregularity of the die surface, is typically in the order of $0.1 \mu\text{m}$, which is much smaller than the size of the particles ($\sim 1 \mu\text{m}$). As a result, the die wall can be represented by a smooth surface.

The proposed model interprets the movement of granulate during compaction. It requires the assumption that the initial distribution of granulate in the die is homogeneous. In practice, differences in the granule size, density and packing exist, causing local density variations. When these differences are significant, the continuum approach is invalid.

Post-compaction effects such as the influence of force during ejection and relaxation of the compact are also not included. The force required to eject the compact increases with the density of the compact. When the compact consists of small particles, large cracks can develop during ejection. In practice, this effect can be suppressed by the presence of a suitable binder. Relaxation of the compact, or expansion due to recovery of elastic deformation, increases with the density of the compact. This partially alleviates density gradients but also distorts the shape of the compact. However, the latter is relatively insignificant compared to the distortion of the shape after sintering a compact containing density gradients.

3.6. Analysis of potcores

The term potcore refers to products with a cup-shaped geometry. A potcore can be subdivided into two distinct sections: the tablet-shaped bottom and the ring-shaped rim. After compaction, the density of these sections should be equal: variations in the density within the compact lead to differential shrinkage during the subsequent sintering process. The latter could produce cracks or make polishing or grinding of the product necessary.

When pressing the bottom and the rim separately, it is relatively easy to obtain compacts with a constant density throughout. Single-sided uniaxial compaction is generally sufficient to obtain homogeneous tablet-shaped compacts. With the ring-shaped rim, double-sided uniaxial pressing can be employed to minimize the density gradient which results from internal and external friction. The difficulty with pressing potcores is that the bottom restricts the double-sided pressing of the rim. This can lead to a significant variations of the density in the rim. Similarly, the density in the bottom section varies because the resistance offered by the central rod is much larger than the resistance offered by the granulate in the rim. Consequently, the density near the die wall is always slightly lower than the density in the centre of the compact.

The pressing of potcores is governed by displacements rather than pressure in order to obtain compacts with the desired dimensions. The filling height of the rim and the bottom are based on the dimensions of the potcore and the required density. Note that the filling height of the bottom and the rim may have be modified on account of the movement of granulate.

The density gradients in a potcore can be reduced by optimizing the pressing action. As a starting point, the double-sided pressing of a potcore in two stages is considered. When pressing the rim first, the density of the bottom near the die wall always remains higher than the density in the centre of the bottom. The opposite is observed when pressing the bottom

first: the density in the centre of the bottom is always higher than the density of the bottom near the die wall. The occurrence of opposite radial gradients indicates that an optimum in the pressing process exists. Because the radial density gradients in the bottom lead to the formation of circumferential cracks during sintering, the optimum pressing process must be established. This requires subdivision of the pressing process into more than two stages. A process consisting of three stages could proceed as follows: first, the punch at the potcore bottom end imposes a part of the required displacement. Subsequently, the punch at the potcore rim end compacts the rim before the punch at the other end completes its scheduled displacement.

Axial density gradients in the rim are inevitable and can only be minimized by lowering the internal and external friction. The internal friction between the particles can be reduced by addition of suitable lubricants during the granulation process. External friction, on the other hand, can be lowered by i) addition of a suitable lubricant to the granulate (eg. Zn-stearate), ii) lowering the roughness of the internal die surfaces and iii) increasing the hardness of the internal die surfaces. The latter can be achieved by coating the die wall with materials which possess a high hardness (e.g. tungsten carbide, titanium carbide).

The influence of internal and external friction on the magnitude of the density gradients in the rim depends on the length and thickness of the rim. The dimensions of the potcores investigated are shown in fig. 3.5.

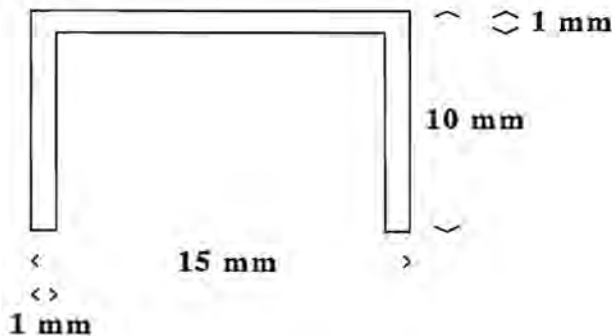


Fig. 3.5: Two-dimensional representation of the potcores analysed in this study. The dimensions are relatively small in order to establish the effects encountered during miniaturization.

Potcores have been pressed in three stages (I, II and III) with the pressing equipment of TNO-Apeldoorn using granulate containing acrylic I binder. Two parameters are varied: i) the subdivision of the punch displacement at the potcore bottom end (fig. 3.6) and ii) the pressing velocity. Both parameters could influence the movement of granules from the middle section of the bottom to the rim or vice versa.

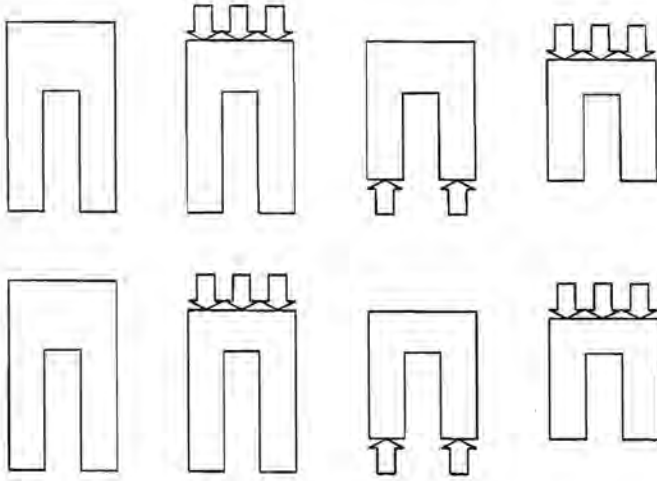


Fig. 3.6: Three-stage compaction of a potcore with small initial displacement (top) and a large initial displacement (bottom). Note that the total displacement in either direction is similar: only the subdivision of the displacement of the punch at the bottom of the potcore is varied.

Table 3.3 compares the scheduled displacements with the experimental values for two different pressing velocities.

Table 3.3: Scheduled and actual displacements (in mm)

Stage	Scheduled	Velocity	Stage I	Stage II	Stage III
I	0.25	1 mm/s	0.47	10.73	0.73
II	11.0				
III	0.75				
I	0.50	10 mm/s	0.68	10.78	0.62
II	11.0				
III	0.50				
I	0.75	1 mm/s	0.80	10.82	0.26
II	11.0				
III	0.25				
I	0.75	10 mm/s	1.05	10.79	0.09
II	11.0				
III	0.25				

Table 3.3 indicates that the scheduled displacement for stage I is exceeded for both velocities. Note that this effect becomes more significant with increasing velocity. Furthermore, the scheduled displacement is not realized for stage II, while the sum of the displacements during stage I and III is not constant. Although these problems can be partly alleviated by correcting for the compliance of the pressing equipment, table 3.3 illustrates the difficulty of displacement-controlled pressing of small compacts.

Insight into the density distribution is obtained by sectioning the potcore into four parts: three rings originating from the rim and the bottom. The density distribution of each part is measured with mercury intrusion porosimetry (MIP). Results are given in table 3.4. Table 3.4 (page 44) shows that, for the velocity of 1 mm/s, the influence of the initial displacement on the density distribution is strong. Note that the largest density is observed in the bottom for the intermediate initial displacement. With the velocity of 10 mm/s, the differences in the density are smaller for comparable initial displacements. For the largest initial displacement, the densities become comparable with those present at the velocity of 1 mm/s for a *smaller* (actual) initial displacement. In other words, a relatively high velocity and short initial pressing stage is advantageous in terms of the homogeneity, although the density in the upper rim section remains significantly larger than the other densities. Note that it is not clear whether these results apply for potcores with other dimensions.

Table 3.4: Density distribution of sectioned potcores (in g/cm³)

	Displacement (mm) 0.25-11.0-0.75		0.50-11.0-0.50		0.75-11.0-0.25	
	Velocity (mm/s) 1	10	1	10	1	10
Upper rim	2.94	3.00	2.93	2.93	2.98	3.01
Middle rim	2.67	2.77	2.59	2.66	2.70	2.72
Lower rim	2.63	2.73	2.59	2.66	2.51	2.50
Bottom	2.62	2.73	2.72	2.74	2.49	2.42

Table 3.4 indicates that the effect of the pressing velocity becomes significant when the effect of external friction is large. The mode of pressing, on the other hand, becomes relevant when the compact has a more complex geometry than the cylinder.

The pore size distributions present in the potcore sections is obtained with the MIP measurement. The distribution are characterized in terms of the mean pore size and the standard deviation. Results are presented in tables 3.5 to 3.7.

Table 3.5: Mean pore size and standard deviation of the pore size distribution
Scheduled displacements (mm): 0.25-11.0-0.75

Position	Velocity = 1 mm/s			
	Mean (μm)	Std. dev. (μm)	Mean (μm)	Std. dev. (μm)
Upper rim	0.11	0.06	0.10	0.07
Middle rim	0.16	0.09	0.14	0.08
Lower rim	0.16	0.09	0.14	0.08
Bottom	0.17	0.10	0.15	0.09

Table 3.6: Mean pore size and standard deviation of the pore size distribution
Scheduled displacements (mm): 0.50-11.0-0.50

Position	Velocity = 1 mm/s			
	Mean (μm)	Std. dev. (μm)	Mean (μm)	Std. dev. (μm)
Upper rim	0.12	0.06	0.11	0.07
Middle rim	0.16	0.09	0.14	0.08
Lower rim	0.18	0.11	0.14	0.08
Bottom	0.16	0.10	0.15	0.09

Table 3.7: Mean pore size and standard deviation of the pore size distribution
Scheduled displacements (mm): 0.75-11.0-0.25

Position	Velocity = 1 mm/s			
	Mean (μm)	Std. dev. (μm)	Mean (μm)	Std. dev. (μm)
Upper rim	0.11	0.07	0.10	0.06
Middle rim	0.14	0.08	0.15	0.08
Lower rim	0.17	0.09	0.19	0.12
Bottom	0.18	0.10	0.18	0.10

Comparison of these results indicates that the influence of the pressing velocity and the mode

of pressing on the pore size distribution is negligible. This confirms the results of section 3.3.

3.7. On the homogeneity of compacts

The homogeneity can be defined as a measure for the irregularity in the packing of the particles. The latter can be expressed in terms of the standard deviation of the pore size distribution. Insight into the fluctuation of the standard deviation is obtained by analysing compacts pressed with a controlled variation of the compaction parameters. Details of the experimental setup have been given in section 3.3. Table 3.8 lists the standard deviation derived from the measured pore size distributions.

Table 3.8: Standard deviation (in μm) of the pore size distribution

	Pressing mode	Three-phased		Synchronous	
	Velocity (cm/s)	0.35	7.00	0.35	7.00
Binder type	Density (g/cm^3)				
Acrylic II	2.6	0.08	0.08	0.08	0.07
	3.2	0.04	0.04	-	-
Mixture	2.6	0.08	0.08	0.08	0.08
	3.2	0.04	0.04	-	-

A more general expression for the homogeneity is obtained by normalizing the standard deviation with the mean pore size. This quantity corresponds to the coefficient of variation of the pore size distribution. Because the homogeneity intuitively increases when the standard deviation decreases, the use of the complement is proposed:

$$\zeta_p = 1 - s_p/r \quad (3-4)$$

where ζ_p is the homogeneity with respect to the pore size distribution, s_p the standard deviation and r the mean pore size. Combining the data in tables 3.1 and 3.3 indicates that the homogeneity ζ_p is constant and equals 0.5. Therefore, it is concluded that the homogeneity ζ_p is independent of the density in the range of densities considered.

The definition of the homogeneity has been based on characterization of differences in the packing structure. However, the significance of this definition depends on two aspects:

the influence of the homogeneity on the compact strength and on the occurrence of differential shrinkage during sintering.

The strength of a compact is influenced by the packing of the particles, the type of binder bonding the particles and the loading conditions. The packing of the particles can be characterized using the porosity and the pore size distribution. With decreasing porosity, the strength of the compact increases while the (average) size of the pores decreases. This indicates that large pores are more detrimental for the strength than small pores. Thus the definition of the homogeneity based on the standard deviation of the pore size distribution only has limited significance for the strength of the compact. Similarly, the presence of more than one peak at lower compact densities implies that the inverse of mean pore size is also not a suitable measure for the strength.

An alternative is to consider the higher-order moments of the pore size distribution. The definitions in section 2.5 show that the values of the higher-order moments are increasingly influenced by the larger pores of the pore size distribution. Because a similar reasoning applies for the strength, the higher-order moments could provide an indication of the strength.

The suitability of two higher-order moments, the skewness and kurtosis, is investigated. By attributing the increase in strength with increasing density to the compression of the largest pores, it can be assumed that the reduction in size of these pores is much larger than the reduction in size of the bulk of the pores. In other words, the largest pores are compressed preferentially. Therefore, in theory, the skewness decreases with the density. The kurtosis, on the other hand, is a measure for the ratio of the height and breadth of the distribution. The relation with the strength is therefore less obvious than is the case with the skewness.

The skewness and the kurtosis have been determined for the pore size distributions of all compacts measured with MIP. For all measurements, the skewness and kurtosis appear to be coupled: a high skewness is accompanied by a high kurtosis and vice versa. However, the correlation of the skewness and kurtosis with the density is not clear. Although a certain variation in the strength of compacts of a similar density is expected, the trend that the strength increases with the density should be obvious. Instead, the skewness and kurtosis are strongly influenced by the measurement technique used. This is understandable because the corresponding pore volume is small and the size of the pores approaches the largest pore size which can be measured. The latter implies that fluctuations in the initial measurement conditions become apparent, which is reflected in a poor accuracy and reproducibility of the initial section of the pore size distribution. Consequently, the definition of homogeneity is not modified in order to have more bearing on the strength of the compact. The relation between the strength and the density, however, will be examined in chapter 7.

The occurrence of differential shrinkage during sintering is related to the presence of *axial* density gradients in the compact. *Radial* gradients, on the other hand, are generally smaller and vary with the axial position. Consequently, the characterization of axial density

gradients is relevant for the prediction of differential shrinkage. Density gradients are reflected in the pore size distribution making the homogeneity defined with eq. (3-4) a suitable measure. However, the pore size distribution is not known as a function of the axial position. Therefore, differences in the homogeneity are not automatically reflected in differential shrinkage.

3.8. Discussion and conclusion

A qualitative compaction model based on the analysis of internal and external friction has been developed. Experimental input for the model is obtained by measuring the pore size and density distributions present in the compact with MIP. Results indicate that, for cylindrical compacts, the type of binder, the pressing velocity and mode of pressing have little influence on the physical structure for a given pressure. By contrast, the relation between the pressure and the density is strong: upon increasing the pressure, the density increases and the mean pore size decreases. It is found that, for densities between 2.6 and 3.0 g/cm³, the mean pore size decreases linearly with the density. Note that, below a density of 2.8 g/cm³, a second peak emerges. This indicates that different types of pores can be found in the granulate. This is due to the nature of the granulate, in which at least two solid units (particles, granules) can be distinguished.

On account of internal and external friction, the pressure varies as a function of the position in the compact. Consequently, the density also varies within the compact. The variation of the frictional forces can be predicted by considering an axial cross-section of the compact. Near the punch, the magnitude of the frictional forces is relatively large. This produces a relatively high-density zone. Because this zone can balance relatively large forces, the axial compaction force decreases, producing an axial density gradient. In the radial direction, the highest density is found in the corner between the die wall and punch as a result of external friction. Because of this high local density, the axial compaction force near the die wall is lower than in the centre of the compact. As a result, the density in the bottom corner is lower than the density in the centre at the bottom of the compact. This shows that the radial density gradient at the top and bottom of the compact are opposite.

The magnitude of the density gradients depends on the dimensions the compact (length L , diameter D), as well as the applied pressure: the higher the pressure, the smaller the gradients. While the model is able to predict density gradient gradients in uniaxially-pressed cylindrical compacts, additional considerations are required when the geometry of the compact is more complex. For example, the density distribution in the potcore is influenced by the pressing velocity and the mode of pressing. Variation of these parameters can be used to manipulate the movement of granules during compaction. The optimum combination, however, varies from case to case.

References

Suggested reading:

- G. Bockstiegel, 'Probability Aspects in Powder Compacts', Proceedings of the First International Conference on the Compaction and Consolidation of Particulate Matter (1972), 51-61.
- E. Ernst, F. Thümmler, P. Beiss, 'Friction measurements during powder compaction', Powder Metallurgy International, vol. 23, no. 2 (1991), 77-84.
- H. Fischmeister, E. Arzt, 'Densification of powders by particle deformation', Powder Metallurgy, vol. 26, no. 2 (1983), 82-88.
- R. Frey, J. Halloran, 'Compaction Behaviour of Spray-Dried Alumina', Journal of the American Ceramic Society, vol. 67, no. 3 (1984), 199-203.
- G. Onoda, F. Urban, 'Mechanics of Stress and Green Density Variation within Ceramic Powder Compacts: a critical assessment', Proceedings of International Symposium of Factors in Densification and Sintering of Oxide and Non-oxide Ceramics (1978), Japan, 89-99.
- E. Pedersen, 'Model for Powder Compression which takes Die Wall Friction into account', Powder Technology, vol. 45 (1986), 155-157.
- R. Thompson, 'Mechanics of Powder Pressing: I, Model for Powder Densification', Ceramic Bulletin, vol. 60, no. 2 (1981), 237-251.
- R. Youshaw, 'Compaction of Spray-Dried Powders', Journal of the American Ceramic Society, vol. 61, no. 2 (1981), 227-230.

Chapter 4

Modelling compaction with representative cells

4.1. Introduction

Data obtained from experiments is related to the structure of (Mn,Zn)-ferrite granulate during compaction using series of cells. Each series of cells represents the development of a particular type of substructure. With (Mn,Zn)-ferrite granulate, two substructures are readily identified: the packing of the granules and the packing of the ferrite particles. Within the granules, the particles form clusters which, if distinct, are known as agglomerates. The packing of agglomerates represents a third type of substructure. Identification of the presence of agglomerates is relevant when optimizing the processing of ferrites.

Experimental data consists of the overall porosity and the pore size distribution of compacts. The porosity and density can be determined from the mass and compact dimensions or using mercury intrusion porosimetry (MIP). The latter also measures the pore size distribution of the compact, which can be characterized with statistical parameters. Modelling the evolution of the pore size distribution during compaction allows identification of the substructures.

In section 4.2, experimental data obtained from the analysis of (Mn,Zn)-ferrite compacts with increasing densities is presented. This data is used to establish a three-stage model of compaction. The development of the substructures during these stages will be represented by series of cells. Construction and characterization of the cells is presented in section 4.3, while correlating the series of cells with the experimental data is done in section 4.4. Aspects of the model are verified with scanning electron microscopy (SEM) in section 4.5.

4.2. Experimental data and compaction model

4.2.1. Definition of the porosity

The porosity ε of a sample with volume V_t is defined as:

$$\varepsilon = V_v/V_t \quad (4-1)$$

where V_v is the void (= pore) volume, which is measured with MIP. The total volume V_t is found by measuring the sample dimensions. Recognizing that granulate consists of solid particles and pores, eq. (4-1) can be rewritten as:

$$\varepsilon = V_v/(V_v + V_s) \quad (4-2a)$$

or

$$\varepsilon = (V_t - V_s)/V_t = 1 - V_s/V_t \quad (4-2b)$$

where V_s is the solid volume, which equals the volume of the ferrite particles and organic binder.

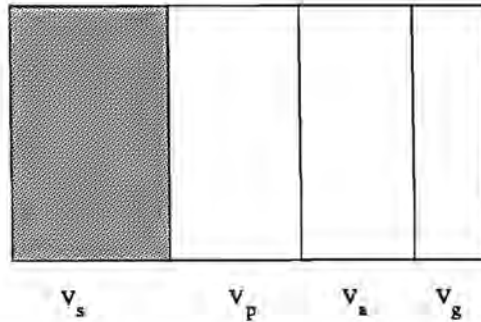


Fig. 4.1: Definition of the porosity ϵ . The porosity is the ratio of the total void volume and the total volume. The void volume consists of the volume of pores between the particles (V_p), the agglomerates (V_a) and the granules (V_g). This makes other definitions of the porosity possible: for example, the porosity between the granules is the ratio of V_g and the total volume.

The pore volume measured with MIP is smaller than the actual pore volume on account of pores which are not intruded. This produces differences in the porosity determined with or without the measured V_v . Therefore, porosities based on the pore volume measured with MIP are indicated as ϵ' . In view of the double dependency of ϵ' on V_v in eq. (4-2a), the definition of ϵ' given by eq. (4-1) is preferred. Therefore:

$$\epsilon \equiv 1 - V_s/V_t \quad (4-3a)$$

$$\epsilon' \equiv V_v/V_t \quad (4-3b)$$

It is necessary to take the difference between ϵ and ϵ' into account when configuring cells.

Similarly, the density ρ determined using the measured pore volume V_v is denoted ρ' . Using eqs.(4-3a) and (4-3b):

$$\rho \equiv \rho_{th}(1 - \epsilon) = mV_t \quad (4-4a)$$

$$\rho' \equiv \rho_{th}(1 - \epsilon') = \rho_{th}(1 - V_v/V_t) \quad (4-4b)$$

where ρ_{th} is the theoretical density of (Mn,Zn)-ferrite corrected for the presence of organic

binder and m the mass of the sample. The difference between ϵ and ϵ' measured for (Mn,Zn)-ferrite compacts is given in table 4.1. The data is measured with the equipment listed in section 3.2.

Table 4.1: Comparison of the densities ρ and ρ'

Density ρ (g/cm ³)	Overall porosity ϵ (%)	Density ρ' (g/cm ³)	Pore porosity ϵ' (%)
2.31	54.8	2.40	53.0
2.42	52.6	2.68	47.6
2.55	50.1	2.76	46.0
2.72	46.8	3.09	39.5
2.98	41.7	3.40	33.5

Plotting ρ versus ρ' produces a linear correlation:

$$\rho' = 1.45\rho - 0.91 \quad (4-5)$$

The goodness-of-fit is reflected in the correlation coefficient which equals 0.9904. Eq. (4-5) indicates that below a density ρ of 2.0 g/cm³, ρ' is smaller than ρ . This suggests that the pores become increasingly inaccessible once the compact has been formed. Therefore, eq. (4-5) only applies when the density is at least 2.0 g/cm³; otherwise ρ' is equal to ρ .

The densities quoted in this section are based on the overall porosity ϵ on account of the practical significance. Where necessary, eq. (4-5) can be used to transform ρ into ρ' .

4.2.2. Subdivision of porosity

Granulate consists of randomly-packed granules, which contain ferrite particles. It is postulated that the particles form clusters known as agglomerates. Using this representation, three types of pores can be distinguished: pores between the granules (*intergranular porosity*), pores between the agglomerates (*interagglomerate porosity*) and pores between the particles (*interparticle porosity*). The size of the pores between each type of solid unit is proportional to the size of the unit. When assuming that the initial packing of the solid units is similar, the following classification can be made:

$$r_{\text{intergranular}} > r_{\text{interagglomerate}} > r_{\text{interparticle}}$$

where r is the average pore size.

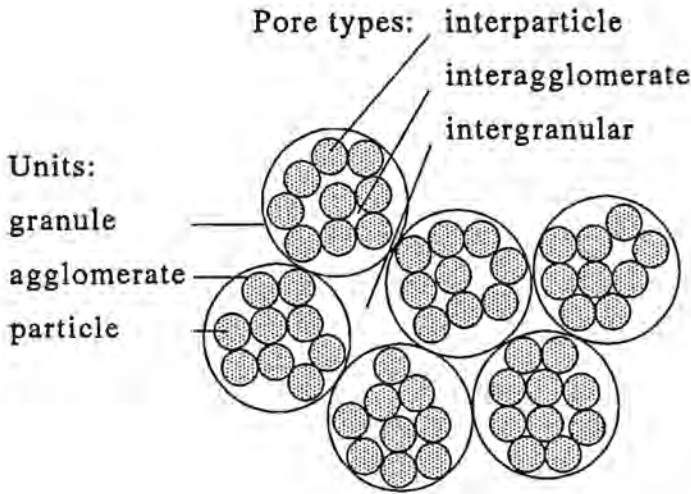


Fig. 4.2: Subdivision of pore space. The size of the pores is roughly proportional to the size of the granules, agglomerates and particles. The size of agglomerates, which cannot be directly measured, will be derived from the model.

The initial pore size distribution based on the subdivision in fig. 4.2 consists of three peaks. The volume of each type of pores present is reflected by the area under each peak. Given the total volume V_t , determined from the sample dimensions, the porosity ϵ' can be split into three contributions:

$$\begin{aligned}\epsilon' &= V_v/V_t \\ &= (V_g + V_a + V_p)/V_t \\ &= \epsilon_g' + \epsilon_a' + \epsilon_p'\end{aligned}\quad (4-6)$$

where subscript g stands for granules (*intergranular porosity*), a for agglomerates (*interagglomerate porosity*) and p for particles (*interparticle porosity*).

It is postulated that, during compaction, the largest pores are compressed preferentially. Using this concept, *three* stages can be distinguished. During the first stage, the intergranular pores decrease in size until the distinction with interagglomerate pores has disappeared. During the second stage, the interagglomerate pores and remainder of the intergranular pores are compressed until their size corresponds to the size of interparticle pores. Finally, all three types of pores are compressed.

Pore size distributions of (Mn,Zn)-ferrite compacts have been measured with MIP (fig. 4.3). The minimum density is 2.31 g/cm^3 , which corresponds to the density where the compact has sufficient strength to be handled.

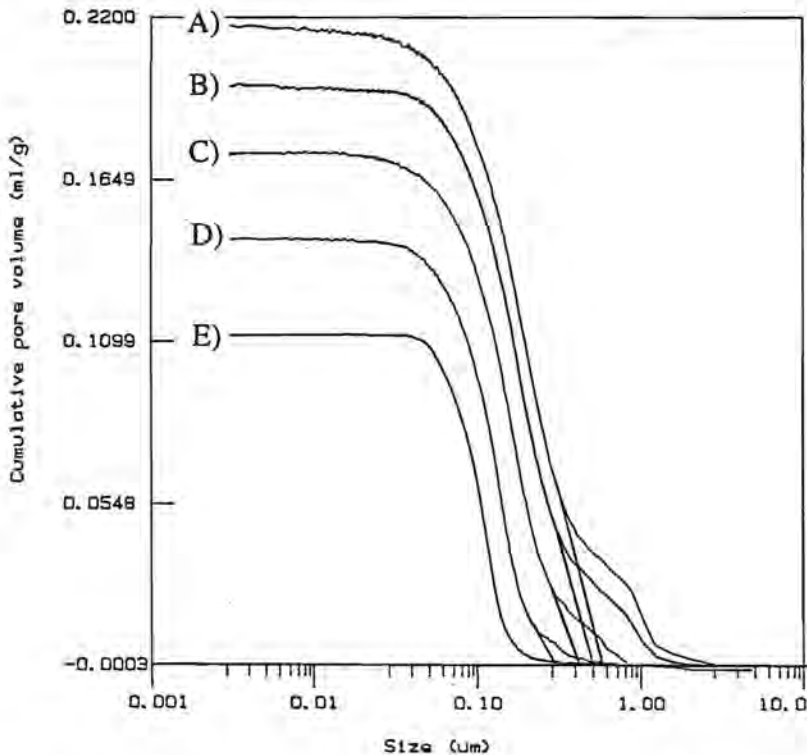


Fig. 4.3: Cumulative pore size distributions of (Mn,Zn)-ferrite compacts. The average size of the granules is $80 \mu\text{m}$. The measured curves show that two types of pores are present in the compacts. Compact densities: A) 2.31 g/cm^3 , B) 2.42 g/cm^3 , C) 2.55 g/cm^3 , D) 2.72 g/cm^3 and E) 2.98 g/cm^3 .

The two types of pores can either be pores between particles and agglomerates or pores between particles and granules. In the latter case, there are no agglomerates in the granules. At this stage, the presence of agglomerates is assumed.

The volume of interagglomerate pores is estimated from fig. 4.3 by extending the intruded volume curve below the shoulder. The pore volumes are subsequently converted to the interagglomerate and interparticle porosity with the following equation:

$$\begin{aligned}\epsilon &= (V/V_v)\epsilon^* \\ &= (V/V_v)(1-\rho'/\rho_w)\end{aligned}\quad (4-7)$$

Note that ρ' is related to the actual density ρ through eq. (4-5). The correlation of ϵ_s and ϵ_p with the density is found to be approximately linear. Expressed in equations:

$$\epsilon_s = 47.1 - 17.0\rho \quad (4-8)$$

$$\epsilon_p = 52.9 - 2.6\rho \quad (4-9)$$

The pore size distribution is obtained from fig. 4.3 by plotting the derivative dV/dr versus the pore size r . The peaks of the pore size distribution can be characterized in terms of the pore size at which a maximum is observed. This corresponds to the modal pore size. Table 4.2 lists the values for the curves shown in fig. 4.3.

Table 4.2: Evolution of modal pore size during compaction.

Density ρ (g/cm ³)	Interparticle modal pore size (μm)	Interagglomerate modal pore size (μm)
2.31	0.19	1.00
2.42	0.17	0.94
2.55	0.15	0.40
2.72	0.12	0.24
2.98	0.11	(0.11)
3.19	0.08	(0.08)

Data in parenthesis indicates that the pore size distribution consists of a single peak only. At the density where the distinction between the size of intra- and interagglomerate pores disappears, the interagglomerate porosity is not zero. By definition, the remaining interagglomerate porosity is classified as interparticle porosity. A similar transition occurs at lower densities when intergranular and interagglomerate pores are equal in size. The intergranular porosity which remains at this density is classified as interagglomerate porosity.

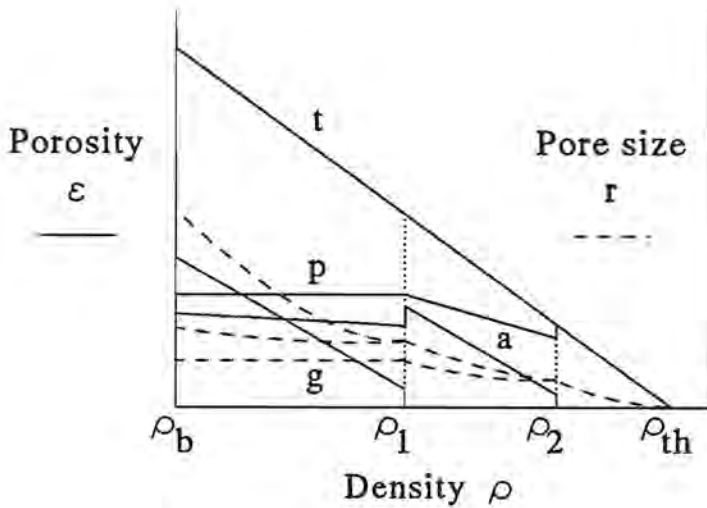


Fig.4.4: Relation between the types of porosity and the density during compaction. Shown are the total (t), intergranular (g), interagglomerate (a) and interparticle (p) porosity. The extremal densities are the bulk (b) and the theoretical (th) density. The transition densities ρ_1 and ρ_2 correspond to a density where the pore sizes of two types of porosity coincide. Remaining pore volume of the initially larger pores is added to the volume of the smaller points. This produces the sharp local variations in the individual porosities.

The data obtained with MIP (fig. 4.3) only provides information on the porosity for a range of densities between ρ_1 and ρ_{th} . In order to model the entire density range, the transition densities must be determined. In addition, the progress of the individual porosities outside the range limited by ρ_1 and ρ_2 must be established.

At densities below the first transition density ρ_1 , the interparticle porosity is considered to be unaffected. The interagglomerate porosity, on the other hand, is reduced by deformation of the granules. Assuming that this reduction in porosity equals the intergranular porosity remaining at ρ_1 , ρ_1 corresponds to the bulk density plus the total intergranular porosity. The second transition density ρ_2 is obtained by assuming that the residual interagglomerate porosity is small. The value of ρ_2 is then given by the density where the interagglomerate porosity becomes zero. Eq. (4-8) can be used to determine ρ_2 . These considerations are illustrated in fig. 4.5.

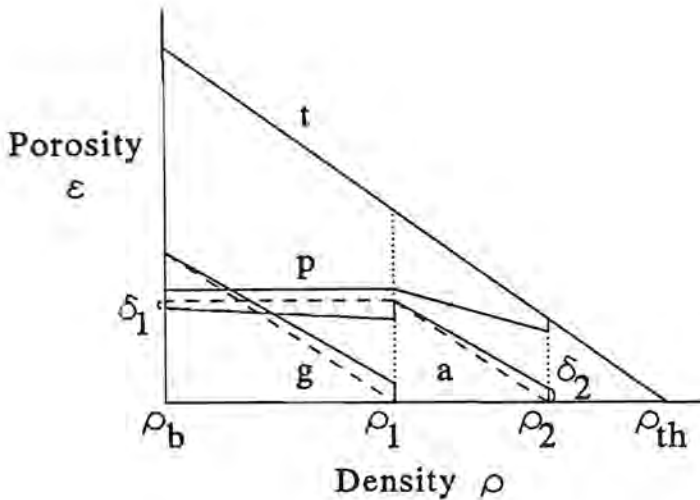


Fig. 4.5: Determination of the transition densities ρ_1 and ρ_2 . Provided that δ_1 and δ_2 are small, ρ_1 and ρ_2 are found from intersections with the ρ axis. ρ_1 equals the sum of the bulk density and total intergranular porosity. ρ_2 equals the minimum density where a single-peaked pore size distribution is found.

Given two transition densities, a three-stage model based on the porosity can be derived. The corresponding evolution of the packing structure is investigated in section 4.3.

4.3. Construction of representative cells

4.3.1. Analysis of the compaction process

The increase in density corresponds to a decrease of the three types of porosity. The relation between each type of porosity and the density is modelled as a three-stage process (section 4.2.2). The porosity types are associated with the presence of three types of solid units: particles, agglomerates and granules. During compaction, these units are subject to:

- rearrangement : change of mutual position
- deformation : change of shape
- compression : change of volume

The effect of these processes varies with the density and the type of solid involved (table 4.3). Note that, at the transition between stages, the distinction between two types of solid units disappears.

Table 4.3: Relation between compaction stages, compaction mechanisms and solid types

Stage	Granules	Agglomerates	Particles
1	Rearrangement	No change	No change
	Compression Deformation	Rearrangement	No change
2	-	Compression Deformation	Rearrangement
3	-	-	Rearrangement
	-	-	Deformation

The development of structure during the compaction stages is represented by cells constructed with granules, agglomerates or particles. In the following, equations are derived for cells constructed from particles. Because granules, agglomerates and particles are initially considered to be spherical, the cells are conceptually similar and the same equations apply for granules and agglomerates.

Three-dimensional cells require information on the connectivity of pores or the number of contacts between the particles. Because details on the latter are unknown, two-dimensional cells are used. Particles are represented by their cross-sections in cells whose layout is governed by the following rules:

- the cell edges are of equal length.
- the cell particles are equisized.
- the cell particles are positioned at two locations only:
 - the centres of the particles coincide with the intersection of the cell edges.
 - the particles are bisected by the cell edge.
- the distance between the centres of neighbouring particles is constant.

The resulting symmetry allows derivation of correlations relating the cell porosity to the pore and particle sizes. In addition, a number of parameters characteristic for the three processes are defined:

- rearrangement:
 - the number of particles covering the cell. This number is termed the coordination N .
 - the number of corners of a cell N_c .
 - the relative length of the cell edge, expressed as the ratio of the edge length L and the particle radius r_p .
- deformation:
 - the sphericity of the particles ψ , which is defined as the ratio of a pseudo particle size $r_{p,d}$ and the undeformed size r_p :

$$\psi \equiv r_{p,d}/r_p \quad (4-10)$$

The pseudo particle size $r_{p,d}$ corresponds to the radius of curvature of the section bordering the pore.

- compression:
 - the compression ratio of the particles λ , which indicates the size of a compressed particle $r_{p,c}$ relative to the uncompressed size $r_{p,0}$:

$$\lambda \equiv r_{p,d}/r_{p,0} \quad (4-11)$$

Note that deformation and compression requires the particles to be directly adjacent, which implies that the L/r_p ratio equals 2. The significance of these parameters is illustrated in fig. 4.6.

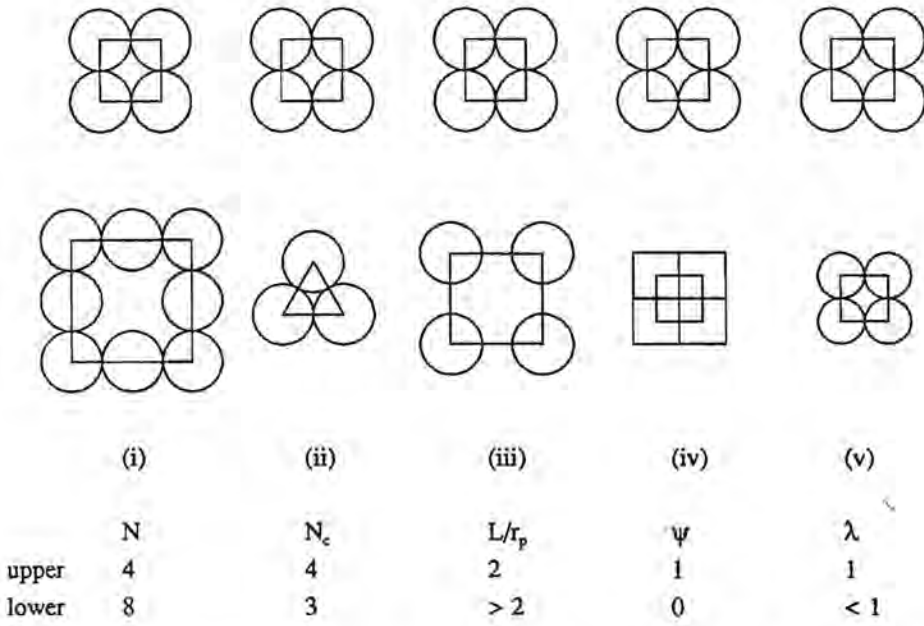


Fig. 4.6: Definition of cell parameters: i) coordination N , ii) number of corners N_c , iii) edge length-to-particle size ratio L/r_p , iv) sphericity ψ and v) compression ratio λ .

A cell is considered to be representative when the experimental ratio of the modal pore and particle sizes ($r/r_{p,exp}$) matches with the cell ratio ($r/r_{p,cell}$) for the same porosity. The relation between the cell porosity and the cell ratio ($r/r_{p,cell}$) is derived for various arrangements of the particles or granules in the following subsection.

4.3.2. Classification of cells

The compaction process is represented by cells, which are configured in a similar manner. Three distinct series are shown in fig. 4.7. Series of cells where all particles cover a corner, i.e. $N=N_c$, are denoted isocornered cells (fig. 4.7(i)), while series of cells with a fixed geometry, i.e. $N_c=constant$, are termed isogeometric cells. Figs. 4.7(ii) and 4.7(iii) show isogeometric cells which differ according to the transition between successive coordinations:

- stepwise elongation of the cell edges, i.e. an increase of the edge length L is accompanied by a change of coordination N (fig. 4.7(ii)).
- continuous elongation of the cell edges, with the coordination N increasing when the cell edge length has increased by $2r_p$ (fig. 4.7(iii)).

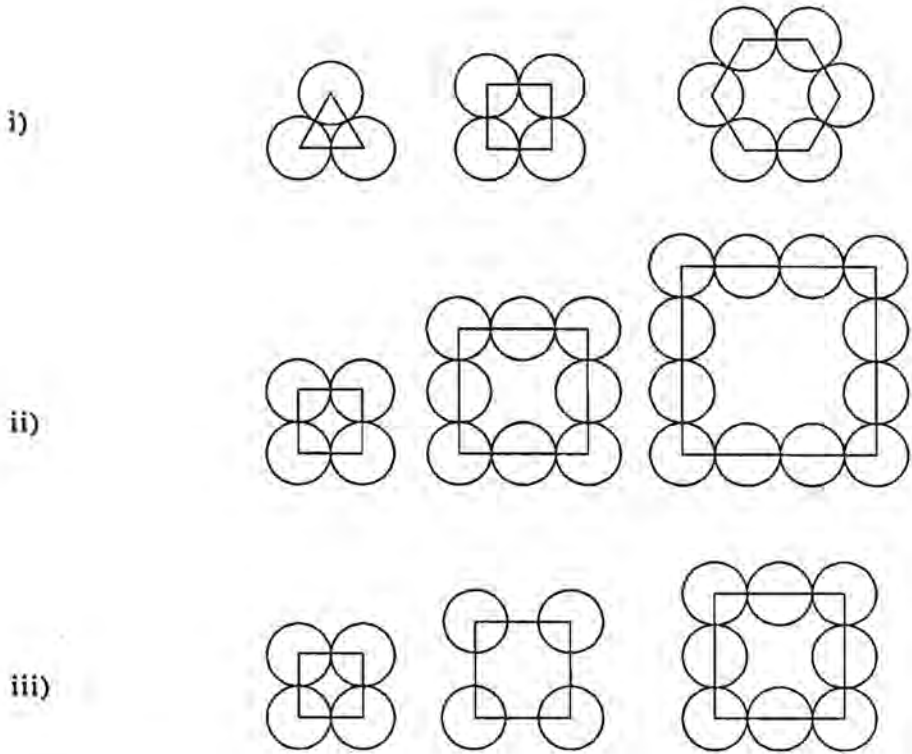


Fig. 4.7: Families of cells

- i) all particles adjacent, $N=N_c$
- ii) all particles adjacent, N multiple of N_c
- iii) continuously expandable, N multiple of N_c

4.3.3. Basic relations for N , N_c and L/r_p

Although the cell is covered by N particles, only a fraction of each particle is located inside the cell. The contribution of a corner particle is proportional to the corner angle α , while a particle bisected by a cell edge contributes half its surface (see fig 4.7). Defining the effective number of particles N_{eff} in the cell:

- for isocornered cells: $N_{\text{eff}} = N_c \alpha / 2\pi$ (4-12a)

- for isogeometric cells: $N_{\text{eff}} = N_c \alpha / 2\pi + (N - N_c) / 2$ (4-12b)

With polygons, the corner angle α depends solely on the number of corners N_c :

$$\alpha = \pi(N_c - 2)/N_c \quad (4-13)$$

Recalling that $N=N_c$ for isocornered cells, substitution of α in eqs.(4-12a) and (4-12b) yields identical expressions for N_{eff} for both types of cells:

$$N_{eff} = N/2 - 1 \quad (4-14)$$

The overall porosity ϵ (eq. 4-3a) equals the cell area **not** covered by particles:

$$\begin{aligned} \epsilon &= 1 - N_{eff}\pi r_p^2/A \\ &= 1 - (N/2 - 1)\pi r_p^2/A \end{aligned} \quad (4-15)$$

where A is the area of the cell. In practice, the porosity varies with the measurement technique: the porosity ϵ' according to eq. (4-3b) differs on account of pores not intruded.

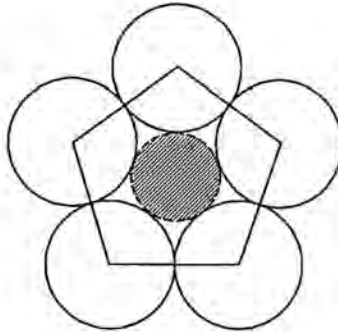


Fig. 4.8: Subdivision of pore area. The central pore is bounded by the largest circle which fits in the pore area of the cell. During a MIP measurement, the central pore is intruded first.

Given that all pores are accessible, the difference between ϵ and ϵ' is attributed to pores which are too small to be intruded. Therefore, subdivision of the pore area in the particle cell as shown in fig. 4.8 is proposed. The size of the shaded circle, which occupies a large fraction of the pore area, corresponds to the modal pore size r of the smallest type of pores measured with MIP. Because a single cell is used to represent these pores, the size distribution of these pores is not modelled. Therefore, it is postulated that the remaining pore area is **not** intruded during a MIP measurement. Consequently, an expression for the porosity ϵ' is obtained:

$$\epsilon' = \pi r^2/A \quad (4-16)$$

If the subdivision of pore area is correct, eqs.(4-15) and (4-16) can be combined:

$$N = 2 + 2(1-\epsilon)(r/r_p)^2/\epsilon' \quad (4-17)$$

Eq. (4-17) allows direct determination of the coordination N from experimental quantities.

The validity of the proposed subdivision can be checked by comparison of the experimental and theoretical difference between ϵ and ϵ' . The theoretical difference $\Delta\epsilon_{th}$ is given by:

$$\Delta\epsilon_{th} \equiv (\epsilon - \epsilon') = 1 - \pi(N_{st}r_p^2 + r^2)/A \quad (4-18)$$

Expression for the cell area

The derivation of a general expression for the cell area A is illustrated in fig. 4.9.

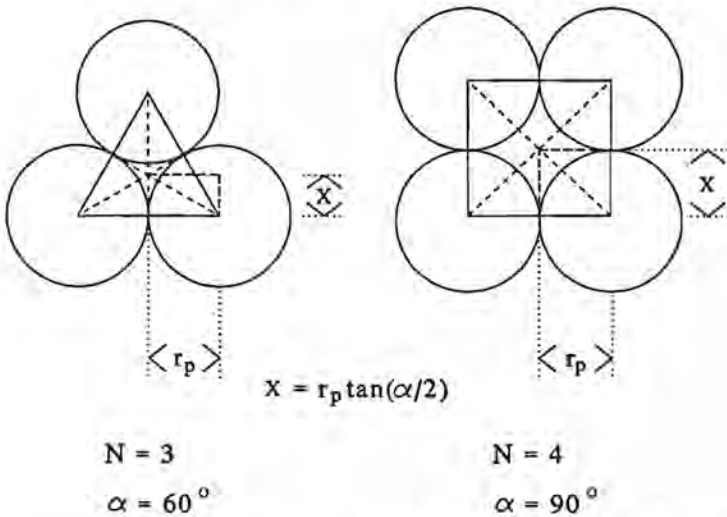


Fig. 4.9: Determination of cell area A . The area A is found by i) dividing the cell into N_c equivalent subsections, ii) calculating the area of one subsection and iii) multiplying by N_c .

The cell area A is a function of edge length L and the cell geometry, expressed in the number of corners N_c and the corner angle α :

$$A = N_c(L/2)^2 \tan(\alpha/2) \quad (4-19)$$

Simplifying eq. (4-19) through substitution of α with eq. (4-13):

$$\begin{aligned} A &= N_c(L/2)^2 \tan(\pi(N_c-2)/2N_c) \\ &= N_c L^2 / (4 \tan(\pi/N_c)) \end{aligned} \quad (4-20)$$

Expression for the edge length L

The edge length L is related to the particle and pore radii through the cell geometry (fig.4.10). The pore radius corresponds to the largest inscribed circle.

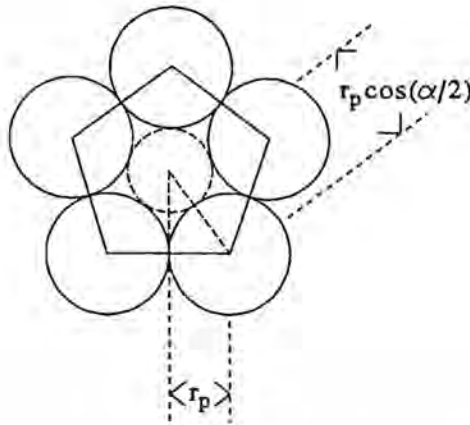


Fig. 4.10: Relation between edge length L, the centre-to-corner distance L_c and the corner angle α . In this case, where $N=N_c$, L_c equals the sum of the pore and particle radius ($r+r_p$).

$$L_c = L / (2 \cos(\alpha/2))$$

or

$$L = 2 L_c \sin(\pi/N_c) \quad (4-21)$$

When N equals N_c , the size of the central pore is limited by the corner particles, so that the centre-to-corner distance L_c equals the sum of the particle and pore radii. The value of L_c is larger than the sum if the central pore is bounded by particles on the cell edges. The latter occurs when N is larger than N_c . If we define the ratio ϕ by:

$$\phi \equiv L_c / (r + r_p) \quad (4-22)$$

Substitution of L_c in eq. (4-21) yields:

$$L = 2\varphi(r+r_p)\sin(\pi/N_c) \quad (4-23)$$

For isocornered cells ($N=N_c$, $L/r_p=2$, $\varphi=1$), an expression for the pore-to-particle ratio is obtained:

$$r/r_p = 1/\sin(\pi/N_c) - 1 \quad (4-24)$$

The value of φ varies as a function of N and N_c . Figs. 4.11 and 4.12 show the derivation of φ for the square and triangular geometries.

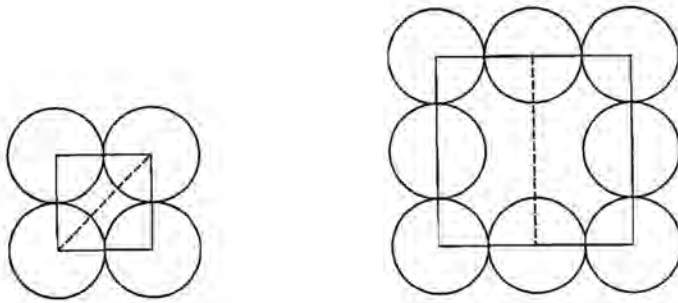


Fig. 4.11: Limitation of the size of the central pore in cells with square geometry ($N_c=4$). When $N=N_c$, $\varphi=1$ while for $N>N_c$, $\varphi=\sqrt{2}$.

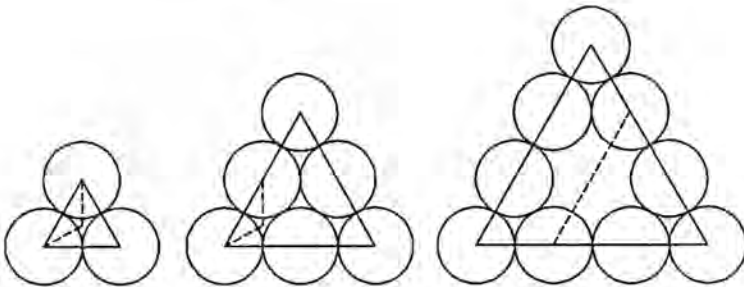


Fig. 4.12: Limitation of pore size in cells with triangular geometry ($N_c=3$). When $N=N_c$, $\varphi=1$. For $N>N_c$, φ varies with the number of particles bisected by the cell edge, denoted N_p : when N_p is even, $\varphi=2N\sin(\arctan(3\sqrt{3}/N))/3\sqrt{3}$, while when N_p is odd, $\varphi=2$. Note that φ is not defined for $N=6$ where the particles are adjacent.

Expressions for the porosity

The general expression for the cell area A (eq. 4-19) can be used to express the porosity ε as a function of N , N_c and L/r_p (eq. 4-14):

$$\begin{aligned}\varepsilon &= 1 - (N/2 - 1)\pi r_p^2/A \\ &= 1 - (2N - 4)\pi \tan(\pi/N_c) / ((L/r_p)^2 N_c)\end{aligned}\quad (4-25)$$

Similarly, the alternative porosity ε' (eq. 4-16) follows from eqs.(4-20) and (4-24):

$$\begin{aligned}\varepsilon' &= \pi r^2/A \\ &= 4\pi \tan(\pi/N_c) (1/(2\varphi \sin(\pi/N_c)) - r_p/L)^2 / N_c\end{aligned}\quad (4-26)$$

In cells where all particles are directly adjacent, the three parameters are related:

$$L/r_p = 2N/N_c \quad (4-27)$$

Use of eq. (4-27) reduces the number of independent parameters in eqs.(4-25) and (4-26) to two.

4.3.4. Basic relations for ψ

The process of deformation is determined by the initial arrangement of the particles, which is characterized by N , N_c and L/r_p . Given values for these parameters, relations between the deformation parameter, the sphericity ψ , and the porosity are derived. The sphericity ψ is the ratio of the local radius $r_{p,d}$ and the undeformed particle radius r_p :

$$\psi = r_{p,d}/r_p \quad (4-28)$$

ψ is unity when the particles are undeformed and zero when completely deformed.

During deformation, the volume of the particles is constant. Consequently, the cell area occupied by particles is also constant. When the particles are completely deformed, the interparticle pore space is zero. The area occupied by the particles then equals the total cell area A :

$$N_{eff} \pi r_p^2 = A = N_c L^2 / 4 \tan(\pi/N_c) \quad (4-29)$$

Substituting N_{eff} with eq. (4-14) and rewriting:

$$L/r_p = (C_1 + (4 - C_1)\psi^2)^{1/2}$$

or

$$\psi^2 = ((L/r_p)^2 - C_1)/(4 - C_1) \quad (4-30)$$

where $C_1 = 4\pi(N/2-1)\tan(180/N_c)/N_c$. Substitution of L/r_p in eq. (4-25) relates the cell porosity to ψ :

$$\epsilon = 1 - (2N-4)\pi\tan(\pi/N_c)/((C_1+(4-C_1)\psi^2)N_c) \quad (4-31)$$

This allows verification whether the actual deformation process corresponds to the process as depicted in fig. 4.13.

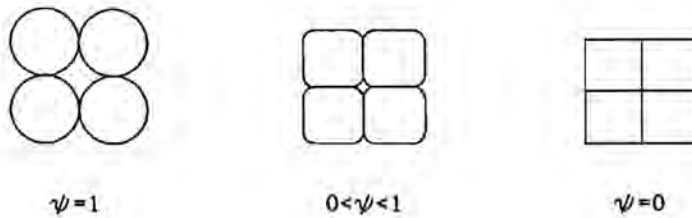


Fig. 4.13: Deformation in cells where $N_c=N=4$. The boundary is progressively flattened by the four neighbouring particles. Note that the corner sections are semi-circles with radius $r_{p,d}$.

4.3.5. Basic relations for λ

Compression is reduction of the size of granules or agglomerates through reduction of the porosity within these units. This decrease is expressed in the compression ratio λ :

$$\lambda = r_{p,c}/r_{p,o} \quad (4-32)$$

where $r_{p,c}$ is the compressed radius and $r_{p,o}$ is the initial radius. Compression only occurs when the granules or agglomerates are directly adjacent. In addition, it is assumed that all granules or agglomerates are compressed isotropically, which implies the geometry of the cell does not change. Consequently, only compression of isocornered cells is considered.

Parameters associated with rearrangement (N , N_c , L/r_p) have constant values during compression. However, compression decreases the cell area A . The relation with the compression ratio λ is found by comparing the initial cell area A_o and the compressed cell area:

$$\begin{aligned}
 A/A_o &= N_c r_{p,c}^2 / \tan(\pi/N_c) / (N_c r_{p,o}^2 / \tan(\pi/N_c)) \\
 &= (r_{p,c} / r_{p,o})^2 \\
 &= \lambda^2
 \end{aligned} \tag{4-33}$$

The cell area occupied by the granules or agglomerates consists of solid and pore space. In view of the correlation between the size and the cell area (eq. 4-32), two relations are obtained. For granules:

$$A/A_o = (A_s + A_p + A_a) / (A_s + A_p + A_a)_o = \lambda^2 \tag{4-34}$$

where subscripts s, p and a represent solid, particle and agglomerate respectively. A similar relation is obtained for agglomerates, which are only compressed after intergranular pores have been compressed to the same size:

$$A/A_o = (A_s + A_p) / (A_s + A_p)_o = \lambda^2 \tag{4-35}$$

In the present model, the subdivision of cell area is translated to porosities. Converting eqs.(4-33) and (4-34):

$$\lambda^2 = (1 - \epsilon_p - \epsilon_s - \epsilon_g)_o (\epsilon_s + \epsilon_p + \epsilon_a) / ((1 - \epsilon_p - \epsilon_s - \epsilon_g) (\epsilon_s + \epsilon_p + \epsilon_a)_o) \tag{4-36a}$$

$$\lambda^2 = (1 - \epsilon_p - \epsilon_s)_o (\epsilon_s + \epsilon_p) / ((1 - \epsilon_p - \epsilon_s) (\epsilon_s + \epsilon_p)_o) \tag{4-36b}$$

where ϵ_s is the fraction of cell area occupied by the solid.

4.3.6. Relation between two- and three-dimensional modelling

The packing of two- and three-dimensional cells containing equisized particles are *not* directly comparable. For example, a two-dimensional cell with coordination 3 with all particles directly adjacent has a porosity of 9.3 %. In a three-dimensional equivalent, the three in-plane particles could form the base of a tetrahedron, which has porosity of 22.0 %. Similarly, a two-dimensional cell with coordination 4 has a (minimum) porosity of 22.4 %, while its three-dimensional derivative, a pyramid, has porosity of 27.9 %.

In three-dimensional packings, tetrahedrons and (bi)pyramids are the most common cell geometries. In practice, however, numerous packing geometries are encountered. Therefore, it is difficult to link the porosities of two- and three-dimensional representations. As a rule, the porosity in a three-dimensional cell will be higher.

The density measured with MIP relates to a three-dimensional structure. However, derivation of the pore size distribution from MIP data is based on a two-dimensional model: pores are represented as cylindrical channels. Consequently, interpretation with two-dimensional cells are inline with MIP measurements but do constitute an approximation. In view of the geometric assumptions underlying this modelling approach, further refinement is not considered to be useful.

4.4. Characterization of the compaction process

4.4.1. Introduction

The processes which occur during the three compaction stages are used to identify the cell layout which is specific for the compaction of (Mn,Zn)-ferrite granulate. This provides insight into the effect of variations in the granulate properties and process parameters. The cell layout is derived from the (development of) pore size distributions measured with MIP.

The methodology of modelling compaction with representative cells is illustrated with the following granulate:

- binder type : PVA
- bulk density : 1.4 g/cm³
- tap density : 1.55 g/cm³
- average granule diameter : 80 µm (as determined with laser diffraction)
- average particle diameter : 1.0 µm (as determined with sedimentation analysis)

4.4.2. Existence of agglomerates

The compaction model presented in section 4.3 consists of three consecutive stages. At the transitions between two stages, the size distinction between two types of pores disappears. With MIP, only uni- and bimodal pore size distributions are measured (fig. 4.3). This allows for two options: either the experimental data relates to the second and third compaction stages or the compaction process consists of two stages only. If the latter is the case, it indicates that there are no clearly distinguishable agglomerates within the granules.

In order to identify the types of pores which are measured, the validity of a two-stage model is tested. In this model, the porosity consists of interparticle and intergranular pores. During the first stage, the granules are first rearranged, then deformed and compressed. This produces simultaneous rearrangement of the particles within. The second stage commences when the pore size distribution consists of a single peak only. During this stage, rearrangement and deformation of the particles occurs.

During the first stage, the change in porosity due to compression $\Delta\epsilon_c$ of the granules equals the change in porosity due to rearrangement of the particles, given by eq. (4-8):

$$\Delta e_c = 2.6\Delta Q \quad (4-37)$$

The change in intergranular porosity as a result of compression and deformation is given by eq. (4-8). Therefore, the change in porosity due to deformation equals:

$$\Delta e_d = 14.4\Delta Q \quad (4-38)$$

Deformation and compression reduce the size of the central pore between the granules. Incorporating ψ and λ in eq. (4-24):

$$r/r_p = \psi\lambda(1/\sin(\pi/N_c) - 1) \quad (4-39)$$

The choice of N_c is determined by the coordination of the granules after filling. In two dimensions, isocornered cells with coordination 3 represent the closest-packed state. Given that this condition is obtained after tapping the granulate, the intergranular porosity then equals 9.3 %. With a tapped density of 1.55 g/cm³, complete compression of the intergranular pores occurs at a density of 2.02 g/cm³. This value is much lower than the transition density determined from a series of MIP measurements, which indicate that the transition occurs at 2.78 g/cm³ (see fig. 4.3). Therefore, a cell with coordination 4, which has a (minimum) porosity of 22.46 %, is used to represent the packing of the granules. The intergranular porosity then disappears at a density of 2.68 g/cm³, a value which shows better correspondence.

After tapping, the size of the central pore between the granules equals 16.6 μm . Subsequent compression and deformation reduces the size of the intergranular pore. Table 4.2 lists the measured intergranular pore size as a function of the density. If the two-stage model is correct, the evolution of the intergranular pore size can be predicted using calculated values for ψ and λ .

A theoretical equation for the difference in porosity due to deformation is established by defining the tap density (1.55 g/cm³) as reference state, where ψ is unity. Using eq. (4-30):

$$\Delta e_d = C_1(1/(C_1+(4-C_1)\psi^2) - 1/4) \quad (4-40)$$

where $C_1 = \pi(2N-4)\tan(\pi/N_c)/N_c$. The effect of compression on the pore size is expressed with eq. (4-36). Note that, when using eq. (4-36), the porosities are calculated using a density corrected for the effect of deformation.

At a density of 2.31 g/cm³, Δe_d equals 0.109 while Δe_c equals 0.019. Using eq. (4-40), ψ is found to be 0.66, while eq. (4-36) yields a λ of 0.98. Substituting these values in eq. (4-39) indicates a pore size of 10.7 μm , which is considerably larger than the measured size of

1.0 μm . Similar differences are found for the other densities in table 4.2. This implies that the two-stage model cannot be used on the basis of the present data and interpretation. At the same time, the existence of agglomerates as distinct structural units is proved.

4.4.3. Compaction of granules

After filling, the structure of the loosely-packed granules can be represented by two types of cells: isogeometric cells with coordination 3 or isocornered cells. The difference between these cells is contained in the parameter varied: with isogeometric cells, the ratio L/t_p is variable while, with isocornered cells, the coordination N varies. In the absence of details which permit determination of the type of cells, an approach based on the definition of the structure after tapping is adopted. The latter corresponds to an optimum packing which is represented by a cell with coordination 3 where all granules are directly adjacent. The difference between the tap and the bulk density is due to rearrangement of the granules. Because the nature of this rearrangement is not defined, a cell representing the initial packing of the granulate is not configured. However, the cell representing the tapped granulate can be used as a starting point for configuring cells at higher densities.

The model proposed in section 4.2 states that when the size of intergranular pores equals the size of the interagglomerate pores, the granules lose their identity. The density at which this occurs corresponds to the density where the intergranular porosity has disappeared. Given an intergranular porosity of 9.3 % in the tapped state, the first transition density ρ_1 equals 2.02 g/cm^3 for this type of granulate. This value is consistent with the experimental data because it is lower than 2.31 g/cm^3 , the density at which only pores between agglomerates and particles are measured.

4.4.4. Compaction of agglomerates

Agglomerates are clusters of particles inside the granules. It is important to determine the density at which agglomerates lose their identity. In addition, the size and packing of agglomerates within the granules is of interest. These details can be obtained by interpretation of the pore size distributions obtained with MIP.

The density at which the size of the pores between particles and agglomerates is equal corresponds to the density where the pore size distribution consists of a single peak. Using the data shown in fig. 4.2, this second transition density ρ_2 is found to be 2.78 g/cm^3 . This is the minimum density at which the compact is physically homogeneous.

Determination of the initial packing of agglomerates requires reconstruction of the compaction behaviour at low densities, where MIP data on the evolution of the pore size distributions is not available. During the first compaction stage, agglomerates are subject to rearrangement on account of compression of the granules. This leads to changes in the coordination N and/or the ratio L/t_p . The corresponding change in the interagglomerate

porosity is unknown but expected to be relatively small. At the end of the first compaction stage, the agglomerates are all directly adjacent, so that further compaction produces deformation and compression. The effect of these processes on the interagglomerate pore size is monitored with MIP. At the onset of the third compaction stage, the agglomerates have been broken down, and only the individual particles can be distinguished.

During the second compaction stage, two relations are known: the development of the interagglomerate pore size and the interagglomerate porosity as a function of the density. The porosity versus density relation, given by eq. (4-8), indicates that at the first transition density (2.02 g/cm³), the interagglomerate porosity is 12.8 %. At the first transition density, the agglomerates are directly adjacent, which corresponds to an isocornered cell. The porosity of an isocornered cell with coordination 3 is only 9.3 %, a cell with coordination 4 (porosity 22.5 %) is more suitable. Given this choice, the development of the pore size can be modelled to provide an estimate of the average agglomerate size.

Rearrangement leads to directly adjacent agglomerates at a density of 2.02 g/cm³. Further compaction therefore leads to deformation and compression. Comparison of eq. (4-37) and (4-38) indicates that the effect of deformation is much more significant than that of compression. Therefore, an initial estimate is based on the assumption that the change in interagglomerate porosity is due to deformation only. In equations:

$$\psi^2 = (1/(0.17(\rho-2.02)/\pi+0.25)-\pi)/(4-\pi) \quad (4-41)$$

and

$$r_p = r/(\psi(2^{1/2}-1)) \quad (4-42)$$

Characteristic values of r versus ρ are given in table 4.2. Using eqs. (4-41) and (4-42), an initial agglomerate diameter of 5.7 μm is found. With the particle diameter being 1.0 μm , agglomerates consist of on average 65 particles. The latter estimate is based on the assumption that the particles are equisized and close-packed.

During compaction, the calculated size of the agglomerates decreases, which could be caused by compression. Another possibility is that fragmentation of agglomerates occurs. This process has not been considered in this model but will be investigated in the section 5.

4.4.5. Compaction of particles

The largest fraction of pore space present in granulate is located between the particles, i.e. interparticle porosity. Determination of the initial packing of the particles is of interest in order to judge whether improvements are possible. In addition, determination of the mechanism underlying the process of rearrangement is useful on account of its effect on the compaction behaviour.

Table 4.4 shows the evolution of the interparticle porosity during the compaction stages.

Table 4.4: Development of the interparticle porosity ϵ_p

Stage	Boundaries (g/cm ³)		Porosity (%)	Process
	Lower	Upper		
1	1.4	2.02	$\epsilon_p = 47.7$	No change
2	2.02	2.78	$\epsilon_p = 52.9 - 2.6Q$	Rearrangement
3	2.78	5.11	$\epsilon_p = 100 - 19.6Q$	Rearrangement/deformation

Three mechanisms representing rearrangement are possible. These are characterized by a variable N , N_c and L/r_p respectively. An indication of the applicable mechanism follows from analysis of the porosity in combination with the pore size. Given the high interparticle porosity during the initial stages of compaction (table 4.4), isocornered cells ($N=N_c$, $L/r_p = 2$) are likely to contain pores which are much larger than the particles. For example, a cell with a coordination of 7 has a porosity of 46.0 % and a central pore which is 1.3 times r_p . In practice, however, the interparticle pores (average radius: $< 0.2 \mu\text{m}$) are significantly smaller than particles (average radius $0.5 \mu\text{m}$). The two other options are isogeometric cells with expandable cell edges (N , N_c constant, L/r_p variable) and isogeometric cells with directly adjacent particles (only N_c constant). In the latter, the pores-to-particle ratio r/r_p is even larger than in isocornered cells with the same coordination. In isogeometric cells with constant N and variable L/r_p , however, high porosities and relatively small pores can be realized. Before calculating L/r_p , a suitable coordination $N (= N_c)$ has to be established.

Determination of the correct coordination is based on matching the theoretical and experimental size of the pores. In practice, the initial pore-to-particle size ratio r/r_p is roughly 0.4. This value becomes smaller during rearrangement and deformation of the particles during compaction. Therefore, the cell with a suitable coordination has a r/r_p ratio which can be smaller than 0.4. Only coordination 3 satisfies this criterion with a minimum r/r_p of 0.155. The next coordination (4) has a minimum r/r_p of 0.414.

Matching the initial interparticle porosity (47.7 %) to the cell porosity reveals that the initial L/r_p ratio is 2.63, which corresponds to a pore size of $0.26 \mu\text{m}$.

4.5. Verification of the model

4.5.1. Introduction

In this section, the validity of two important assumptions underlying the model developed in this chapter are investigated. The first assumption relates to the shape of the granules, the agglomerates within the granules and the individual particles: these are initially considered

to be spherical. The actual shapes are assessed in section 4.5.2. In addition, the shape of the particles after compaction is examined in section 4.5.3.

The second assumption is that the largest pores are preferentially compressed. Given distinct classes of pores, this assumption enables the definition of a transition density. The latter represents the density at which the largest pores present are sufficiently compressed to match the size of the next largest pores. It has been derived from interpretation of MIP data that initially three classes of pores are present (section 4.4.2). This implies that two transition densities can be distinguished. The significance of these transition densities is examined with scanning electron microscopy (SEM) in section 4.5.4. SEM images are obtained using a beam voltage of 30.1 kV.

4.5.2. Initial shape of granules and particles

On account of their size, the initial shape of the granules is readily observed with optical microscopy. By controlling the properties of the slurry and the spray-drying conditions, perfectly spherical granules can be produced. In practice, granules occasionally fuse during the latter stages of spray-drying (fig. 4.14).



Fig. 4.14: Granule produced by spray-drying observed with SEM. Protruding from the granule is a smaller granule which has become attached during spray-drying. The presence of large agglomerates within the granule is not observed.

Fig. 4.14 indicates that the assumption in the model that granules are spherical is appropriate.

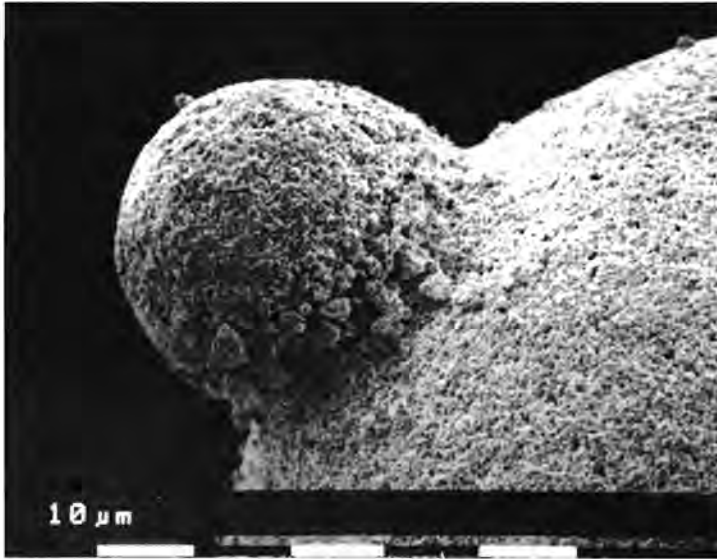


Fig. 4.15: Bonding between two granules fused during spray-drying. Note that the particles at the surface form an intricate network which is regular from a macroscopic point of view.

The shape of the particles is influenced by the nature of the raw materials and the initial powder processing stages (mixing, presintering, milling). SEM images confirm the expectation that the particles have a partly rounded but not necessarily spherical shape. Consequently, the representation of particles in the model with spheres is an approximation.

The shape of agglomerates of particles in the granules is determined by the distribution of relatively large pores in the granules. The model predicts that, when assuming that the agglomerates are spherical, these consist of roughly 65 particles. In two dimensions, the diameter of the agglomerate then equals 5 to 6 particle diameters ($\approx 5.7 \mu\text{m}$). Fig. 4.16 shows that agglomerates are difficult to detect from a two-dimensional image of the surface of a granule. However, the considerable variation in the size of the pores could indicate the presence of agglomerates.

Because it is likely that the bonding of the particles in the agglomerates is stronger than the bonding between the agglomerates, agglomerates can possibly be isolated by carefully fracturing a granule. However, there is no guarantee that this does not affect the agglomerate. In this study, granules have been split with a razor blade. The cross-section of a granule is shown in fig. 4.17.

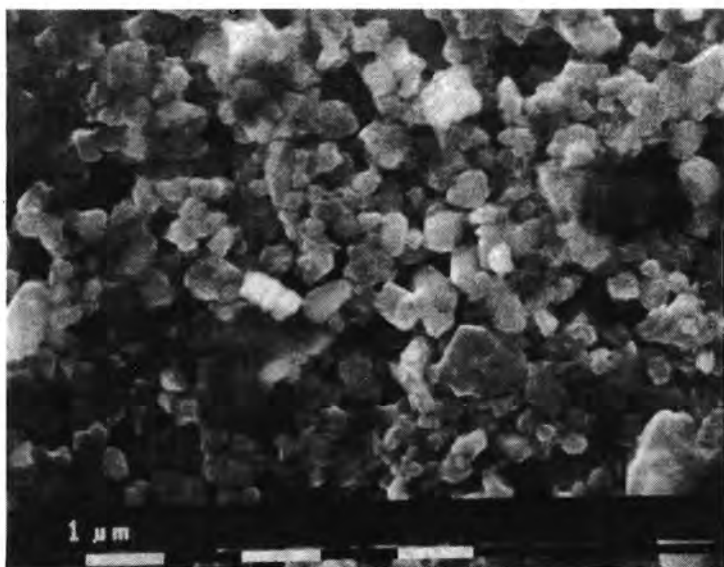


Fig. 4.16: (top) Outer surface of a granule as observed with SEM.

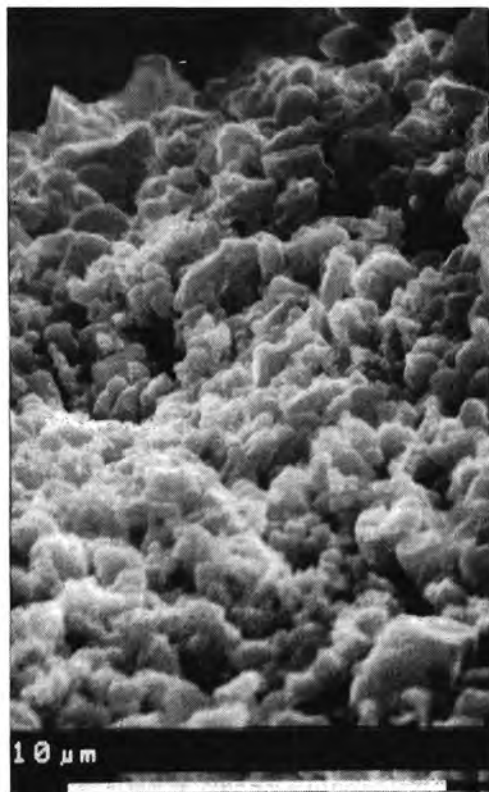


Fig. 4.17: (bottom) Cross-sectional surface of a granule as observed with SEM. Note the inclination of the cross-section.

Fig. 4.16 and 4.17 indicate that agglomerates within the granules are not readily identified. Therefore, representing agglomerates with spheres is a simplification.

4.5.3. Particle deformation during compaction

The model assumes that the particles are only deformed at high densities, when rearrangement of the particles is sufficiently restricted. Table 4.3 indicates that, according to the model, this state occurs at densities well above the second transition density, which equals 2.78 g/cm^3 . The validity of this postulate is checked by pressing a rectangular compact (dimensions: $5 \times 6 \times 55 \text{ mm}$) from granulate containing a mixture of acrylic II and PVA to a density of 3.05 g/cm^3 . Because shear stresses, which could induce fracture of the particles, are largest along the die wall, a SEM image of the *side* of the compact is shown in fig. 4.18.

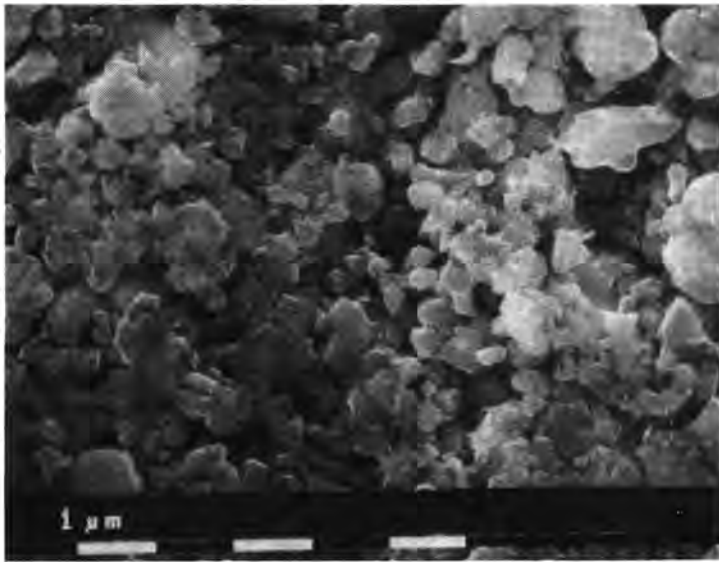


Fig. 4.18: Ferrite particles in compacts viewed sideways. Note that a vertical groove, created by an irregularity in the surface of the die wall, passes through the centre of the image.

Comparison of the particles in fig. 4.16 and 4.18 reveals that the particles are not significantly deformed at a density of 3.05 g/cm^3 . Consequently, fracture of the particles only commences at higher stresses, which correspond to a higher density. Therefore, the assumption that particles only deform at high densities is reasonable.

4.5.4. Significance of transition densities

The two transition densities in the model have been determined for the compaction of granulate containing PVA binder. The first transition density (2.02 g/cm^3) depends on the tapped density of the granulate while the second transition density (2.78 g/cm^3) is determined from pore size distributions measured with MIP.

The tapped density is related to the bulk density of the granulate, which varies with the granule size distribution and the density of the granules. Preliminary investigations indicate that the effect of the granule size distribution on the bulk density is limited: composed size distributions in the range of 60 to 450 μm produce only slight variations in the bulk density. This indicates that the range of granule sizes is too narrow to affect the packing of the granules. Variation of the granule density, on the other hand, is clearly reflected in the bulk density.

The granulates containing acrylic II binder and a mixture of acrylic II and PVA have a higher bulk density than the other granulates used in this study (1.50 g/cm^3 versus 1.40 g/cm^3). In view of the corresponding tapped densities (1.65 g/cm^3 versus 1.55 g/cm^3), the first transition density for the mentioned granulates will be 2.12 g/cm^3 instead of 2.02 g/cm^3 .

Throughout this study, the pore size distributions measured with MIP have been invariant to the *type* of granulate: differences in the type and content of binder, the granule size and density do not affect the pore size distribution of compacts. Therefore, the second transition density holds for all granulates. Note that only a change in the particle size distribution is likely to affect the second transition density.

The difference between the first and second transition densities reflects the interagglomerate porosity. Since the first transition density varies with the granule density while the second transition density is constant, it follows that increasing the granule density during spray-drying reduces the interagglomerate porosity. In order to verify this conclusion, granulate containing acrylic II binder is pressed to various densities in a die. The surface of the granulate directly below the punch is subsequently observed with SEM. Figs. 4.19 to 4.22 show the deformation of the granules as a function of the density.

Fig. 4.19 shows that the loosely-packed granules are initially fractured. According to the model, at this density, the intergranular pores are the largest pores present, which appears to be correct. Fig. 4.20 shows the density just above the first transition density (2.12 g/cm^3). The intergranular and interagglomerate pores are now assumed to be equal in size. Fig. 4.21 shows that the size of intergranular pores is increasingly reduced. Finally, the density in fig. 4.22 exceeds the second transition density. According to the model, the pore size distribution consists of a single peak. Apart from a few isolated pores, this appears to be the case.

Fig. 4.20 reveals no details about the agglomerate structure within the granules. However, in view of the size of the granules, interagglomerate pores of a size similar to that of the intergranular pores can be present within the granules.

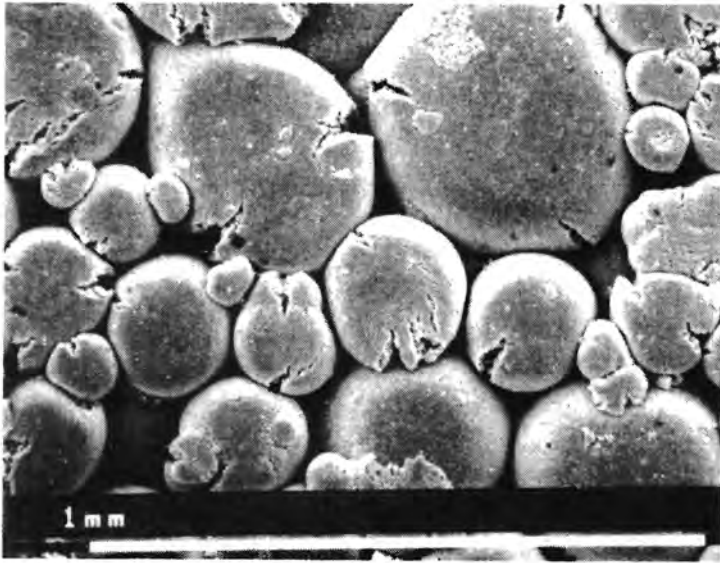


Fig. 4.19: Granulate pressed to 1.81 g/cm³

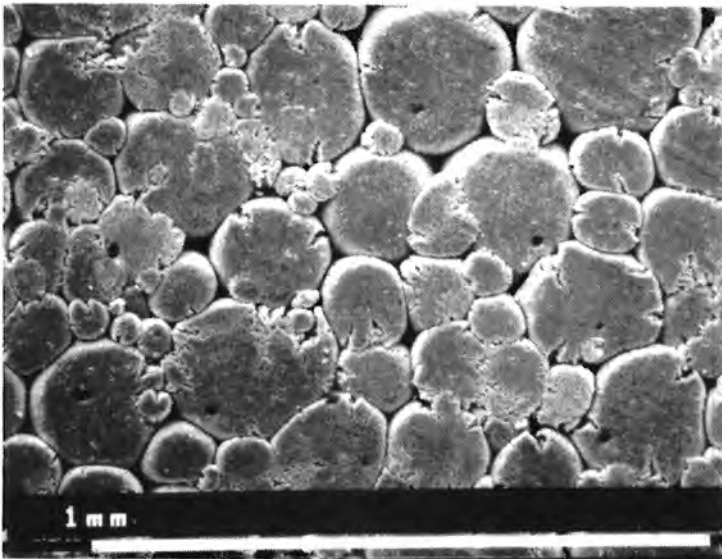


Fig. 4.20: Granulate pressed to 2.25 g/cm³

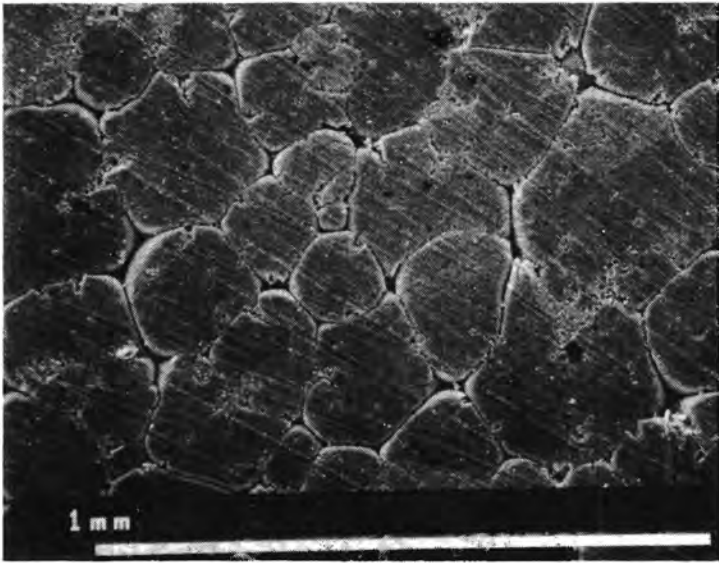


Fig. 4.21: Compact surface (density 2.64 g/cm³)

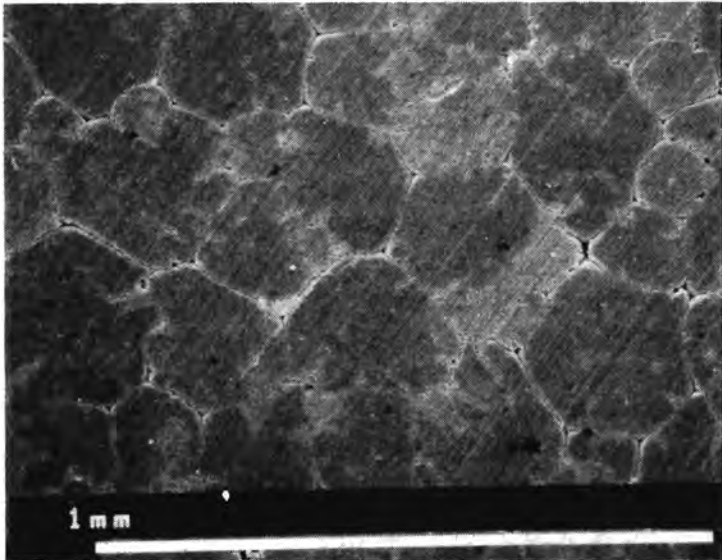


Fig. 4.22: Compact surface (density 2.96 g/cm³)

This would imply that the interagglomerate pores are much larger than the agglomerates themselves. Because MIP tends to underestimate the pore size, this implication is not unreasonable.

Alternatively, the displacement of the granules at the die surface could differ from that in the bulk. Up to now, SEM images have been made of the outer granules of the granulate mass or compacts. In order to determine whether these are representative, granulate containing acrylic II binder is pressed to three different densities. Subsequently, these have been fractured through bending. The fracture surfaces are shown in figs. 4.23 to 4.25.

Fig. 4.23 shows that at a density of 1.81 g/cm^3 , no bonding between the granules exist. Because deformation is still relatively insignificant, the increase in density is mainly due to rearrangement of the granules. Fig. 4.24 shows that at a density of 2.39 g/cm^3 , which is higher than the first transition density (2.12 g/cm^3), the bonding between the granules is still weak so that the granules break out as a whole. Note that at the same time the granules are significantly deformed and compressed, resulting in a lower interagglomerate porosity within the granule. If pores between the particles in the agglomerates had been compressed instead, the bonding between the particles would have been more apparent. This is additional evidence for the presence of large pores within the granules, which are also termed interagglomerate pores. Finally, at a density of 2.89 g/cm^3 , which is higher than the second transition density (fig. 4.25), the bonds between the particles have become sufficiently strong for the granules to fracture. This is an indication that the homogeneity is high.

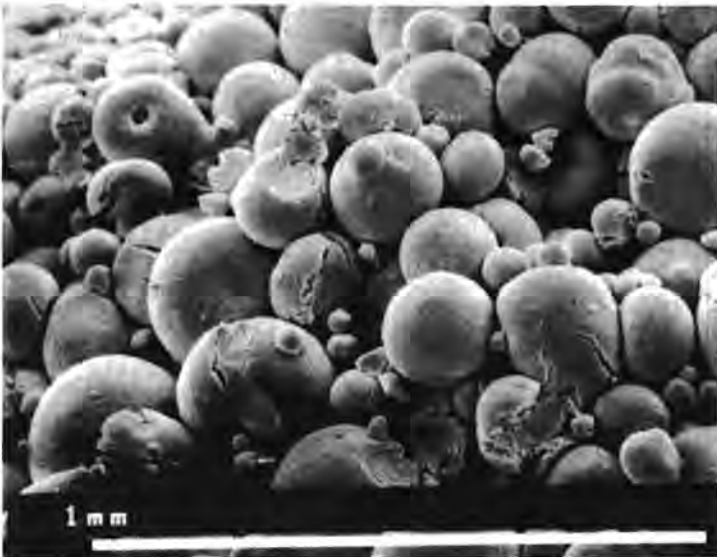


Fig. 4.23: Granulate pressed to 1.82 g/cm^3 .

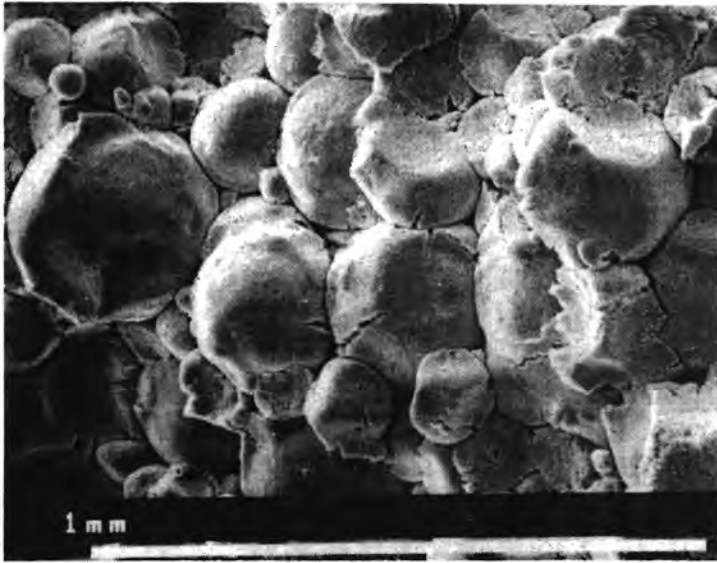


Fig. 4.24: Fractured compact (density 2.39 g/cm³)

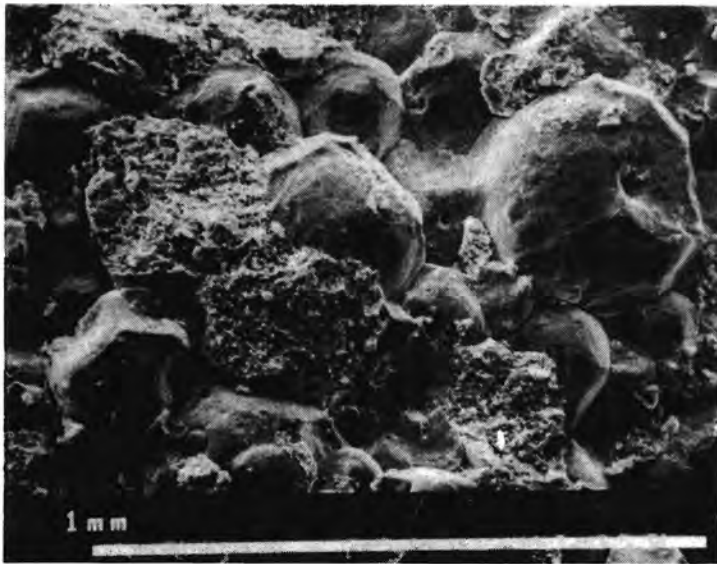


Fig. 4.25: Fractured compact (2.89 g/cm³)

The SEM images confirm that the model captures many aspects of compaction and offers, to a certain extent, a faithful representation of the evolution of the structure. Possibly the size of the interagglomerate pores is underestimated as these are initially less accessible than the intergranular pores during a MIP measurement.

4.6. Discussion and conclusion

The approach using representative cells provides insight into microstructure of the granulate before and after compaction. Knowledge of the initial structure allows assessment of the influence of the process stages preceding compaction. These determine, among others, the particle size distribution and the packing of the particles in the granules. Fig. 4.14 shows the initial structure of (Mn,Zn)-ferrite granulate containing PVA binder.

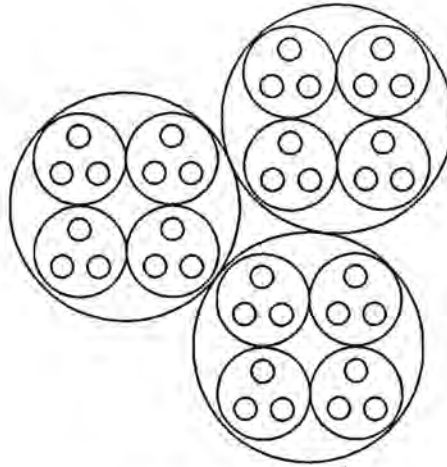


Fig. 4.26: Schematic representation of the initial structure of granulate in the tapped state (not to scale)

Fig. 4.14 shows that three types of solid units are present: granules, agglomerates and particles. Because these solid units have significantly different sizes, three classes of pores are expected. However, pore size distributions of compacts measured with MIP show at most two distinct peaks. Using a model based on two-dimensional representative cells, it is shown that the third peak has disappeared at the densities where a compact has been formed. Consequently, a two-stage compaction model is incapable of correctly characterizing the development of the pore morphology. In view of the capability of the three-stage model to represent the compaction process, the assumption that the largest pores are compressed preferentially is substantiated.

Further evidence of the structure of granulate during compaction is obtained from SEM

images. These indicate that the model correctly represents several aspects of the compaction process. On account of the highly irregular nature of the particle packing and the difficulty in observing agglomerates, it is likely that agglomerate packing cannot be characterized with a single representative cell. In addition, the granule size and density will also influence the size and shape of agglomerates. Based on these considerations, a 'realistic' initial microstructure is given in fig. 4.27. Future work will have to be based on such a type of microstructure.

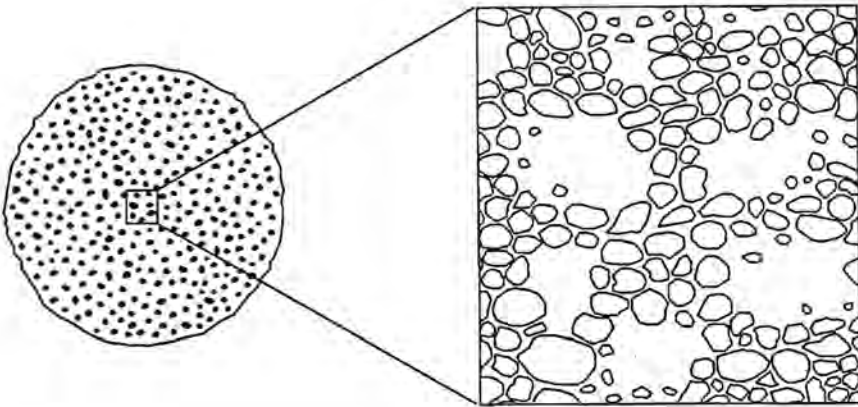


Fig. 4.27: Schematic representation of a granule (left) and (agglomerated) particles (left).

References

Suggested reading:

L. Kuhn, R. McMeeking, F. Lange, 'A Model for Powder Consolidation', *Journal of the American Society*, vol. 74, no. 3 (1991), 682-685.

T. Shaw, 'Model for the Effect of Powder Packing on the Driving Force for Liquid-Phase Sintering', *Journal of the American Ceramic Society*, vol. 76, no. 3 (1993), 664-670.

P. Wang, M. Zaidi, 'Thermomechanical deformation of powder-based porous aluminium. Part I: Evolution of pore structure', *Powder Technology*, vol. 66 (1991), 9-19.

J. Zheng, J. Reed, 'Effects of Particle Packing on Solid-State Sintering', *Journal of the American Ceramic Society*, vol. 72, no. 5 (1989), 810-817.

Chapter 5

Modelling compaction using the concept of fractal scaling

5.1. Introduction

The concept of fractal scaling applies to structures or processes which are self-similar. Self-similarity implies that the structure or process is the same when observed on a different scale. In this chapter, the use of fractal scaling for the characterization of powders and the compaction of powders is assessed. With respect to the powder, the analysis is focussed on characterization of the particle shape, the particle size distribution and the packing of the particles. Subsequently, the concept of fractal scaling is used to characterize the evolution of structure during compaction of the powder. Initially assuming that the concept of fractal scaling applies, the fractal dimension D serves as a characteristic parameter in each case.

Significance of the fractal dimension D

The fractal dimension D is a characteristic measure for self-similar structures or processes. The notion of self-similarity is illustrated in fig. 5.1.

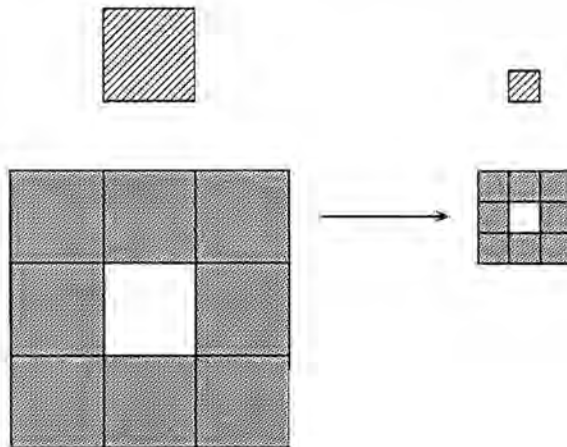


Fig. 5.1: Self-similar structures. The shaded squares represent zones where a property is observed. When the scale factor M increases from 3 to 9, the initially shaded zones are found to contain subzones where the property is absent. Because of self-similarity, the number of shaded subzones within each of the squares shaded at $M=3$, equals the total number of shaded squares at $M=3$.

In the following, the fractal dimension D is derived using fig. 5.1. For illustrative purposes, the mapping in fig. 5.1 is assumed to refer to a cross-sectional view of loosely-packed particles. Only squares where *no* particles are found are blanc; all other squares are shaded. This allows definition of the fraction of the total surface area A_t occupied by shaded squares f_M :

$$f_M = NL_M^2/A_t \quad (5-1)$$

where N is the number of shaded squares and L_M is the edge length of a square corresponding to a scale factor M . Recognizing that A_t/L_M^2 equals M^2 (see fig. 5.1):

$$f_M = N/M^2 \quad (5-2)$$

The number of shaded squares N increases with increasing scale factor M . However, on account of progressive blanking of squares, the increase in N is smaller than the corresponding increase of M^2 . Consequently, f_M decreases with increasing scale factor M . An expression for this relation has been derived from fig. 5.1:

$$f_M = f_0^{\ln(M)/\ln(M_0)} \quad (5-3)$$

where f_0 is the invariant fraction covered and M_0 the invariant scale factor. Invariant indicates that independence of the scale factor M . Fig. 5.2 shows some computed curves.

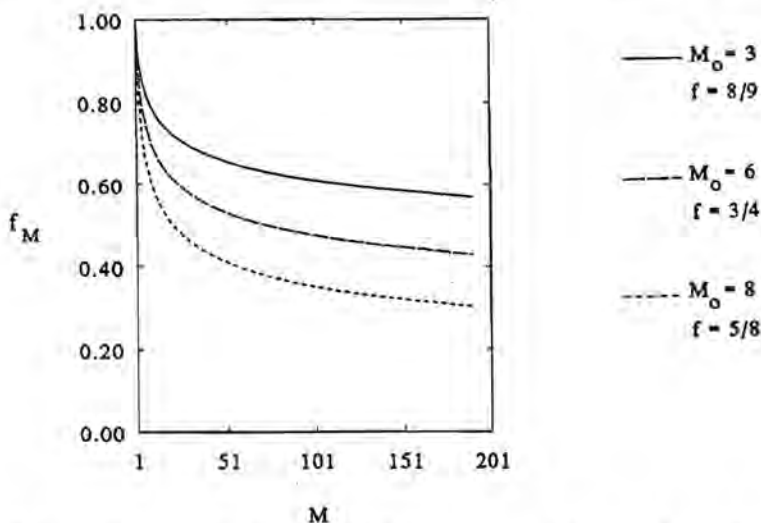


Fig. 5.2: Relation between the fraction of the area covered f_M and the scale factor M . With increasing M , f_M appears to reach a constant value.

The parameter M_0 represents the ratio of the successive edge lengths in a structure where self-similarity is observed. In the example given in fig. 5.1, f_0 equals 8/9 and M_0 is 3. In order to characterize the curves in fig. 5.2 with a single parameter, an expression in terms of the invariants f and M_0 is required. Substituting f_M in eq. (5-3) with eq. (5-2), taking the logarithm and dividing by $\ln(M)$ yields:

$$\ln(N)/\ln(M) - 2 = \ln(f_0)/\ln(M_0) \quad (5-4)$$

Note that the right hand side of eq. (5-4) has a constant value. This allows definition of the fractal dimension D :

$$D \equiv \ln(N)/\ln(M) \quad (5-5a)$$

$$= \ln(f_0)/\ln(M_0) + 2 \quad (5-5b)$$

$$= \ln(f_M)/\ln(M) + 2 \quad (5-5c)$$

The relation used to determine the fractal dimension depends on the type of data available.

This approach can be generalized to characterize any structure by adapting the dimension of the cover d and the significance of the overall dimensions, which is expressed in a factor C :

$$C = (L_M M)^d \quad (5-6)$$

Table 5.1: Dimension of covers and the significance of C (eq. 5-6)

Cover	d	C
point	0	total number P_t
unit line	1	total length L_t
unit surface	2	total area A_t
unit volume	3	total volume V_t

The value of D is smaller or equal to the dimension of the cover d . The interpretation of non-integer values is given in table 5.2. Values smaller than zero are unrealistic while values larger than three only occur when an additional dimension (e.g. a property) is

available.

Table 5.2: Non-integer values of D

Range	Interpretation
$0 < D < 1$	line with gaps
$1 < D < 2$	surface with holes
$2 < D < 3$	volume with pores

5.2. Fractal characterization of the granulate

5.2.1. Introduction

The compaction process is strongly influenced by the nature of the granulate. Two types of properties can be distinguished: static properties, such as the particle size (distribution), the particle shape and the particle packing, and dynamic properties, which are related to the deformation behaviour of the particles. In this section, relations based on the concept of fractal scaling are used to characterize the static properties of the particles. The data consists of two-dimensional images which are generated numerically. In section 5.2.2, the fractal characterization of a single particle is presented. This analysis yields a series of parameters which essentially reflect the particle shape. Given insight into the characteristics of single particle, the analysis is extended to ordered packings of particles (section 5.2.3).

Fractal characterization of (Mn,Zn)-ferrite granulate is focussed on the packing of the granules (section 5.2.4). The structure of the packing present after filling of the die can influence the density distribution of the compact if i) the compact has a low density (see chapter 4) or ii) the granules are relatively large when compared with the size of the die. The granule packing is simulated using models which differ with regard to the effect of friction between the granules.

5.2.2. Single particle

The fractal dimension D of a solid particle is 3, or, when considering its cross-section, 2. Note that these values are only measured when the mapping covers the particle exactly. With irregularly-shaped particles, this requires optimization of the mapping. However, optimization of the mapping removes all details of the particle shape. This can be avoided by introducing a standard mapping technique. Restricting attention to the

analysis of two-dimensional images, a square grid is used. With a square grid, the scale factor M is easy to define: when no subdivisions are present, M is unity, otherwise M equals unity plus the number of subdivisions.

The following technique is proposed: first, a square which circumscribes the particle is defined. Subsequently, the square is arbitrarily subdivided into 49 squares ($= 7 \times 7$) to form a grid. Now the number of squares which do not cover part of the particle are counted and denoted N' . The grid is then refined by subdividing each square into 4 squares ($= 2 \times 2$). Again the number of squares which do not cover the particle are counted. Halving the edge length can be repeated until a perfect mapping is obtained. With a perfect mapping, every square of the grid is either completely covering or completely beside a particle.

The fractal dimension D , given by eq. (5-5), is independent of the magnitude of the scale factor M because it is based on the concept of fractal scaling: the fraction of solid present within each square which previously did not appear to cover any solid, has a constant value. When mapping a particle with the standard mapping technique, an increase of the scale factor M only improves the definition of the particle contours. Squares *not* covering part of the particle, will not do so for any larger scale factor. Consequently, the fractal dimension D as determined with the standard mapping technique is only valid for a single scale factor M . This dependency will be indicated with a subscript M :

$$\begin{aligned} D_M &= \ln(M^2 - N'_M) / \ln(M) \\ &= \ln(N_M) / \ln(M) \end{aligned} \quad (5-6)$$

where N_M is the number of squares covering (part of) the particle for a particular scale factor M .

Fig. 5.3. illustrates that a perfect mapping, i.e. where the boundary of the particle coincides with the boundaries of the covering squares, is not sufficient to determine the fractal dimension D when using the standard mapping technique.

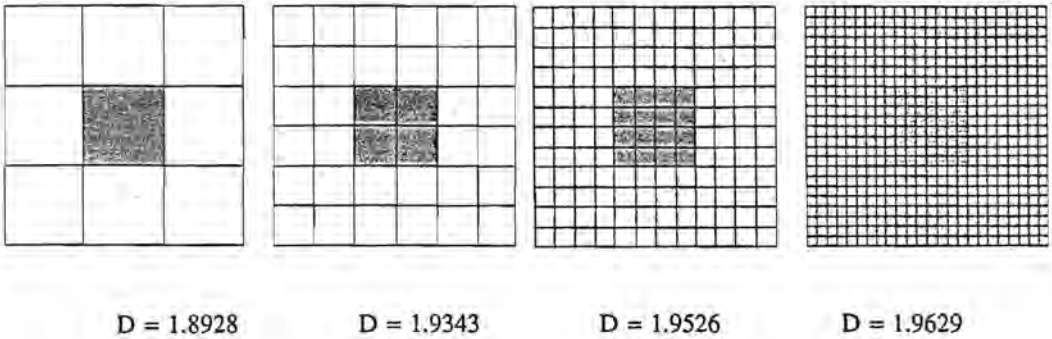


Fig. 5.3: Successive perfect mappings of a square particle (or pore). The fraction of the grid area occupied is constant (= 1/9), but the fractal dimension is not constant. When fractal scaling is present, the fractal dimension remains constant while the fraction of the grid area which appears to be occupied increases.

Given a perfect mapping, the fractal dimension D_M approaches 2 when the scale factor M is infinitely increased. The trend of D_M can be predicted with eq. (5-6) as long as the mapping is perfect. Using the standard mapping technique, comparison of two successive grids denoted by subscripts i and $i+1$ yields two relations:

$$M_{i+1} = 2M_i \quad (5-7a)$$

$$N'_{i+1} = 4N'_i \quad (5-7b)$$

Eq. (5-7a) applies for all successive grids after the initial grid where $M_{i+1} = 7M_i$. Eq. (5-7b) is the result of perfect mapping. Substituting M and N' in eq. (5-6):

$$D_i = \ln(M_i^2 - N'_i) / \ln(M_i) \quad (5-8a)$$

$$D_{i+1} = \ln(4(M_i^2 - N'_i)) / \ln(2M_i) \quad (5-8b)$$

Combination of eqs. (5-8a) and (5-8b) links the fractal dimensions D_i and D_{i+1} :

$$D_{i+1} = (D_i \ln(M_i) + 2 \ln(2)) / (\ln(M_i) + \ln(2)) \quad (5-9)$$

Eq. (5-9) can be generalized to relate the fractal dimensions of any two grids after the initial grid:

$$D_{i+n} = (D_i \ln(M_i) + 2n \ln(2)) / (\ln(M_i) + n \ln(2)) \quad (5-10)$$

Eq. (5-10) illustrates the influence of the initial scale factor M_i : the smaller M_i is, the faster D_M approaches 2. Because M_i is arbitrary, the variation of D_M can be controlled.

The fractal dimension D_M approaches 2 for large values of M irrespective of the shape of the particle. However, if the mapping is not perfect, a higher scale factor is required to observe this trend. This is due to a stronger increase of N' on account of boundary effects, which makes the coefficient in eq. (5-7b) larger than 4.

In order to obtain a perfect mapping with the standard mapping technique, three conditions must be fulfilled: 1) the particle cross-section to be square, 2) the edge length to be a multiple of the size of covering squares and 3) the boundary of the particle must coincide with the boundary of the covering square. The variation of the fractal dimension D_M for imperfect mappings is analysed using the cross-section of a perfectly-spherical particle. Fig. 5.4 illustrates that, with a circular cross-section, the orientation of the grid has no influence.

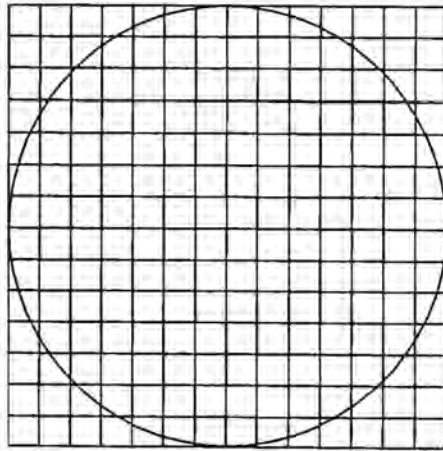


Fig. 5.4: Mapping of the cross-section of a spherical particle with a grid containing 14^2 subspaces ($M=14$).

When the scale factor becomes large, the fractal dimension D_M approaches 2 and the fraction of the grid area occupied by the particle reflects the theoretical value. In fig. 5.4, the theoretical fraction equals $\pi/4$ (≈ 0.7854). On the other hand, when the scale factor becomes small, the fractal dimension D_M also becomes 2 because the squares always cover part of the cross-section. The evolution of the fractal dimension D_M and f_M using the standard mapping technique is given in table 5.3.

Table 5.3: Fractal dimension D_M for a circular cross-section (fig. 5.4)

Scale factor M	f_M (*)	Fractal dimension D_M	Fractal dimension D_M (**)
1	1.0000	2.0000	2.0000
7	0.9184	1.9562	1.9562
14	0.8776	1.9505	1.9677
28	0.8469	1.9501	1.9744
56	0.8163	1.9500	1.9788
112	0.8023	1.9533	1.9819
224	0.7937	1.9573	1.9843
∞	0.7854	2.0000	2.0000

(*) f_M is the fraction of the grid area occupied by squares covering part of the particle.

(**) according to eq. (5-10), valid for a perfect mapping.

Table 5.3 shows that the fractal dimension D_M passes through a minimum. The fractal dimension has a value of 2 when 1) a perfect mapping is obtained (very large M) or 2) the grid is coarse (small M). Table 5.3 also confirms that the fractal dimension D_M approaches 2 faster than when the mapping is perfect. Because the fractal dimension D_M always increases with the scale factor when the mapping is perfect, it is postulated that the minimum of D_M corresponds to a pseudo-perfect mapping.

The series of fractal dimensions D_M provide a fingerprint of the shape of the particle. When expressed in terms of a single parameter, the minimum value of D_M could be used. A complication, however, is the influence of the grid orientation: for non-circular cross-sections, the values of D_M are not invariant with respect to rotation of the grid. This greatly restricts the application of this technique.

5.2.3. Ordered particle packing

The standard mapping technique proposed in the previous section can be used to analyze packing of particles. Given a two-dimensional representation of packed particles, a square grid is placed on a central section of the image. As with a single non-circular cross-section, the position of the grid affects the fractal dimension. This influence can be reduced by avoiding discontinuities at the grid boundary and ensuring that the grid covers a sufficiently large number of particles. Because the number of subdivisions of the grid is finite, too many particles reduce the sensitivity of the technique. Therefore, an optimum in the ratio between the edge length of the grid and the size of the particles has to be

established.

Packed particles are treated as a single irregularly-shaped particle. In order to allow comparison with a single spherical particle, regular packings of equisized spherical particles are constructed (fig. 5.5).

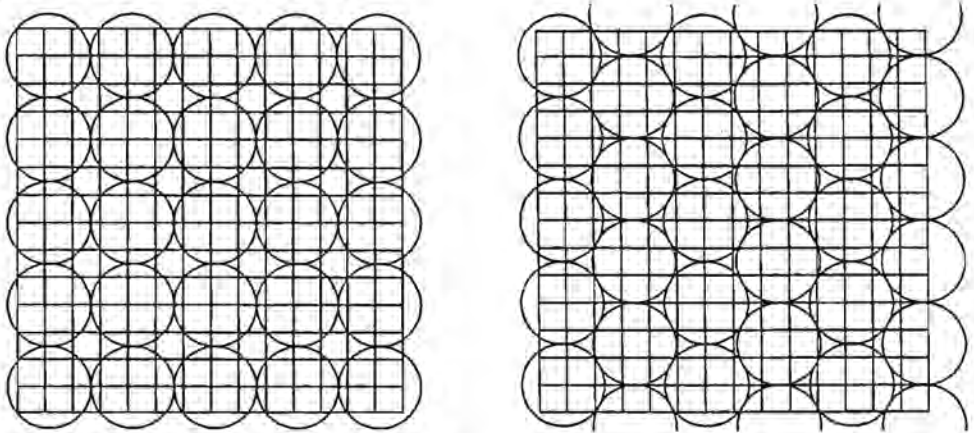


Fig. 5.5: Two-dimensional representations of packed spherical particles. When characterized in terms of representative cells, a square geometry (left) and a triangular geometry (right) are observed.

Note that the ratio of the particle and the grid size is $1 : 14/3$. The fractal characterization of the packings in fig. 5.5 is given in table 5.4.

Table 5.4: Fractal dimension D_M for particle packings (fig. 5.5)

Scale factor M	Square packing		Triangular packing	
	f_M (*)	D_M	f_M (*)	D_M
1	1.0000	2.0000	1.0000	2.0000
7	1.0000	2.0000	1.0000	2.0000
14	1.0000	2.0000	1.0000	2.0000
28	0.9362	1.9802	1.0000	2.0000
56	0.9043	1.9750	0.9971	1.9993
112	0.8206	1.9581	0.9668	1.9928
224	0.7965	1.9580	0.9435	1.9893
∞	0.7854	2.0000	0.9069	2.0000

(*) f_M is the fraction of the grid area occupied by squares covering particles.

The lower f_M values of the square packing are reflected in lower values of the fractal dimension D_M for large values of M . It is a property of the standard mapping technique that the minimum fractal dimension D_M decreases with increasing porosity.

The single particle analysed in section 5.2.1 corresponds to the square packing. Comparison of the series of fractal dimensions (table 5.3 and 5.4) after correcting for the relative size of the particles reveals a difference in the third decimal. This reflects the effect of the random positioning of the grid. As a result, the interpretation of the fractal fingerprint should be restricted to two decimals.

5.2.4. Packing of granules

The fractal characterization of actual packings is investigated by simulating the packing of granules in a die. A simulation program, written with Turbo Pascal 5.0, represents the filling process as follows: the granule enters the die at a random radial position. Subsequently, the granule falls until it hits another granule or the bottom of the die. When two granules collide, the course of events is determined by friction between the granules and the associated stability of the packing. Because data on the friction between the granules is not available, two extremes are simulated: infinite friction and zero friction. With infinite friction, the granule sticks to the granule at the position where impact has occurred. Because the granules stick to each other irrespective of the structure, an open packing is obtained. With zero friction, the granule slides off a stationary granule until it reaches a stable position. A stable position is obtained when the granule is at the lowest point, where it is supported by at least two granules.

By positioning the granules one-by-one, it is assumed that the interference between falling granules is negligible. The simulation process is illustrated in fig. 5.6.

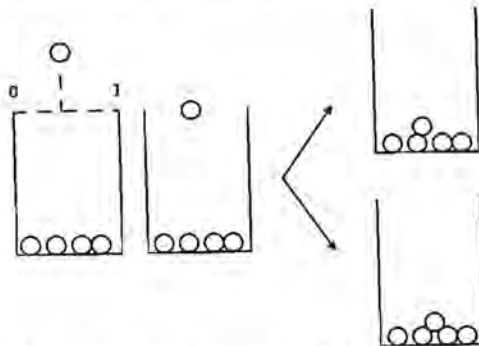


Fig. 5.6: Simulation of the packing of granules. The initial radial position of the granule is random. Subsequently, the granule drops until it hits another granule or the bottom of the die. In case of infinite friction, the granule is fixed to the position where contact is made (top right), while, in case of zero friction, the granule settles in a stable position (bottom right).

Note that, when the friction is zero, granules can settle against the die wall. Other effects, such as granules bouncing off the wall, are not considered. The characteristic packing obtained when the friction between the (equisized) granules is infinite is shown in fig. 5.7.

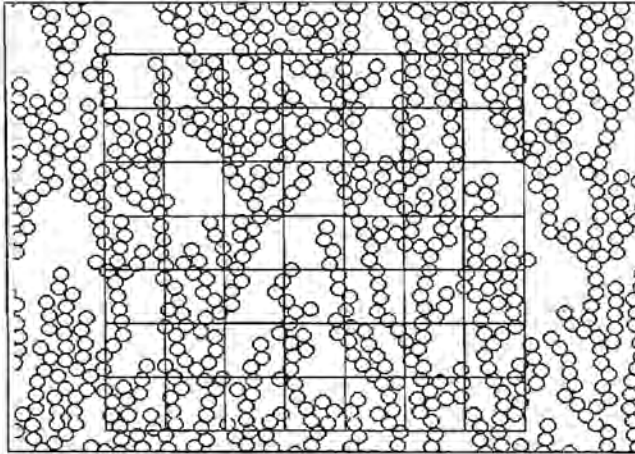


Fig. 5.7: Simulation of granule packing when the friction between the granules is infinitely large. All packings have an open structure where the direction in which the particles drop can be clearly distinguished.

Similarly, the characteristic packing obtained when assuming zero friction between the granules is shown in fig. 5.8.

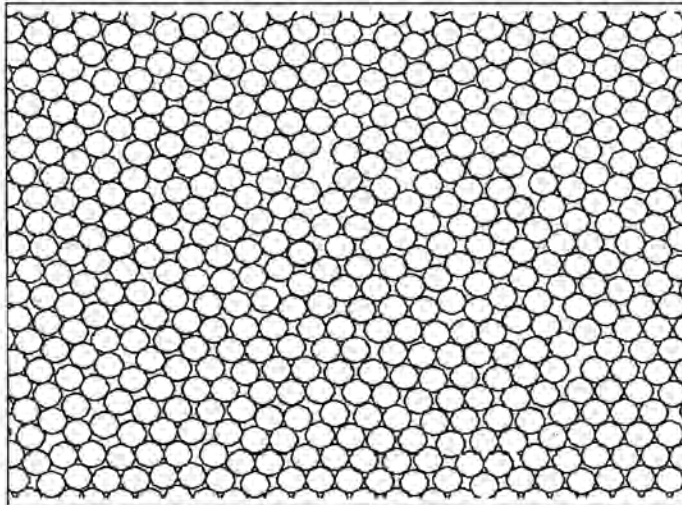


Fig. 5.8: Simulation of granule packing when the friction between the granules is zero. Note that the majority of the granules form cells with coordination three and four.

The packings shown in figs. 5.7 and 5.8 have been analysed using the covering technique previously described. Results are shown in table 5.5.

Table 5.5: Fractal dimension D_M for particle packings (figs. 5.7 and 5.8)

Scale factor M	Infinite friction		Zero friction	
	f_M (*)	D_M	f_M (*)	D_M
1	1.0000	2.0000	1.0000	2.0000
7	1.0000	2.0000	1.0000	2.0000
14	0.9796	1.9922	1.0000	2.0000
28	0.8712	1.9582	1.0000	2.0000
56	0.7136	1.9162	0.9656	1.9958
112	0.5807	1.8848	0.9045	1.9834
224	0.4709	1.8608	0.8404	1.9732
∞	< 0.4709	2.0000	< 0.8404	2.0000

(*) f_M is the fraction of the grid area occupied by squares covering particles.

Clearly, the assumption of infinite friction between the granules is not applicable. This type of structure could be expected in systems where i) anisotropy is encountered and ii) the effect of gravity is insignificant. The sputtering of thin films of atoms can serve as an example. The opposite case, that of zero friction between the particles, leads to much denser packings. Comparison of tables 5.4 and 5.5 indicates that this packing can be characterized with a mixture of cells with coordination 3 and 4. This corresponds with the result obtained in chapter 4. Therefore, zero friction between the granules provides a more realistic representation of the packing of granules.

The packings simulated up to now contain equisized granules only. However, simulations with three sizes of granules produce slightly denser packings which only has a minor effect on the series of fractal dimensions D_M . Consequently, the relation between the granule size distribution and the series of fractal dimensions D_M is not apparent. However, the concept of fractal scaling can be used to characterize the granule size distribution itself. Unfortunately, this removes the influence of the packing structure. Characterization of the particle size distribution with sedimentation data is presented in section 5.3.3.

5.3. Fractal characterization of compaction

5.3.1. Introduction

In this section, the determination of the fractal dimension D for four different aspects of the compaction process is developed. Recall that the concept of fractal scaling is based on the process of coverage, which can be applied to either the solid structure or the pore structure. When covering the solid structure, the size of the pores determine the scale factor M and the edge length L_M . When covering the pore structure, it is the size of the particles which determine the values of M and L_M .

The pore size distribution measured with mercury intrusion porosimetry (MIP) can be characterized with the fractal dimension D (section 5.3.2). Because this represents the structure at a single density, the evolution of the fractal dimension D as a function of the density is of interest. The characterization of the initial particle size distribution obtained from sedimentation analysis reflects the effect of previous processing stages (section 5.3.3).

The determination of the fractal dimension D of the pore size distribution is subject to considerable scatter. Therefore, a single, average pore size is used to represent the pore size distribution. Determination of the fractal dimension D for a single scale factor M is presented in section 5.3.4. Again, the evolution of the fractal dimension as a function of the density is of interest.

The relation between the average pore size and the density can also be modelled when assuming that the compaction process is itself governed by the concept of fractal scaling. Therefore, the comparison of two stages of compaction can be characterized with a fractal dimension D . This novel interpretation of the fractal dimension is presented in section 5.3.5.

5.3.2. MIP data

The intrusion of mercury into smaller pores as the pressure is increased, is conceptually similar to the process of covering the solid structure (section 5.1). After filling the larger pores, smaller pores in the initially solid structure become accessible as the pressure is further increased. This corresponds to replacing the solid matter by cubes of decreasing size.

MIP data consists of the cumulative pore volume as a function of pressure. Accepting the above similarity, the cumulative intruded pore volume is directly related to the total fraction covered f_M through the total volume V_T . Using the Washburn equation, the pressure can be converted to the pore radius, so that both the scale factor M and the edge length L_M are known. This allows determination of the fractal dimension D .

In view of the assumption that pores are cylindrical, covers other than a cube are considered. Options are given in table 5.6.

Table 5.6: Volume covers

Cover	Principal dimensions	Unit volume
Cube	Edge E	E^3
Sphere	Radius r	$4\pi r^3/3$
Block	Edges E, length L	E^2L
Cylinder	Radius r, length L	πr^2L

In the absence of experimental information on the shape of clustered particles, the analysis is generalized to suit all types of covers.

Starting point in the analysis is subdivision of the total volume V_t into the solid and pore volumes:

$$V_t = V_s + V_v \quad (5-11)$$

where subscripts s and v stand for solid and void respectively. Imaginary cover units are placed in all zones where ferrite particles are present. Note that the size of the cover unit corresponds to the size of the largest pores present. Subsequently, cover units of decreasing size are placed within the largest units exposing the smaller pores present. In mathematical terms:

$$V_t = NV_c + V_v \quad (5-12)$$

where V_c is the volume of a cover unit. The value of N depends on the scale factor M and the fractal dimension D (eq. 5-5a), while M is related to the characteristic length L_M and the total volume V_t through eq. (5-6):

$$N = M^D = (V_t^{1/3}/L_M)^D \quad (5-13)$$

With arbitrarily shaped cover units, L_M is not obvious. Therefore, L_M is defined as a measure of the size of a representative plane in the cover unit. This measure is indicated as the principal dimension x. The other principal dimensions, y and z, can be expressed in terms of using constants C_1 and C_2 :

$$y/x = C_1$$

$$z/x = C_2$$

In a structure where fractal scaling occurs, C_1 and C_2 are independent of the magnitude of x . Note that when the cover is characterized by a single dimension, C_1 and C_2 are unity. Expressing the volume of a cover V_c in terms of its principal dimensions:

$$V_c = C_cxyz = C_cC_1C_2x^3 \quad (5-14)$$

where C_c is shape factor. Substituting N and V_c in eq. (5-12) produces:

$$V_t = V_v + V_t^{D/3}C_cC_1C_2x^{3-D} \quad (5-15)$$

Selecting the pore radius r to represent the principal dimension x is useful when interpreting MIP data. The fractal dimension D is then found from a plot of $\ln(-dV_v/dr)$ versus $\ln(r)$:

$$\ln(-dV_v/dr) = \ln(V_t^{D/3}C_cC_1C_2(3-D)) + (2-D)\ln(r) \quad (5-16)$$

Eq. (5-16) shows that fractal scaling occurs if a (partly) straight line is observed. Realistic values of D are between 2 and 3, so that the graph should slope downwards. The intercept, by definition where $\ln(r)$ is zero, yields the product C_1C_2 given values of D , C_c and V_t .

If the cover is characterized by two principal dimensions only, either C_1 or C_2 is unity. This allows determination of the unknown constant from the intercept. For cylindrical cover units, the constants are $C_c=\pi$, $C_1=1$ and $C_2=L_v/r$. Consequently, the use of alternative cover units yields an additional characteristic parameter in the form of the aspect ratio L/r .

5.3.3. Sedimentation data

Because sedimentation analysis requires suspension of the particles, fractal analysis is restricted to characterization of the particle size distribution and not the arrangement within a compact. However, characterization of the particle size distribution is useful on account of its effect on the porosity within the granules.

Sedimentation data consists of the mass of particles present as a function of the particle size. Assuming a constant particle density, the mass is proportional to the volume of particles of a particular size. The analysis then proceeds similarly to the analysis of MIP data. Defining a representative volume V_v , which can be divided into a solid and a void volume:

$$V_t = V_s + V_v \quad (5-17)$$

Assuming the concept of fractal scaling applies, the number of particles N required to fill the void volume V_v is a function of the scale factor M . Representing the particles as ideal spheres and substituting N with eq. (5-13), eq. (5-17) becomes:

$$V_t = V_s + 4V_t^{D/3}\pi r_p^{3-D}/3 \quad (5-18)$$

where r_p is the radius of the particle. Differentiating with respect to r and taking the natural logarithm yields:

$$\ln(-dV_v/dr_p) = \ln(4V_t^{D/3}\pi(3-D)/3) + (2-D)\ln(r_p) \quad (5-19)$$

Plotting $\ln(-dV_v/dr_p)$ versus $\ln(r_p)$ yields the fractal dimension D .

5.3.4. Averaged compaction data

When a size distribution consists of a single, sharp peak, fractal scaling can only occur over a narrow size range. In this case, an alternative interpretation is proposed: the fractal dimension D is only used to characterize the material for a single scale factor M . The required material characteristics are obtained in the following derivation. Defining f_M (eq. (5-1) for a three-dimensional structure:

$$f_M = NL_M^3/V_t \quad (5-20)$$

Assuming the concept of fractal scaling is valid, N can be substituted with eq. (5-13):

$$f_M = V_t^{D/3-1}L_M^{3-D} \quad (5-21)$$

The significance of f_M depends on the nature of the available data. When L_M corresponds to the average pore size r , f_M represents the total solid fraction, or the complement of the porosity. Given the average particle size r_p , f_M equals the porosity. Note that L_M is defined as the average size rather than the size of the smallest pore or particle present.

Apart from L_M and f_M , the fractal dimension D is related to the total volume V_t . During compaction, the decrease of V_t can be expressed as:

$$V_t = V_s/(1-\varepsilon) = m/(\rho_{th}(1-\varepsilon)) \quad (5-22)$$

where V_s is the solid volume. Because V_s is considered invariant throughout compaction, V_t is the ratio of the mass m and theoretical (or zero porosity) density ρ_{th} . Substituting V_t , f_M and L_M in eq. (5-21), given either the pore size r or the particle size r_p :

$$(1-\varepsilon)^{D/3} = (m/\rho_{th})^{D/3-1} r_p^{3-D} \quad (5-23a)$$

or

$$\varepsilon(1-\varepsilon)^{D/3-1} = (m/\rho_{th})^{D/3-1} r_p^{3-D} \quad (5-23b)$$

During compaction, the pore size r decreases while the particle size r_p remains constant. Values for D from eqs. (5-23a) and (5-23b) are therefore necessarily different.

The dependency of D on the mass m as expressed by eq. (5-23) complicates the interpretation of D : it is desirable that samples with identical porosities and average pore sizes have the same fractal dimension D , irrespective of the mass.

5.3.5. Compaction process data

The concept of fractal scaling is applied to the compaction process itself by extending the approach using averaged data. The fractal dimension now relates the reduction in the pore size to the increase in density. Recognizing that the complement of the porosity is proportional to the density:

$$(1-\varepsilon) = \rho/\rho_{th} \quad (5-24)$$

Substituting $(1-\varepsilon)$ in eq. (5-23a) yields:

$$(\rho/\rho_{th})^{D/3} = (m/\rho_{th})^{D/3-1} r_p^{3-D}$$

or

$$\rho^{D/3}/(\rho_{th} m^{D/3-1}) = r_p^{3-D} \quad (5-25)$$

Comparison of two (compaction) states eliminates the dependency on the mass and the theoretical density:

$$(\rho_2/\rho_1)^{D/3} = (r_2/r_1)^{3-D}$$

or

$$D = \frac{9}{(3 + \ln(\rho_2/\rho_1)/\ln(r_2/r_1))} \quad (5-26)$$

The *minimum* value of D is 3. As D approaches 3, the number of pores sharply increases: pores are compressed to form numerous smaller pores.

For three-dimensional structures, the fractal dimension only has a physical significance for values between 2 and 3. Therefore, it is more appropriate to denote D in eq. (5-26) as the *fractal exponent* D_* . The difference with the traditional fractal dimension

is a result of variation of the scale factor M , which is normally relative to the initial volume. During the compaction process, the scale factor M is not only determined by the pore size, which equals L_M , but also by the reduction in volume. The latter effectively reduces the scale factor M , thereby increasing D .

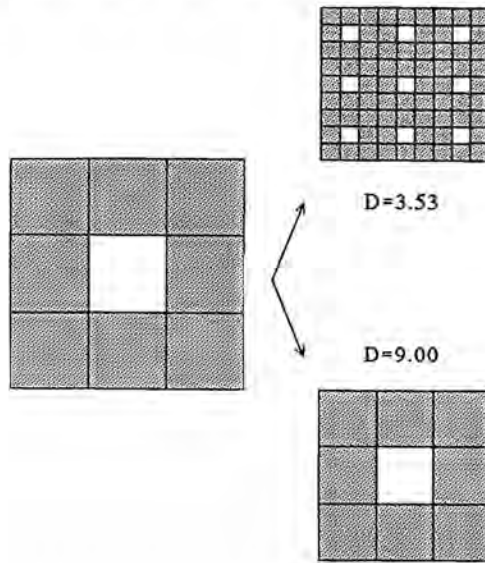


Fig. 5.9: Significance of the fractal exponent D during compaction. The cross-section of a pore is represented by a blanc square. With an increasing number of blanc squares, D approaches a minimum value of 3 (in two dimensions: 2). Note that D varies independently of the porosity which is equal for the compacted granulate (right).

Eq. (5-26) applies to a unimodal pore size distribution. During the first two stages of the compaction process, the pore size distribution consists of more than one peak. Because the pores are compressed simultaneously, the change in density is not related to the change in a single pore size. One option is to relate the volume of each type of pores to the pore size. Comparing two states:

$$D = \frac{9}{(3 + \ln((1 - \epsilon_2)/(1 - \epsilon_1))/\ln(r_2/r_1))} \quad (5-27)$$

Note that ϵ_2 and ϵ_1 are based on the theoretical density of the ferrite. Eq. (5-27) has the setback that it does not accommodate the simultaneous compression of different types of pores.

5.4. Fractal characterization of the compaction process

5.4.1. MIP analysis

The fractal dimension D is determined from the pore size distribution of compacts by transforming MIP data with eq. (5-16). A typical plot is shown in fig. 5.10.

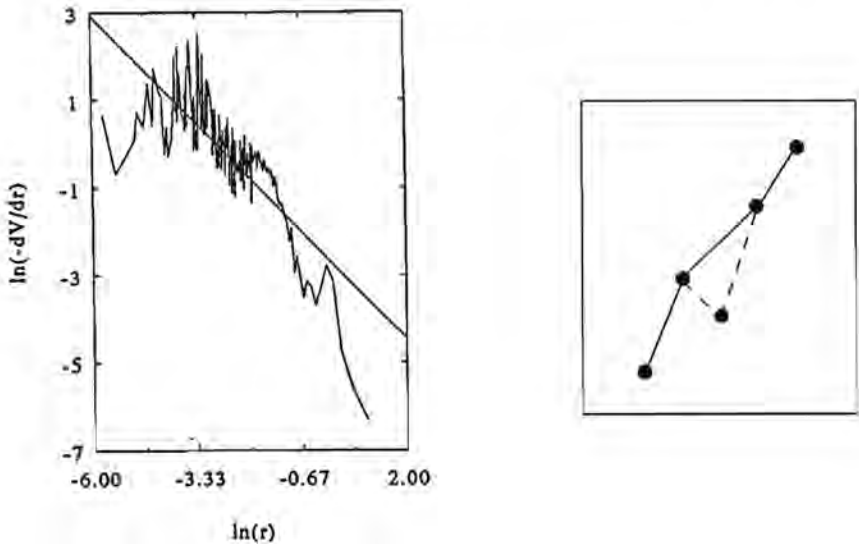


Fig. 5.10: Transformation of MIP data. Intervals where dV/dr is negative are avoided by omitting the downward point (see insert). Fitting linear relations to the left and right sections of the curve produces unrealistic values for D . However, the best fit using all the data points produces values for D between 2.7 and 3 (in this example $D=2.92$).

The difference between the best fit and the transformed data indicates that the significance of fractal scaling in compacts is limited.

The reproducibility of the fractal dimension D determined with MIP has been verified by measuring 9 compacts using a similar measurement profile (264 pressure points). The density of the compacts was 2.82 g/cm^3 with a standard deviation of 1.5 %. The fractal dimension was found to be 2.86 with a standard deviation of only 0.03. The corresponding variation (0.010) is smaller than the variation in the average pore size (0.023) obtained from the same measurement. This indicates relative insensitivity to measurement errors. However, using different or less pressure points during a MIP measurement significantly affects the absolute value of D . In other words, MIP measurements do not guarantee an accurate assessment of D . Therefore, it is recommended to use a standardized measurement profile.

With decreasing compact density, the presence of interagglomerate pores is reflected

in the pore size distribution, which then consists of two peaks. The peak attributed to the (large) interagglomerate pores produces a shoulder to the right in fig. 5.4. The reduction of the slope of the curve fitted through *all* points decreases the fractal dimension D . Because the contribution of the interagglomerate pores increases with decreasing compact density, the fractal dimension D is continuously decreased.

Consequently, the fractal dimension D increases during compaction, which appears to be consistent with the standard interpretation: a denser structure generally has a higher fractal dimension. However, the decrease of the total volume during compaction reduces the increase of the scale factor. As a result, the fractal dimension D could also *decrease* during compaction. This aspect is discussed in section 5.3.4.

5.4.2. Sedimentation analysis

The particle size distribution measured with sedimentation analysis is transformed using eq. (5-19). A typical plot is shown in fig. 5.11. The data shown in fig. 5.11 has not been smoothed because this affects the value of the fractal dimension D . However, smoothing the data using a 4.00 % fast Fourier transform operation removes the spread. This indicates that considerable measurement noise is present which is probably due to instability of the X-ray beam. Furthermore, sedimentation analysis with ferrite particles is complicated by the mutual (magnetic) attraction of particles. This leads to overestimation of the particle size and, consequently, a lower fractal dimension D .

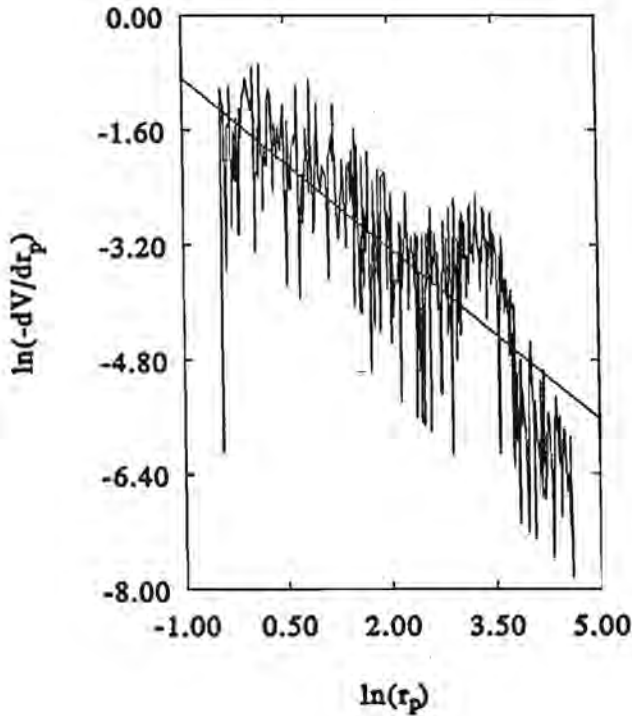


Fig. 5.11: Transformation of sedimentation analysis data. Although a satisfactory best fit is obtained, the actual correlation is poor on account of the spread: the correlation coefficient is only 0.75. The fractal dimension has a value of 2.79. Note that the data has not been smoothed. The granulate suspension was prepared with 50 % ethylene glycol and 50 % water and mixed ultrasonically for 4 minutes.

5.4.3. Averaged compaction data

The scale factor is based on the ratio of the local and the total dimensions. Local dimensions are either the average pore or particle size. The average pore size depends on the compaction stage (section 4). Initially the pore size distribution consists of three peaks, which disappear sequentially during compaction. During the final stage, only the peak attributed to the interparticle pores remains. This stage, starting at a density of 2.78 g/cm^3 , can be characterized with the averaged data approach. The average particle size is considered constant during compaction and is approximately $0.5 \text{ }\mu\text{m}$. Two aspects make the approach based on particles unattractive:

- because the particle size is constant, the fractal dimension varies with the porosity and the total volume or mass only.
- because the particles are larger than the interparticle pores, the process of covering

pores is not accurate.

Therefore, particles are covered with pores whose size is established with MIP as a function of the density (section 4.2). The fractal dimension determined from eq. (5-19a) varies between 2.95 and 2.98. This insignificant variation is the consequence of the large scale factor: with pores less than 10^{-6} m in size and a volume of roughly 10^{-6} m³, the scale factor is in the order of 10^4 .

5.4.4. Compaction process data

By comparing two compaction states, the strong influence of the scale factor on D is avoided. The fractal exponent D_c is found as a function of the density using the MIP data presented in section 4.3 (fig. 5.12).

The particles remain intact during compression so that the increase in the number of pores during compression is limited. By contrast, the agglomerates are fragmented to form numerous smaller pores. This explains the lower value of the fractal exponent.

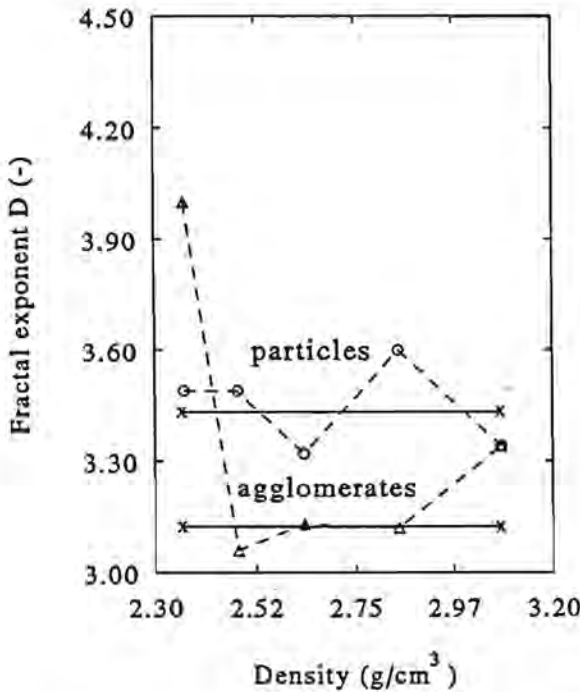


Fig. 5.12: Development of the fractal exponent D_c . The value of each point is determined by comparing successive states. The average value follows from comparison of the lowest and the highest density.

5.5. Discussion and conclusion

The concept of fractal scaling has been applied to characterize the structure of granules, compacts and the compaction process itself. With respect to the packing of granules, the limited significance of the fractal dimension D is demonstrated from analysis of images. However, the determination of the fractal dimension from mercury intrusion data indicates a number of interesting features.

Characterization of compact structures indicates that the fractal dimension D increases during compaction while the fractal exponent D_e is constant for a particular type of pores. The two approaches are complementary: the increase in the fractal dimension D indicates that rearrangement of the particles occurs while the fractal exponent D_e shows that this rearrangement leads to fragmentation of the agglomerate substructure.

The determination of the fractal dimension D of the compact structure is complicated by the fluctuations in the log-log plots obtained with MIP. This is understandable in view of the distinct types of pores present. The best option is to take determine the linear relation fitting *all* data points. In this way, the effect of local variations is reduced. The thus determined fractal dimension has significance for pores ranging over 3 orders of magnitude in size. During compaction, an increase of the fractal dimension is observed. Although the reproducibility is high, the accuracy is doubtful.

The building blocks of the structure, ferrite particles, have been characterized with the fractal dimension. At best, the fractal dimension provides an alternative to the characterization of the particle size distribution with statistical parameters. This reflects the effects of previous processing steps (mixing, pre-sintering, milling). However, the limited correlation makes the accuracy of the fractal dimension doubtful.

Finally, the compaction process is characterized with the fractal exponent D_e . When D_e approaches 3, fragmentation of the pores occurs. This is a result of smaller particles filling cavities between larger particles or the disintegration of agglomerates. Because the presence of agglomerates is proved by the cell approach introduced in section 4, it provides a quantitative measure for characterization of agglomerates.

The approach using D_e can be extended to the sintering process. During sintering, the material shrinks although the pores become larger. Using eq. (5-27), this leads to values for D_e between 0 and 3.

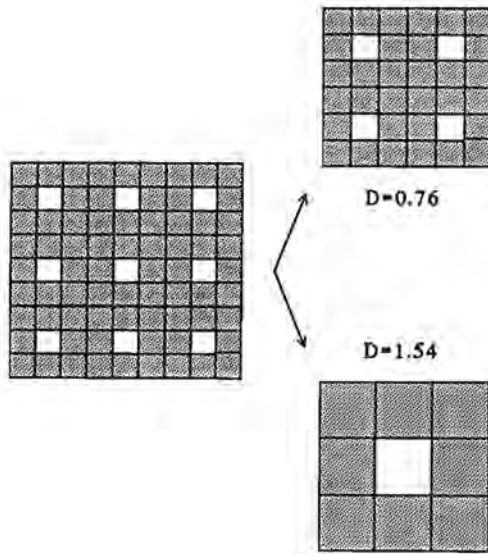


Fig. 5.13: Significance of the fractal exponent D , during sintering. As the porosity decreases, the average pore size increases. In two-dimensions, the fractal exponent approaches 2 when the pore growth is more pronounced.

References

Suggested reading:

- W. Ackermann, H. Spindler, 'The fractal dimension as a characteristic for catalysts', *Zeitschrift physikalische Chemie*, vol. 269 (1988), 1000-1009.
- M. Benohoud et.al., 'Surface-Area, Mass Fractal Dimension, and Apparent Density of Powders', *Journal of Colloid and Interface Science*, vol. 124, no. 1 (1988), 156-161.
- C. Essex, M. Nerenberg, 'Fractal Dimension - Limit Capacity or Hausdorff Dimension', *American Journal of Physics*, vol. 58, no. 10 (1990), 986-988.
- B. Mandelbrot, 'The Fractal Geometry of Nature', Freeman, San Francisco, California, 1982.
- K. H. Schlüßler, L. Walter, 'Computer Simulation of Randomly Packed Spheres - a Tool for Investigating Polydisperse Materials', *Particle Characterization*, no. 3 (1986), 129-135.
- J. Theiler, 'Estimating fractal dimension', *Journal of the Optical Society of America A*, vol. 7, no. 6 (1990), 1055-1072.

Chapter 6

Analysis of compaction curves

6.1. Introduction

A compaction curve represents the relation between the density of a powder and the required compaction pressure (fig. 6.1). This relation is strongly influenced by the conditions under which it is measured. Therefore, the influence of the measuring conditions is analysed first (section 6.2). Subsequently, the influence of important compaction parameters is investigated (section 6.3). Parameters varied are:

- the binder type and content
- the die diameter
- the die-wall roughness
- the granule size

Finally, the compaction curve is interpreted with a model, which allows prediction of the strength of the compact. Because the compact strength is determined by the binder type and content, it provides a rapid indication of the suitability of binders.

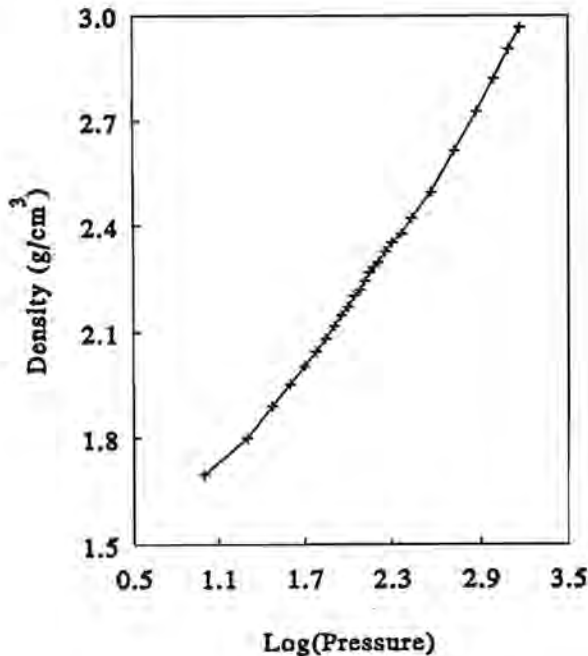


Fig. 6.1: Compaction curve obtained when pressing (Mn,Zn)-ferrite granulate.

6.2. Measurement of compaction curves

Compaction curves are obtained by single-sided compaction of granulate in a cylindrical die. The density is obtained either *during* compaction by recording the displacement of the punch or *after* compaction by measuring mass and volume of the compact. Measuring the density during compaction has two advantages:

- only a single compaction experiment is required.
- the compaction curve is also recorded at densities below the density where the compact has sufficient strength to be handled.

However, measuring the density after compaction is more realistic because it includes the effects associated with ejection and relaxation. Ejection of the compact from the die requires pressure because the compact is jammed in the die. This can produce further compaction, especially because the compact is moved in the direction opposite to which it was compacted. Relaxation is the spontaneous expansion of the compact volume which commences after ejection. This occurs on account of the recovery of elastically-deformed binder and particles. Although the largest effect of relaxation is observed immediately after ejection of the compact, further expansion occurs in the course of time. The expansion is determined by factors such as compact density, binder type, atmospheric conditions (humidity, temperature) and the compliance of the pressing equipment. Fig. 6.2 shows the two types of compaction curves for the same granulate.

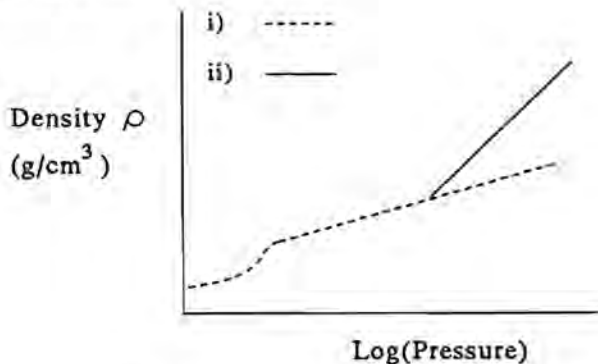


Fig. 6.2: Compaction curves obtained by i) continuously measuring the density and the applied pressure and ii) measuring the compact density as a function of the maximum applied pressure.

Note that the density is plotted versus the logarithm of the pressure instead of the pressure. This is a more convenient representation because it often yields (locally) linear correlations.

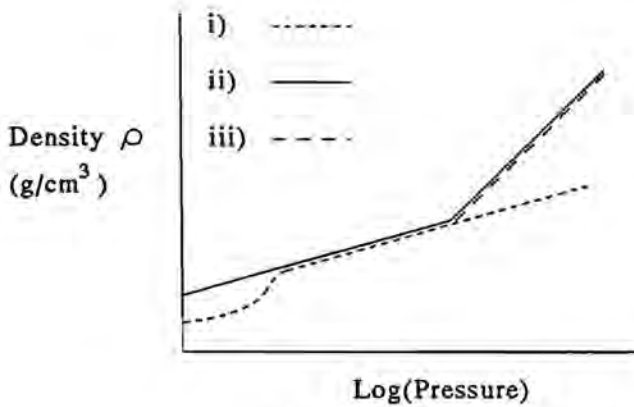


Fig. 6.3: Compaction curves obtained by measuring the density i) during continuous compaction, ii) during discontinuous compaction and iii) after compaction and ejection.

In order to establish the reason for the difference between the curves in fig. 6.2, a third method, based on discontinuous compaction, is devised: the pressure is held constant until the displacement of the punch, which is related to the density, has reached a stable value. Upon instating a constant punch pressure, further rearrangement of the particles increases the density. This rearrangement occurs on account of relaxation in a confined space. Fig. 6.3 shows that the density achieved with discontinuous compaction is initially higher than obtained with continuous compaction. This is due to temporal rearrangement of the granules, which reduces the resistance to compaction. No further rearrangement occurs when the two curves converge. The density and the pressure at which the curves converge become smaller with decreasing die diameter. This observation supports the proposed explanation because granule rearrangement is expected to be less in smaller dies.

Above a density of 2.3 to 2.5 g/cm³, the discontinuously-measured compaction curve coincides with the compaction curve obtained from compacts. This suggests that compaction due to relaxation in the die is more significant than the combined effects of ejection or relaxation outside the die.

6.3. Characterization of compaction curves

6.3.1. Introduction

Three types of compaction curves have been recorded, which are measured directly in a continuous (i) or discontinuous (ii) manner or indirectly with compacts (iii). Characterization of these compaction curves is required in order to establish the influence of the process parameters. Two pressure ranges are distinguished which are separated by the pressure where the three curves join. This transition pressure also coincides with the density where compacts

have sufficient strength to be handled. Hence it corresponds to the origin of the compaction curve obtained by measuring the density of compacts. The range below this pressure is denoted as zone I, above this pressure zone II.

A two-parameter equation of the following form is suitable to represent the curves in either zone:

$$\rho = A \log(P) + B \quad (6-1)$$

where A and B are empirical compaction parameters. Parameter A represents the compressibility of the granulate while parameter B reflects the density of the initial packing. Fig. 6.4 depicts the sections which are characterized. Note that the initial stage of continuously-measured curves is not considered because of poor reproducibility. In the following sections, the influence of granulate and process conditions on the parameters is determined.

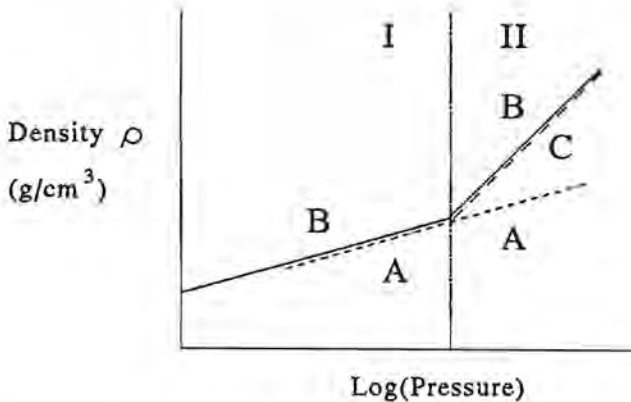


Fig. 6.4: Interpretation of sectioned compaction curves. Only sections which are approximately linear are shown. These are characterized by equations of the form $\rho = A \log(P) + B$, where A and B are parameters obtained by regression.

6.3.1. Influence of the granulate

Two aspects are investigated: the type of binder and the size of the granules. With respect to the type of binder, the compaction curves are measured by recording 30 pressure-density points discontinuously (method ii). The parameters of zone I are determined from approximately 20 points while the remaining points are used to calculate the parameters of zone II. The results for a number of binders are presented in tables 6.1 and 6.2.

Table 6.1: Influence of binder type and content on the compaction curve (zone I)Technique: discontinuous pressing, die diameter: 12.0 mm, roughness: < 0.05 μm

Binder type	Content (wt-%)	A (g/cm^3)	B (g/cm^3)	Correlation coefficient	Density range (g/cm^3)
Acrylic I	1.25	0.50	1.13	0.9995	1.95 - 2.35
Acrylic II	0.86	0.51	1.16	0.9987	1.94 - 2.47
Acrylic II	1.70	0.53	1.15	0.9971	1.70 - 2.50
Mixture	0.72	0.52	1.18	0.9999	1.68 - 2.44
PVA	1.00	0.58	0.99	0.9998	1.55 - 2.33

Table 6.1 shows that for zone I the granulate containing PVA binder displays different compaction behaviour.

Table 6.2: Influence of binder type and content on the compaction curve (zone II)Technique: discontinuous pressing, die diameter: 12.0 mm, roughness: < 0.05 μm

Binder type	Content (wt-%)	A (g/cm^3)	B (g/cm^3)	Correlation coefficient	Density range (g/cm^3)
Acrylic I	1.25	0.66	0.76	0.9998	2.36 - 2.90
Acrylic II	0.86	0.69	0.70	0.9987	2.48 - 2.93
Acrylic II	1.70	0.73	0.72	0.9971	2.51 - 2.99
Mixture	0.72	0.59	1.02	0.9999	2.45 - 2.94
PVA	1.00	0.69	0.73	0.9998	2.34 - 2.98

Table 6.2 shows that the compaction curve of granulate containing a mixture of binders (PVA, acrylic II) is markedly different. The large value of B indicates that the initial packing of the granulate is dense and that the compression of intergranular pores proceeds more efficiently than with the other granulate. However, in the relevant range of densities (2.4-2.9 g/cm^3), the granulate containing 1.70 wt-% of acrylic II requires the lowest compaction pressure. Because the differences are minor, a tentative conclusion is that the binder has no effect on pressure-density relation in zone II.

The compaction curve in zone II is also determined by measuring the density of a series

of compacts, which have been subjected to a fixed pressure. For each type of binder, 10 compacts with densities between 2.4 and 3.2 g/cm³ have been measured. Table 6.3 shows the values of the compaction parameters.

Table 6.3: Influence of the binder type on the compaction curve (zone II)

Technique: measuring compacts, die diameter: 18.0 mm, roughness: < 0.05 μm

Binder type	A (g/cm ³)	B (g/cm ³)	Correlation coefficient
Acrylic I	0.63	0.83	0.9995
Acrylic II (*)	0.64	0.87	0.9998
Mixture	0.62	0.93	0.9966
PVA	0.68	0.74	0.9971

(*) contains 0.86 wt-% binder.

Comparison of tables 6.3 and 6.4 shows that, with the exception of PVA granulate, the values of A and B differ. This could be attributed to elastic relaxation and variation in the diameter of the die (see section 6.3.2).

When constructing a compaction curve using the data in tables 6.1 to 6.3, the transition density between zone I and II is given by the intersection of the respective curves. Table 6.4 gives the transition densities by using table 6.1 for zone I and tables 6.2 or 6.3 for zone II.

Table 6.4: Transition density between zone I and II.

The compaction curve in zone I is measured discontinuously.

Binder type	Content (wt-%)	Zone II: pressing discontinuously	Zone II: measuring compacts
Acrylic I	1.25	2.31	2.31
Acrylic II	0.86	2.56	2.23
Acrylic II	1.70	2.15	-
Mixture	0.72	2.29	2.50
PVA	1.00	2.36	2.50

All transition densities are located between 2.15 and 2.56 g/cm³, which corresponds to the range where the (large) intergranular pores are compressed and a compact is formed.

The influence of the granulate size (distribution) is investigated by sieving acrylic II (0.86 wt-%) into three fractions. The compaction curve of each of these fractions has been measured by recording 20 points discontinuously in zone I.

Table 6.5: Influence of the granule size on the compaction curve (zone I)

Die diameter: 25.4 mm, roughness: < 0.05 μm

Granule size range (μm)	A (g/cm ³)	B (g/cm ³)	Correlation coefficient
106-150	0.58	0.95	0.9981
212-250	0.58	0.95	0.9980
355-425	0.58	0.95	0.9980

Table 6.5 shows that the compaction behaviour of granulates with a narrow size distribution is similar. This is attributed to the relatively large diameter of the die. When the die is relatively small, the effect of friction with the wall is likely to produce an inhomogeneous packing of the granules.

Comparison with acrylic II in table 6.1 shows that the narrow granule size distribution increases the pressure dependency of the compact density. However, the value for B of the sieved granulate is lower (0.95 versus 1.16), indicating that the packing after filling is less dense. As a result, a narrow granule size distribution only reduces the required pressure when the compact density is larger than 2.69 g/cm³. At this density, the intergranular pores have been compressed. This implies that the advantage of compacting packings of equisized granules only become apparent after the relatively larger intergranular pores have been compressed.

6.3.2. Influence of the die characteristics

Two aspects are analysed: the size of the die and the roughness of the die-wall. In table 6.6, the influence of the die diameter is shown. The parameters A and B are determined from the relation between the pressure and the density of series of 10 compacts. Table 6.6 shows that the value of B decreases strongly with the die diameter. This reflects an increasing effect of the die wall on the initial packing of the granules. Because the die diameter is much larger than the granules, the mode of filling will be of influence. During the experiments, the

granulate is passed through a funnel during filling of the die. However, no data on the filling process (e.g. rate, height above die) is available.

Table 6.6: Influence of die diameter on the compaction curve (zone II)
Die-wall roughness: < 0.05 μm

Die diameter (mm)	L/D ratio (-)	A (g/cm^3)	B (g/cm^3)	Correlation coefficient
14.10	0.36	0.65	0.77	0.9991
18.09	0.33	0.64	0.85	0.9971
28.12	0.33	0.62	0.94	0.9993

Table 6.7 indicates the effect of wall roughness on the compaction curve parameters. Series of 10 compacts with varying densities were pressed each of the dies.

Table 6.7: Influence of die-wall roughness on the compaction curve (zone II)

Die diameter (mm)	Wall roughness (μm)	A (g/cm^3)	B (g/cm^3)	Correlation coefficient
18.02	> 0.20	0.64	0.83	0.9987
18.09	< 0.05	0.64	0.85	0.9971
26.02	> 0.20	0.62	0.93	0.9992
28.12	< 0.05	0.62	0.94	0.9993

The positive effect of smoother walls is negligible: as long as the particles (average size: 0.5 μm) are larger than irregularities in the surface of the die wall, no differences are observed.

6.4. Interpretation of compaction curves

6.4.1. Description of model

Given the characterization of the experimental compaction curves, a theoretical interpretation is sought. In this section, a model based on characterization of the state of stress

during compaction is presented. The state of stress can be represented in a second-order stress tensor, which contains six independent stresses. Fig. 6.5 illustrates the orientation of these stresses.

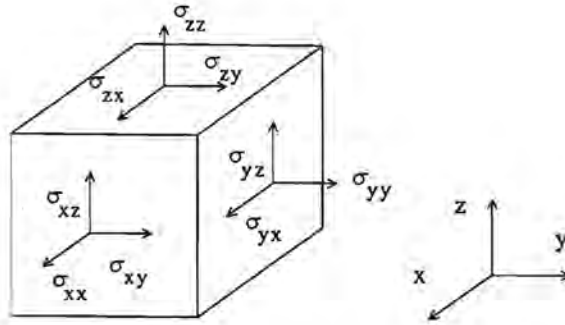


Fig. 6.5: Schematic representation of the stresses acting on a cube. The size of the cube is arbitrary, varying between an infinitesimal volume and the whole body. With compaction, variations in the magnitude and orientation of the stresses within the granulate cannot be measured. Therefore, it is convenient to consider the stresses acting on the entire granulate mass in the die.

The state of stress of the granulate in a die can be represented graphically with a Mohr circle, which is obtained by plotting the normal stresses versus the shear stresses. The normal stresses, which act perpendicular to the surface, are given by σ_{xx} , σ_{yy} and σ_{zz} (see fig. 6.5). The stresses parallel to the surface are shear stresses, which will be indicated with τ instead of σ . Fig. 6.6 shows the Mohr circle for a three-dimensional state of stress.

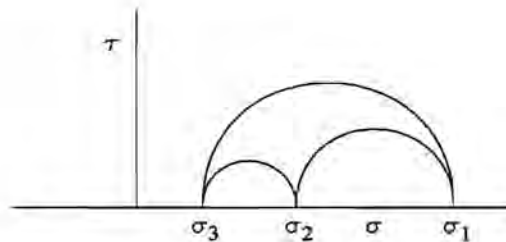


Fig. 6.6: Mohr circle representing a three-dimensional state of stress. The positions at which the Mohr circle intersects the σ -axis (zero shear stress) corresponds to the principal stresses (σ_1 , σ_2 , σ_3). Note that any point on the Mohr circle can be reached by rotation of the body under consideration.

For modelling purposes, it is necessary to reduce the number of variable stresses. This is achieved by considering compaction in dies where an axis of symmetry is present. The axis of symmetry allows representation of the state of stress in two dimensions. A two-dimensional state of stress is characterized by a major (σ_1) and a minor (σ_3) principal stress, which produce a single shear stress, as illustrated in fig. 6.7.

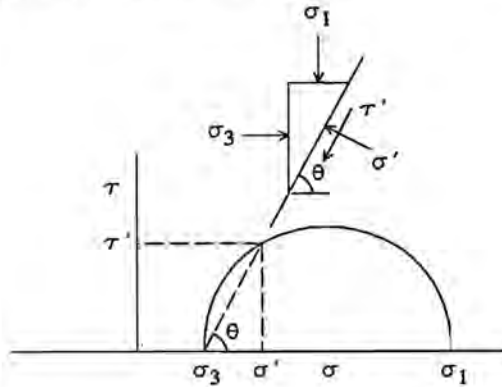


Fig. 6.7: Mohr circle representing a two-dimensional state of stress. The figure above the Mohr circle shows the orientation of the stresses at a point (σ', τ') on the Mohr's circle.

With a cylindrical die, it is convenient to use polar coordinates instead of cartesian coordinates. On account of symmetry, all shear stresses acting on the granulate in the circumferential direction are zero. Fig. 6.8 shows the stresses acting on granulate in a cylindrical die.

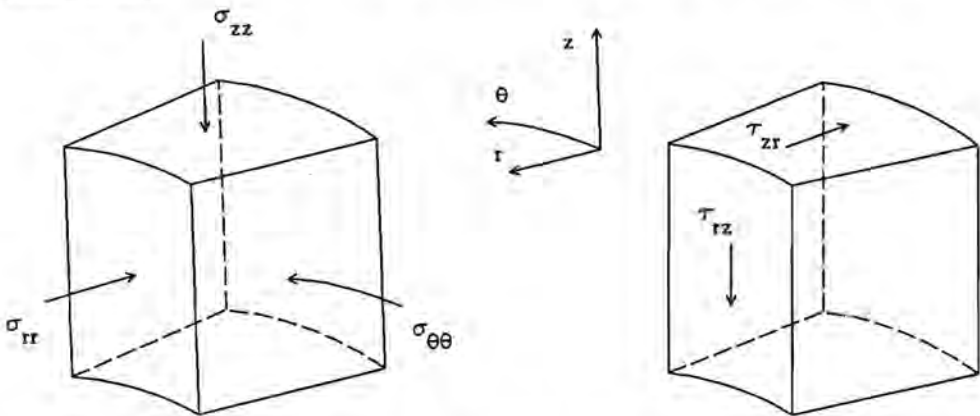


Fig. 6.8: Stresses during compression of cylindrical body. Using polar coordinates (r, θ, z), the normal stresses in an arbitrary section are depicted (left). The only remaining shear stresses are also shown (right).

Note that the normal stresses in the axial and radial direction (σ_{zz} , σ_r) are not equivalent to the principal stresses σ_1 and σ_3 defined in fig. 6.7. However, the sum of the normal stresses in any orthogonal coordinate system, given by the trace of the stress tensor $\underline{\sigma}$, is constant. Therefore the following equality holds:

$$\sigma_1 + \sigma_2 + \sigma_3 = \sigma_{zz} + \sigma_r + \sigma_{\theta\theta} \quad (6-2)$$

A Mohr circle represents a stable situation, which implies that the stresses acting on a differential element are balanced. Equating the stresses in the axial direction:

$$\partial\sigma_{zz}/\partial z + \partial\tau_{rz}/\partial r + \tau_{rz}/r = 0 \quad (6-3)$$

Similarly, in the radial direction:

$$\partial\sigma_r/\partial r + \sigma_r/r + \partial\tau_{rz}/\partial z - \sigma_{\theta\theta}/r = 0 \quad (6-4)$$

Finally, in the circumferential direction:

$$\partial\sigma_{\theta\theta}/\partial r + \sigma_{\theta\theta}/r - \sigma_r/r = 0 \quad (6-5)$$

In the following, it is assumed that the radial gradient in the circumferential stress is sufficiently small to be neglected. In that case, eq. (6-5) shows that the circumferential and radial normal stresses are equal. This simplifies eq. (6-4):

$$\partial\sigma_r/\partial r + \partial\tau_{rz}/\partial z = 0 \quad (6-6)$$

Because the shear stresses τ_{rz} and τ_{rz} are equal, the balances given by eqs. (6-3) and (6-6) contain four unknowns: σ_{zz} , σ_r , $\sigma_{\theta\theta}$ and τ_{rz} . This number is reduced to three when a correlation between σ_r and σ_{zz} is known. It is convenient to assume that σ_r is proportional to σ_{zz} :

$$\sigma_r = K\sigma_{zz} \quad (6-7)$$

where K is a constant. Literature suggests that K has a value of approximately 0.5. Consequently, the Mohr circle is obtained by plotting σ_{zz} versus τ_{rz} .

Upon application of pressure, the granulate is compacted until the imposed stress is balanced by the internal forces. When the applied pressure is removed, relaxation occurs, producing recovery of reversible or elastic deformation. The remaining irreversible or plastic

deformation is reflected in expansion of the Mohr circle. This evolution is known as hardening (fig. 6.9).

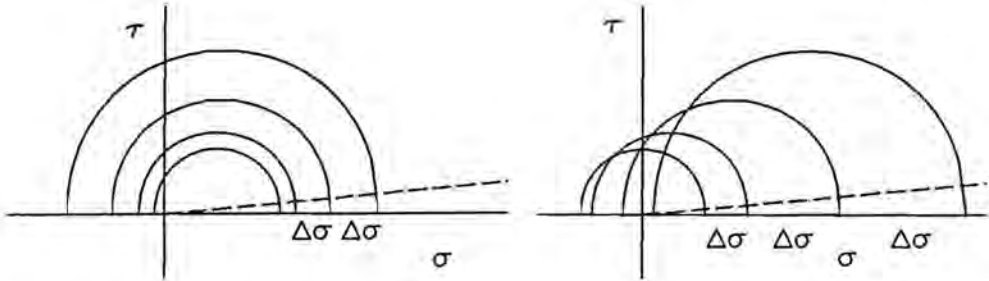


Fig. 6.9: Isotropic and kinematic hardening. The evolution of Mohr circles in the left figure indicates isotropic hardening, which is characterized by a fixed position of the centre of the Mohr circle. During kinematic hardening, the centre of the Mohr circle shifts to higher stresses. The dashed line tentatively indicates the path followed during uniaxial die compaction.

When increasing the axial pressure (σ_z) during compaction in a die, the pressure exerted on the die wall (σ_r) is expected to increase. This implies that the hardening during die compaction is likely to be kinematic. In the following section, the evolution of the Mohr circles during die compaction is characterized in order to model compaction curves.

6.4.2. Mathematical formulation

The model is focussed on characterization of the evolution of Mohr circles in order to derive an indication of the strength of the compact. In the σ - τ plane, a measure for the strength of a compact is reflected by the shear stress required to produce failure when no normal stress is applied. This is denoted as the shear strength S of the compact. The shear strength S of powders can be estimated by drawing a tangent to the left side of a series of circles. This line, known as the yield locus, has a constant slope for a single density of a particular powder. An increase of the powder density increases the values of the slope and the intercept. For the powder compaction, the yield locus has no formal significance: the tangent to the left side of the circle indicates when the weakest links are broken, i.e. when failure occurs. Compaction, on the other hand, requires that the strongest resistance is overcome, which is represented by the right side of the circle. As indicated in fig. 6.9, the path followed during uniaxial compaction is given by a line with formula $\tau = \nu\sigma$. However, the yield locus provides a link between the size of the circle and the strength S .

Starting point for the model is recognition that the compaction curve consists of two distinct stages. During stage I, the granulate behaves as a powder without cohesive strength.

During stage II, a compact has been formed whose strength increases with pressure. This difference is illustrated in fig. 6.10.

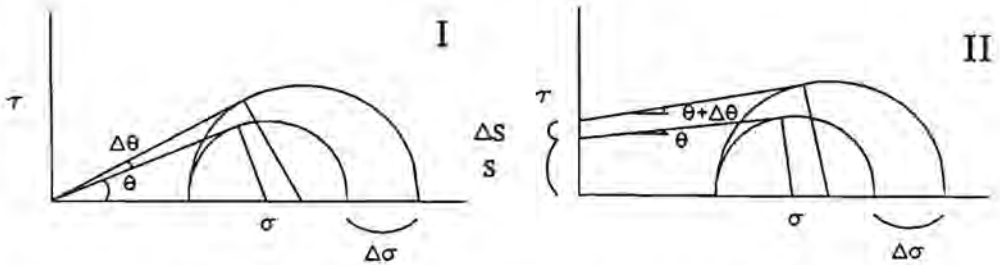


Fig. 6.10: Evolution of Mohr circles and corresponding yield locii during uniaxial die compaction. During stage I, the shear strength S is zero (left). During stage II, buildup of shear strength S is reflected by the increase of the value of the intercept (right).

The increase of the pressure during compaction is reflected in the increase of the major principal stress. Comparing two Mohr circles representing arbitrary compaction states allows definition of the increase of the isotropic pressure $\Delta\sigma_1$:

$$\begin{aligned} \Delta\sigma_1 &\equiv (\sigma_1 - \sigma_{1,0}) \\ &= 2(r - r_0)/(1 - K) \end{aligned} \tag{6-8}$$

where $r = (\sigma_1 - \sigma_3)/2$ is the radius of the Mohr circle and K is the ratio of the minor and major principal stresses. Note that $\Delta\sigma_1$ is not necessarily equal to the increase in the axial stress σ_{zz} during die compaction. The difference between the axial stress σ_{zz} , which equals the applied pressure P , and σ_1 is illustrated in fig. 6.11.

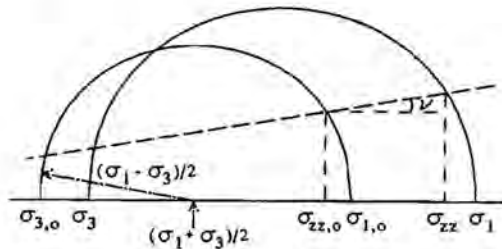


Fig. 6.11: Relation between the major principal stress σ_1 and the axial stress σ_{zz} . With die compaction, σ_{zz} equals the pressure P .

A relation between $\Delta\sigma_1$ and $\Delta\sigma_{zz}$ ($\equiv \sigma_{zz} - \sigma_{zz,o}$) is obtained by calculating the intersection of the compaction path and the right side of the Mohr circle. The Mohr circle can be expressed as:

$$\tau^2 + (\sigma - (\sigma_1 + \sigma_3)/2)^2 = (\sigma_1 - \sigma_3)^2/4 \tag{6-9}$$

During die compaction, the ratio between the shear and normal stresses is constant and represented by v . Substituting τ with $v\sigma$ yields the following second-order equation:

$$\sigma^2(1 + v^2) - \sigma(\sigma_1 + \sigma_3) + \sigma_1\sigma_3 = 0 \tag{6-10}$$

The larger stress of the solutions of eq. (6-10) is the axial stress σ_{zz} :

$$\sigma_{zz} = ((\sigma_1 + \sigma_3)/2 + ((\sigma_1 - \sigma_3)^2 - 4\sigma_1\sigma_3v^2)/2)^{1/2}/(1 + v^2) \tag{6-11}$$

Assuming that the relation between σ_1 and σ_3 is similar to the relation between σ_{π} and σ_{zz} (eq. 6-7), eq. (6-11) can be simplified:

$$\begin{aligned} \sigma_{zz} &= \sigma_1((1 + K) + ((1 - K)^2 - 4Kv^2)^{1/2})/(1 + v^2) \\ &= \sigma_1 C \end{aligned} \tag{6-12}$$

where C is a constant. Consequently, $\Delta\sigma_{zz}$ is directly proportional to $\Delta\sigma_1$.

The next step is to link the radius of the circle to the slope and intercept of the yield locus. For stage I, when the yield locus passes through the origin, the following apply:

$$\begin{aligned} r &= \sin(\theta+d\theta)\sigma_1 \\ r_o &= \sin(\theta)\sigma_{1,o} \end{aligned} \tag{6-13}$$

Recognizing that $\sigma_1 = \sigma_{1,o} + \Delta\sigma$ and substituting in eq. (6-8) yields:

$$\Delta\sigma_1 = 2(\sin(\theta+d\theta) - \sin(\theta))\sigma_1 / (1 - 2\sin(\theta+d\theta)(1-K)) \tag{6-14}$$

Invoking the definition of a first-order differential:

$$\sin(\theta+d\theta) - \sin(\theta) = d\theta \cos(\theta) \tag{6-15}$$

Simplifying eq. (6-14) with eq. (6-15) and considering infinitesimal changes in σ and θ :

$$d\sigma_1 = 2 d\theta \cos(\theta)\sigma_1/((1-2\sin(\theta))(1-K))$$

or

$$d\sigma_1/\sigma_1 = 2 d\theta \cos(\theta)/((1-2\sin(\theta))(1-K)) \quad (6-16)$$

Because σ_1 is proportional to σ_{zz} (eq. 6-12), eq. (6-16) can be used to represent die compaction:

$$dP/P = 2 d\theta \cos(\theta)/((1-2\sin(\theta))(1-K)) \quad (6-17)$$

The same method is used to obtain an expression for dP during stage II. Additional terms are introduced by the inclusion of the shear strength S , which increases by dS when passing from one Mohr circle to another. The initial equation has the following form:

$$dP = 2(P d\theta \cos(\theta)+dP \sin(\theta+d\theta)-S d\theta \sin(\theta)+dS \cos(\theta+d\theta))/(1+K) \quad (6-18)$$

Evidence [1] suggests that the strength increases linearly with the density. Because the density varies with the logarithm of the pressure, the strength also varies with the logarithm of the pressure during stage II. Expressed in equations:

$$S = C'\ln(P)$$

and

$$dS = (C'/P)dP \quad (6-19)$$

where C' is a proportionality constant. Substituting S and dS in eq. (6-18) produces a non-linear equation which is difficult to solve analytically. Therefore, the relation between the strength S and the pressure P is approximated by the first term of the Taylor expansion:

$$S = C'P \quad (6-20a)$$

and

$$dS = C'dP \quad (6-20b)$$

Substituting S in eq. (6-18) and considering an infinitesimal change in θ :

$$dP/P = 2(\cos(\theta)-C'\sin(\theta)) d\theta/((1-2\sin(\theta)+C'\cos(\theta))(1-K)) \quad (6-21)$$

Eqs. (6-17) and (6-21) can be integrated to yield a pressure-density relation when the relation between $d\theta$ and the change in density, $d\rho$, is known. Numerous options can be found in [2].

For lack of further details, $d\theta$ is taken to be proportional to $d\rho$. Integration produces an equation which is similar in form to the compaction curve equation. The equation is similar for stage I and II, although the constants have different values.

$$\rho = C_1 \rho_{th} (\ln(P) - \ln(P_o)) + \rho_o \tag{6-22}$$

where ρ_{th} is the theoretical (or fully-dense) density, C_1 a constant and where subscript o refers to the initial state. For stage I:

$$1/C_1 = 2\cos(\theta) / ((1 - 2\sin(\theta))(1 - K)) \tag{6-23}$$

For stage II:

$$1/C_1 = 2(\cos(\theta) - C' \sin(\theta)) / ((1 - 2\sin(\theta) - 2C' \cos(\theta))(1 - K)) \tag{6-24}$$

Eq. (6-22) therefore contains 5 parameters: P_o , ρ_o , θ , K and C' . Of these, K can be measured independently using strain gauges. Previously published results (e.g. [3]) suggest that K varies slightly with the applied pressure: at low and high pressures, K is larger than at intermediate pressures. A good approximation is to use $K = 0.5$.

When characterizing the compaction curves with equations of the form $\rho = A \ln(P) + B$, two parameters can be determined. For stage I, ρ_o equals the bulk density of the granulate after filling the die. Because C' is zero during stage I, P_o and θ can be established. The density at which the transition between stage I and stage II occurs can be found from experimental data. Assuming that θ is constant throughout the compaction process, P_o and C can be determined for stage II. Table 6.8 shows the parameters as determined for a number of binders.

Table 6.8: Model parameters determined for various binders

Binder	Stage	1	1	2	2	1	1	2	C'
		ρ_o	P_o	ϵ_o	P_o	C_1	θ	C_1	
Acrylic I		1.4	3.5	2.3	256	0.23	0.72	0.30	0.0179
Acrylic II (*)		1.5	4.6	2.5	434	0.23	0.71	0.31	0.0192
Acrylic II (**)		1.5	4.6	2.5	287	0.23	0.69	0.32	0.0200
Mixture		1.5	4.1	2.5	349	0.23	0.69	0.27	0.0070
PVA		1.4	5.1	2.3	202	0.26	0.61	0.31	0.0062

(*) Contains 0.86 wt-% binder

(**) Contains 1.70 wt-% binder

Note that a lower bulk density translates to a lower density at which the transition between the two stages occurs. The corresponding transition pressures are also lower for a lower bulk density. When calculating C , the strength parameter, large differences are found between the various binders despite the similarity of the compaction curves. This is due to the complex dependency of C_1 on θ and C .

6.4.3. Verification of the model

Direct verification of C' is not possible because a pure shear test, i.e. a test where the normal stresses are zero, is not available. Therefore diametral compression of compacts is used as an alternative. The test involves measurement of the crushing strength of ring-shaped compacts placed sideways. The test procedure is illustrated in fig. 6.12.

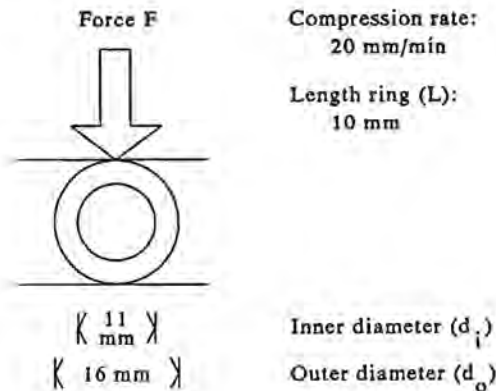


Fig. 6.12: Diametral compression test

Six ring-shaped compacts were pressed to densities of 2.7 and 3.0 g/cm³ using three of the previously examined granulates. The strength S found with the diametral compression test is calculated as follows (DIN 30911 part 2):

$$S = 6F(d_o + d_i) / \pi L (d_o - d_i)^2 \quad (6-25)$$

where F is the force at which the rings breaks.

The strength is derived from compaction curves as follows: first, the pressure corresponding to the densities of 2.7 and 3.0 g/cm³ is obtained from table 6.2. The pressure and the corresponding C' (table 6.8) are then substituted in eq. (6-20a). Comparison of the strength determined with either method is given in table 6.9.

Table 6.9: Strength of compacts

Binder	Density (g/cm ³)	Strength S (MPa)	
		Diametral compression	Compaction curves
Acrylic I	2.7	1.38	1.55
Mixture		0.41	0.57
PVA		0.72	0.55
Acrylic I	3.0	2.66	4.43
Mixture		1.57	2.21
PVA		1.12	1.81

Table 6.9 indicates that, with a single exception, the strength determined from the compaction curve is larger than the strength determined with the diametral compression test. This trend could be attributed to the difference in the definitions of the strength. This can be explained by considering the representation of the state of stress in the (σ, τ) plane. During compaction, the Mohr circle expands while its centre moves to the right (fig. 6.10). This process is known as kinematic hardening (fig. 6.9). The envelope of all Mohr circles up to certain size is known as the yield surface, which indicates the transition from elastic to plastic deformation of the compact. Because the Mohr circle expands, the left slope of the yield surface is positive. When the compact breaks during a diametral compression test, a point on the yield surface is obtained. Because the compact is in tension, this point is located on the negative σ -axis. Consequently, the strength determined with diametral compression is always smaller than the pure shear strength.

Table 6.9 also shows that the diametral compression strength increases with the density. This indicates that the size of the Mohr circle becomes larger than predicted by a yield surface which is tangent to all smaller Mohr circles. A tentative explanation is that the hardening behaviour is both of a kinematic and isotropic nature (fig. 6.13). Note that the combination of kinematic and isotropic hardening shown in fig. 6.13 provides an indication only: other combinations may occur in practice.

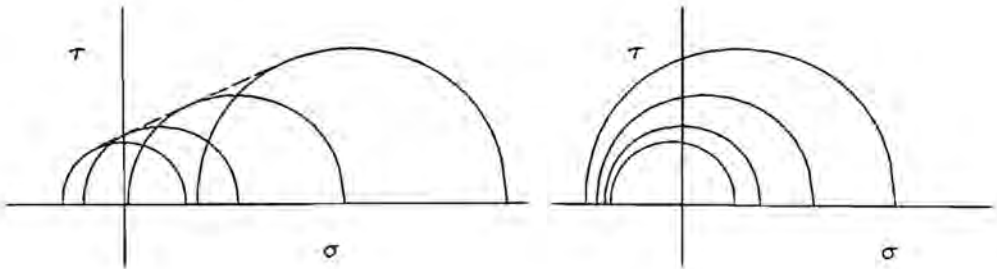


Fig. 6.13: Evolution of Mohr circles based on kinematic hardening only (left) and a combination of isotropic and kinematic hardening (right). The yield surface is given by a dashed line when it is tangent to intermediate circles as it the case with kinematic hardening.

6.5. Discussion and conclusion

The determination of the strength S from the compaction curve is based on characterization of this curve with two linear relations. The parameters of these relations are obtained from the two distinct linear sections observed when compacting granulate. A complete characterization is obtained because the intersection between the two linear relations is on the curve. The transition indicates that a change occurs in the mechanisms underlying the compaction process. This change in compaction behaviour is not necessarily related to the strength of the granulate. Note that the strength is influenced by a number of chemical and structural characteristics. One of these, the interstitial pore size, varies with the density and can be related to the underlying compaction mechanisms (see chapter 4). However, the variation of other characteristics, notably the cohesion between particles, agglomerates and granules, as a function of the density is unknown. Consequently, the model can only be applied to powders which display a kink in the compaction curve at a density where a compact is just formed. Therefore, the use of the model for powders where the intersection is not positioned on the compaction curve is questionable.

For the compaction of granulate, the model allows rapid estimation of the compact strength. Table 6.9 shows that the relative strength of compacts with different types of binder is confirmed by the analysis of the compaction curve for the density of 3.0 g/cm^3 . For the lower density (2.7 g/cm^3), however, this trend is not equally obvious.

The magnitude of the strength determined from the compaction curve is generally larger

than the strength measured with the diametral compression test. This difference cannot be entirely attributed to the occurrence of a combination of isotropic-kinematic hardening instead of kinematic hardening only. This can only be the case if the ratio's between the change in strength and the change in density are similar, which is not the case (table 6.9).

Finally, table 6.9 reveals an interesting difference between granulate containing a mixture of PVA and acrylic and PVA only. Between a density of 2.7 and 3.0 g/cm³, the strength of the compact with a mixture of binders becomes larger than the strength of the compacts with PVA binder only. A possible explanation is that the softer nature of the mixture of binders facilitates improved adhesion between the particles.

References

1. D. Niesz et al., 'Strength Characterization of Powder Aggregates', *Ceramic Bulletin*, vol. 51, no. 9 (1972), 677-680.
2. D. Dužević, 'A Three-Stage Description of Powder Compaction', *Science of Sintering*, vol. 22, no. 1 (1990), 11-19.
3. J. Williams et al., 'Measurement of Static Stresses on the Wall of a Cylindrical Container for Particulate Solids', *Powder Technology*, vol. 50 (1987), 163-175.

Suggested reading:

- M. Es-Saheb, 'Powder compaction interpretation using the power law', *Journal of Materials Science*, vol. 28 (1993), 1269-1275.
- K. Kawakita, K.-H. Lüdde, 'Some Considerations on Powder Compression Equations', *Powder Technology*, no. 4 (1970/71), 61-68.
- N. Stanley-Wood, M. Sarrafi, 'Variations in, and Relationships of Surface Area, Internal Angle of Friction and Compact Diametral Fracture Strength with Degree of Compaction', *Particle Systems Characterization*, vol. 5 (1988), 186-192.
- N. Stanley-Wood, A. Ibrahim, 'A Correlation between Angle of Friction, Angle of Failure Plane and Strength for Compacts of Tartaric Acid, Microcrystalline Cellulose and Mixture of the Two', *Powder Technology*, vol. 51 (1987), 151-157.
- S. Strijbos, 'Phenomena of the Powder-Wall Boundary During Die Compaction of a Fine Oxide Powder', *Ceramurgia International*, vol. 6, no. 4 (1980), 119-121.
- P. Vermeer, 'A double hardening model for sand', *Géotechnique*, vol. 28, no. 4 (1978), 413-433.
- J. Windheuser, J. Misra, S. Eriksen, T. Higuchi, 'Physics of Tablet Compression XIII', *Journal of Pharmaceutical Sciences*, vol. 52, no. 8 (1963), 767-772.

Chapter 7

Modelling compaction using mechanical tests

7.1. Introduction

During compaction, the density increases on account of three processes: rearrangement, deformation and compression of the powder. Models for these processes (see chapter 4) can be derived assuming that the state of stress is similar throughout the powder. With die compaction, however, the stresses within the powder vary because force is applied in the axial direction only. As a result, internal and external friction lead to stress gradients which are reflected by local variations in the density. Because variations in the density are detrimental for the mechanical and dimensional properties, it is necessary to model the compaction process on a local scale in order to optimize compaction parameters or granulate properties.

The following approach is adopted: first, suitable mechanical tests are used to characterize the compaction behaviour of the powder. Subsequently, the space within the die is discretized into elements whose compaction behaviour corresponds to that of the powder. The compaction process is then simulated by applying force on the elements directly below the punch and calculating the deformation of all elements. The influence of the die wall is incorporated by including a force at the die wall which resists compaction. This approach allows determination of the density distribution within the compacted powder irrespective of the shape of the die. In this chapter, the compaction behaviour of granulate based on mechanical tests is established. The procedure to calculate the density distribution is presented in chapter 8.

7.2. Review of mechanical tests

Two types of tests are considered: those performed on compacts and those performed on granulate. With the former, compacts are subjected to loading under well-defined circumstances. Three tests of this type are used:

- three-point bend test: loading of a simply-supported rectangular compact at midspan.
- diametral compression test: loading of a cylindrical compact positioned sideways.
- free compression test: axial loading of an upright cylindrical compact.

These tests provide insight into the deformation behaviour of the whole compact. Furthermore, the force required to break the compact provides a measure for the strength. Breaking of the compact is associated with failure, a process which can be represented by strain-softening plastic flow: in the process of breaking, interparticle bonds are severed, so that the stress supported by the compact decreases. On the other hand, two tests relating directly to the deformation of granulate are used:

- die compaction test: axial loading of granulate which has been placed in a cylindrical die.
- isotropic compaction test: loading of precompacted granulate from every angle.

These tests reflect yielding of the granulate, which can be modelled as strain-hardening plastic flow.

The difference between these tests is illustrated by plotting the normal and shear stresses experienced by the compact or granulate. Each of the tests occupies a characteristic position in the (σ, τ) -plane. The position of each tests can be explained as follows:

- three-point bend test: during bending of a simply-supported compact, the upper section of the compact is in compression, while the bottom section of the compact is in tension. When the compact is sufficiently narrow, only the normal stress along the axis is significant. Along the bottom plane, the compact is in tension. When considering the bottom plane, this test is located on the (negative) σ -axis.
- diametral compression test: a circumferential normal stress ensures that the surface of the compact is in tension. The normal stress produces an equally large shear stress within the compact, so that diametral compression is positioned on the $\sigma = \tau$ line left of the τ -axis.
- free compression test: because the edges of the compact support no stress, the axial normal stress produces a shear stress within the compact. As a result, free compression is placed on the $\sigma = \tau$ axis right of the τ -axis.
- die compaction test: the shear stress within the granulate mass is smaller than with free compression because the die walls support stress. The ratio between the normal and shear stresses is approximately constant. This test is positioned close to the (positive) σ -axis.
- isotropic compaction test: after compaction of the granulate into a tablet shape, it is packed and subjected to pressure from all sides. On a macroscopic scale, no shear stresses can exist. Therefore, isotropic compaction is located on the (positive) σ -axis.

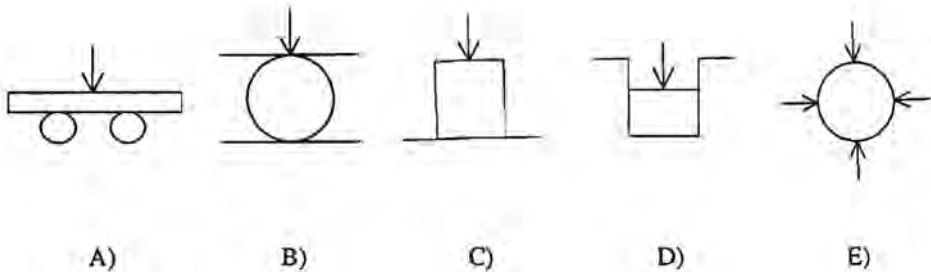


Fig. 7.1: Mechanical tests

A) *three-point bend test*

B) *diametral compression test*

C) *free compression test*

D) *die compaction test*

E) *isotropic compaction test*

The position of a test in the (σ, τ) -plane is uniquely defined when plotting a yield surface. The yield surface represents the combinations of normal and shear stresses where the transition from elastic to plastic deformation is observed. Because this transition is influenced by the density, the yield surface is plotted for a single density.

For the tests performed on compacts of a certain density, deformation is assumed to be elastic until the compact breaks. Therefore, the position of these tests is determined by the state of stress which produces failure. During the tests performed on granulate, elastic and plastic deformation occur simultaneously. Because the density is determined by the plastic strain, the process of loading is interrupted to allow recovery of elastic strain to take place. The state of stress corresponding to a certain density defines the position on the yield surface. For the isotropic compaction test, the position on the σ -axis is determined by the pressure applied as a function of the density. Determination of the position of the die compaction test is complicated by the presence of shear stresses. For compaction in an axisymmetric die, the normal stress σ experienced by the granulate can be written as:

$$\sigma = (\sigma_z + \sigma_r + \sigma_\theta)/3 \quad (7-1)$$

where σ_z is the axial, σ_r the radial and σ_θ the circumferential normal stress. Eq. (7-1) can be simplified by assuming that the circumferential stress σ_θ and the radial stress σ_r are equal. The shear stress τ in the (r, z) -plane is the difference between the axial and radial normal stresses:

$$\tau = \sigma_z - \sigma_r \quad (7-2)$$

Because the radial stress σ_r is unknown, a further assumption is required. In chapter 6, the ratio of the axial and radial normal stresses is taken to be constant and equals 0.5. This enables determination of the position of the die compaction test.

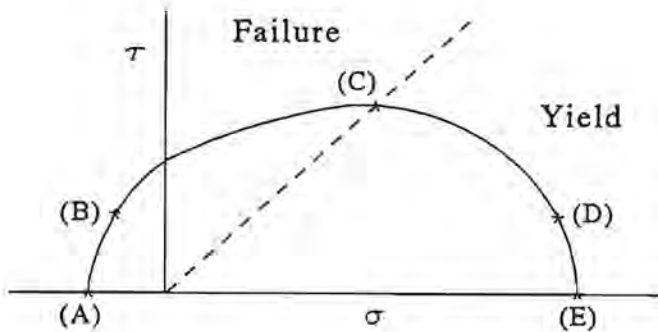


Fig. 7.2: Representation of the yield surface based on mechanical tests. The yield surface, which indicates when plastic deformation commences (failure tests) or continues (yield tests), is valid for a single density only.

A) three-point bend test

D) die compaction test

B) diametral compression test

E) isotropic compaction test

C) free compression test

Upon increasing the density, the yield surface expands. In chapter 6, it was shown that the yield surface coincides with the largest Mohr circle. Although the mechanical tests prove that the yield surface is elliptical, a similar trend is expected (fig. 7.3).

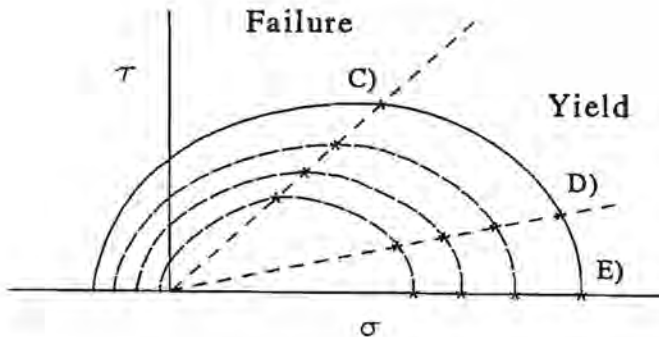


Fig. 7.3: Expansion of the yield surface with increasing density.

7.3. Densification and deformation

Instead of distinguishing mechanical tests on the basis of normal and shear stresses, an alternative classification is developed to extend the interpretation of the mechanical tests. For this purpose, the densification and deformation behaviour during the tests is considered. Densification refers to the change in density given a fixed compact shape, while deformation denotes the change in shape given a constant compact density. Pure densification occurs during the isotropic compression test because the shape of the compact is, in principle, not affected. Similarly, pure deformation occurs during the three-point bend test, where the density is approximately constant. With the other tests, a significant change in the density *and* the shape of the compact is observed. Note that, in the (σ, τ) -plane, both the isotropic and three-point bend tests are located on the σ -axis.

With the isotropic compaction test, rearrangement, deformation and compression of the particles occurs. The average distance between the particles decreases as particles slide past each other. During this process, particles are deformed and compressed on account of the interparticle friction. The sliding of particles is counteracted by the binder between the particles. However, the forces required to overcome interparticle friction are much larger than the forces required to stretch or break the bonds formed by the binder. Therefore, the influence of the binder during compaction is relatively small. This is confirmed by comparison of compaction curves measured during compaction in a die (see chapter 6).

With the three-point bend test, a concentrated force is applied to the top surface of the compact, which results in bending. The compact is compressed near the top side while the bottom of the compact is in tension. Because the force required to compact particles is much greater than the force required to pull particles apart, compaction during the three-point bend test is negligible. Consequently, the force required to bend the compact is related to the strength and adhesive properties of the binder. Note that van der Waals attraction can also influence the cohesion of particles at short range.

Modelling densification and deformation using macroscopic data requires that the compact or granulate is homogeneous. This implies that the response of the compact to force is similar to the response of individual particles. On the scale of the particles, fluctuations in the force required to produce compaction are significant. Therefore, it is assumed that a cell exists which contains a representative arrangement of particles where this condition is met. The process of deformation is characterized using the data obtained from the three-point bend test. The significance of the applicable parameters is discussed in section 7.4.1.

The process of densification has been characterized using representative cells in section 4. This approach is based on characterization of the spatial arrangement of the particles rather than balancing the forces between the particles. Because the simulation of compaction is based on the latter, it is necessary to model data from the isotropic compaction test. The relation with the interpretation of the deformation behaviour is given in section 7.4.2.

7.4. Modelling mechanical tests

7.4.1. Characterization of deformation

Deformation can be reversible (elastic) or irreversible (plastic) in nature. With elastic deformation, an increase of the strain produces an increase in the stress. When the loading of an elastically-deformed material is stopped, the imposed strain is recovered. With perfect plastic deformation, on the other hand, straining occurs when the stress reaches a critical value. This critical stress is not exceeded as further loading only produces an increase in the plastic strain.

The difference between elastic and perfect plastic deformation is illustrated by considering uniaxial loading (free compression) of an arbitrary material. When the deformation is elastic, the stress and strain in the axial direction are related by:

$$\sigma = E\varepsilon \quad (7-3)$$

where E is the elasticity modulus. When the deformation is plastic, the stress has a constant value:

$$\sigma = \sigma_y \quad (7-4)$$

where σ_y is the yield stress of the material. Fig. 7.4 illustrates the stress-strain curves for elastic and (perfect) plastic deformation.

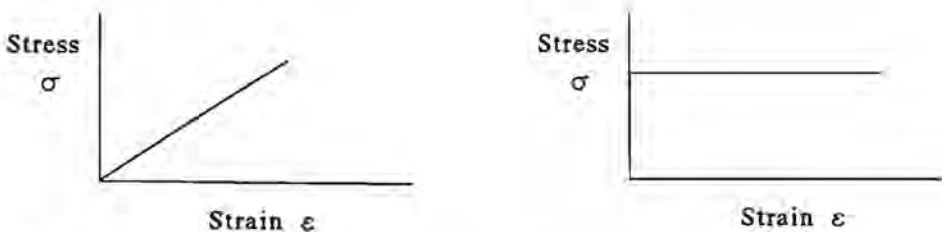


Fig. 7.4: Relation between stress and strain during uniaxial loading for elastic (left) and perfect plastic (right) deformation. The stress and strain are measured in the axial direction only. The strain in other directions, although probably non-zero, is not represented.

It is assumed that the stress-strain curve is not influenced by time. This implies that the stress is independent of the imposed strain rate.

A material can exhibit both elastic and plastic deformation behaviour. Because plastic

deformation requires that a yield stress σ_y is exceeded, elastic deformation always precedes plastic deformation. Furthermore, strain-hardening can occur, which implies that the stress in the compact increases with increasing plastic deformation. Strain-hardening, which is a type of imperfect plastic deformation, can be expressed as follows:

$$\sigma = \sigma_y + H\epsilon \quad (7-5)$$

where H is the plasticity modulus. Combined elastic and plastic deformation is illustrated in fig. 7.5.

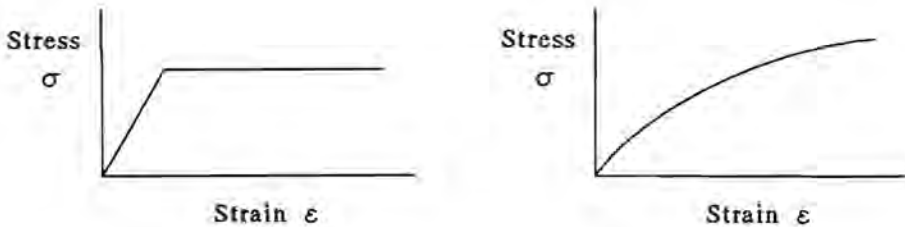


Fig. 7.5: Relation between stress and strain during uniaxial loading for elastic deformation followed by perfect (left) and strain-hardening (right) plastic deformation.

Whereas elastic deformation is characterized by a linear relation between the stress and the strain, this is not necessarily the case for strain-hardening plastic deformation. Fig. 7.6 shows two further options.

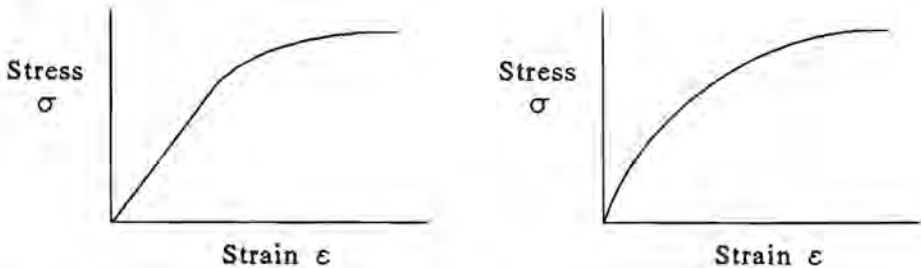


Fig. 7.6: Relation between stress and strain during uniaxial loading for elastic deformation followed by strain-hardening plastic deformation (left) and strain-hardening plastic deformation only (right).

The strain-hardening behaviour in fig. 7.6 can be expressed with:

$$\sigma = \sigma_y + H\epsilon^n \quad (7-6)$$

where n is a hardening parameter. Note that eq. (7-5) is a special case of eq. (7-6), with $n=1$. The hardening parameter n varies between zero and unity because the strain is smaller than unity and increases with increasing stress.

The determination of the yield stress σ_y depends on the presence of a clear transition between elastic and plastic deformation. Fig. 7.6 shows that the transition is difficult to establish when the initial slope is steep. Furthermore, the stress-strain curves shown in figs. 7.4 to 7.6 represent small changes in the strain only so that the density of the compact is practically constant. With increasing compact density, the strength of the compact increases because the particles are in closer contact. Therefore, the entire stress-strain curve changes with the density, as shown in fig. 7.7.

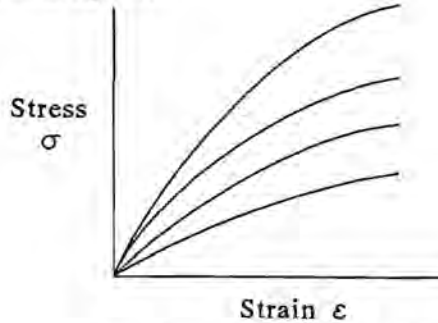


Fig. 7.7: Relation between stress and strain during uniaxial loading for strain-hardening plastic deformation. The curve shifts upwards as the density of the compact is increased. Note that the strain is small compared to the differences in the density of the compacts.

The determination of the parameters E , H , σ_y and n as a function of the density provides a complete characterization of the granulate, especially with respect to the influence of the binder. This makes comparison of different types of binders possible. In section 7.5.1, the experimental setup is outlined.

7.4.2. Characterization of densification

Densification expresses the increase of the density during the compaction of granulate. The density increases on account of particle motion, which causes filling of the pores. The force required to move particles equals the force required to slide particles past each other. In this respect, densification and deformation are fundamentally different: as indicated in the previous section, deformation is governed by the strength of the bonds between the particles rather than friction between particles. Because the forces associated with friction are much larger, the two processes are not comparable.

The process of densification can be represented in terms of the relation between the stress and strain. The main difference with the stress-strain relation representing deformation is the magnitude of the stress and the strain, which are much larger in the case of densification. The force required to slide particles past each other depends on the distance between the particles, which decreases with increasing density. For a single density, this motion can be represented by strain-hardening plastic deformation. Because the force and the particle motion are reflected in the stress-strain relation, iso-density curves can be plotted. Because the strain during compaction is large, the actual relation between the stress and the strain is obtained by connecting the curves at the strain corresponding to a certain density (fig. 7.8).

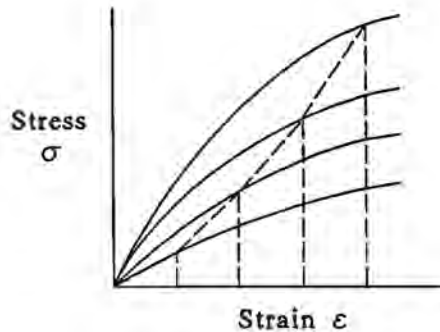


Fig. 7.8: Relation between stress and strain during densification (dashed curve) constructed from four stress-strain points. The solid curves, representing strain-hardening plastic deformation, are not actually measured during compaction tests. Note that the solid curves, although similar in shape to those shown the previous section, have a different significance.

The stress-strain curve representing densification can be constructed when the measured strain completely determines the density. Recall that a strain indicates the relative change in size in a single direction only. Therefore, without considering shear strains, three normal strains have to be known in order to calculate the density. This condition is fulfilled during the die compaction test, where two normal strains are zero, and during the isotropic compaction test, where the normal strains are all equal (fig. 7.9).

The relation between the strain and the density is derived by comparing an arbitrary density with the initial density of the uncompacted granulate. The ratio of these densities is inversely proportional with the ratio of the volumes, so that they can be expressed in terms of the principal dimensions. By relating the actual dimensions to the initial dimensions, the strain is introduced.

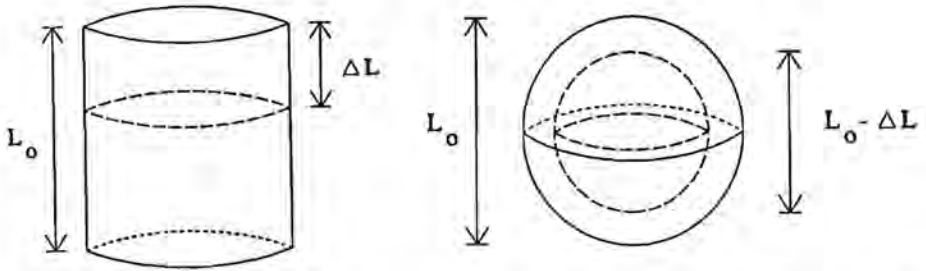


Fig. 7.9: Definition of the strain measured with the die compaction test (left) and the isotropic compaction test (right). The strain $\Delta L/L_o$ completely determines the change in density.

For the die and isotropic compaction tests, the relation between the measured strain and the density is unambiguous. However, with the diametral and free compression tests, assumptions with respect to the deformation behaviour of the compact during the test are required. With the free compression test, it is assumed that the shape of the compact remains cylindrical irrespective of the axial strain. This implies that two normal strains can characterize the change in density. With the diametral compression test, it is assumed that the unconfined edge remains circular during the test. Therefore, progressive loading flattens the top and bottom surfaces to an equal degree, while the curvature of edge increases. As a result, the cross-section can be subdivided into two equal semicircles and a rectangle in between. Because the length of the compact is assumed to be approximately constant throughout the test, two arbitrary strains are defined to characterize the change in density. The significance of the relevant strains for the free and diametral compression tests is illustrated in fig. 7.10.

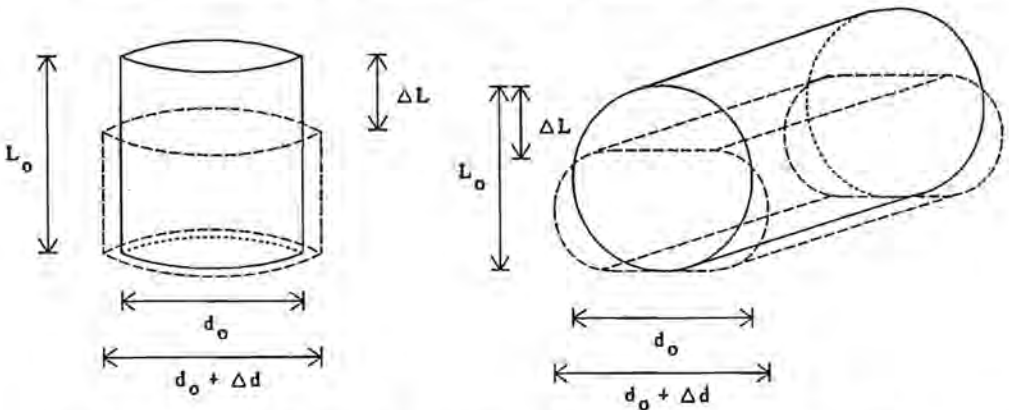


Fig. 7.10: Definition of the strain for the free compression test (left) and the diametral compression test (right). In both cases, only the strain $\Delta L/L_o$ is measured.

Note that the strain given by $\Delta d/d_0$ has to be known in order to establish a change in density.

Table 7.1 lists expressions for the ratio of the initial (ρ_0) and actual (ρ) density which are derived using the strains illustrated in figs. 7.9 and 7.10.

Table 7.1: Relation between the strain and the density

Test	Relative density ρ_0/ρ
Die compaction	$(1 - \epsilon_L)$
Isotropic compaction	$(1 - \epsilon_L)^3$
Free compression	$(1 - \epsilon_L)(1 + \epsilon_d)^2$
Diametral compression	$(1 - \epsilon_L)(4(\epsilon_L + \epsilon_d)/\pi + (1 - \epsilon_L))$

Direct measurement of the expansive strain ϵ_d during the test is not practical because fluctuations as a function of position, applied force and sample are large. For similar reasons, interpretation of images of the compact during the test is not routinely performed. As a result, the change in density during these tests is not known. Therefore, the free and diametral compression tests can only be used to characterize the deformation behaviour at a single compact density.

The die and isotropic compaction tests can be used to establish the densification behaviour of the granulate. The stress increases sharply with the strain for both tests. In chapter 6, it is found that the density obtained during the die compaction test varied with the logarithm of the (axial) stress:

$$\rho = A \log(\sigma_L) + B \quad (7-7)$$

where A and B are constants. This empirical equation can also be used to characterize densification during the isotropic compaction test.

The process of densification is modelled using granulate containing acrylic II binder. In section 7.5.2 to 7.5.4, the experimental setup for three of the four tests discussed in this section is given. Data for the die compaction test is taken from chapter 6. Modelling compaction with these tests is developed in section 7.7. Note that, when the density is measured from compacts, only plastic or irreversible strain is observed. During compaction, the strain includes an elastic contribution. This elastic strain equals the relaxation of the compact, which commences when the imposed stress is removed. Measuring the density as

a function of the axial stress *during* the die compaction test results in different values for the parameters A and B (section 6.3). Because simulation of compaction requires that the elastic strain is taken into account, the phenomenon of relaxation is investigated in section 7.5.5. This could make adaptation of data obtained by testing compacts possible.

7.4.3. Characterization of strength

During the tests where failure occurs, the force required to break the compact provides a measure for the strength. The dependency of the strength on the dimensions is removed by expressing the force in terms of stress. The strength is therefore defined as the stress at failure σ_f . The significance of the strength or stress at failure varies with the loading conditions, as is illustrated in fig. 7.11. Note that compressive stresses are positive.

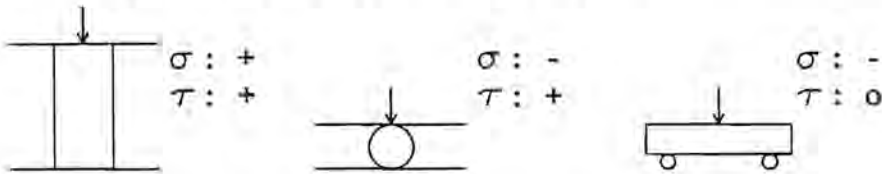


Fig. 7.11: Review of tests used to determine the strength. The indication of the normal (σ) and shear (τ) stresses reflects the overall state of stress during the test.

The compact is capable of resisting much larger compressive stresses before failure occurs than when the stresses are tensile. Therefore, the largest strength is determined from the free compression test, followed by the diametral compression test and the three-point bend test.

For the three-point bend test, the relation between the force and the stress is derived in section 7.6.1. For the free compression test, the stress at failure is defined as the axial stress. The stress in the axial direction is obtained by normalizing the force with the cross-sectional area. During the test, the cross-sectional area varies as a function of the axial position. The largest area is observed in the middle of the compact, where expansion of the compact at either end is opposed by friction with the confining surfaces. In order to characterize the entire compact, an average cross-sectional area could be used. However, on account of poor reproducibility, the stress at failure σ_f is related to the *initial* cross-sectional area:

$$\sigma_f = F/A = 4F/(\pi d_0^2) \quad (7-8)$$

where d_0 is the initial diameter of the compact.

With the diametral compression test, the stress at failure is defined as the stress in the radial loading direction. This stress is obtained by dividing the force required to produce failure by the area of the interface between the compact and the loading surface. Initially, the

interfacial area is zero but it increases during the test on account of progressive flattening of the cross-section. The interfacial area A is the product of the (flattened) width d and the height h . The latter is assumed to be constant throughout the test and equals the initial length of the compact. The width d at failure is determined by the strains in the vertical (ϵ_v) and the horizontal (ϵ_h) directions. Because the expansive strain ϵ_d (see section 7.4.2) is unknown, a model to determine the width d is developed: it will be assumed that the width d is determined by the intersection with the initial circular cross-section (fig. 7.12).

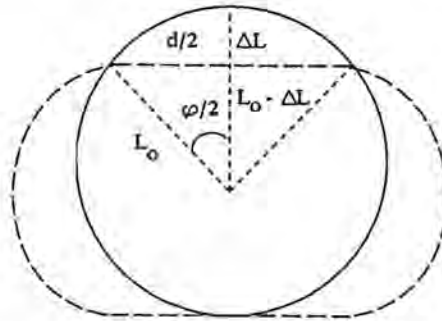


Fig. 7.12: Cross-section of a cylindrical compact during the diametral compression test. The initially circular cross-section is progressively flattened.

Two relations are derived from the triangle shown in fig. 7.12:

$$\cos(\varphi/2) = (L_0 - \Delta L)/L_0 \quad (7-9a)$$

$$\sin(\varphi/2) = d/(2L_0) \quad (7-9b)$$

where φ is the corner angle. The sum of the square of a sine and cosine equals unity, so that the dependency on the corner angle φ can be removed:

$$d = 2(2L_0\Delta L - \Delta L^2)^{1/2} \quad (7-10)$$

The stress at failure σ_f for diametral compression follows from:

$$\sigma_f = F/A = F/(2(2L_0\Delta L - \Delta L^2)^{1/2}h) \quad (7-11)$$

where h is the compact height. Values for the strength are given in section 7.8.

7.5. Experimental

7.5.1. Three-point bend test

Series of rectangular compacts have been pressed to densities of 2.4, 2.6, 2.8 and 3.0 g/cm³ using the following granulates:

- acrylic II
- mixture of acrylic II and PVA
- acrylic I

The addition of Zn-stearate should be beneficial for compaction because it acts as a lubricant between the particles. In order to establish the effect of the Zn-stearate, two further granulates are prepared. These contain 0.05 and 0.20 wt-% of Zn-stearate respectively.

The dimensions of all compacts are similar: height 6 mm, width 5 mm and length 60 mm. The compacts are positioned upright and supported by two rollers which are 36 mm apart. The compact is loaded at midspan with a constant rate of 0.2 mm/s. The displacement in the vertical direction is denoted as the deflection ϕ . The relation between the deflection ϕ and the force F which resists bending is shown in fig. 7.13.

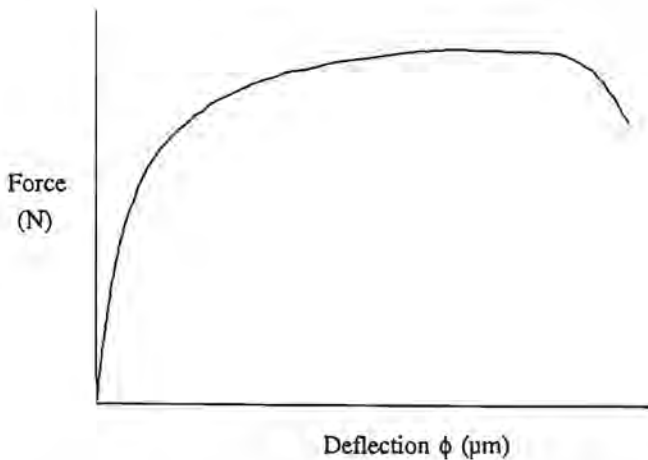


Fig. 7.13: Characteristic force-deflection curve measured with the three-point bend test.

Five compacts of each density and granulate are analysed. This number of tests produces an average variation of 5 % in the values of the strength or stress at failure σ_r . For high densities, the variation is smaller than the variation observed at lower densities. The deflection ϕ at which the force reaches a maximum is in the order of 0.5 mm. Because this is relatively small compared to the compact height (6 mm), it supports the assumption that the compact

density is constant during a measurement.

The relations between the force F and the axial stress σ and the deflection ϕ and the strain ϵ are developed in section 7.6.1. Given these relations, interpretation of the stress-strain curve is presented in section 7.6.2.

7.5.2. Diametral compression test

Tablet-shaped compacts are pressed isotropically using granulate containing acrylic II binder. The diameter of the compacts is approximately 24.5 mm, while the height is only 4.5 mm. Three different densities are obtained by pressing to 1000, 2000 and 4000 bar. Fig. 7.14 shows the characteristic force-deflection curve observed when the compact is subjected to diametral compression.

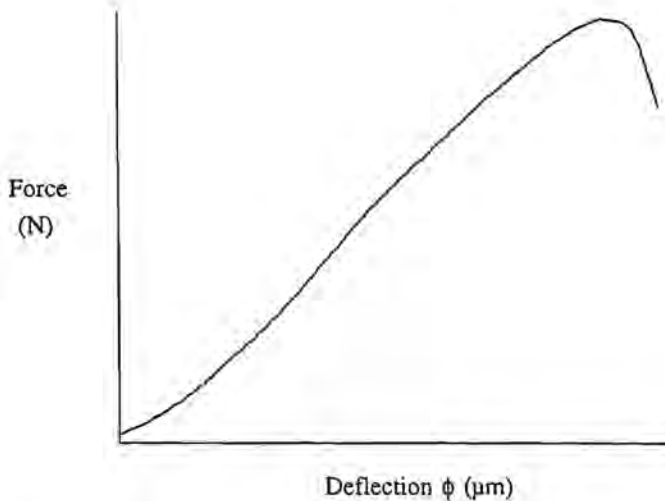


Fig. 7.14: Characteristic force-deflection curve measured with the diametral compression test.

Five compacts of each density are compressed, which ensures that the variation in the measured strength is less than 4 %.

7.5.3. Free compression test

Cylindrical compacts (diameter: 6.05 mm) are pressed uniaxially using granulate containing acrylic II binder. Three different densities are obtained by varying the axial pressure. The length-to-diameter (L/D) ratio of all compacts is roughly equals 2, which is assumed to be sufficient to mitigate the effect of friction with confining surfaces. The force-deflection curve measured during the free compression test is shown in fig. 7.15.

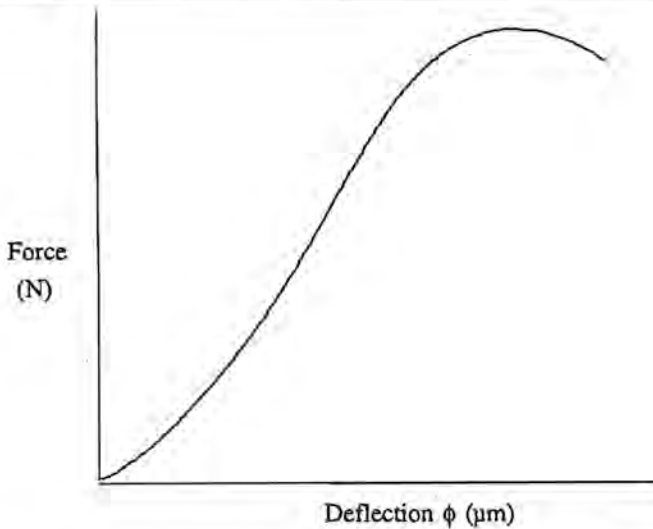


Fig. 7.15: Characteristic force-deflection curve measured with the free compression test.

The reproducibility improves with increased density. In order to limit the variation in the strength to 4 %, the number of compacts tested is 5, 6 and 9 for densities of 3.31, 2.93 and 2.84 g/cm³ respectively.

7.5.4. Isotropic and die compaction tests

Tablet-shaped compacts are pre-pressed uniaxially to 680 bar using granulate containing acrylic II binder. Subsequently, the compacts are pressed isotropically to 1000, 1500, 2000, 3000 and 4000 bar. The diameter of the final compact is approximately 24.5 mm while the height is 4.5 mm. The density of five compacts subjected to a similar pressure is averaged in order to obtain pressure-density points. These can be used to determine the isotropic compaction curve. Substituting the parameters in eq. (7-7):

$$q = 0.71 \log(P) + 0.60 \quad (7-12)$$

where P is the isotropic pressure. At the lowest pressure used (1000 bar), the density is already 2.77 g/cm³, which is relatively high. However, packaging of the compact prior to isotropic compaction makes pre-pressing to a density where it can be handled necessary. The die compaction curve for the same granulate is taken from table 6.3:

$$q = 0.64 \log(P) + 0.87 \quad (7-13)$$

where P is the uniaxial pressure. Note that eq. (7-13) only applies for densities above 2.23 g/cm³ (table 6.4).

$$e = 0.64 \log(P) + 0.87 \quad (7-13)$$

where P is the uniaxial pressure. Note that eq. (7-13) only applies for densities above 2.23 g/cm³ (table 6.4).

7.5.5. Recovery of elastic strain

Cylindrical compacts have been pressed using granulate containing a mixture of acrylic II and PVA binders. The compact diameter was measured immediately after pressing with a Heidenhahn extensometer. Comparison with the die diameter provides an indication of the instantaneous relaxation in the radial direction. Subsequently, the compacts were stored in a chamber where a constant temperature (20 °C) and relative humidity (40 %) was maintained. Daily measurement of the compact dimensions revealed that, after approximately one month, the compact dimensions had reached stable values. Comparison of the final compact diameter with the diameter immediately after pressing indicates the post-compaction radial relaxation.

Table 7.2 shows the relation between the radial relaxation, the compaction pressure and the length-to-diameter (L/D) ratio of the compact. The diameter varies with the axial position where it is measured. Therefore, the diameter is measured at three positions: at either end and in the middle. The average value has been used to represent the diameter. It was found that the end of the compact which was directly below the punch always has the largest diameter.

Table 7.2: Radial relaxation

Binder: mixture of acrylic II and PVA

Compact diameter: 14.10 mm

Uniaxial pressure (bar)	Initial L/D ratio (-)	Instantaneous relaxation (%)	Post-compaction relaxation (%)	Total radial relaxation (%)
1185	0.28	0.27	0.29	0.56
	0.57	0.37	0.20	0.57
	0.95	0.42	0.17	0.59
	1.42	0.50	0.07	0.57
1690	0.17	0.48	0.21	0.69
	0.52	0.49	0.22	0.71
	0.66	0.50	0.18	0.68
	1.26	0.50	0.17	0.67

Table 7.2 shows that, for the lower pressure (1185 bar), the instantaneous radial relaxation increases with the L/D ratio. However, because this trend is reversed in the period after ejection from the die, the total radial relaxation is approximately constant. At a pressure of 1690 bar, the instantaneous radial relaxation is larger, although the dependency on the L/D ratio is no longer observed. In terms of the total radial relaxation, an increase is observed with increasing pressure.

The influence of the die diameter and the binder is investigated by pressing compacts in two dies with differing diameters and using two types of granulate. Results are given in table 7.3. Each value reflects the average of four compacts.

Table 7.3: Total radial relaxation (initial L/D ratio = 0.3)

Binder type	Die diameter (mm)	Pressure (bar)	Total radial relaxation (%)
Acrylic II	14.10	1185	0.63
	18.09	1185	0.56
	14.10	1690	0.69
Mixture	14.10	1185	0.57
PVA/acrylic II	18.09	1185	0.54
	14.10	1690	0.68

The difference in relaxation as a result of the type of binder disappears with increasing compaction pressure while an increase of the die diameter reduces the radial relaxation.

In the axial direction, only the post-compaction relaxation is measured. For the granulate containing a mixture of acrylic II and PVA binders, the relative change in compact height varies between 0.22 and 0.45 %, irrespective of the density or the L/D ratio. The variation is probably due to the variation in the instantaneous axial relaxation, which commences during ejection of the compact. The latter, which is expected to be relatively large, is difficult to measure accurately.

A model of relaxation is developed using a microscopic representation. Ferrite particles, which are bonded by binder molecules, move closer together during compaction. During this process, the bonds between the particles are either stretched or broken. Because broken bonds reduce relaxation, the binder consisting of a mixture of acrylic II and PVA is relatively brittle when compared with the acrylic II binder. This is confirmed by SEM images of the surface

of compacts pressed from either granulate (fig. 7.16).

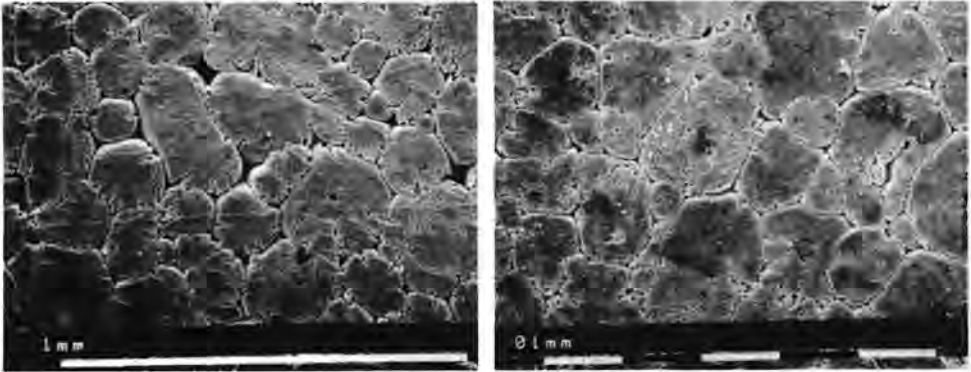


Fig. 7.16: Comparison of compacts pressed from granulate containing a mixture of acrylic II and PVA (left) and acrylic II only (right). The SEM images of the top surface of compacts pressed to 422 bar show that the bonding of a mixture of binders is more brittle.

Upon removal of the external pressure, the stretched bonds tend to shorten, exercising force on the particles. This prompts particle rearrangement, which increases the volume of the compact. The higher the density, the more the bonds have been stretched, and, therefore, the larger relaxation will be. Note, however, that relaxation is counteracted with increasing density by an increase of the number of broken bonds and hindrance from other particles. Especially the latter is significant because the difference in relaxation of the two granulates decreases with pressure. Near the compact edges, relaxation is less impeded by other particles. In addition, shear stresses near the edges during compaction produce significant stretching of the bonds. Therefore, the relaxation of thin products is relatively large.

The decrease of the density on account of post-compaction axial and radial compaction for a pressure of 1185 and 1689 bar is approximately equal: 0.7 %. Because relaxation is stimulated during ejection of the compact, the instantaneous relaxation is expected to be larger than the post-compaction relaxation. Therefore, relaxation will reduce the compaction density by an estimated 2 %. Therefore, differences between the compaction and the compact density are accounted for by relaxation when in the order of 2%.

7.6. Analysis of the three-point bend test

7.6.1. Interpretation of measured data

During the test, the force F which resists bending of the compact is measured as a function of the deflection ϕ . For modelling purposes, it is necessary to translate this data into a stress σ and strain ϵ . Because the rectangular compacts have a small cross-section, the stresses in the cross-section are assumed to be negligible. Therefore, the force F produces a stress in the axial direction only. The magnitude of this stress varies with the vertical position: near the top, the stress is compressive while, near the bottom, the stress is tensile. The transition between compression and tension is given by a plane which supports no stress. Viewed sideways, the surface is indicated by the so-called neutral axis, whose length is always equal to the initial length of the compact. Fig. 7.17 shows the compact during bending.

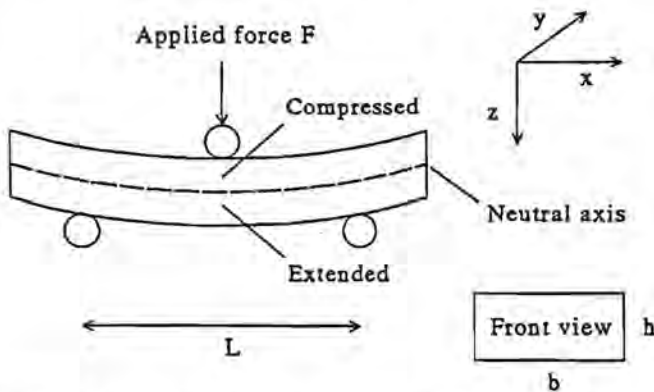


Fig. 7.17: Three-point bend test. During bending, part of the compact is compressed while another part is extended. The transition between these parts is given by the neutral surface. Abbreviations: h = height, b = width, L = length between supports.

In the elastic range of deformation, the axial stress can be expressed as follows:

$$\sigma = Mz/I \quad (7-14)$$

where M is the bending moment, z the vertical coordinate and I the moment of inertia. For a simply-supported compact, the bending moment M is given by:

$$M = Fx/2 \quad (7-15)$$

where x is the horizontal coordinate. Consequently, the bending moment at midspan equals

$FL/4$. The moment of inertia I is found from:

$$I = \int z^2 dA \quad (7-16)$$

where A is the cross-sectional area ($= bh$). The moment of inertia I is defined relative to the neutral axis, which, for small deflections, is positioned halfway the compact. Expressing the area A in terms of the coordinates y and z and integrating between the top ($z = h/2$) and bottom ($z = -h/2$) of the compact:

$$I = bh^3/12 \quad (7-17)$$

Substituting M and I in eq. (7-14) shows that the stress is proportional to the vertical coordinate z :

$$\sigma = 3FLz/(bh^3) \quad (7-18)$$

The stress of interest is the largest tensile stress, which is found at the bottom of the compact ($z = -h/2$). Substituting z in eq. (7-18) provides the relation between the stress, force and compact dimensions:

$$\sigma = -3FL/(2bh^2) \quad (7-19)$$

Eq. (7-19) is valid in the elastic range of deformation. When the deformation is plastic, a modified form of eq. (7-14) can be used:

$$\sigma = Mz^n/I_n \quad (7-20)$$

where n is the hardening parameter introduced in section 7.4.1. The modified moment of inertia I_n is given by:

$$I_n = bh^{n+2}/((n+2)2^{n+1}) \quad (7-21)$$

Evaluating eq. (7-20) at $z = -h/2$ yields:

$$\sigma = -FL(n+2)/2bh^2 \quad (7-22)$$

When the hardening parameter n is unity, the elastic and plastic relations between the force and the stress are identical. Because the hardening parameter has a value between zero and

unity, the force required to produce a certain stress is larger when the deformation is (strain-hardening) plastic instead of elastic. The combined use of the elastic relation ($n=1$) and the plastic relation ($0 < n < 1$) is not practical in view of the discontinuity in the stress when the yield stress is reached. Therefore, either the elastic (eq. 7-17) or the plastic (eq. 7-20) relation is used.

The stress σ in eq. (7-19) and (7-22) is negative by definition because it is a tensile stress. For the interpretation of the three-point bend test, this convention is reversed so that all stresses are positive.

The strain ϵ is obtained by assuming that the neutral axis forms a semicircle. The semicircle can be characterized with the radius of curvature, which is denoted R . The strain ϵ is defined as the deflection ϕ relative to the radius of curvature R :

$$\epsilon = \phi/R \quad (7-23)$$

Note that the radius of curvature decreases during bending of the compact. Fig. 7.18 shows the relation between the radius R and the deflection ϕ .

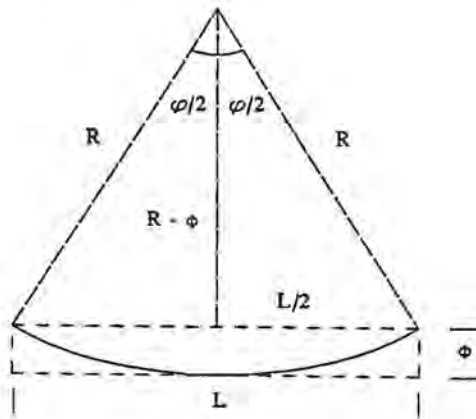


Fig. 7.18: Characterization of the neutral axis with a semicircle. For relatively small deflections, the span L is assumed to be constant and equals the distance between the points where the compact is supported.

Using the representation in fig. 7.18, the deflection ϕ and the radius of curvature R are related through the corner angle φ :

$$\cos(\varphi/2) = (R - \phi)/R \quad (7-24)$$

Furthermore, the span L and the radius of curvature R are related through the corner angle ϕ :

$$\sin(\phi/2) = L/2R \quad (7-25)$$

Eqs. (7-24) and (7-25) can be combined because the sum of the squares of the sine and cosine equals unity. The resulting equation is quadratic and is solved for the radius of curvature R . One of the solutions is trivial ($R = \infty$) while the other solution yields the required expression for the radius of curvature R :

$$R = ((L^2/4 + \phi^2)/2\phi) \quad (7-26)$$

Substitution of R in eq. (7-23) relates the deflection ϕ to the strain ϵ through the distance L between the points where the compact is supported. In view of the assumption that the deflection is small compared to the span L , a simplified expression for the strain is obtained:

$$\epsilon = 8(\phi/L)^2 \quad (7-27)$$

Eq. (7-27) is valid irrespective of the nature of the deformation.

Stress-strain data, obtained by conversion of force-deflection data, indicates that, after initial elastic deformation, non-linear strain-hardening plastic deformation occurs. In section 7.4.1, a four-parameter (E, H, σ_y, n) model has been developed to characterize this behaviour. However, because a transition between elastic and plastic deformation is not clearly observed, the yield stress σ_y is initially considered to be zero. The data is then interpreted in terms of plastic deformation only, which is characterized as follows:

$$\sigma = H\epsilon^n \quad (7-28)$$

Note that the stress is related to the force through eq. (7-22), which includes the hardening parameter n . Therefore, the values of H and n are determined from a suitably modified eq. (7-28):

$$F = 2bh^2He^n/(L(n+2)) \quad (7-29)$$

Values for the parameters H and n are given in section 7.6.3.

Experiments where the bending process is terminated before the compact breaks indicates that the strain is partly elastic. Therefore, the lack of a clear transition suggests that plastic deformation is influenced by the elastic deformation. Up to now, plastic deformation has been

modelled as an independent process. The combined elastic and plastic deformation behaviour can be represented with a mechanical model. In section 7.6.2, a suitable mechanical model is developed.

7.6.2. Mechanical model

The deformation behaviour of a compact is modelled with an arbitrary combination of mechanical elements. The three basic elements are shown in fig. 7.19.

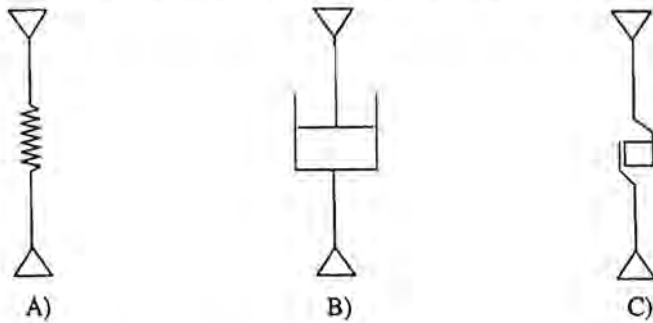


Fig. 7.19: Basic mechanical elements.

- A) spring, elastic behaviour given by $\sigma = E\varepsilon$
 B) dashpot, viscous behaviour given by $\sigma = \eta d\varepsilon/dt$
 C) friction element, failure when $\sigma = \sigma_y$

Elastic deformation is instantaneous and modelled with Hooke's law. Plastic deformation, on the other hand, is represented by viscous flow, which is governed by the viscosity η and the time t . Given a constant strain rate, the dashpot reflects perfect plastic deformation. Finally, the friction element snaps open when a certain stress is reached. On its own, this element can be used to model failure, where the strain becomes infinitely large and the stress becomes zero. However, it will be shown that, in combination with other elements, the friction element can also model the transition between elastic and plastic deformation, which is given by the yield stress σ_y .

Representing a combination of elastic and plastic deformation behaviour requires that the mechanical model contains both a spring and a dashpot. Two fundamental combinations are illustrated in fig. 7.20.

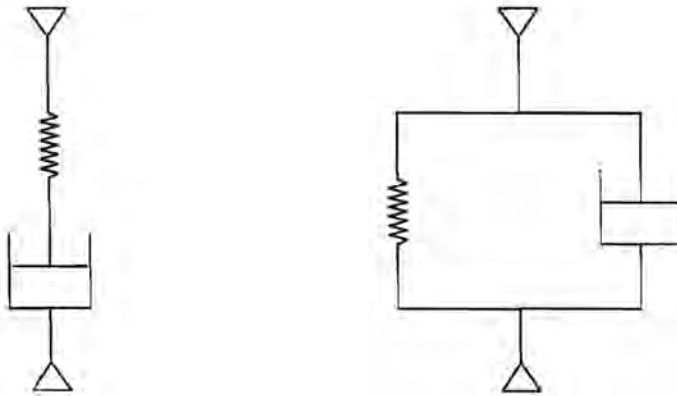


Fig. 7.20: Models for elasto-plastic deformation behaviour. When the spring and dashpot are in series, the strain ϵ is the sum of the strain of either element, while the stress σ is similar for both elements. When the elements are in parallel, a single strain ϵ is defined, so that the stress σ is partially supported by both elements.

In order to establish which type of model represents the bending of a compact, stress-strain equations are derived. First, an expression for the strain ϵ is derived when a constant stress σ_0 is applied. For a spring and dashpot *in series*, known as a Maxwell element, the strain ϵ is given by:

$$\epsilon = \sigma_0(1/E + t/\eta) \quad (7-30)$$

Eq. (7-30) shows that the spring is extended at $t=0$, while extension of the dashpot can, in theory, continue infinitely. For a spring and dashpot *in parallel*, known as a Kelvin element, the strain ϵ is given by:

$$\epsilon = \sigma_0(1 - \exp(-Et/\eta))/E \quad (7-31)$$

Eq. (7-31) shows that instantaneous extension of the spring is resisted by the dashpot. After prolonged extension, the strain ϵ stabilizes at the strain supported by the spring for the applied stress σ_0 . Although eqs. (7-30) and (7-31) illustrate the difference between the two types of models, neither represents the process of bending. During bending, the stress varies as a result of the imposed strain, which increases at a constant rate. When the strain rate is constant, expressions for the stress σ can be derived. For the spring and dashpot in series:

$$d\epsilon/dt = (d\epsilon/dt)_{\text{spring}} + (d\epsilon/dt)_{\text{dashpot}}$$

$$= (d\sigma/dt)/E + \sigma/\eta \quad (7-32)$$

The overall strain rate $d\epsilon/dt$ is constant and denoted $\dot{\epsilon}$. Integrating eq. (7-32) with respect to the stress σ :

$$\sigma = \eta\dot{\epsilon}(1 - \exp(-E\dot{\epsilon}t/\eta)) \quad (7-33)$$

For large values of the time t , the stress σ is determined by the resistance of the dashpot only. When the spring and dashpot are in parallel, the strain rate of either element is equal to the overall strain rate:

$$(d\epsilon/dt)_{\text{spring}} = (d\epsilon/dt)_{\text{dashpot}}$$

or

$$(d\sigma/dt)/E = \sigma/\eta \quad (7-34)$$

Integration of eq. (7-34) with respect to the stress σ leads to a strain-rate independent equation:

$$\sigma = \sigma_0 \exp(E\dot{\epsilon}t/\eta) \quad (7-35)$$

where σ_0 is the initial stress. Because the strain rate is constant, the time t and the strain ϵ are directly related:

$$t = \epsilon/\dot{\epsilon} \quad (7-36)$$

Eq. (7-36) can be used to substitute the time t in eqs. (7-33) and (7-35). For the spring and dashpot in series:

$$\sigma = \eta\dot{\epsilon}(1 - \exp(-E\epsilon/\eta\dot{\epsilon})) \quad (7-36)$$

For the spring and dashpot in parallel:

$$\sigma = \sigma_0 \exp(E\epsilon/\eta\dot{\epsilon}) \quad (7-38)$$

Comparison of eqs. (7-37) and (7-38) reveals that only eq. (7-37) is capable of representing the measured stress-strain curve. Consequently, the bending of a compact can be modelled with a spring and dashpot in series. Because the relation between stress σ and strain ϵ is non-linear, the parameters E and η cannot be determined from the measured stress-strain curve

by linear regression. Therefore an iterative scheme known as the Simplex method is used. With this method, the minimum difference between the measured and modelled stresses is sought in a space where the parameters are plotted along orthogonal axes.

In practice, the initial deformation is found to be elastic. This behaviour can be incorporated into the elasto-plastic model using a friction element. When the friction element is placed parallel to the dashpot, the deformation is elastic until the yield stress σ_y is reached. Subsequently, the friction element snaps and the deformation becomes elasto-plastic. Fig. 7.21 shows the assembly of this model.

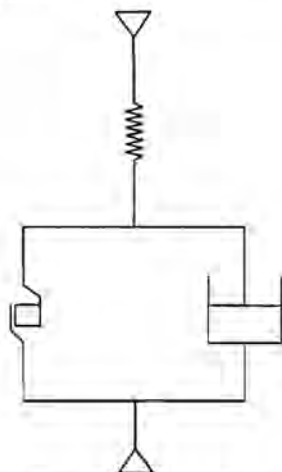


Fig. 7.21: Model for sequential elastic and elasto-plastic deformation behaviour. When the stress reaches the yield stress σ_y , a combination of elastic and plastic deformation behaviour is observed when subjected to a constant strain rate.

Eq. (7-37) models the elasto-plastic deformation behaviour only. This implies that the elasto-plastic stress and strain are zero when the yield stress σ_y is reached. This requires that the yield stress σ_y and corresponding strain are incorporated into eq. (7-37). The elasto-plastic stress σ_{ep} is the difference between the actual stress and the yield stress σ_y :

$$\sigma_{ep} = \sigma - \sigma_y \quad (7-39)$$

The elasto-plastic strain ϵ_{ep} is zero when the time is zero. Therefore, the actual time t has to be corrected for the time which has elapsed prior to the onset of elasto-plastic deformation. Given a constant strain rate, the latter is given by $\sigma_y/(E\dot{\epsilon})$. Subtracting this value from the time t (eq. 7-34) indicates the time during which elasto-plastic deformation occurs:

$$t = (\epsilon - \sigma_y/E)/\dot{\epsilon} \quad (7-40)$$

Substituting the elasto-plastic stress σ_{ep} and time t in eq. (7-33) with eqs. (7-39) and (7-40) produces the applicable model equation for the elasto-plastic range of stresses:

$$\sigma = \sigma_y + \eta e(1 - \exp(-E(\epsilon - \sigma_y/E)/\eta e)) \quad (7-41)$$

Finally, breaking of the compact can be included in the model by positioning a second friction element in series with the model shown in fig. 7.21. This friction element snaps open when the failure stress σ_f is reached. Prior to failure, the stress approaches a constant value. Considering the elasto-plastic model equation (eq. 7-39), a constant stress is found when the exponential contribution vanishes. The model equations for the entire range of stresses can now be established:

$$\sigma = E\epsilon \quad \text{for } \sigma < \sigma_y \quad (7-42a)$$

$$\sigma = \sigma_y + \eta e(1 - \exp(-E(\epsilon - \sigma_y/E)/\eta e)) \quad \text{for } \sigma_y \leq \sigma < \sigma_f \quad (7-42b)$$

$$\sigma = \sigma_y + \eta e \quad \text{for } \sigma = \sigma_f \quad (7-42c)$$

Note that the stress σ becomes zero after failure has occurred. The model contains three parameters: the elasticity modulus E , the viscosity η and the yield stress σ_y . Because the failure stress σ_f is known, eq. (7-42c) provides an additional relation between the parameters. The viscosity η in eq. (7-41) can then be substituted using the following relation:

$$\eta = (\sigma_f - \sigma_y)/e \quad (7-43)$$

This implies that only two parameters (E and σ_y) have to be determined from the measured stress-strain curve. Values for the parameters are given in the next section.

7.6.3. Determination of model parameters

Two approaches to analyze the three-points bend test data have been developed in the previous sections. Comparison of the parameters from either approach provides a comprehensive characterization of the influence of the binder type.

With the model presented in section 7.6.1, the measured force-deflection data is used to determine the values of the plasticity modulus H and the strain-hardening parameter n (eq. 7-29). On account of the non-linearity, a two-parameter Simplex method is employed to determine the values in table 7.4. Note that the hardening parameter n becomes larger than unity for higher densities with the granulate containing a mixture of PVA and acrylic II binder. This indicates that the model is not suitable for characterization of the stress-strain

data for this type of binder at these densities.

The values of the parameters of the mechanical model developed in section 7.6.2 are given in table 7.5.

Table 7.4: Plasticity modulus H and hardening parameter n

Binder type	Density (g/cm ³)	H (x 10 ⁶ Pa)	Variation in H (%)	n (-)	Variation in n (%)
Acrylic II	2.4	1.389	5.8	0.608	32.4
	2.6	2.928	6.2	0.334	11.3
	2.8	5.435	8.6	0.284	16.6
	3.0	7.995	4.5	0.243	3.4
Mixture PVA/acrylic II	2.6	2.029	21.3	0.877	35.8
	2.8	3.485	7.1	1.843	6.7
	3.0	5.420	8.9	1.783	9.0

Table 7.5: Elasticity modulus E, viscosity η and yield stress σ_y

Binder type	Density (g/cm ³)	E (x 10 ⁷ Pa)	Variation in E (%)	η (x 10 ⁶ Pa s)	Variation in η (%)	σ_y (x 10 ⁴ Pa)
Acrylic II	2.4	1.831	23.9	1.333	22.5	6.64
	2.6	5.018	11.6	4.575	3.8	0
	2.8	7.562	5.4	9.644	2.8	0
	3.0	10.272	3.3	13.476	5.8	0
Mixture PVA/acrylic II	2.6	1.890	24.7	0.153	239.2	10.55
	2.8	2.400	4.4	1.217	10.1	29.61
	3.0	4.884	16.4	6.380	48.1	41.15
Acrylic I (*)	2.4	2.769	8.6	4.378	3.5	0
	2.6	4.741	5.0	7.561	2.0	0
	2.8	7.309	10.7	11.076	5.6	0
	3.0	12.134	3.1	16.486	2.7	0
Acrylic I (**)	2.4	2.721	2.0	3.953	7.4	9.58
	2.6	4.920	7.8	7.479	4.0	0
	2.8	7.953	8.4	11.083	4.8	0
	3.0	11.685	4.6	16.464	2.8	0

(*) Addition of 0.05 wt-% Zn-stearate

(**) Addition of 0.20 wt-% Zn-stearate

Table 7.5 shows that the yield stress σ_y is generally zero which indicates that the experimental data can be modelled without taking elastic deformation into account separately. With granulate containing a mixture of PVA and acrylic II binder, however, the non-zero yield stress σ_y reflects the presence of residual stress in the compact. This indicates that this type of binder is relatively brittle. Furthermore, the non-zero yield stress σ_y confirms that the values of the hardening parameter n (table 7.4) are too large because an (elasto-) plastic model alone cannot characterize the experimental data.

7.7. Modelling compaction behaviour

7.7.1. Introduction

The weakness of models relating to the whole compact is their inability to predict density gradients within the compact quantitatively. Therefore, compaction has to be modelled on a local scale. This requires that the granulate mass is subdivided into smaller elements. On account of internal and external friction, the force experienced by an element varies with its position in the compact. When the element deforms in a similar manner as the granulate within, the local forces and displacements are related through the compaction behaviour of the granulate. In this section, the compaction behaviour of granulate subject to compaction in a die will be established. This enables the calculation of the local forces and displacements, which is presented in chapter 8.

A first consideration is that the overall compaction behaviour corresponds to the compaction behaviour on a local scale as long as the loading conditions are similar. The loading conditions are reflected in the state of stress, which is characterized in terms of normal and shear stresses present in the granulate mass. The variation of the state of stress with the type of mechanical test has been illustrated by plotting the normal stresses (σ) versus the shear stresses (τ). Each state of stress has reference to a single state of strain, which is characterized by the density (see section 7.2). This study is focussed on modelling the die compaction test, where both normal and shear stresses produce densification. The individual effects of the normal and shear stresses on the change of density can be modelled with the isotropic compaction and free compression tests. However, the state of stress during the die compaction test is unknown unless a value for ratio of the axial and radial normal stresses is assumed. Because the validity of this assumption is questionable, alternative approaches are developed. These vary with the dimension in which the die space is represented and subdivided into elements.

Compaction in axisymmetric dies can be represented in a single dimension by considering the axial direction only. Subsequently, the die space is subdivided into a series of equisized elements, whose compaction behaviour corresponds to the compaction behaviour of the whole granulate mass. Because the stress-strain relation for the whole granulate mass

is given by the compaction curve, the local displacements can be calculated once the local force is established. Note that the local force is determined at the transition between two elements, which is known as a nodal point. When assuming that the local displacement is proportional to the change in density, an indication of the axial variation in the density is obtained.

In general, the radial variation in the density is not negligible, which makes a two- or even three-dimensional approach necessary. Similar to the one-dimensional situation, the die space is subdivided into equisized elements which are connected at the nodal points. In order to subdivide the cylindrical die space into elements of equal size, ring-shaped elements with a triangular cross-section ('turban' elements) are defined. In two-dimensions, these elements are represented with triangles (fig. 7.22).

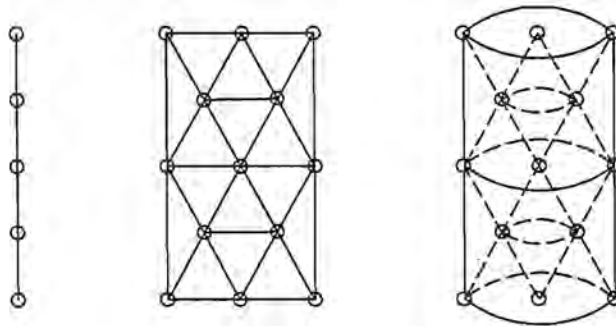


Fig. 7.22: Representation of the cylindrical die space in one (left), two (middle) and three (right) dimensions. The elements are connected at the nodal points (circles). Note that the number of elements is arbitrary.

In two-dimensions, triangular elements have an advantage over other element geometries because the condition of isotropy is automatically satisfied. Isotropy implies that the compaction behaviour of an element is independent of the direction in which force is applied. Therefore, as long as an element is significantly larger than a single granule, the condition of isotropy applies. When the element shape guarantees isotropy, the deformation of the element edges can be matched to the compaction of the granulate. The compaction behaviour of granulate is given by the (die) compaction curve, which includes the effect of external friction. Because the effect of internal friction is much more significant, the deformation of the element edges can be modelled with the compaction curve. This approach is presented in section 8.2.

Characterization of the compaction behaviour of granulate within a two-dimensional element requires at least two parameters, which determine the magnitude of the axial and radial displacements. This also applies to a three-dimensional element when the element is

axisymmetric because the latter may be considered pseudo two-dimensional. In section 7.7.2, the compaction behaviour of the granulate is derived using the three mechanical tests where compression occurs (fig. 7.23).

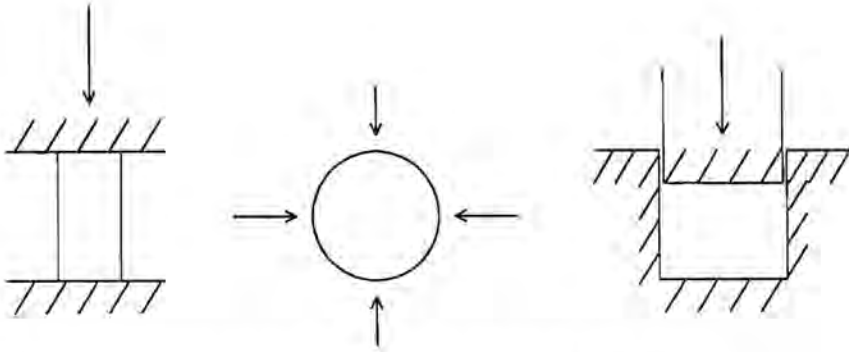


Fig. 7.23: Mechanical tests where the granulate is subject to compression.

7.7.2. Two- and three-dimensional interpretation

The interpretation of the compression tests (fig. 7.23) is based on the analysis of the state of stress and strain of the whole compact. Because the compact is subdivided into imaginary elements, the compact has to be homogeneous on the scale of the elements. Therefore, the elements have to be significantly larger than the granules because variations in the stress-strain relations occur at this scale. Consequently, no distinction between the effect of the processes underlying compaction (rearrangement, deformation and compression of the particles) on the stress-strain relations is made. Given sufficiently large elements, the condition of isotropy is fulfilled. In the following, it is assumed that the condition of isotropy applies at every stage of the compaction process.

During the free compression test, the relation between the axial stress σ_z and strain ϵ_z can be expressed as:

$$\sigma_z = H\epsilon_z \quad (7-44)$$

where H is an elasto-plastic modulus, which is determined from the slope of a stress-strain curve. On account of strain-hardening, the value of H varies with the density of the compact. Because the change in density during the free compression test is unknown, the elasto-plastic modulus H is determined as a function of the initial density of the compact.

During the free compression test, the normal stresses in the circumferential (σ_θ) and radial (σ_r) directions are zero at the unconfined surface of the compact. However, the radial normal strain ϵ_r , although not measured, is not zero. This indicates that the axial normal stress can produce a normal strain in the radial direction. The measurement of the radial strain

suffers from a lack of reproducibility on account of crack formation during the test. The general trend is that the radial normal strain increases with the axial normal strain. Therefore, a linear relation between the radial and axial normal strains is assumed:

$$\epsilon_r/\epsilon_z = -\nu \quad (7-45)$$

where ν is the plastic Poisson's ratio. Substituting the axial strain ϵ_z with eq. (7-44) expresses the radial normal strain σ_r in terms of the axial normal stress σ_z :

$$\epsilon_{r,z} = -\nu\sigma_z/H \quad (7-46)$$

where $\epsilon_{r,z}$ indicates that the radial strain is caused by an axial stress. Note that the value of the elasto-plastic modulus H varies with the density of the compact. Therefore, the plastic Poisson's ratio ν is also a function of the density.

The plastic Poisson's ratio ν can be determined from the isotropic compaction test after generalization of eqs. (7-44) and (7-45). On account of isotropy, the relation between a normal stress and strain in one direction is similar. Therefore, eq. (7-44) can be written for every direction:

$$\epsilon_z = \sigma_z/H \quad (7-47a)$$

and

$$\epsilon_r = \sigma_r/H \quad (7-47b)$$

and

$$\epsilon_\theta = \sigma_\theta/H \quad (7-47c)$$

The influence of a normal stress on the normal strain in another direction is independent of the direction of the stress. Therefore, six equations similar to eq. (7-45) apply:

$$\epsilon_{r,z} = \epsilon_{\theta,z} = -\nu\sigma_z/H \quad (7-48a)$$

and

$$\epsilon_{z,r} = \epsilon_{\theta,r} = -\nu\sigma_r/H \quad (7-48b)$$

and

$$\epsilon_{z,\theta} = \epsilon_{r,\theta} = -\nu\sigma_\theta/H \quad (7-48c)$$

When assuming that superposition of strains is allowed, expressions for the normal strains in each direction are obtained by summing eqs. (7-47) and (7-48):

$$\epsilon_z = (\sigma_z - \nu(\sigma_r + \sigma_\theta))/H \quad (7-49a)$$

and

$$\epsilon_r = (\sigma_r - \nu(\sigma_z + \sigma_\theta))/H \quad (7-49b)$$

and

$$\epsilon_\theta = (\sigma_\theta - \nu(\sigma_z + \sigma_r))/H \quad (7-49c)$$

With the isotropic compaction test, the normal stresses and strains are in theory equal in every direction. Therefore, eqs. (7-49a) to (7-49c) reduce to a single equation:

$$\epsilon = \sigma(1 - 2\nu)/H \quad (7-50)$$

The isotropic compaction test is used to establish the density of the compact as a function of the isotropic pressure. Because the density is related to the strain ϵ (see table 7.1) and the isotropic pressure equals the normal stress σ , the plastic Poisson's ratio can be determined as a function of the compact density. As a result, the plastic Poisson's ratio ν reflects plastic densification only and corrects for the elastic densification expressed with the elasto-plastic modulus H .

Relations for the elasto-plastic modulus H and the plastic Poisson's ratio ν are derived in section 7.7.3. The validity of these relations can be verified by deriving a model equation for the die compaction test. When assuming that the external friction is less significant than the internal friction, eqs. (7-49a) to (7-49c) can be used. With compaction in a die, the normal strains in the radial (ϵ_r) and circumferential (ϵ_θ) directions are zero when considering the die wall to be rigid. The normal stresses in the radial (σ_r) and circumferential (σ_θ) directions at the die wall are, however, non-zero. Therefore, combination of eqs. (7-49b) and (7-49c) allows expression of these stresses in the axial normal stress σ_z .

$$\sigma_r = \sigma_\theta = \sigma_z \nu / (1 - \nu) \quad (7-51)$$

Substitution of the circumferential and radial stress in eq. (7-49a) produces a relation between the axial stress and strain for the die compaction test:

$$\epsilon_z = \sigma_z (1 - 2\nu^2 / (1 - \nu)) / H \quad (7-52)$$

The density of compacts is related to the axial strain ϵ_z (see table 7.1) while the axial pressure equals the axial stress σ_z . Comparison of the measured and predicted densities indicates the validity of this approach.

Shear stresses develop when the normal stresses in the three principal directions are not equal in magnitude. This is the case with the free compression and die compaction tests. However, the significance of the shear stresses is limited: a shear stress (τ) can only cause

a shear strain (γ) in the same plane. The shear stress is assumed to be related to the shear strain linearly:

$$\tau = G\gamma \quad (7-53)$$

where G is the shear modulus. The relation between the shear modulus G and the elasto-plastic modulus H is derived by considering the loading of a compact in two directions. For example, when the normal stresses in the axial and radial directions are equal but opposite ($\sigma_z = -\sigma_r$), eqs. (7-49a) and (7-49b) become:

$$\epsilon_z = -\epsilon_r = (1 + \nu)\sigma/H \quad (7-54)$$

where σ represents the axial or the negative radial stress. Using a Mohr circle representation, the major and minor principal stresses can be equated to the axial and radial stresses respectively. In this case, the shear stress τ_{zr} equals half the difference between the axial and radial stresses:

$$\tau_{zr} = (\sigma_z - \sigma_r)/2 = \sigma_z \quad (7-55)$$

The shear strain γ_{zr} is the difference between the axial and radial normal strains:

$$\gamma_{zr} = \epsilon_z - \epsilon_r = 2\epsilon_z \quad (7-56)$$

Substitution of the shear stress and strain in eq. (7-53) with eqs. (7-55) and (7-56) as well as the normal stress with eq. (7-54) relates the elasto-plastic modulus H to the shear modulus G :

$$G = H/(2(1 + \nu)) \quad (7-57)$$

Using this relation, the compaction behaviour of the granulate can be modelled in two- or three dimensions using the expressions for the elasto-plastic modulus H and the plastic Poisson's ratio ν as a function of the density.

7.7.3. Correlations for compaction parameters

The elasto-plastic modulus H is determined from the slope measured during the free compression test. Although the slope varies during the test, the effect of variation of the slope on the density determined for the density compaction test is limited because the value of ν changes accordingly. Therefore, the slope determined up to maximum stress supported by the

compact. Analysis of 18 points reveals that the relation between the elasto-plastic modulus H and the density ρ is linear in the range of densities ($2.77 < \rho < 3.13 \text{ g/cm}^3$) considered:

$$H = (0.5106\rho - 1.3045)10^9 \quad (7-58)$$

The correlation coefficient of the two parameters equals 0.994883. Note that the elasto-plastic modulus becomes smaller than zero when the density drops below 2.55 g/cm^3 . This is due to the nature of the compression test, which measures the loading of compacts rather than of granulate. This indicates that, below the density of 2.55 g/cm^3 , the compacts have insufficient strength to be measured.

The values for the plastic Poisson's ratio ν are obtained from the isotropic compaction test, which is modelled with eq. (7-50), and eq. (7-58). Analysis of 10 points shows a large variation in the values of ν as a function of the density ρ . Therefore, a linear relation is fitted:

$$\nu = 0.0518\rho + 0.2510 \quad (7-59)$$

The correlation coefficient of the two parameters is only 0.627117. Note that the plastic Poisson's ratio equals 1/2 when the density is 4.81 g/cm^3 .

Substituting eqs. (7-58) and (7-59) in the model equation for the die compaction test (eq. 7-52) shows that the predicted density is lower than the value given by the compaction curve for low (axial) pressures and higher at high pressures. The intersection occurs at a density of approximately 2.9 g/cm^3 . This aspect, in combination with the limited density range (larger than 2.55 g/cm^3) make an alternative derivation of the parameters necessary. Because the die compaction test is also completely characterized by the parameters, it can be used instead of the free compression test. Substituting the axial strain in eq. (7-52) with the density using table 7.1 yields:

$$1 - \rho_0/\rho = P_a(1 - 2\nu^2/(1 - \nu))/H \quad (7-60)$$

where P_a is the pressure in the axial direction. Similarly substituting the strain in the model equation for the isotropic compaction test (eq. 7-50):

$$1 - (\rho_0/\rho)^{1/3} = P_i(1 - 2\nu)/H \quad (7-61)$$

where P_i is the isotropic pressure. Combining eqs. (7-60) and (7-61) to eliminate the elasto-plastic modulus H produces an expression for the plastic Poisson's ratio:

$$\nu = (1 - \rho/\rho)P_1 / ((1 - (\rho/\rho)^{1/3})P_2) - 1 \quad (7-62)$$

Substituting the plastic Poissons's ratio in either the die or isotropic compaction model equation produces an expression for the elasto-plastic modulus H . The axial and isotropic pressures are related to the density through the respective compaction curves, given by eqs. (7-12) and (7-13). The use of these correlations to calculate the density distribution in the compact is presented in section 8.3.

7.8. Strength of compacts

The strength, which is defined as the stress required to produce failure, is determined with different tests. With the three-point bend test, the force is converted to the stress assuming the deformation is completely elastic (eq. 7-19). The strength is given as a function of the density and binder type in table 7.6.

Table 7.6: Strength measured with three-point bend test ($\times 10^5$ Pa)

Density (g/cm^3)	2.4	2.6	2.8	3.0
Binder type				
Acrylic II	1.99	4.73	9.57	13.48
Mixture	-	1.23	5.33	9.34
Acrylic I	6.06	9.40	13.22	19.36
Acrylic I (*)	4.38	7.56	11.17	16.44
Acrylic I (**)	4.20	7.48	11.30	16.34

(*) Addition of 0.05 wt-% Zn-stearate

(**) Addition of 0.20 wt-% Zn-stearate

Significant is the detrimental effect of the addition of Zn-stearate on the strength of the compact. Even with the addition of Zn-stearate, the granulate containing acrylic I binder produces the strongest compacts. The low strength of the granulate containing a mixture of PVA and acrylic II indicates that the bonds between the particles are relatively brittle.

The strength determined with the free compression (eq. 7-8) and diametral compression (eq. 7-11) tests is given in table 7.7 for a selected densities.

Table 7.7: Strength measured with compression tests

Binder type: acrylic II

Diametral compression ($L/D = 0.2$)		Free compression ($L/D = 2.0$)	
Density (g/cm^3)	Strength ($\times 10^5$ Pa)	Density (g/cm^3)	Strength ($\times 10^5$ Pa)
2.77	15.83	2.81	46.37
2.88	24.05	2.94	57.06
3.13	45.00	3.31	124.72

Tables 7.6 and 7.7 confirm that the strength increases when the applied stresses are compressive.

7.9. Discussion and conclusion

Five mechanical tests have been selected to study the deformation behaviour of (compacted) granulate. In section 7.2, the loading conditions during the tests are qualitatively characterized in terms of the normal and shear stresses present in the granulate. By connecting the positions of the tests in the (σ, τ) -plane for a single density, an elliptical yield surface is constructed. The evolution of the yield surface with the density provides a model for the compaction process. An alternative classification of the tests based on the distinction between deformation and densification is presented in section 7.3. This reveals that the three-point bend test is suitable for the characterization of the properties of the binder, while, with the other tests, densification has to be taken into account. In section 7.4, a comprehensive methodology to characterize the processes of deformation and densification is developed. In addition, the determination of the compact strength from the tests where failure occurs is presented. The experimental setup is described in section 7.5. Furthermore, experiments relating to the expansion or relaxation of compacts after ejection from the die is presented. This data is relevant to link the density of compacts to the density during compaction. Unfortunately, the results indicate that a reliable correction is not possible. In section 7.6, the interpretation of the three-point bend test is developed. The distinction between elastic, plastic and elasto-plastic deformation is clearly indicated. Results indicate that, on the basis of the deformation behaviour, two different types of binder have been analysed. With the mixture of PVA and acrylic II binders, elastic deformation is followed by elasto-plastic deformation when a yield stress is exceeded. The acrylic I and II binders show strain-hardening plastic or elasto-plastic deformation only. Images of compacts show that the mixture of PVA and acrylic II binders leads to relatively widespread microcracking, which could be due to recovery of elastic deformation of the binder. Consequently, the mixture of PVA and acrylic II binders

can be classified as relatively brittle. The observation that the compacts containing the mixture of binders are relatively weak supports this conclusion.

In section 7.7, the compaction process is modelled on a local scale. The latter implies that a number of granules are considered. This is necessary in order to satisfy the condition of isotropy, which is used to interpret the overall compaction behaviour during the tests. The relation between the tests for a similar density is given by a quasi-elastic model. The term quasi is due to the irreversible nature of the strain and the variation of the parameters with the density. The two main assumptions are that a linear relation exists between a stress and a strain in another direction and that strains are additive. The inability to predict the compaction curve when using the free compression and isotropic compaction tests suggests that these assumptions may not apply when the parameters are density dependent. However, combination of the die and isotropic compaction tests automatically fulfills this condition.

In section 7.8, the strength determined from the three failure tests is compared. Results confirm that the strength increases when the stresses become compressive instead of tensile.

References

Suggested reading:

- D. Bortzmeyer, 'Modelling ceramic powder compaction', *Powder Technology*, vol. 70 (1992), 131-139.
- D. Bortzmeyer, M. Abouaf, J. Chané-Ching, N. Paraud, 'Proceedings 2nd International Conference: Ceramic Powder Processing Science', edited by H. Hausner, G. Messing and S. Hirano, DKG, 1989, 561-568.
- D. Bortzmeyer, G. Langguth, G. Orange, 'Fracture Mechanics of Green Products', *Journal of the European Ceramic Society*, vol. 11 (1993), 9-16.
- A. Broese van Groenou, 'Pressing of Ceramic Powders: A Review of Recent Work', *Powder Metallurgy International*, vol. 10, no. 4, 1978, 206-211.
- A. Broese van Groenou, 'Theory of Dust Pressing, part I: Models for Die Compaction', *Ceramic Monographs - Handbook of Ceramics*, supplement to *Inter-ceram*, vol. 31, no. 6 (1982), 1-10.
- J. Carstensen, P. Toure, 'Compression Cycles in Tableting', *Powder Technology*, vol. 26 (1980), 199-204.
- R. Cytermann, 'A New Way to Investigate the Dependence of Elastic Moduli on the Microstructure of Porous Metals', *Powder Metallurgy International*, vol. 19, no. 4 (1987), 27-30.
- D. Drucker, W. Prager, 'Soil Mechanics and Plastic or Limit Design', *Journal of Applied Physics*, vol. 10, no. 2 (1952), 157-165.
- P. Lade, 'Elasto-plastic stress-strain theory for cohesionless soil with curved yield surfaces', *International Journal of Solid Structures*, vol. 13 (1977), 1019-1035.

D. Lee, H. Kim, 'Plastic yield behaviour of porous metals', *Powder Metallurgy*, vol. 35, no. 4 (1992), 275-279.

I. Nelson, M. Baron, 'Application of variable moduli models to soil behaviour', vol. 7 (1971), 399-417.

G.Schober, H. Mörtel, 'Plastische keramischen Massen in Scherversuch und im Vergleich mit einem rheologischen Modell', *Berichte Deutsche Keramische Gesellschaft*, no. 3/4 (1988), 67-69.

S. Shima, M. Oyane, 'Plasticity theory for porous metals', *International Journal Mechanical Science*, vol. 18 (1976), 285-291.

S. Timoshenko, J. Goodier, 'Theory of Elasticity', 3rd edition, Mc Graw-Hill.

K. Venkatachari, R. Raj, 'Shear deformation and densification of powder compacts', *Journal of the American Ceramic Society*, vol. 69, no. 6 (1986), 499-506.

Chapter 8

Simulation of die compaction

8.1. Introduction

Simulation of die compaction serves to determine the density distribution within the compact. The density distribution can be characterized in terms of the homogeneity ζ , which can be defined as follows:

$$\zeta = 1 - s/\rho_m \quad (8-1)$$

where s is a measure for the variation of the density (e.g. the standard deviation) and ρ_m the average density. A high homogeneity has a positive effect on the compact strength and the uniformity of the shrinkage during sintering (fig. 8.1). Therefore, prediction of the homogeneity through simulation provides insight into the compact properties which is otherwise only obtained after extensive testing.

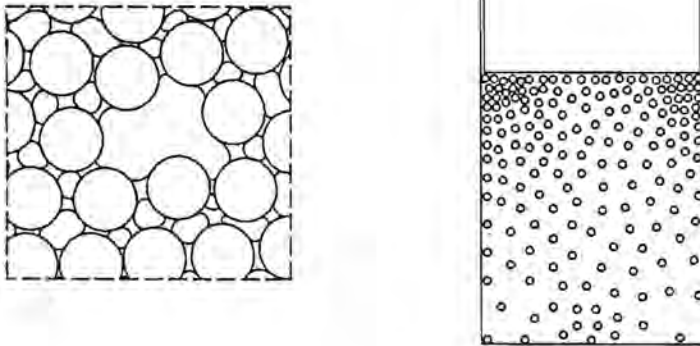


Fig. 8.1: Influence of the homogeneity on the compact properties. The strength decreases when large differences in the local density are present. This is due to the presence of relatively large pores (left). When density differences occur on a larger scale (right), the shrinkage during sintering can vary locally.

Review of simulation techniques

The density on a local scale is determined by the packing of the particles. The most rigorous approach is therefore to balance the applied pressure with the stresses between the the particles and the die wall and the particles themselves. This requires that the initial packing of the granules in the die and the particles within the granules is generated

numerically. Subsequently, a suitable algorithm and knowledge of the stick-slip behaviour of the particles is required to calculate the displacement of each particle. In view of the huge number of particles which have to be considered and the enormous number of permutations, the input data and computing time requirements are excessively large. To date, this approach has only been fully developed for two-dimensional situations (e.g. [1,2]).

An alternative is to identify a group of particles which is representative for the packing. After establishing the compaction behaviour of a single group, appropriate stresses are imposed on the groups adjacent to the punch and die surfaces. Because the groups are directly adjacent to each other, reduced stresses are transmitted throughout the die. The cumulative deformation of the groups indicates the overall compaction behaviour of the granulate.

A generalization of this approach is to consider the particles located in cross-sectional segments. The pressure applied by the punch is then balanced by the stresses acting on a series of segments. The number of segments is determined by the relative height of the segment and the die. Fig. 8.2 illustrates the differences between these approaches by comparing the initial filling of the die.

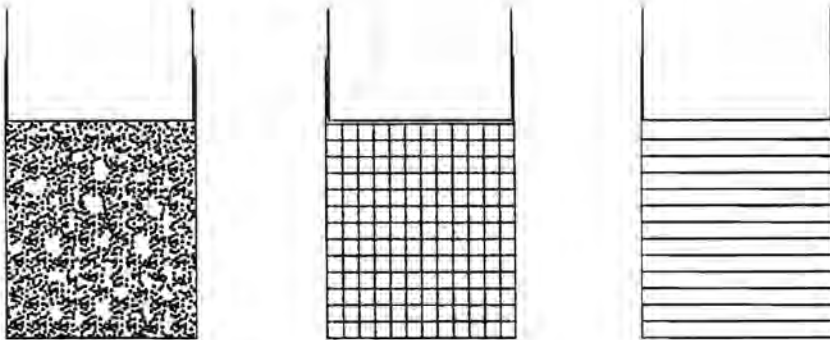


Fig. 8.2: Initial packing within the die when considering the particles individually (left), representative groups of particles (middle) or the particles in the cross-section of the die (right). The initial packing is not homogeneous only when individual particles are considered. This is due to the difference in size of the pores between the particles, agglomerates and granules.

Two of the three approaches in fig. 8.2 assume that the granulate mass is a *continuum*. In order to satisfy this condition, the representative groups or cross-sectional segments have to be sufficiently large. In this chapter, the simulation of die compaction with the two models based on continuum mechanics is investigated.

Continuum mechanics models

While the simulation based on groups of particles is capable of predicting both axial and radial gradients in the density, the simulation based on segments of the cross-section only indicates axial density gradients. Consequently, the simulation based on segments is adapted: first, the height of each segment is reduced to infinitesimal proportions. This relaxes the relation between the segment volume and the particles. By defining an infinite number of segments, the stresses acting on a single segment can be expressed in a differential equation. Subsequent integration reveals the development of the stress in the axial direction. The density distribution is obtained by taking the logarithm of the pressure. The model equation is then modified to take radial variations in the stress into account by incorporating experimental data. This approach allows rapid assessment of the homogeneity of cylindrical compacts of any size when a limited set of experimental data is available. Development of the model equation is presented in section 8.3.

The simulation based on groups of particles is more sophisticated than the previous approach and therefore more flexible in terms of application. It requires specification of granulate, process and product parameters. Granulate parameters relate to the compaction behaviour, which has been characterized in section 7.7 for the acrylic II binder. Process parameters include the compaction pressure, the pressing velocity and the mode of pressing. In section 3.3, it has been shown that compaction is rate-independent at normal compaction velocities. Therefore, the stress-strain relation is influenced by the density itself rather than the rate at which the density is reached. Therefore, the correlations derived in section 7.7 can be applied directly. The mode of pressing imposed during the simulation depends on the compact shape: with cylindrical or tablet-shaped compacts, single-sided uniaxial pressing is sufficient, while, with complex-shaped compacts such as potcores, double-sided sequential pressing is employed. Finally, product parameters are the shape and size of the compact as well as the overall density. A first estimate of the pressure required to obtain a certain overall density follows from the compaction curve (chapter 6).

With die compaction, friction between the die wall and the granulate has to be taken into account. This implies that knowledge of a further process parameter is necessary. Determination of the wall friction coefficient μ is given in section 8.2. While the compaction behaviour of the granulate expresses the internal friction, the wall friction coefficient expresses the external friction. Combining the effects of internal and external friction enables the calculation of the simultaneous compaction of all groups with the finite element method (FEM). This type of approach is presented from section 8.4 onwards.

8.2. Die wall friction

Friction between the die wall and the granulate is expressed in terms of the wall friction coefficient μ , which is defined as follows:

$$\mu = F_{z,R}/F_{r,R} \quad (8-2)$$

where $F_{z,R}$ is the axial force required to move granulate along the die wall surface and $F_{r,R}$ is the radial force exercised by the granulate on the die wall. The value of μ is determined with the experimental setup shown in fig. 8.3.

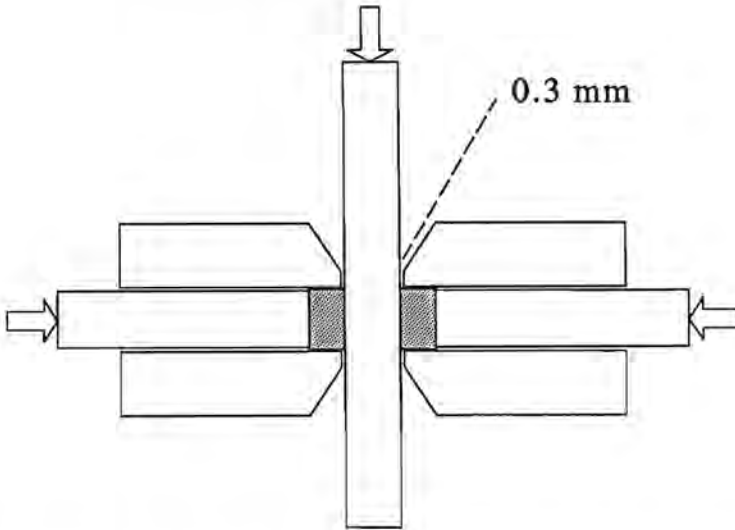


Fig. 8.3: Die wall friction measurement. Granulate, which is indicated by the shaded sections, is precompacted before being pressed against the central plate with a certain pressure. In this study, a compaction pressure of 2220 bar is used, while the test pressure amounts to 192 bar. The force required to move the central plate, produced from hardened steel (type: N1019), downwards at a velocity of 6 mm/min, is measured.

Granulates containing acrylic I and a mixture of acrylic II and PVA have been tested. For these granulates, the axial force $F_{z,w}$ is found to be independent of the rate with which the central plate is moved. Three measurements with each type of granulate are performed. For acrylic I, the wall friction coefficient μ equals 0.45, while for the mixture of binders, the value of μ is 0.43. Despite the significant difference between these binders (see section 7.6), the difference in the wall friction coefficient is small. Consequently, the wall friction

coefficient μ is considered to be independent of the type of binder. The dependency of the wall friction coefficient on the density of the compact is difficult to measure at low compact densities. Therefore, for simulation purposes, the wall friction coefficient μ is constant and equal to 0.44 for all densities.

8.3. Differential method

8.3.1. Axial stress model

In this section, a model for simulating the density distribution in cylindrical compacts is investigated. Basis is the derivation of the axial stress distribution imposed during compaction. Considering the stresses acting on an arbitrary segment located between the axial coordinates $z+dz$ and z (fig. 8.4).

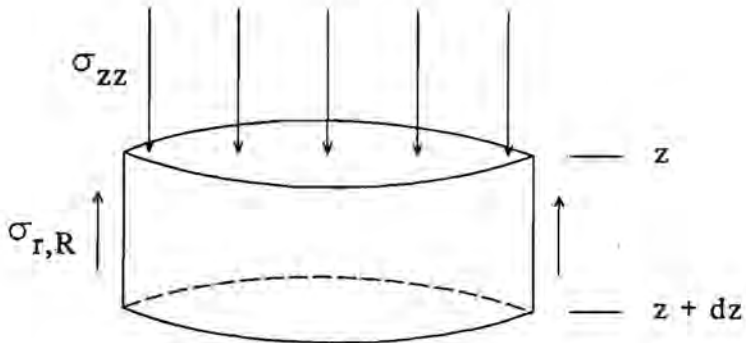


Fig. 8.4: Stresses acting on a cross-sectional segment with an infinitesimal height dz . Note that the segment where $z=0$ is located directly below the punch.

Balancing the difference in the stress applied on the upper and lower cross-sectional surfaces with the stress acting along the outer surface of the segment yields:

$$\pi R^2(\sigma_{zz}(z+dz) - \sigma_{zz}(z)) = -2\pi R\sigma_{z,R}dz \quad (8-3)$$

where R is the radius of the die, σ_{zz} the pressure applied on the cross-section and $\sigma_{z,R}$ the axial stress at the die wall. Eq. (8-3) can be rewritten as:

$$(d\sigma_{zz}/dz)dz = -(2\sigma_{z,R}/R)dz$$

or

$$d\sigma_{zz}/dz = -2\sigma_{z,R}/R \quad (8-4)$$

Eq. (8-4) suggests that the axial gradient in the applied pressure is due to the axial stress acting along the die wall. The latter, which expresses the effect of external friction, is related to the wall friction coefficient μ . Rewriting eq. (8-2) in terms of stresses:

$$\mu = \sigma_{z,R}/\sigma_{r,R} \quad (8-5)$$

where $\sigma_{r,R}$ is the radial stress at the die wall. Assuming that the radial stress is proportional to the applied pressure σ_{zz} :

$$\sigma_{r,R} = k\sigma_{zz} \quad (8-6)$$

where k is a constant representing the effect of internal friction. Combining eqs. (8-4), (8-5) and (8-6) produces a relation which can be integrated:

$$d\sigma_{zz}/dz = -2k\mu\sigma_{zz}/R \quad (8-7)$$

Integration between top of the granulate mass ($z=0$), where the axial stress equals the pressure P applied by the punch, and an arbitrary axial position yields:

$$\sigma_{zz}/P = \exp(-2k\mu z/R) \quad (8-8)$$

Neglecting the influence of ejection of the compact on the stresses in the compact, eq. (8-8) can represent the axial stress distribution in a compact of height L and radius R . Characterization of the stress distribution provides an indication of the compact homogeneity. After calculating the moments of the distribution, the homogeneity ζ with respect to the axial stress is obtained from eq. (8-1):

$$\zeta = R/(2k\mu L) \quad (8-9)$$

Eq. (8-9) indicates that the homogeneity ζ of a compact improves with a larger compact diameter D , a smaller length-to-diameter (L/D) ratio and smaller values of the friction coefficients k and μ . This conclusion, which is also valid in practice, indicates the relative significance of the axial stress gradient.

The axial stress can be translated to the local density, which is proportional to the

logarithm of the axial stress:

$$\rho_z - \rho_0 = \ln(\sigma_{zz}/P) \quad (8-10)$$

where ρ_z is the density at any axial position and ρ_0 is the density directly below the punch ($z=0$). Combining with eq. (8-8) relates the density to the geometry of the compact and friction coefficients:

$$\rho_z = \rho_0 - 2k\mu z/R \quad (8-11)$$

Eq. (8-11) shows that the density varies linearly with the axial position in the compact. This is the second important conclusion derived from this model. In the next section, these conclusions are used in the development of a model which also takes the radial gradient into account.

8.3.2. Gradient model

The gradient model represents a novel technique for simulating the density distribution in cylindrical compacts. The density distribution, which can be characterized in terms of the homogeneity, is obtained by interpolating between measured local densities. The interpolation process is influenced by three quantities: the axial density gradient $\Delta\rho_z$ and the radial density gradients at the top $\Delta\rho_{r,t}$ and at the bottom of the compact $\Delta\rho_{r,b}$. In order to determine these gradients, four local densities must be established (fig. 8.5).

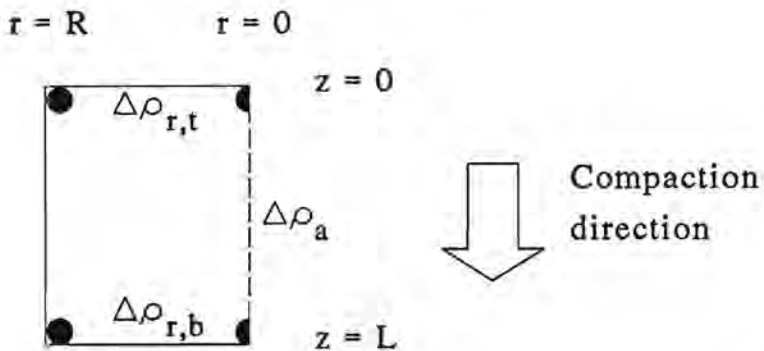


Fig. 8.5: Characterization of cylindrical compacts for derivation of the gradient model. The (semi-) circles indicate the positions where the local density must be established. The density can be measured with porosimetry after sectioning a compact or by a non-destructive technique like X-ray absorption. Subscripts: r = radial, a = axial, t = top, b = bottom.

The axial density gradient $\Delta \rho_z$ can be used to determine the internal friction coefficient k in the axial stress model. Comparing the densities at $z=0$ and $z=L$ with eq. (8-11):

$$\Delta \rho_z = (\rho_{z=0} - \rho_{z=L}) = 2k\mu L/R$$

or

$$k = \Delta \rho_z R / (2\mu L) \quad (8-12)$$

The internal friction coefficient k can be found from the measured density distributions presented in section 3.4. Given that the external friction coefficient equals 0.44 (section 8.2), the internal friction coefficient is found to vary between 0.01 and 0.05. Note that the coefficient of internal friction can also be obtained from the slope of the yield locus of the granulate. In the literature, higher values of the friction coefficient are reported (e.g. [3]). Therefore, it is not clear whether the internal friction coefficient k in this model corresponds to the friction coefficient obtained from a yield locus. The latter, obtained from the slope of the tangent to the left side of the Mohr circle, can be determined with a Jenike shear cell. Preliminary measurements indicate that this friction coefficient equals 0.5 to 0.7 for (Mn,Zn)-ferrite granulate.

The gradient model is based on modification of the axial stress model using experimental data. Recalling eq. (8-11) and introducing the compact height L :

$$\rho_z = \rho_0 - 2k\mu L(z/L)/R \quad (8-13)$$

Combining with eq. (8-12):

$$\rho_z = \rho_0 - \Delta \rho_z (z/L) \quad (8-14)$$

Eq. (8-14) suggests that the density at the top of the compact ($z=0$) is constant and equals ρ_0 . However, given knowledge of the radial density gradient $\Delta \rho_{r,z}$, eq. (8-14) can be adapted. In analogy to the linear variation of the density with the axial position, it is assumed that the density also varies linearly with the radial position. Redefining ρ_0 as the density in the top corner of the compact ($z=0, r=R$), eq. (8-14) becomes:

$$\rho = \rho_0 - \Delta \rho_z (z/L) - \Delta \rho_{r,z} (1 - r/R) \quad (8-15)$$

where $\Delta \rho_{r,z} = (\rho_{r=R} - \rho_{r=0})$ at the top of the compact ($z=0$). With eq. (8-15), the radial gradient at the bottom of the compact is fixed. In order to take the actual radial gradient at the bottom of the compact ($\Delta \rho_{r,b}$) into account an additional term is included:

$$\rho = \rho_0 - \Delta\rho_z(z/L) - \Delta\rho_r(1 - r/R) - (\Delta\rho_{r,z} + \Delta\rho_{z,r})(z/L)(r/R) \quad (8-16)$$

where $\Delta\rho_{r,b} = (\rho_{r=0} - \rho_{r=R})$ at the bottom of the compact. Note that the gradients are defined to have, in theory, positive values: the highest density is expected in the top corner ($z=0, r=R$), followed by the top centre ($z=0, r=0$), bottom centre ($z=L, r=0$) and finally, the bottom corner ($z=L, r=R$).

Eq. (8-16) can be used to predict the density at any position in a cylindrical compact when the relevant gradients have been established. Fig. 8.6 shows the density distribution obtained when classifying the local density.

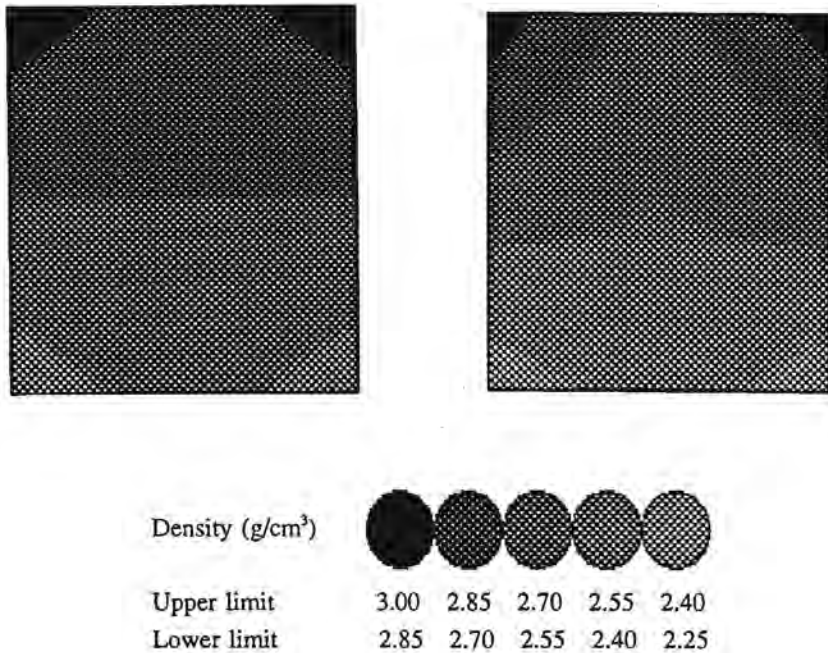


Fig. 8.6: Simulated density distributions of compacts with a maximum density of 3.00 g/cm³ ($= \rho_0$). The distribution is symmetric when the gradients are equal (left): $\Delta\rho_z = \Delta\rho_{r,b} = \Delta\rho_{r,z} = 0.15$. In practice, the effect of external friction produces an asymmetric distribution (right): $2\Delta\rho_z = 2\Delta\rho_{r,b} = \Delta\rho_{r,z} = 0.3$.

When using porosimetry to determine the gradients, large compacts should be used to prevent averaging of the gradients. The gradients can then be used for smaller compacts with the same density and length-to-diameter ratio.

Simulation of a measured density distribution, which has been presented in section 3.4, with the gradient model is shown in fig. 8.7.

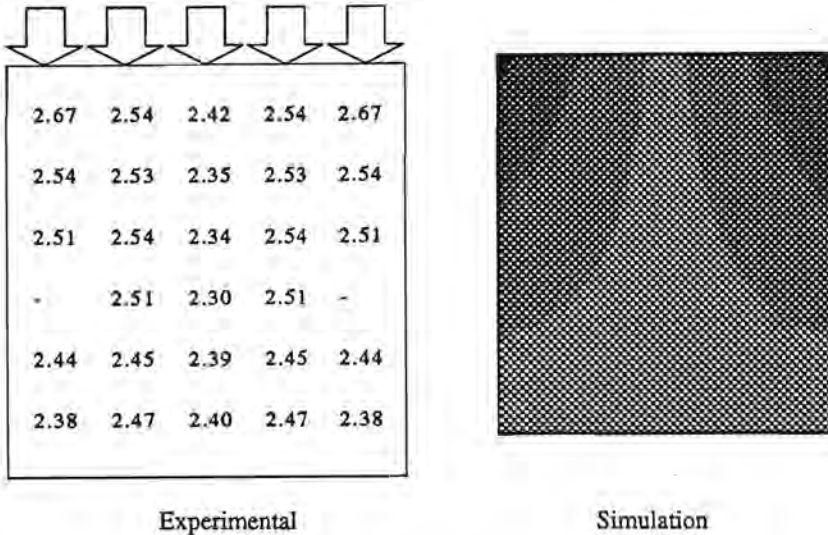


Fig. 8.7: Simulation of the density distribution in a cylindrical compact (diameter 28.1 mm, height 32.4 mm). Each grey shade indicates a density range of 0.07 g/cm^3 is obtained.

Fig. 8.7 shows that good correspondence between the measured and simulated density distributions is obtained. The simulation accentuates that the inversion of the radial density gradient is practically absent.

The homogeneity is calculated during the determination of the density distribution using eq. (8-1). For example, the homogeneity for the compact shown in fig. 8.7 is found to be 0.983. This indicates that the differential shrinkage during sintering will be limited.

The gradient model is a useful tool for the determination of the homogeneity in cylindrical compacts. However, the application to simulate the density distribution in other geometries is not obvious. Therefore, the more flexible finite element method is developed in the following sections.

8.4. Finite element method

8.4.1. Introduction

In the present study, the compaction of granulate in axisymmetric dies is considered. Given this geometry, the granulate mass in the die is conveniently subdivided into ring-shaped elements with a triangular cross-section (fig. 8.8).

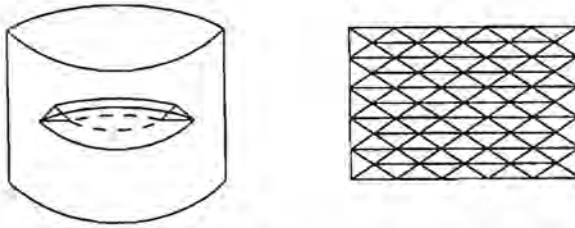


Fig. 8.8: Subdivision of the initial granulate mass into elements. Each ring-shaped element has three planes (left). In a two-dimensional representation, the edge of the plane coincides with a nodal point (right).

In this study, every element is characterized with three nodal points, which are located along the edges of the element. During compaction, the compaction of an element is reflected in the displacement of its nodes. The nodal displacements (δ) are related to the nodal strains (ϵ) by arbitrary polynomials. In general form:

$$\underline{\epsilon} = \underline{B}\delta \quad (8-17)$$

where $\underline{\epsilon}$ and δ are vectors containing the nodal strains and displacements while \underline{B} is a matrix linking the strain and the displacement. The compaction behaviour of the granulate is characterized by the relations between the stress σ and the strain ϵ . In general form:

$$\underline{\sigma} = \underline{D}\epsilon \quad (8-18)$$

where \underline{D} is a matrix containing the stress-strain relation. In practice, the relation between the displacement and the force F rather than the stress σ is required:

$$\underline{F} = \underline{K}\delta \quad (8-19)$$

where \underline{K} is the element-stiffness matrix. Using the principle of virtual work, the force and stress are related as follows:

$$\underline{F} = \int (\underline{B}^T \underline{\sigma}) dV \quad (8-20)$$

Combining eqs. (8-17) and (8-18) and substituting $\underline{\sigma}$ produces an expression for the element-stiffness matrix \underline{K} defined in eq. (8-19):

$$\underline{K} = \int (\underline{B}^T \underline{D} \underline{B}) dV \quad (8-21)$$

Summing the stiffness matrix for all elements produces the system-stiffness matrix \underline{K} :

$$\underline{K} = \Sigma \underline{K} \quad (8-22)$$

The system-stiffness matrix relates the nodal displacements to the external forces \underline{F} :

$$\underline{F} = \underline{K} \underline{\delta} \quad (8-23)$$

Eqs. (8-17) to (8-23) form the basis of finite element calculations [4]. The components of the force and displacement vectors and the matrices \underline{B} and \underline{D} depend on the nature of the problem under consideration. In the following subsections, two different approaches are developed. In section 8.3.2, the granulate mass is represented by a two-dimensional network of trusses, which coincide with the vertices of ring-shaped elements. This approach has a significant advantage in terms of computing speed over the three-dimensional element model. The element model, which is based on subdivision of the granulate mass into ring-shaped elements, is presented in section 8.3.3.

8.4.2. Truss model

In this section, the axial cross-section of the die is modelled with a network of trusses. A truss network consists of beams which are connected to each other through frictionless pin-joints at either end of the beam. Force is exerted on the beam through these pin-joints only. Consequently, the deformation behaviour of the beam in the axial direction is given by:

$$\sigma = (d\sigma/d\varepsilon)\varepsilon \quad (8-24)$$

where σ and ε are the axial stress and strain. In section 7.7.1, it has been shown that the differential $(d\sigma/d\varepsilon)$ is obtained from the compaction curve. Note that the strain can be expressed in terms of the displacement δ and the initial length L_0 of the beam:

$$\varepsilon = \delta/L_0 \quad (8-25)$$

Because only the stress-strain behaviour in the axial direction is considered, the matrices \underline{B} and \underline{D} (eqs. 8-17 and 8-18) become scalar quantities. Using eqs. (8-24) and (8-25):

$$B = 1/L_0 \quad (8-26a)$$

and

$$D = d\sigma/d\varepsilon \quad (8-26b)$$

In this application, the beam is characterized by its length L rather than its volume. In order to obtain a volume integral (eq. 8-21), a fictive cross-sectional area A is introduced which equals the radial cross-sectional area of the die. Because the latter is constant, the differential volume of the beam becomes:

$$dV = AdL \quad (8-27)$$

Substitution of B and D (eq. (8-26)) and dV (eq. 8-27) into eq. (8-24) followed by integration between 0 and L_0 produces an expression for the element-stiffness K :

$$K = (d\sigma/d\varepsilon)A/L_0 \quad (8-28)$$

Force can be applied on the nodes at either end of the beam. In a two-dimensional representation, the forces can be decomposed into two components. Similarly, the displacement of each node is given by two components. The force and displacement are now contained in the following vectors:

$$\begin{pmatrix} F_{r,1} \\ F_{z,1} \\ F_{r,2} \\ F_{z,2} \end{pmatrix} = \underline{K} \begin{pmatrix} \delta_{r,1} \\ \delta_{z,1} \\ \delta_{r,2} \\ \delta_{z,2} \end{pmatrix} \quad (8-29)$$

Because the beam is not bent during compaction, the force and displacement components are related through the orientation of the beam. The latter is expressed in terms of the angle α which the beam makes with the horizontal plane. Incorporating the influence of the orientation into the element-stiffness matrix leads to the following relation:

$$\underline{K} = \frac{(d\sigma/d\varepsilon)A}{L_0} \begin{pmatrix} \cos^2\alpha & \sin\alpha\cos\alpha & -\cos^2\alpha & -\sin\alpha\cos\alpha \\ \sin\alpha\cos\alpha & \sin^2\alpha & -\sin\alpha\cos\alpha & -\sin^2\alpha \\ -\cos^2\alpha & -\sin\alpha\cos\alpha & \cos^2\alpha & \sin\alpha\cos\alpha \\ -\sin\alpha\cos\alpha & -\sin^2\alpha & \sin\alpha\cos\alpha & \sin^2\alpha \end{pmatrix} \quad (8-30)$$

8.4.3. Element model

The cylindrical die space is subdivided into ring-shaped elements with a triangular cross-

section. The deformation behaviour of these elements is given by the quasi-elastic density-dependent model developed in section 7.7. The model contains four strains as a function of as many stresses. For determination of the element-stiffness matrix, the inverse relation is required. Defining the total strain \mathbf{e} :

$$\mathbf{e} \equiv \mathbf{e}_z + \mathbf{e}_r + \mathbf{e}_\theta \quad (8-31)$$

Summation of the model equations in the three principal directions and substituting into the original equations yields:

$$\sigma_z = H(\nu e / (1 - 2\nu) + \mathbf{e}_z) / (1 + \nu) \quad (8-32a)$$

$$\sigma_r = H(\nu e / (1 - 2\nu) + \mathbf{e}_r) / (1 + \nu) \quad (8-32b)$$

$$\sigma_\theta = H(\nu e / (1 - 2\nu) + \mathbf{e}_\theta) / (1 + \nu) \quad (8-32c)$$

Similarly, the shear stress τ_{rz} is expressed in the shear strain γ_{rz} :

$$\tau_{rz} = H / (2(1 + \nu)) \gamma_{rz} \quad (8-33)$$

Eqs. (8-32) and (8-33) can be arranged in the matrix $\underline{\mathbf{D}}$, which is defined by eq. (8-18):

$$\begin{pmatrix} \sigma_z \\ \sigma_r \\ \sigma_\theta \\ \tau_{rz} \end{pmatrix} = \frac{H(1-\nu)}{(1+\nu)(1-2\nu)} \begin{pmatrix} 1 & \frac{\nu}{1-\nu} & \frac{\nu}{1-\nu} & 0 \\ \frac{\nu}{1-\nu} & 1 & \frac{\nu}{1-\nu} & 0 \\ \frac{\nu}{1-\nu} & \frac{\nu}{1-\nu} & 1 & 0 \\ 0 & 0 & 0 & \frac{1-2\nu}{2(1-\nu)} \end{pmatrix} \begin{pmatrix} \mathbf{e}_z \\ \mathbf{e}_r \\ \mathbf{e}_\theta \\ \gamma_{rz} \end{pmatrix} \quad (8-34)$$

On account of symmetry of the die, each node has two degrees of freedom only: in the axial (z) and radial (r) direction. The nodal displacement in these directions varies linearly with the coordinates of the node:

$$\delta_i = \beta_1 + \beta_2 r + \beta_3 z \quad (8-35a)$$

and

$$\delta_z = \beta_4 + \beta_5 r + \beta_6 z \quad (8-35b)$$

where $\underline{\beta}$ represents a set of arbitrary coefficients. Expressing eq. (8-35) in matrix form:

$$\begin{Bmatrix} \delta_r \\ \delta_z \end{Bmatrix} = \begin{bmatrix} 1 & r & z & 0 & 0 & 0 \\ 0 & 0 & 0 & 1 & r & z \end{bmatrix} \begin{Bmatrix} \beta_1 \\ \beta_2 \\ \beta_3 \\ \beta_4 \\ \beta_5 \\ \beta_6 \end{Bmatrix} \quad (8-36)$$

Because the coordinates of the nodes are known, the components of the matrix in eq. (8-36) are substituted for each of the three element nodes, which are numbered i , j and k :

$$\begin{Bmatrix} \delta_{r,i} \\ \delta_{r,j} \\ \delta_{r,k} \\ \delta_{z,i} \\ \delta_{z,j} \\ \delta_{z,k} \end{Bmatrix} = \begin{bmatrix} 1 & r_i & z_i & 0 & 0 & 0 \\ 1 & r_j & z_j & 0 & 0 & 0 \\ 1 & r_k & z_k & 0 & 0 & 0 \\ 0 & 0 & 0 & 1 & r_i & z_i \\ 0 & 0 & 0 & 1 & r_j & z_j \\ 0 & 0 & 0 & 1 & r_k & z_k \end{bmatrix} \begin{Bmatrix} \beta_1 \\ \beta_2 \\ \beta_3 \\ \beta_4 \\ \beta_5 \\ \beta_6 \end{Bmatrix} = \underline{C} \underline{\beta} \quad (8-37)$$

On account of continuity, eq. (8-36) is valid for every point within the element. Substituting the coefficients $\underline{\beta}$ in eq. (8-36) with eq. (8-37) relates the displacement of the element to the displacement of the nodes:

$$\begin{Bmatrix} \delta_r \\ \delta_z \end{Bmatrix} = \begin{bmatrix} 1 & r & z & 0 & 0 & 0 \\ 0 & 0 & 0 & 1 & r & z \end{bmatrix} \underline{C}^{-1} \begin{Bmatrix} \delta_{r,i} \\ \delta_{r,j} \\ \delta_{r,k} \\ \delta_{z,i} \\ \delta_{z,j} \\ \delta_{z,k} \end{Bmatrix} \quad (8-38)$$

In an axisymmetric geometry, four components of strain have to be considered. These are related to the two displacements as follows:

$$\begin{pmatrix} \epsilon_r \\ \epsilon_z \\ \epsilon_\theta \\ \gamma_{rz} \end{pmatrix} = \begin{pmatrix} \frac{\partial \delta_r}{\partial r} \\ \frac{\partial \delta_z}{\partial z} \\ \frac{\delta_r}{r} \\ \frac{\partial \delta_r}{\partial z} + \frac{\partial \delta_z}{\partial r} \end{pmatrix} \quad (8-39)$$

Obtaining the partial derivatives from eq. (8-38) produces the following relation:

$$\begin{pmatrix} \epsilon_r \\ \epsilon_z \\ \epsilon_\theta \\ \gamma_{rz} \end{pmatrix} = \begin{pmatrix} 0 & 1 & 0 & 0 & 0 & 0 \\ 0 & 0 & 0 & 0 & 0 & 1 \\ 1/r & 1 & z/r & 0 & 0 & 0 \\ 0 & 0 & 1 & 0 & 1 & 0 \end{pmatrix} \underline{\underline{C}}^{-1} \begin{pmatrix} \delta_{r,i} \\ \delta_{r,j} \\ \delta_{r,k} \\ \delta_{z,i} \\ \delta_{z,j} \\ \delta_{z,k} \end{pmatrix} \quad (8-40)$$

Recalling that the nodal strains and displacements are related through the matrix $\underline{\underline{B}}$ (eq. 8-17), an expression for the matrix $\underline{\underline{B}}$ is obtained from eq. (8-40):

$$\underline{\underline{B}} = \frac{1}{2\Delta} \begin{pmatrix} a_i & a_j & a_k & 0 & 0 & 0 \\ 0 & 0 & 0 & b_i & b_j & b_k \\ c_i & c_j & c_k & 0 & 0 & 0 \\ b_i & b_j & b_k & a_i & a_j & a_k \end{pmatrix} \quad (8-41)$$

where Δ is the cross-sectional area of the element and a, b and c are coefficients which depend on the nodal coordinates:

$$a_i = z_j - z_k \quad a_j = z_k - z_i \quad a_k = z_i - z_j \quad (8-42a)$$

$$b_i = r_k - r_j \quad b_j = r_i - r_k \quad b_k = b_j - b_i \quad (8-42b)$$

$$c_i = a_i + b_j z/r + d_j/r \quad c_j = a_j + b_k z/r + d_k/r \quad c_k = a_k + b_i z/r + d_i/r \quad (8-42c)$$

where the coefficients d_i , d_j and d_k are given by:

$$d_i = r_j z_k - r_k z_j \quad d_j = r_k z_i - r_i z_k \quad d_k = r_i z_j - r_j z_i$$

Note that the coefficients c_i , c_j and c_k are a function of coordinates r and z , which implies that the strains are not constant within the element. In order to obtain the element-stiffness matrix \underline{K} , the matrix \underline{B} is evaluated at a centroidal point whose coordinates ($\langle r \rangle$, $\langle z \rangle$) are given by:

$$\langle r \rangle = (r_i + r_j + r_k)/3 \quad (8-43a)$$

and

$$\langle z \rangle = (z_i + z_j + z_k)/3 \quad (8-43b)$$

The differential volume of the ring-shaped element can be written as:

$$dV = 2\pi r dr dz \quad (8-44)$$

Substituting dV in eq. (8-24) yields:

$$\underline{K} = 2\pi \int (\underline{B}^T \underline{D} \underline{B} r) dr dz \quad (8-45)$$

The integral in eq. (8-45) may be approximated by:

$$\underline{K} = 2\pi \langle \underline{B} \rangle^T \underline{D} \langle \underline{B} \rangle \langle r \rangle \Delta \quad (8-46)$$

8.4.4. Solution of equations

The finite element method consists of two stages: 1) determination of the system-stiffness matrix \underline{K} and 2) simultaneous solution of the force-displacement equations. The system-stiffness matrix \underline{K} has been established in the preceding sections for two different approaches. Note that, in both cases, the matrix \underline{D} depends on the density ρ of the granulate. Because the density is related to the displacements through the strain, the system-stiffness matrix \underline{K} is a function of the displacement. Rewriting eq. (8-23):

$$F_i = K_i(\delta) \delta \quad (8-47)$$

This dependency is a result of the strain-hardening nature of compaction: in a one-dimensional representation, the force F increases more than proportionally with the displacement δ . Consequently, the displacements δ have to be determined using an iterative procedure by repeating stage 1) and 2) until sufficient convergence is obtained.

The iterative calculation of the displacement vector is based on division of the total force into increments. The displacement vector corresponding to each increment of force is calculated and used to update the total displacement vector. After each increment, the element stiffness is recalculated using the (intermediate) density distribution. This procedure is illustrated for the generalized one-dimensional case in fig. 8.9. Note that the relative magnitude of the force increments ΔF is arbitrary. Because errors propagate during the solution process, the force increments ΔF are initially chosen to be significantly smaller.

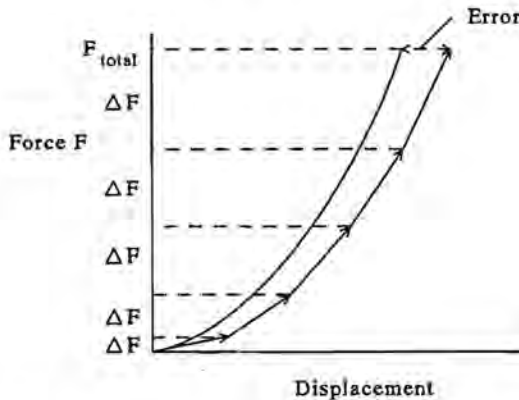


Fig. 8.9: Iterative determination of the displacement by adjusting the stiffness. Each iteration cycle is indicated with an arrow. Note that the force increments ΔF are increased during the calculation.

On account of the non-linear nature of the force-displacement relation, an error is introduced in the calculated displacements. Therefore, the solution process is refined by applying a Newton-Raphson type of iteration. After an increment of force, the difference between the calculated forces and the actual forces corresponding to the new displacements is considered. Given updated values for the stiffness, a set of displacements balancing these residual forces is determined. The set of displacements is subsequently used to correct the total displacement vector. Following recalculation of the stiffness, a further increment of force is applied. This procedure is illustrated in fig. 8.10.

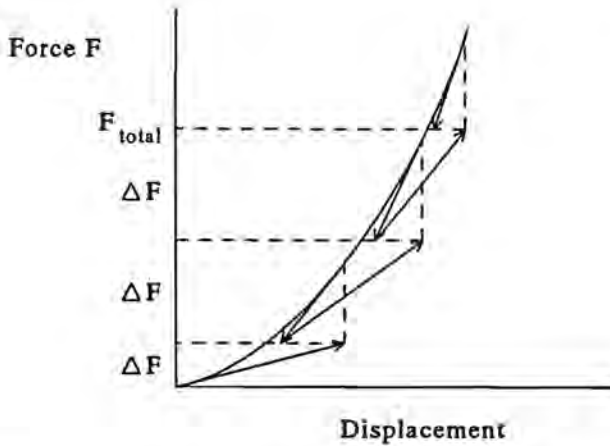


Fig. 8.10: Iterative determination of the displacement with improved accuracy. After each increment of force, the displacement is corrected by a single Newton-Rhapson type of iteration. Note that the incremental application of force is still required in order to prevent excessive unbalanced forces.

The single Newton-Rhapson iteration used represents a trade-off between improved accuracy and calculation speed.

During the calculation, the nodes can only move when this motion is physically realistic. Therefore, nodes which are positioned on the die wall cannot move outwards. Similarly, nodes located on the lower punch surface cannot move downwards. Whenever the motion of a node in a particular direction is restricted, the corresponding displacement is by definition zero. Consequently, the force acting in these directions is unknown. However, the radial force is of interest because the frictional force at the die wall is the product of the radial force and the friction coefficient μ (section 8.2). Therefore, the interpretation of the wall friction coefficient is generalized by assuming that it not only represents the ratio of two perpendicular forces but also of two opposite but parallel forces. In other words, the wall friction coefficient also indicates the ratio of the frictional force and the force applied by the punch *along* the die perimeter. Given the axial force acting on the perimeter nodes, the frictional force can be calculated. Because the frictional force has to be known before the solution of the equations, the first estimate of the frictional force is based on the assumption that the frictional forces are initially equal at each node on the perimeter. After an iteration, the frictional force is updated locally by calculating the axial forces acting on the nodes at the boundary. The non-linearity introduced by updating the frictional forces is found to be relatively small compared to the non-linearity resulting from updating the stiffness of the element. Therefore, the solution of the equations is not affected.

The nodal displacements $\underline{\delta}$ are calculated using the Gaussian elimination technique. This implies that the system-stiffness matrix \underline{K} is first reduced to its lower triangular form and then to its upper triangular form. The displacements are found from the ratio of the force and diagonal elements of the matrix \underline{K} .

8.5. Simulation results

8.5.1. Introduction

A PC-based computer program has been written in Turbo Pascal 5.0 to perform the simulation procedures developed in the preceding sections. All calculations are carried out using variables with 7 to 8 significant digits. Because the system-stiffness matrix \underline{K} is stored in the normal RAM memory, the number of nodes is limited to 63. This number is considered sufficient because the elements have to be relatively large in order to satisfy the condition of isotropy.

The density distribution in two different compact shapes is simulated: a massive cylindrical compact and a cup-shaped compact known as the potcore. The cylindrical compact requires specification of the diameter of the die, the filling height, the density of the granulate mass ($\approx 1.4 \text{ g/cm}^3$), the friction coefficient μ (section 8.2) and the applied force F . The number of iterations is arbitrarily set to 10.

With the potcore, more elaborate specifications are required because the compaction of potcores is displacement-controlled rather than force-controlled. Therefore, besides the initial dimensions of the die (diameter of the bottom, thickness of the rim) and the filling height of the bottom and the rim, the dimensions of the potcore compact are specified. As a result, the solution process of the equations is modified: because the displacement of the nodes directly adjacent to the punch is prescribed, the required force can be calculated. Subsequently, the displacement of the other nodes is found by assuming that the force due to wall friction is constant in the axial direction. In other words, the wall friction force at all nodes on the perimeter is similar although its magnitude is recalculated after each iteration. The wall friction force is then obtained by distributing the fraction of the total axial force which is balanced by wall friction, over the nodes on the perimeter of the die, allowing calculation of the displacements of the nodes which are not located on the punch surface. Similar to the force-controlled simulation process, the total displacement is divided into fractions which are imposed on the nodes directly adjacent to the punch. After determination of all the displacements, the system-stiffness matrix is recalculated and the next increment is applied.

8.5.2. Cylinders and tablets

An actual and simulated density distribution are compared in order to verify the validity of the force-controlled simulation of compaction (fig. 8.11). The density distribution of a massive cylinder has been determined experimentally by measuring compact sections with mercury intrusion porosimetry. The experimental setup is described in section 3.4. The simulation is carried out with 90 three-dimensional ring-shaped elements, which are located on six levels.

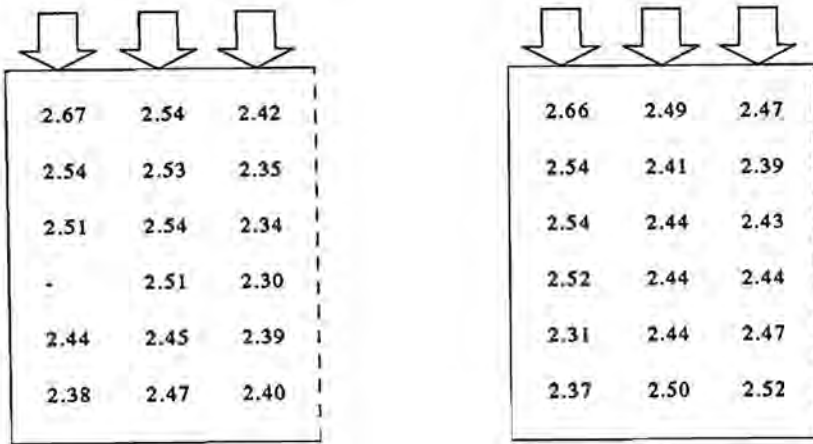


Fig. 8.11: Density distribution of a cylindrical compact determined experimentally (left) and by simulation (right). The simulated densities are obtained by averaging the density of the elements which are located in the sections measured with mercury intrusion porosimetry.

Fig. 8.11 shows that the density distribution predicted by the simulation is indicative of the actual density distribution. Note that the type of binder represented in the simulation (acrylic II) is slightly different from the binder used during the compaction experiment (acrylic I).

The homogeneity of the compact in fig. 8.11 can be expressed in terms of the parameter ζ (eq. 8-1). This parameter passes through a minimum when the density is increased from the filling density of the granulate ($= 1.4 \text{ g/cm}^3$) to the zero-porosity density ($= 5.11 \text{ g/cm}^3$). For each of the extremal densities, the homogeneity ζ equals unity. The progress of the homogeneity ζ as a function of the density depends on the length-to-diameter ratio (L/D) ratio of the compact: the lower the L/D ratio, the higher the homogeneity ζ and the lower the density where the homogeneity ζ has its minimum value.

Using the two-dimensional truss elements, the density distribution of tablet-shaped compacts is simulated. Upon increasing the L/D ratio to values under 0.1, an interesting

inversion in the density distribution is observed: the density near the lower (stationary) punch is higher than the density near the upper punch (fig. 8.12).

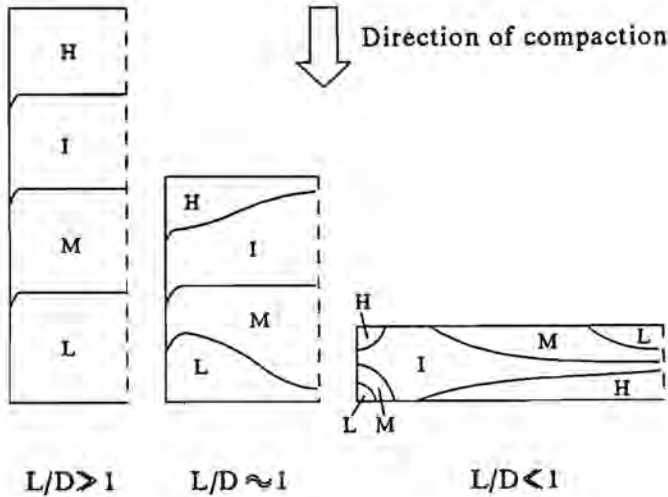


Fig. 8.12: Simulation of the density distribution in cylindrical compacts. Abbreviations: H = high, I = intermediate, M = medium, L = low. Note that the indications reflect relative differences instead of absolute differences in density.

The inversion is difficult to observe experimentally: the differences in the density within tablets are much smaller than the differences present in cylindrical compacts. Therefore, the practical significance of this inversion is small, although it contradicts the model where internal friction produces a negative axial gradient in the density. A possible explanation is that the upper punch produces movement of the granules which results in enhanced compaction near the lower punch.

Comparison of the simulation of density distributions using the truss and the element model shows that the truss model is significantly faster but less accurate than the element model. With the truss model, the gradient along the perimeter of the die is generally overestimated.

8.5.3. Potcores

The compaction of potcores requires double-sided pressing. Therefore, the simulation consists of two stages. During the first stage, the punch pressing the bottom of the potcore is moved with a prescribed displacement. Subsequently, the punch pressing the rim of the potcore is moved by a predetermined displacement. Using the truss model, a typical simulation result is shown in fig. 8.7.

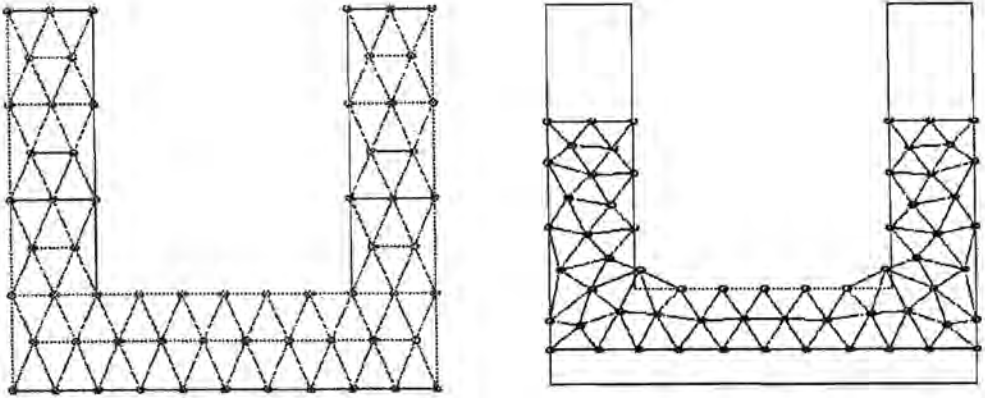


Fig. 8.7: Simulation of the compaction of potcores using a two-stage approach. The die space is subdivided into equisized elements (left) and subjected to double-sided pressing. In the final state (right), the elements at the corner of the rim and the bottom have exceeded the physical boundary. Potcore dimensions: bottom diameter 20.0 mm, bottom thickness 2.2 mm, rim height 8.2 mm, rim thickness 2.2 mm.

Fig. 8.7 shows that the elements in the corner between the bottom and the rim overlap with the central rod. This makes remeshing during the solution process necessary. Remeshing is the subdivision of the available die space with new elements while retaining the density of the original elements. The transfer of the density raises the question of the inter-element transport of granulate. It has been assumed that the density is related to the volume of an element because the granulate remains within the element throughout compaction. Consequently, the occurrence of overlap itself violates this condition, and remeshing only provides a partial remedy: it cannot prevent the tendency of elements to overlap with the middle pen. For this reason, remeshing is not incorporated in the present simulation program.

Simulation of the compaction of potcores shows that movement of granulate in the interface between the bottom and the rim occurs. During the pressing of the bottom, granulate is forced into the rim. On account of the radial density gradient in the bottom, more granules are moved into the bottom *near* the central rod. Therefore, a radial density distribution is obtained in the bottom section of the rim. Subsequent pressing of the rim forces granules near the die wall from the rim into the bottom. Near the central rod, the high density obstructs granule movement. Therefore, the radial density gradient in the interface between the rim and the bottom is aggravated.

The formation of the radial gradient presents difficulties when simulating the potcore with the truss model. When the elements in the rim are skewed during pressing of the bottom,

'buckling' can occur during pressing of the rim. This is due to the property of the truss model that force is applied at the nodal points only. With the element model, this problem is not encountered.

8.6. Discussion and conclusion

In this chapter, techniques to simulate the density distribution are developed. Starting point is the assumption that the granulate is considered to be a continuum. The most simple method is based on modelling the stresses in the cross-section of the compact. This method is not able to predict radial density gradients unless the model equation is adapted with experimental data. However, this method does indicate the relative significance of internal and external friction and allows prediction of the homogeneity of *cylindrical* compacts.

Simulation of the compaction process with the finite element method can be applied to any die geometry because small elements within the granulate are considered instead of the entire cross-section. Although the finite element method has been used previously for this purpose, the definition of the constitutive behaviour as developed in chapter 7 reduces the complexity associated with the formulation of the finite element method. Previously, elastoplasticity has been modelled with a yield criterium and associated flow rule. In this thesis, a direct (non-linear) approach is developed which requires only a single element-stiffness matrix whereas the traditional approach requires two element-stiffness matrices. As a result, this novel approach is sufficiently compact to be implemented on a PC.

The simulation results show that this approach is capable of predicting the density distribution with reasonable accuracy and that trends in the density are faithfully represented. Because the simulation can be used for products with any geometry, the approach developed in this section can be used to reduce the number of experiments which are otherwise required.

References

1. A. Drescher, G. de Josselin de Jong, 'Photoelastic verification of a mechanical model for the flow of a granular material', *Journal of the Mechanics and Physics of Solids*, vol. 20 (1972), 337-351.
2. T. Ikegami, 'A Model for Two-Dimensional Compaction of Cylinders', *Journal of the Ceramic Society of Japan, International Edition*, vol. 98-530 (1990), 101-104.
3. N. Stanley-Wood, A. Ibrahim, 'A Correlation between Angle of Friction, Angle of Failure Plane and Strength for Compacts of Tartaric Acid, Microcrystalline Cellulose and Mixture of the Two', *Powder Technology*, vol. 51 (1987), 151-157.
4. S. Rajasekaran, 'Finite Element Analysis in Engineering Design', Wheeler Publishing, 1993.

Suggested reading:

A. Broese van Groenou, R. Lissenburg, 'Inhomogeneous Density in Die Compaction: Experiments and Finite-Element Calculations', *Communications of the American Ceramic Society*, no. 10 (1983), C156-C158.

Y. Kanoh, T. Nakata, H. Okumura, K. Ohtake, N. Koike, 'Large Deformation Finite Element Analysis on the Parallel Machine Cenju', *NEC Research and Development*, vol. 34, no. 3 (1993), 350-359.

S. Singh, 'Theory of Plasticity', Khanna Publishers Dehli, 1981.

N. Smitbhan, W.-F. Chen, 'Elastic-Plastic Large Deformation of Soil Slopes', *Computer & Structures*, vol. 9 (1978), 567-577.

Chapter 9

Discussion and final remarks

9.1. Framework of thesis

This thesis is focussed on three aspects: a) the development of techniques for the characterization of physical structures (chapter 2), b) the derivation of models for powder compaction by characterization of the physical structure (chapters 3, 4 and 5) and c) the derivation of models for powder compaction through characterization of the state of stress (chapters 6, 7 and 8).

Physical structures are characterized by measuring the pore size distribution. Two techniques have been studied: mercury intrusion porosimetry (MIP) and nitrogen adsorption/desorption, which is referred to as the BET technique. The MIP technique measures pores ranging from 0.01 to 2 μm , while the BET technique measures pores in the range of 0.005 to 0.02 μm . The size of the pores in actual compacts depends on the size of the smallest units, the particles. When using (Mn,Zn)-ferrite granulate, the particles have an average size of 1 μm , while clusters of particles ranging in size between 60 and 300 μm are also present. Therefore, the BET technique only measures irregularities in the surface structure of the particles. The MIP technique, on the other hand, is capable of measuring the pores between the particles. Therefore, the data obtained with the MIP technique is of greater significance and has been critically examined in chapter 2.

Two main approaches to model the compaction process have been developed. One type of model is based on the evolution of the physical structure during compaction, while the other type is based on the evolution of the state of stress during compaction. With each approach, different details of the compaction process are revealed.

In chapter 3, a qualitative model interpreting the effects of internal and external friction is developed. In principle, this is a continuum approach, which allows prediction of density gradients in compacts. The validity of this approach is verified by measurement of the density and average pore size in sectioned compacts with MIP.

In chapter 4, the evolution of the pore size distribution measured with MIP is modelled with representative cells. The packing of particles and granules are modelled with separate cells. After establishing the initial packing of the either type of solid, a prediction of the evolution of the pore size distribution can be made. Comparison with actual development enables the identification of other packing structures in the granulate.

In chapter 5, the concept of fractal scaling is applied to characterize the evolution of the physical structure during the compaction process. First, the significance of the characterization based on fractal scaling is investigated through analysis of images. Subsequently, the evolution of the pore size distribution measured with MIP is analysed.

In chapter 6, the compaction curve, which reflects the relation between the pressure

and the overall density, is presented. It is found that the overall density varies linearly with the logarithm of the pressure in *two* successive pressure ranges. The transition occurs at a density where the compact has just sufficient strength to be handled. Therefore, the difference between the two zones is linked to the buildup of the compact strength. Using this observation when analyzing the state of stress during compaction allows prediction of the strength from the compaction curve.

In chapter 7, data for the characterization of the state of stress is derived from analysis of selected mechanical tests. Modelling of three-point bend test data allows characterization of the properties of the binder, while modelling of the free compression, die and isotropic compaction tests can be used to characterize the compaction behaviour of granulate. The compaction behaviour models are implemented in a simulation program in chapter 8. This allows prediction of the density distribution in compacts, which can find application in the industrial ferrite production process.

9.2. Results

The measurement of pore size distributions with mercury intrusion porosimetry (MIP) has been critically examined. When modelling the pores as cylinders, it is shown that the intrusion equation is consistent with the underlying thermodynamic and mechanical considerations. The use of other pore shapes is erroneous from a theoretical point of view. When assuming that the pores are cylindrical, the method is useful for measuring the pore size distribution present in compacts. This is not the case with the nitrogen adsorption technique, which only measures pores which are smaller than those found in compacts. Note that the minimum pore size in compacts is proportional to the size of the particles unless the particles fracture during compaction. With (Mn,Zn)-ferrite, however, the particles remain intact up to relatively high densities (chapter 2).

The compaction of (Mn,Zn)-ferrite powder can be modelled by analysing the effects of internal and external friction. Internal friction, which refers to the interaction between particles, is found to be insensitive to the pressing velocity, the mode of pressing or the type of binder. Internal friction is, however, a strong function of the state of stress, which correlates directly with the density: the higher the density, the greater the interparticle friction and the larger the force required for further compaction of the particles. External friction, which refers to the interaction between particles and the die surfaces, has the same effect as internal friction on the compaction of the particles close to the die surfaces. Therefore, the effects of internal and external friction can be combined to predict the density distribution in compacts. For compacts with more complex geometries than cylinders (e.g. potcores), the pressing velocity and the mode of pressing can also influence the density distribution (chapter 3).

The (Mn,Zn)-ferrite powder consists of granules, which contains agglomerates of particles. On account of the difference in size between these solid units, three distinct pore

sizes are initially present in the granulate. The evolution of each class of pores during compaction has been modelled successfully with two-dimensional representative cells. Relations characterizing the cell properties are developed using a novel classification of the processes which occur during compaction. Experimental data are obtained from the analysis of compacts with MIP. Two aspects complicate the configuration of the cells: i) a compact is only formed at densities significantly larger than the initial density and ii) the pore size distributions of compacts are uni- or bimodal rather than trimodal. Using the assumption that the largest pores are compressed preferentially, representative cells for the initial structure of the granulate can be established. Based on this representation, it is shown that the bimodal distribution is due to pores between particles and agglomerates rather than pores between particles and granules. This proves the existence of agglomerates within the granules (chapter 4).

The pore size distribution in compacts as measured with MIP can be characterized with the fractal dimension. However, the fractal dimension offers no significant advantage over conventional statistical measures such as the mean pore size or the standard deviation. Similar to the mean pore size and standard deviation, the fractal dimension is a function of the compact density, increasing monotonously to its limit value of 3. Furthermore, the fractal dimension is highly sensitive to the measurement conditions. The latter is a result of the presence of only two distinct pore sizes in compacts. This effectively implies that the concept of fractal scaling is, at best, only valid for a narrow range of pore sizes (chapter 5).

Determination of the fractal dimension from images using a grid shows that the fractal dimension varies with the number of subdivisions of the grid. The evolution of the fractal dimension as a function of the number of subdivisions is, however, not unique and depends on the initial position of the grid. Therefore, a position-independent technique to determine the fractal dimension has been developed by relating the mean pore size to the total volume. When comparing two different pore sizes and corresponding volumes, the dependency on the mass of the sample can be removed. This makes definition of novel parameter, the fractal exponent, possible. The fractal exponent is larger than 3 when the pore size decreases with increasing density. Characterization of the evolution of the two peaks of the pore size distributions measured with MIP shows that the peaks represent pores between solid units with different sizes. This confirms that the original size distribution of the pores is determined by the size of the particles, agglomerates and granules (chapter 5).

Uniaxial die compaction of (Mn,Zn)-ferrite granulate can be characterized by two successive linear correlations between the overall density and the logarithm of the pressure. Variation of type and content of binder is found to influence the pressure-density relation. Another granulate property, the size of the granules, has no effect on the pressure-density relation. With respect to the die, it is found that the die-wall roughness

has no effect, whereas variation of the die diameter does: when the diameter is increased, the effect of external friction decreases. This results in a higher overall density for a given pressure, which is reflected in the correlations (chapter 6).

The necessity to characterize the relation between the pressure and density with two correlations indicates the existence of a transition during compaction. In view of the densities at which the correlations intersect ($2.2 - 2.6 \text{ g/cm}^3$), depending on the type of binder), a tentative explanation is that the transition is related to the strength of the compact. This observation is used to develop a model to determine the variation of the strength of compacts with the type of binder. The model is based on the evolution of the state of stress represented by Mohr circles. Measurement of the strength with the diametral compression test confirms the validity of this model (chapter 6).

In order to compare uniaxial die compaction with other types of compaction, two different classification methods are developed. The first method is based on characterization of the applied normal and shear stresses. The second is based on the distinction between deformation and densification, which indicate a change of shape and volume respectively. When subjecting a compact to bending, only deformation occurs because the compact breaks before overall densification can occur. Interpretation of the deformation behaviour using data obtained with three-point bend test reveals the nature of the binder bonding the particles. Two types of binder are shown to exist: binders where elastic deformation precedes elasto-plastic deformation, and binders which only deform elasto-plastically. The strength of the latter is found to be significantly larger than the strength of the former. That the strength of a compact increases when the stresses are compressive rather than tensile follows from the comparison of the strength measured with the three-point bend, the diametral compression and the free compression tests (chapter 7).

The compaction behaviour of (Mn,Zn)-ferrite is characterized by developing a quasi-elastic model. It differs from conventional elasticity models in that the parameters are a function of the density. The parameters can be determined from the free compression and isotropic compaction tests, although the significance is limited to densities where the granulate has sufficient strength to be denoted a compact. In order to span the entire range of densities, the die compaction test is used instead of the free compression test. This model is general in the sense that it represents the compaction behaviour on any scale above a certain minimum as long as the compaction conditions are defined (chapter 7).

The overall compaction behaviour can be predicted by combining the effects of local compaction using the finite element method. The necessary subdivision of the die space into elements is achieved by defining a truss framework, where compaction of the granulate is represented by deformation of the trusses, and by defining elements, which deform as a whole. The deformation behaviour of trusses is given by the pressure-density relation while the deformation of the elements can be characterized by the quasi-elastic model. The truss framework is computationally simpler and has been used to simulate the

compaction of cylinders and potcores. While simulating the latter, 'buckling' of trusses can occur. This is a consequence of applying force on the truss at the nodal points only. This can be avoided by using the more realistic elements to represent the granulate. For the compaction of a cylinder, the quasi-elastic model and the subdivision into elements is shown to be capable of accurate prediction of the density distribution (chapter 8).

9.3. Discussion and final remarks

Ceramic products are generally manufactured with a three-stage process. First the raw materials are prepared in order to obtain a suitable powder. Subsequently, the powder is consolidated in the shape of the product. Finally, this so-called green product is sintered at temperatures slightly below the melting temperature of the material. This thesis describes an investigation into the most widely applied technique for the consolidation of ceramic powders: the dry-pressing of powder in a die.

The goal of this investigation is to study the relation between the powder properties, the pressing conditions and the quality of the green product or compact. The compact has to meet two requirements: 1) the compact has to possess sufficient strength and 2) the density inside the product has to be uniform. If the latter condition is not met, differential shrinkage is observed during the subsequent sintering process.

The models and results in this thesis are based on the compaction behaviour of a ceramic powder called manganese-zinc-ferrite ($\text{Mn}_{0.66}\text{Zn}_{0.25}\text{Fe}_{2.09}\text{O}_4$). In practice, this type of powder is processed to products with numerous applications: from transformer cores to yoke rings (in TV sets) and radio antennae. The material owes this range of applications to its favourable electro-magnetic properties: a high electrical resistivity coupled to a high initial permeability.

After preparation of the ferrite powder, it is mixed with water and a binder to form a slurry. This slurry is subsequently spray-dried, a process during which the particles form clusters called granules. Because the granules display an improved flowability compared to the original particles, the die can be filled more homogeneously. Furthermore, granules reduce local differences in the density which are created during compaction: granules represent partially consolidated units.

The granulate can be characterized through the granule size distribution and the granule density. These influence the bulk density of the granules in the die and, subsequently, the compaction behaviour of the powder. In practice, the bulk density should be as high as possible in order to reduce the energy required to evaporate the moisture during spray-drying. Measurements of the bulk density indicated that a broad granule size distribution produces a slightly denser packing. In this way, the size of the pores between the granules is minimized. For small compacts, however, the use of small granules with a narrow size distribution produces a more uniform pore structure. The relation between the applied pressure and the density revealed that the broad granule size distribution is

advantageous: the density at each pressure is higher than the density of a granulate with a narrow size distribution.

The density of the granules could be influenced by adapting the volume of water added to the slurry. Measurements of the pore size distribution indicate that particles within the granules are spatially not distributed uniformly: the particles have formed agglomerates. These are separated by pores which are smaller than the pores between the granules and larger than the pores between the particles. When increasing the density of the granules, the formation of agglomerates in the granules is reduced. This increases the toughness of the granules and, consequently, the pressure required to force particles into the pores between the granules. This is confirmed by a model which interprets the relation between the applied pressure and the density during compaction: the kink which is observed shifts to higher densities when the density of the granules is increased. It was possible to relate the occurrence of the kink to the strength of the compact: before the kink, the cohesion of the granules is too weak so that a compact does not yet exist whereas the cohesion has increased sufficiently after the kink. This explanation has been verified experimentally and through a model which has been confirmed through indirect measurements of the strength.

Because pore size distributions of compacts pressed from granules with different densities are similar, a tentative explanation is that the effect of the pores between granules and agglomerates on the strength is different. Consequently, the pores between the granules could have a more detrimental effect on the compact strength than the pores between the agglomerates. The differences between these pores are underlined during sintering, when pores between the granules initially increase in size while pores inside the granules disappear.

In order to press compacts with sufficient strength, the density of the compact should be significantly higher than the density where the kink is observed. The higher the density, the higher the required pressure. Pressing conditions, such as the roughness of the die wall, the geometry and size of the die, the mode of pressing and the binder, only have a small influence on the compaction behaviour. In practice, the density of compacts is a trade-off between the compact strength, die wear and machining requirements. A high density increases the compact strength and reduces the shrinkage required during sintering. The latter reduces the effect of density gradients in the compact, which, in turn, reduces the machining required to correct for differential shrinkage. However, a disadvantage of pressing compacts to high densities is that it promotes die wear.

The spray-dried granules are generally spherical and contain pores. By optimizing the granule size distribution it is possible to obtain a higher filling density. This density is influenced by the binder: measurement of the strength of a compact subjected to tension and interpretation of the relation between the density and the applied pressure show that the binder has a significant influence on the strength. In other words, with one binder the

strength increases more sharply as a function of the density as with another binder. A suitable binder can therefore reduce the required compact density.

The influence of and differences between the binders are accentuated when the compact is subjected to tension. By interpreting applied force versus displacement data with a model, differences in the deformation and adhesion behaviour of the binders could be quantified. It was shown that the bonds between the particles which are formed by a mixture of polyvinylalcohol and acrylic are already irreversibly severed by low loads. The individual polyvinylalcohol and acrylic, on the other hand, produced bonds which could resist significantly higher loads. This leads to differences in the strength of the compact.

A disadvantage of binders which adhere strongly to the particles is that these also tend to stick to the die and punch surfaces. This causes the particles or even granules to stick to these surfaces during ejection of the compact, which could produce surface cracks in the compact. These considerations indicate that both the choice of the granule density and the binder are subject to optimization.

During compaction, axial differences in the pressure exist, which produces local differences in the density. This could lead to chipping or fracture during ejection or transport of the compact. Furthermore, if the axial density differences are present throughout the cross-section, differential shrinkage will occur during the subsequent sintering process. As noted above, this makes machining (grinding) necessary. On account of these reasons, the density differences in the compact should be minimized.

In order to predict the density distribution, qualitative and quantitative models have been developed. These are based on balancing the forces acting on segments of the granulate in the die. The applied pressure is balanced by particle-particle friction and die wall-particle friction. With this representation, the experimental density distribution in cylindrical compacts was simulated: the highest density is found in the corner directly below the punch and adjacent to the die wall. The density below the punch decreases inwards and axially. Near the bottom punch, however, the radial density gradient is reversed: the density near the die wall is lower than in the centre. The differences in the density can be limited by reducing the friction with the die wall by either coating the wall with a tough material (e.g. W-C) or a lubricant (e.g. glycerin). Note that the addition of a lubricant to the granulate can reduce the friction between the particles but also severely affects the strength of the compact. In addition, the flowability of the granules is reduced while sticking to the die surfaces is increased. Therefore, the presence of a lubricant between the particles is not beneficial.

With complex geometries such as the potcore the differences between the local densities can be significantly higher than is the case with cylindrical geometries. With simulation, the differences in density in potcores could be predicted for different modes of pressing.

List of symbols

symbol	significance	SI units
A	area	m ²
B	length of boundary	m
C	constant	Nm
D	fractal dimension	-
D _c	fractal exponent	-
E	elasticity modulus	Nm ⁻²
f	fraction of surface covered with units	-
F	force	N
G	Gibbs free energy	Nm
	shear modulus	Nm ⁻²
H	(elasto-) plastic modulus	Nm ⁻²
I	moment of inertia	m ⁴
K	ratio of major and minor principal stress	-
L	length of edge	m
	length in axial direction	m
m	mass	kg
M	scale factor	-
	bending moment	Nm
N	number of units (e.g. particles)	-
N _c	number of corners	-
P	pressure	Nm ⁻²
r	radius	m
R	gas constant	Nm(Kmol) ⁻¹
	radius of curvature	m
S	surface area	m ²
T	temperature	K
u	displacement	m
V	volume	m ³
W	work	Nm
z	vertical coordinate	m
α	corner angle	rad
α _s , α _v	shape factors	-
β	compressibility	m ² N ⁻¹
γ	surface tension	Nm ⁻¹
ε	porosity	-
η	viscosity	Ns/m ²
θ	contact angle	rad
λ	compression ratio	-
ρ	density	kg/m ³
σ	normal stress	Nm ⁻²
τ	shear stress	Nm ⁻²
ν	(plastic) Poisson's ratio	-
φ	pore size correction factor	-
ψ	sphericity	-

Summary

This thesis contains an investigation into the compaction behaviour of granulated manganese-zinc-ferrite powder. The main goal is establishing relations between the properties of the granulate, the compaction conditions and the properties of the compact. Insight is obtained from analysis of the spatial structure of compacts, the relation between the compaction pressure and the density and the behaviour of compacts under various loading conditions.

The compacts contain a pore size distribution which can be measured using porosimetry. The use of mercury intrusion and nitrogen adsorption has been evaluated (chapter 2). In view of the size of the pores in compacts, mercury porosimetry is more suitable than nitrogen adsorption.

The influence of the compaction parameters on the density and the corresponding pore size distribution is investigated in chapter 3. Using this data, a qualitative model of the compaction process was established.

Series of measured pore size distributions have been interpreted with two-dimensional representative cells (chapter 4). This approach is verified by direct (visual) observation.

The application of the concept of fractal scaling for the characterization of images and pore size distributions follows in chapter 5. As with representative cells, this approach indicates that the granules contain agglomerates of particles.

The relation between the compaction pressure and the density during compaction is determined by the size, shape and packing of the ferrite particles. The relation is found to be insensitive to the compaction conditions. The relation does show a kink at a density where the granulated powder has just acquired sufficient strength to be denoted a compact. This observation has been modelled by analysing the state of stress during compaction. (chapter 6). It was concluded that the (shear) strength of the compact is reflected in the compaction behaviour.

The behaviour of the compact varies with the loading conditions. By subjecting the compact to a tensile force, the influence of the binder was observed. A model has been developed to characterize the deformation of the binder. The compaction behaviour was established by subjecting the compact to various combinations of compressive and shear stresses (chapter 7).

The compaction process has been simulated in order to predict the homogeneity of the compact. For this purpose, techniques which consider the granulate to be a continuum have been successfully applied (chapter 8).

Samenvatting

Dit proefschrift beschrijft een onderzoek naar het persgedrag van gegranuleerd mangaan-zink-ferriet poeder. Hoofddoel is het onderzoeken van de samenhang tussen de poedereigenschappen, de perscondities en de eigenschappen van het geperste produkt. Inzicht is verkregen uit de analyse van de ruimtelijke structuur van persprodukten, de relatie tussen de persdruk en de dichtheid en het gedrag van persprodukten onder uiteenlopende belastingen.

De geperste produkten bevatten poriën van uiteenlopende groottes. De porie-grootteverdeling kan gemeten worden met behulp van porosimetrie. Zowel het indringen van kwik als de adsorptie van stikstof zijn op geschiktheid onderzocht (hoofdstuk 2). Gelet op de poriegrootte binnen geperste produkten is kwikporosimetrie een geschiktere techniek dan stikstof-adsorptie.

De invloed van perscondities op de dichtheid en de bijbehorende porie-grootteverdeling is onderzocht in hoofdstuk 3. Aan de hand hiervan kon een kwalitatief beeld van het persproces afgeleid worden.

De interpretatie van gemeten porie-grootte-verdelingen met behulp van tweedimensionale ruimtelijke cellen is ontwikkeld in hoofdstuk 4. Aan de hand van direkte visuele waarnemingen is de geldigheid van het model geverifieerd.

De toepassing van het principe van eigen gelijkvormigheid om beelden en porie-grootte-verdelingen te karakteriseren volgt in hoofdstuk 5. Evenals uit het model gebaseerd op ruimtelijke cellen volgt dat de granules agglomeraten van deeltjes bevatten.

De relatie tussen de persdruk en de dichtheid tijdens het persen wordt bepaald door de grootte, vorm en pakking van de ferrietdeeltjes. De relatie blijkt ongevoelig te zijn voor de perscondities. De relatie vertoont wel een knik bij een dichtheid waarbij het geperste produkt net voldoende samenhang heeft. Deze waarneming is aan de hand van een analyse van de spanningstoestand gemodelleerd (hoofdstuk 6). Hieruit kon een relatie tussen de (afschuif-) sterkte van het geperste produkt en het persgedrag gevonden worden.

Onder invloed van de soort belasting varieert het gedrag van het geperste produkt. Wanneer een trekbelasting opgelegd wordt, kan de invloed van de binder waargenomen worden. Teneinde het deformatiegedrag van de binder te karakteriseren, is een model ontwikkeld. Het persgedrag kon gemodelleerd worden aan de hand van een kwasi-elastische beschrijving door het geperste produkt te onderwerpen aan verschillende combinaties van compressie- en afschuifbelastingen (hoofdstuk 7).

Teneinde de homogeniteit van het geperste produkt te voorspellen, is het persgedrag gesimuleerd. Hiervoor zijn technieken die het granulaat beschouwen als een continuum met goed gevolg toegepast (hoofdstuk 8).

Acknowledgements

First of all, I would like to thank everyone who has, in one way or another, assisted me during the course of the PhD project. In particular, the guidance and constructive comments of prof.dr. G. de With and prof.dr. R. Metselaar during the writing of this thesis have been greatly appreciated. Special thanks are also due to ing. N. Sweegers for conducting the strength test measurements, ing. P. Witbreuk for his help in updating the nitrogen adsorption equipment, W. van der Meulen for sectioning the compacts, ing. R. van der Drift for pressing numerous compacts and C. Geenen for his assistance with SEM. In addition, the interesting discussions with ing. M. de Graaf and ir. J. Vrolijk are acknowledged.

Furthermore, I would like to thank prof.dr. F. Meijer, dr. F. Carpay and prof.dr. G. de With for providing me with the opportunity to conduct my PhD work at the Philips Research Laboratories ('Nat.Lab.') in Eindhoven. It has been a privilege to work in such a stimulating and interesting environment. Finally, the funding provided jointly by Philips Research and Philips Components (dr. R. Wernicke) is gratefully acknowledged.

Curriculum vitae

Hylke Jan Glass was born in Delft, the Netherlands, on the 4th of April 1965. After completing the secondary school with the highest grades of the school (Nederlands Lyceum, the Hague, 1983), he studied Chemical Engineering at the Technical University of Delft. During this period, he was a member of the students union "Delftsch Studenten Corps". In 1986, he participated on a study tour of Japan, which was followed by practical training in Singapore. In May 1988, he obtained his Masters degree after completing a thesis titled "Analysis of Gas-Solids Flow in Fast Fluidized Beds and in Standpipes". Subsequently, he worked for Keuken en de Koning, a firm specialized in process engineering.

In 1989, he started work on a PhD project at the Philips Research Laboratories, Eindhoven, under supervision of the Technical University of Eindhoven. During this project, the processing of a ceramic material with important commercial applications was studied. Results relating to the compaction process stage are presented in this thesis.

Stellingen behorende bij het proefschrift

Compaction behaviour of (Mn,Zn)-ferrite granulate

H.J. Glass

14 april 1994

1. De waarneming dat verhoging van de vochtigheid tijdens de opslag van granulaat dat polyvinylalkohol bevat, een toename van de sterkte van het persprodukt tot gevolg heeft, duidt op onnauwkeurigheid in de proefnemingen.

J. Brewer, R. Moore, J. Reed, 'Effect of Relative Humidity on the Compaction of Barium Titanate and Manganese Zinc Ferrite Agglomerates Containing Polyvinyl Alcohol', Ceramic Bulletin, vol. 60, no. 2 (1981), 212-220.

2. Bij het bepalen van de spanning en de korrelgrootte in een materiaal dient meer dan èèn reflectie uit het Röntgen-diffractie patroon gebruikt te worden.

V. Sankaranarayanan, N. Gajbhiye, 'Low-Temperature Preparation of Ultrafine Rare-Earth Iron Garnets', Journal of the American Ceramic Society, vol. 73, no. 5 (1990), 1301-1307.

3. De bepaling van de 'fractal' dimensie van twee-dimensionale beelden zoals voorgesteld door H. Schwarz en H. Exner is onjuist.

H. Schwarz, H. Exner, 'The implementation of the concept of fractal dimension on a semi-automatic image analyzer', Powder Technology, 27 (1980), 207-213.

4. Bij vergelijking van de deeltjesgrootte bepaald met transmissie-elektronen-microscopie, Röntgen-diffractie en stikstof-adsorptie dient expliciet rekening gehouden te worden met de onderliggende aannames.

V. Sankaranarayanan, N. Gajbhiye, 'Low-Temperature Preparation of Ultrafine Rare-Earth Iron Garnets', Journal of the American Ceramic Society, vol. 73, no. 5 (1990), 1301-1307.

5. Het bepalen van de echte vorm van de poriën aan de hand van indirecte meetmethoden, zoals kwikporosimetrie en stikstof-adsorptie, is niet mogelijk.

Ö. Cebeci, 'The Intrusion of Conical and Spherical Pores in Mercury Intrusion Porosimetry', Journal of Colloid and Interface Science, 78 (1980), 383-388.

6. De constatering van Zheng en Reed dat verkleining van de granulegrootte tot homogenere persproducten leidt, is niet gebaseerd op experimentele analyse van het granulaat en het persgedrag.

J. Zheng, J. Reed, 'Effects of Particle Packing Characteristics on Solid-State Sintering', Journal of the American Ceramic Society, 72 (1989), 810-817.

7. Een relatie tussen de elasticiteits-modulus E en de dichtheid ρ gebaseerd op de fractie van het korreloppervlak dat zich tussen de korrels bevindt, heeft alleen empirische betekenis.

R. Cytermann, 'A New Way to Investigate the Dependence of Elastic Moduli on the Microstructure of Porous Materials', Powder Metallurgy International, 19 (1987), 27-30.

8. De populariteit van 'fractals' valt te verklaren uit de behoefte van onderzoekers om complexe verschijnselen met eenvoudige kentallen te beschrijven.

9. De democratie zal gestimuleerd worden als verkiezingen buiten de schoolvakanties gehouden worden.

10. Het is opmerkelijk dat Nederlanders spreken van uitnodigen waar er bij Duitsers, Engelsen en Fransen sprake is van "in-nodigen".